

**Ultrafast Snapshots: Understanding the photoinduced charge transfer in donor–(bridge)–acceptor systems**

Wei, Z.

**DOI**

[10.4233/uuid:1a3f3c21-1d83-400f-8040-726f18258f4d](https://doi.org/10.4233/uuid:1a3f3c21-1d83-400f-8040-726f18258f4d)

**Publication date**

2023

**Document Version**

Final published version

**Citation (APA)**

Wei, Z. (2023). *Ultrafast Snapshots: Understanding the photoinduced charge transfer in donor–(bridge)–acceptor systems*. [Dissertation (TU Delft), Delft University of Technology]. <https://doi.org/10.4233/uuid:1a3f3c21-1d83-400f-8040-726f18258f4d>

**Important note**

To cite this publication, please use the final published version (if applicable). Please check the document version above.

**Copyright**

Other than for strictly personal use, it is not permitted to download, forward or distribute the text or part of it, without the consent of the author(s) and/or copyright holder(s), unless the work is under an open content license such as Creative Commons.

**Takedown policy**

Please contact us and provide details if you believe this document breaches copyrights. We will remove access to the work immediately and investigate your claim.

# **Ultrafast Snapshots**

Understanding the photoinduced charge transfer in  
donor-(bridge)-acceptor systems

**Zimu WEI**





# **Ultrafast Snapshots**

Understanding the photoinduced charge transfer in  
donor-(bridge)-acceptor systems

## **Dissertation**

for the purpose of obtaining the degree of doctor  
at Delft University of Technology  
by the authority of the Rector Magnificus Prof. dr. ir. T.H.J.J. van der Hagen,  
chair of the Board for Doctorates

to be defended publicly on  
Monday 20 November 2023 at 12:30 o'clock

by

**Zimu WEI**

Master of Science in Chemical Engineering,  
Delft University of Technology, the Netherlands  
born in Ma'anshan, China.

This dissertation has been approved by the promotor.

Composition of the doctoral committee:

Rector Magnificus,	chairperson
Prof. dr. F. C. Grozema	Delft University of Technology, promotor
Prof. dr. H. S. J. van der Zant	Delft University of Technology, promotor

*Independent members:*

Prof. dr. R. A. J. Janssen	Eindhoven University of Technology
Prof. dr. J. M. Thijssen	Delft University of Technology
Prof. dr. J. H. van Esch	Delft University of Technology
Prof. dr. S. S. Faraji	University of Groningen
Dr. L. Protesescu	University of Groningen



This work received financial support from the Dutch Research Council (NWO) through the research programme “Natuurkunde Vrije Programmas”, project nr. 680.92.18.01 — Chirality-induced spin selectivity.

*Printed by:* Ipskamp printing

*Cover designed by:* Zimu Wei

Copyright © 2023 by Z. Wei

ISBN 978-94-6473-280-1

An electronic version of this dissertation is freely available at  
<https://repository.tudelft.nl/>.

*The Universe is under no obligation to make sense to you.*

Neil deGrasse Tyson



# Contents

<b>1. Introduction</b>	<b>1</b>
1.1. Photoinduced charge transfer . . . . .	2
1.2. Organic donor–bridge–acceptor system . . . . .	3
1.3. Hybrid donor–acceptor system . . . . .	5
1.4. Outline of the thesis . . . . .	6
<b>2. Theoretical background and experimental methods</b>	<b>9</b>
2.1. Basic theory of electron transfer in donor-bridge-acceptor systems .	10
2.1.1. Marcus–Hush theory . . . . .	10
2.1.2. Assumptions and limitations . . . . .	13
2.2. Experimental techniques . . . . .	16
2.2.1. Femtosecond transient absorption spectroscopy . . . . .	16
2.2.2. Circularly polarized transient absorption spectroscopy . . . . .	19
<b>3. Excited state dynamics of acceptor–donor–acceptor systems based on BODIPY</b>	<b>25</b>
3.1. Introduction . . . . .	26
3.2. Results and discussion . . . . .	27
3.2.1. Steady-state optical properties . . . . .	27
3.2.2. Femtosecond transient absorption . . . . .	29
3.2.3. Global analysis . . . . .	31
3.2.4. Electronic structure calculations . . . . .	33
3.3. Conclusions . . . . .	36
3.4. Methods . . . . .	37
<b>A. Appendix to Chapter 3</b>	<b>43</b>
<b>4. Fast charge separation driven by relaxation of hot excited state</b>	<b>55</b>
4.1. Introduction . . . . .	56
4.2. Results and discussion . . . . .	58
4.2.1. Steady-state optical properties . . . . .	58
4.2.2. Femtosecond transient absorption . . . . .	62
4.2.3. Global and target analysis . . . . .	64
4.2.4. Electronic structure calculations . . . . .	68
4.3. Conclusions . . . . .	71
4.4. Methods . . . . .	72
<b>B. Appendix to Chapter 4</b>	<b>83</b>

---

<b>5. Functional molecules on the surface of perovskite nanoplatelets</b>	<b>101</b>
5.1. Introduction	102
5.2. Results and discussion	103
5.2.1. System design	103
5.2.2. Steady-state optical properties	104
5.2.3. Photoexcitation at 490 nm	106
5.2.4. Photoexcitation at 380 nm	110
5.3. Conclusions	114
5.4. Methods	115
<b>C. Appendix to Chapter 5</b>	<b>121</b>
<b>6. Towards probing chirality-induced spin selectivity</b>	<b>137</b>
6.1. Introduction	138
6.2. Optical spin injection	140
6.2.1. Working principle	140
6.2.2. Chiral donor–bridge–acceptor molecule	141
6.2.3. Bulk perovskite thin film	143
6.2.4. Perovskite nanoplatelets	146
6.3. Experiment design	148
6.3.1. System design	148
6.3.2. Proposed measurements	152
6.4. Conclusions	155
<b>D. Appendix to Chapter 6</b>	<b>163</b>
<b>Summary</b>	<b>173</b>
<b>Samenvatting</b>	<b>177</b>
<b>Acknowledgments</b>	<b>181</b>
<b>Curriculum Vitae</b>	<b>185</b>
<b>List of Publications</b>	<b>187</b>
<b>List of Presentations</b>	<b>189</b>

# 1

## Introduction

*Life, according to Albert Szent-Györgyi<sup>1</sup>, is nothing but an electron looking for a place to rest. Figuring out how an electron finds a place to rest is the cornerstone of the present thesis. Or, to be specific, understanding the mechanism of electron transfer in the so-called "donor-acceptor" systems. Such a model system is designed to enable the transfer of an electron from the donor to the acceptor upon photoexcitation, a process known as "photoinduced charge transfer". This captivating phenomenon lies at the heart of solar energy conversion, encompassing domains like artificial photosynthesis, photovoltaics, and photocatalysis. A comprehensive grasp of this process bears tremendous significance across a broad spectrum. In this chapter, we introduce the process of photoinduced charge transfer and two types of model systems for studying this process. Finally, the outline of this thesis is provided.*

---

<sup>1</sup>The Nobel Prize in Physiology or Medicine 1937 was awarded to Albert von Szent-Györgyi Nagyrápolt "for his discoveries in connection with the biological combustion processes, with special reference to vitamin C and the catalysis of fumaric acid. <https://www.nobelprize.org/prizes/medicine/1937/summary/>.



## 1.1. Photoinduced charge transfer

As you are reading this thesis, light is entering your eyes, stimulating photosensitive pigments in your retina, and initiating a series of photochemical reactions. These photochemical reactions ultimately generate electrical signals in your brain, enabling your visual perception. If you are reading this on an organic light-emitting display (OLED), countless charges (electrons and holes) are currently recombining relentlessly to emit light, allowing you to read the contents laid before you. This technology pivots on one particular example of photochemical reactions, known as "photoinduced charge transfer (CT)".

During the process of photoinduced CT, a photon is absorbed, and its energy creates a Coulombic bound electron–hole pair, known as an exciton. Upon overcoming this electrostatic Coulomb potential, the electron (hole) can be separated from its counterpart and transferred over a certain distance. The transfer of charges can occur in several ways, depending on the specific system and its electronic structure. It may involve electron (hole) transfer from one molecule to another, charge separation within a single molecule, or movement of charges between different regions of a material. Eventually, the journey of this electron–hole pair can result in two trajectories. The first one is a permanent separation when charges are extracted by external drains. This process is at the core of photosynthesis[1–3] and organic solar cells[4–6]. The second one is charge recombination, where this electron–hole pair releases its excess energy through the emission of photons or heat dissipation. This process holds great relevance for light-emitting applications, such as OLED[7–9].

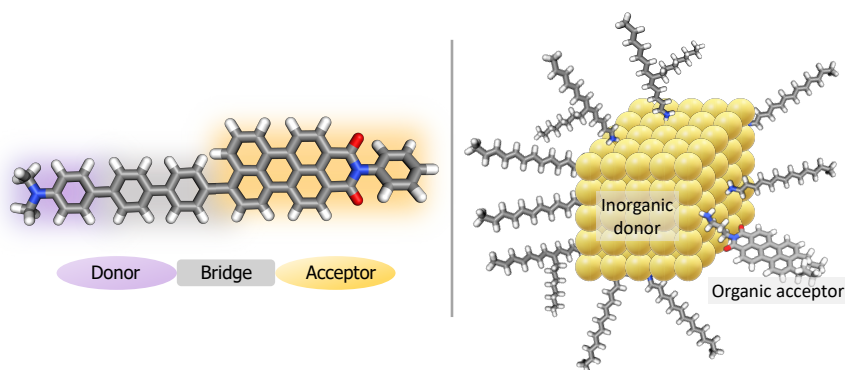


**Figure 1.1.** Schematic illustration of a DBA molecule (left) and a hybrid DA system (right).

To understand and ultimately tailor or optimize the photoinduced CT for specific applications, model systems are typically required to break down its complexity and study the CT process systematically. Donor-bridge-acceptor (DBA) molecules serve as such model systems, offering a versatile platform for

the systematic study of photoinduced CT. A DBA system typically entails an electron-rich (donor) and an electron-deficient (acceptor) moieties intervened by a molecular bridge, as illustrated in Figure 1.1. It is designed in such a way that photoexcitation will lead to an electron being transferred from donor to acceptor, forming a charge-separated (CS) state.

Photoinduced CT in DBA systems has been extensively studied with organic molecules for more than half a century. Following the discovery of colloidal quantum dots in 1981[10], research of photoinduced CT has ventured into novel territories, embracing hybrid donor–acceptor (DA) assemblies based on semiconductor nanocrystals and organic molecules (Figure 1.1). In this thesis, we focus on both conventional DBA systems and hybrid DA systems, aiming to understand how the key parameters of the system influence the photoinduced CT process.

## 1.2. Organic donor–bridge–acceptor system

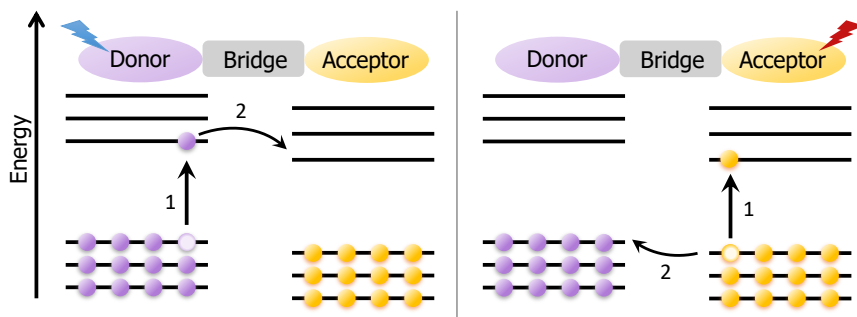


**Figure 1.2.** Schematic representation of photoinduced electron transfer (left) and hole transfer (right) in a DBA molecule. 1: photoexcitation; 2: CT.

A large part of this thesis focuses on covalently bonded DBA molecules and their derivatives. They are designed to enable the charge rearrangement within the molecule upon photoexcitation. Typically, an electron donor with a low ionization potential and an electron acceptor with a high electron affinity are employed. These donor and acceptor moieties are indirectly connected through a molecular bridge. Figure 1.2 schematically shows the photoinduced CT process in a DBA molecule. Upon photoexciting the electron donor at a suitable wavelength, an electron is excited from the highest occupied molecular orbital of the donor to its lowest unoccupied molecular orbital, yielding the excited state of the donor. Subsequently, this excited electron moves to the lowest unoccupied molecular orbital of the acceptor, which is at a lower energy. As a result, a new species is formed, with a positive charge on the donor and a negative charge on the acceptor. This species is commonly referred to as the CT state or the CS state. Similarly, photoexcitation can also create the excited state

of the acceptor. In this case, a hole is subsequently transferred from the highest occupied molecular orbital of the acceptor to that of the donor. Finally, the same CT or CS state is formed as in the electron transfer process but it is important to realize that this state is formed by a different pathway.

Given the significant relevance of moving electrons through an organic molecule, the implication of CT in DBA molecules extends far beyond its applications in photosynthesis and photovoltaics. In fact, it has inspired the field of molecular electronics. In 1974, Aviram and Ratner proposed the notion of molecular diodes based on DA molecules[11], marking a pivotal moment in this field. Since then, extensive studies have been devoted to exploring the potential of organic molecules as molecular wires in molecular junctions[12–14]. Despite the distinct nature of molecular electron transfer compared to electron transport between two electrodes through a molecule, studies of CT in DBA molecules have revealed important mechanisms that both processes rely on[15, 16]. A notable example is the transition from coherent tunneling to incoherent hopping as the length of the molecule increases[17–19]. As shown in Figure 1.3, coherent tunneling occurs when the bridge energy levels are too high to be occupied during the CT process. However, as the bridge length increases, the tunneling probability decreases exponentially. Meanwhile, the wave function of the bridge becomes more delocalized, leading to overall lower energy levels. When the tunneling probability diminishes and the bridge orbitals become thermally accessible, the CT process predominantly involves real intermediate states with a reduced or oxidized bridge, leading to the incoherent hopping mechanism[20]. These two mechanisms have profound implications for CT properties in DBA molecules. For instance, coherent tunneling is typically associated with an exponential decrease in the CT rate as the DA distance increases, while a weak distance dependence of the CT rate is anticipated for incoherent hopping[21, 22].

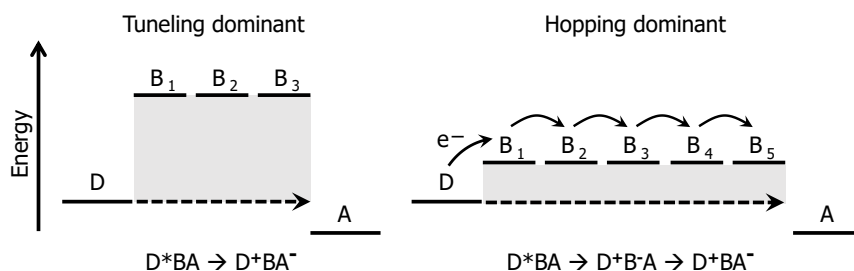


**Figure 1.3.** Schematic representation of the tunneling (left) and hopping (right) mechanisms for electron transfer in a DBA system. Dashed arrow: tunneling pathway. Solid arrows: hopping pathway.

Unfortunately, the observed CT behaviors tend to be more complicated in many real cases. This can be due to the coexistence of both mechanisms and/or the strong influence of the molecule's conformational dynamics and its

surrounding solvent on the measured CT rates. Examples of such complications are discussed in this thesis. Specifically, in [Chapter 3](#), we demonstrate how subtle differences in the DA distance and the conformational freedom determine the CT behavior. [Chapter 4](#) provides a more comprehensive understanding of the distance dependence of the CT rate and how it can be controlled by the ultrafast relaxation of the excited state.

The versatility of DBA systems offers a customized approach to deepen our fundamental understanding of intriguing and intricate phenomena. Specifically, this can be achieved by smart variations of individual moieties in the DBA system. One classic example is using DNA as a bridge to gain insights into the mechanisms underlying DNA damage and repair[23–26]. Another interesting idea is to use a chiral bridge to study the chirality-induced spin selectivity (CISS) effect, a recently discovered phenomenon with profound implications for spintronics and biological processes[27]. Thus far, there has been only one synthetic pursuit of such DBA molecules, employing 2,2'-dimethoxy-1,1'-binaphthalene as the chiral bridge[28]. In [Chapter 6](#), we present a chiral DBA system featuring a similar chiral bridge and discuss the suitability of such systems for studying spin-selective CT.

### 1.3. Hybrid donor–acceptor system

This thesis explores photoinduced CT beyond organic DBA molecules. In principle, any moieties with suitable electron-donating or electron-accepting abilities are potential candidates for a DA system. One particularly promising candidate for such a system is semiconductor nanocrystals. These nanocrystals offer abundant surface sites for the covalent or ionic adsorption of organic electron donors or acceptors that contain suitable anchoring groups ([Figure 1.1](#)). Together, they form an ideal platform for exploring the unique CT properties in nanoscale systems. These hybrid systems not only alleviate the strenuous efforts in organic synthesis but also have the potential to provide fruitful insights that are not commonly observed in their organic counterparts. One intriguing research area is to understand the CT mechanism in these hybrid systems based on the theoretical model of conventional DBA molecules[29]. Alongside its fundamental importance, the practical significance of CT in these hybrid systems has been harnessed for catalysis for more than two decades[30]. In [Chapter 5](#), we explore in depth the photoinduced CT in such a hybrid DA system by selectively exciting the donor and acceptor. This study further inspires the system design in [Chapter 6](#) for probing the CISS effect.

## 1.4. Outline of the thesis

This thesis presents a systematic approach to study photoinduced CT in a variety of DBA systems. We focus on understanding the interplay between system parameters and CT behaviors in both organic DBA derivatives and hybrid DA systems involving semiconductor nanocrystals. The CT mechanisms and the corresponding rate constants are obtained through data analysis of femtosecond transient absorption spectra. Electronic structure calculations are employed in some chapters as a complementary approach to interpret experimental findings.

Here we provide the outline of this thesis. After this introductory chapter, the subsequent chapter, [Chapter 2](#), presents the relevant theoretical background and experimental methods. In [Chapter 3](#), we investigate the excited state dynamics of three acceptor–donor–acceptor molecules in solvents of varying polarities. By combining ultrafast spectroscopy with complementary electronic structure calculations, we demonstrate the relation between structure and photophysical behaviors in these triads. Specifically, how delocalization in the excited state and subsequent CT process can be strongly suppressed by a larger DA distance and restricted conformational freedom.

In [Chapter 4](#), we present a comprehensive study on the distance-dependent photophysics of three DBA derivatives with varying numbers of phenyl bridges ( $n = 0, 1, 2$ ). The study reveals distinct CS behaviors at different DA distances. At the shortest distance, a strong DA interaction leads to a hot excited state with significant CT character, resulting in subpicosecond CS. At the longest distance, a surprisingly fast CS process is observed, albeit with suppressed CT character in the hot excited state. We attribute this unanticipated CS behavior to ultrafast geometry relaxation and concomitant charge delocalization in the relaxed excited state. These findings highlight the importance of considering relaxation dynamics when discussing distance dependence in DBA molecules.

In [Chapter 5](#), we delve into the CT mechanism in hybrid organic-inorganic DA systems, with an emphasis on manipulating the CT rate by tuning the driving force. This chapter provides a systematic study of the effects of tuning both the thickness of the semiconductor nanoplatelets and the electron-accepting capabilities of the molecular acceptors on the CT processes. Through careful analysis of the transient absorption data, distinct CT mechanisms are identified when selectively exciting either the electron donors or acceptors. These results shed light on the photophysics in these hybrid DA systems and pave the way for tailoring them for various light-harvesting applications.

Finally, in [Chapter 6](#), we explore the possibility of studying the CISS effect in an electrodeless way. We begin by discussing the generation of spin-polarized excited states in three different systems, namely chiral DBA molecules, perovskite thin films, and colloidal perovskite nanoplatelets. Drawing from these observations, we propose a design of a chiral DA system for probing CISS using circularly polarized light. Furthermore, we address the potential challenges of implementing the proposal and suggest additional measurements to mitigate them.

## References

1. Imahori, H., Mori, Y. & Matano, Y. Nanostructured artificial photosynthesis. *Journal of Photochemistry and Photobiology C: Photochemistry Reviews* **4**, 51–83 (2003).
2. Wahadoszamen, M., Margalit, I., Ara, A. M., Van Grondelle, R. & Noy, D. The role of charge-transfer states in energy transfer and dissipation within natural and artificial bacteriochlorophyll proteins. *Nature communications* **5**, 5287 (2014).
3. Scholes, G. D., Fleming, G. R., Olaya-Castro, A. & Van Grondelle, R. Lessons from nature about solar light harvesting. *Nature chemistry* **3**, 763–774 (2011).
4. Song, P., Li, Y., Ma, F., Pullerits, T. & Sun, M. Photoinduced electron transfer in organic solar cells. *The Chemical Record* **16**, 734–753 (2016).
5. Chen, Z. & Zhu, H. Photoinduced charge transfer and recombination dynamics in star nonfullerene organic solar cells. *The Journal of Physical Chemistry Letters* **13**, 1123–1130 (2022).
6. Dou, L., You, J., Hong, Z., Xu, Z., Li, G., Street, R. A. & Yang, Y. 25th anniversary article: a decade of organic/polymeric photovoltaic research. *Advanced materials* **25**, 6642–6671 (2013).
7. Burroughes, J. H., Bradley, D. D., Brown, A., Marks, R., Mackay, K., Friend, R. H., Burns, P. L. & Holmes, A. B. Light-emitting diodes based on conjugated polymers. *nature* **347**, 539–541 (1990).
8. Armstrong, N. R., Wang, W., Alloway, D. M., Placencia, D., Ratcliff, E. & Brumbach, M. Organic/organic' heterojunctions: organic light emitting diodes and organic photovoltaic devices. *Macromolecular rapid communications* **30**, 717–731 (2009).
9. Sarma, M., Chen, L.-M., Chen, Y.-S. & Wong, K.-T. Exciplexes in OLEDs: Principles and promises. *Materials Science and Engineering: R: Reports* **150**, 100689 (2022).
10. Ekimov, A. I. & Onushchenko, A. A. Quantum size effect in three-dimensional microscopic semiconductor crystals. *ZhETF Pisma Redaktsiiu* **34**, 363 (1981).
11. Aviram, A. & Ratner, M. A. Molecular rectifiers. *Chemical physics letters* **29**, 277–283 (1974).
12. Heath, J. R. Molecular electronics. *Annual Review of Materials Research* **39**, 1–23 (2009).
13. Valianti, S. & Skourtis, S. S. Observing Donor-to-Acceptor Electron-Transfer Rates and the Marcus Inverted Parabola in Molecular Junctions. *The Journal of Physical Chemistry B* **123**, 9641–9653 (2019).
14. Kondratenko, M., Moiseev, A. G. & Perepichka, D. F. New stable donor-acceptor dyads for molecular electronics. *Journal of Materials Chemistry* **21**, 1470–1478 (2011).
15. Nitzan, A. A relationship between electron-transfer rates and molecular conduction. *The Journal of Physical Chemistry A* **105**, 2677–2679 (2001).

16. Mujica, V. & Ratner, M. A. Current–voltage characteristics of tunneling molecular junctions for off-resonance injection. *Chemical Physics* **264**, 365–370 (2001).
17. Davis, W. B., Svec, W. A., Ratner, M. A. & Wasielewski, M. R. Molecular-wire behaviour in p-phenylenevinylene oligomers. *Nature* **396**, 60–63 (1998).
18. Goldsmith, R. H., Sinks, L. E., Kelley, R. F., Betzen, L. J., Liu, W., Weiss, E. A., Ratner, M. A. & Wasielewski, M. R. Wire-like charge transport at near constant bridge energy through fluorene oligomers. *Proceedings of the National Academy of Sciences* **102**, 3540–3545 (2005).
19. Hines, T., Diez-Perez, I., Hihath, J., Liu, H., Wang, Z.-S., Zhao, J., Zhou, G., Müllen, K. & Tao, N. Transition from tunneling to hopping in single molecular junctions by measuring length and temperature dependence. *Journal of the American Chemical Society* **132**, 11658–11664 (2010).
20. Wenger, O. S. How donor- bridge- acceptor energetics influence electron tunneling dynamics and their distance dependences. *Accounts of Chemical Research* **44**, 25–35 (2011).
21. Lewis, F. D., Liu, J., Weigel, W., Rettig, W., Kurnikov, I. V. & Beratan, D. N. Donor-bridge-acceptor energetics determine the distance dependence of electron tunneling in DNA. *Proceedings of the National Academy of Sciences* **99**, 12536–12541 (2002).
22. Gilbert, M. & Albinsson, B. Photoinduced charge and energy transfer in molecular wires. *Chemical Society Reviews* **44**, 845–862 (2015).
23. Hall, D. B., Holmlin, R. E. & Barton, J. K. Oxidative DNA damage through long-range electron transfer. *Nature* **382**, 731–735 (1996).
24. Lewis, F. D., Letsinger, R. L. & Wasielewski, M. R. Dynamics of photoinduced charge transfer and hole transport in synthetic DNA hairpins. *Accounts of chemical research* **34**, 159–170 (2001).
25. Genereux, J. C. & Barton, J. K. Mechanisms for DNA charge transport. *Chemical reviews* **110**, 1642–1662 (2010).
26. Kanvah, S., Joseph, J., Schuster, G. B., Barnett, R. N., Cleveland, C. L. & Landman, U. Oxidation of DNA: damage to nucleobases. *Accounts of chemical research* **43**, 280–287 (2010).
27. Naaman, R., Paltiel, Y. & Waldeck, D. H. Chiral molecules and the electron spin. *Nature Reviews Chemistry* **3**, 250–260 (2019).
28. Junge, M. J., Kordan, M. A. & Chernick, E. T. Synthesis of chiral donor–acceptor dyes to study electron transfer across a chiral bridge. *The Journal of Organic Chemistry* **85**, 13793–13807 (2020).
29. Zhu, H., Yang, Y., Wu, K. & Lian, T. Charge transfer dynamics from photoexcited semiconductor quantum dots. *Annual review of physical chemistry* **67**, 259–281 (2016).
30. Harris, R. D., Bettis Homan, S., Kodaimati, M., He, C., Nepomnyashchii, A. B., Swenson, N. K., Lian, S., Calzada, R. & Weiss, E. A. Electronic processes within quantum dot-molecule complexes. *Chemical reviews* **116**, 12865–12919 (2016).

# 2

## Theoretical background and experimental methods

*In this chapter, we introduce the theoretical and technical foundations of this thesis. Firstly, we provide a review of the basic theory of electron transfer in conventional donor-bridge-acceptor systems, highlighting the main assumptions and limitations of this theory. It is important to note that this section aims to provide a general understanding of the key parameters governing the electron transfer process rather than a comprehensive overview of the entire theoretical framework. The second half of this chapter focuses on explaining the working principle of the main technique used in this thesis: femtosecond transient absorption spectroscopy. We cover both the conventional setup that utilizes linearly polarized light and the newly adapted setup for generating circularly polarized light. This section aims to provide a tutorial explanation of the technique, guiding the future use of the setup.*



## 2.1. Basic theory of electron transfer in donor-bridge-acceptor systems

### 2.1.1. Marcus–Hush theory

For nearly seven decades, Marcus–Hush theory[1–4] has been arguably the most important model for describing electron transfer reactions.

In the classical model, it characterizes the electron transfer rate,  $k_{\text{ET}}$ , in merely three parameters: the overall Gibbs free energy of reaction,  $\Delta G^0$ , the reorganization energy,  $\lambda$ , and the electronic coupling between the donor and acceptor,  $H_{\text{DA}}$ .

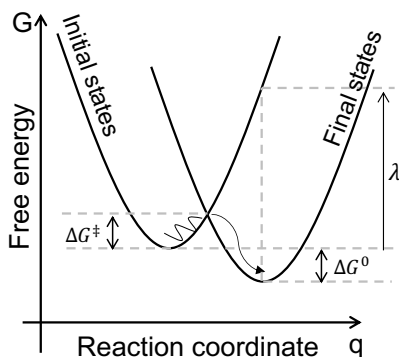


**Figure 2.1.** Free energy curves for non-adiabatic electron transfer reactions.

As an extension of transition state theory[5], the free energy curves of the initial (reactant or DA) and final (product or  $\text{D}^+\text{A}^-$ ) states in the system are represented by two identical parabolas (Figure 2.1). The reaction coordinate ( $q$ ) effectively embodies all the degrees of freedom of the system including the donor and acceptor and the surrounding solvent. The reorganization energy,  $\lambda$ , is the amount of energy required to deform the initial state from its equilibrium coordinate to that of the final state while staying on the same energy curve so that no electron is transferred. Thus,  $\lambda$  increases with the steepness of the potential curve and the increasing separation between the equilibrium coordinates of the initial and final states. The driving force,  $\Delta G^0$ , is the energy difference between the initial and final states at their equilibrium coordinates. The free energy barrier,  $\Delta G^\ddagger$ , is defined as the energy difference between the crossing point and the minimum of the initial energy curve. As the energy curves are parabolic,  $\Delta G^\ddagger$  is related to  $\lambda$  and  $\Delta G^0$  by

$$G^\ddagger = \frac{1}{4\lambda}(\Delta G^0 + \lambda)^2. \quad (2.1)$$

At room temperature, the rate constant for non-adiabatic electron transfer ( $k_{\text{ET}}$ )

can be expressed by

$$k_{\text{ET}} = \frac{2\pi}{\hbar} |H_{\text{DA}}|^2 \sqrt{\frac{1}{4\pi\hbar k_{\text{B}} T}} \exp\left(-\frac{(\Delta G^0 + \hbar)^2}{4\hbar k_{\text{B}} T}\right). \quad (2.2)$$

Here,  $k_{\text{B}}$  is the Boltzmann constant and  $T$  is the temperature.  $H_{\text{DA}}$  denotes the electronic interaction between the localized initial and final states at the nuclear configuration of the crossing point, and  $|H_{\text{DA}}|^2$  is the probability of an electron tunneling through the potential barrier. The value of the Gibbs free energy,  $\Delta G^0$ , is negative so that the final state is more favorable. This equation yields three regions for the electron transfer reaction: In the normal region ( $-\Delta G^0 < \hbar$ ),  $k_{\text{ET}}$  increases with increasing  $-\Delta G^0$  owing to the decreasing free energy barrier; when  $-\Delta G^0 = \hbar$ ,  $k_{\text{ET}}$  reaches the maximum, as the electron transfer reaction becomes barrier-less ( $\Delta G^\ddagger = 0$ ); in the inverted region ( $-\Delta G^0 < \hbar$ ),  $k_{\text{ET}}$  is predicted to decrease with increasing  $-\Delta G^0$ , as the energy barrier is reappearing.

### Reorganization energy

In general,  $\hbar$  in Equation (2.2) includes contributions from both inner-sphere,  $\hbar_i$ , and outer-sphere,  $\hbar_o$ , components. This means both the intramolecular nuclear reorganization and the reorganization of the surrounding solvent environment contribute to the overall reorganization energy. The latter is typically estimated based on a dielectric continuum model by Marcus[2]. In this model, the donor and the acceptor are approximated by two spheres with radii  $a_1$  and  $a_2$ :

$$\hbar_o = (\Delta e)^2 \left( \frac{1}{2a_1} + \frac{1}{2a_2} - \frac{1}{r_{\text{DA}}} \right) \left( \frac{1}{\epsilon_{\text{op}}} - \frac{1}{\epsilon_s} \right) \quad (2.3)$$

where  $\Delta e$  is the amount of charge transferred, and  $r_{\text{DA}}$  is the center-to-center distance between the donor and the acceptor.  $\epsilon_{\text{op}}$  and  $\epsilon_s$  are the optical (the square of the solvent refractive index) and static dielectric constants of the solvent, respectively. This equation has several physical implications. For example,  $\hbar_o$  is predicted to increase with increasing distance, decrease with increasing radii and vanish in non-polar solvent ( $\epsilon_{\text{op}} = \epsilon_s$ ).

### Driving force

The so-called Rehm-Weller equation[6], derived from the dielectric continuum model of solvation, has been widely used to estimate the driving force,  $\Delta G^0$  for photo-induced electron transfer over a distance of  $r_{\text{DA}}$ :

$$\Delta G^0 = E_{\text{ox}} - E_{\text{red}} - \frac{e^2}{r_{\text{DA}} \epsilon_s} + e^2 \left( \frac{1}{2a_{\text{ox}}} + \frac{1}{2a_{\text{red}}} \right) \left( \frac{1}{\epsilon_s} - \frac{1}{\epsilon_{\text{ref}}} \right) - E_{\text{ex}} \quad (2.4)$$

where  $E_{\text{ox}}$  and  $E_{\text{red}}$  are the oxidation and reduction potentials of the donor and acceptor, respectively.  $e$  is the elementary charge.  $E_{\text{ox}}$  is the energy of the lowest excited state of the donor. Similar to the assumption made in Equation (2.3), the radii of the radical cation  $a_{\text{ox}}$  and anion  $a_{\text{red}}$  are treated as spherical here.  $\epsilon_s$  is

the static dielectric constant of the solvent in which electron transfer takes place, and  $\epsilon_{\text{ref}}$  is the dielectric constant of the solvent in which the cyclic voltammetry measurements were performed to determine the  $E_{\text{ox}}$  or  $E_{\text{red}}$ .

### Effective electronic coupling

The effective electronic coupling depends on the electronic properties of the donor and the acceptor, but also on the details of the intervening medium. In a DBA system, where the donor and the acceptor are covalently connected to a bridge, the electronic states on the connecting bridge play a determining role in the electron transfer process. For systems where the bridge consists of  $N$  identical units with only the nearest neighbor interaction, the McConnell superexchange model[7] can be applied. According to this model, the intervening bridge mediates the electron transfer from the localized donor to acceptor by an effective electronic coupling, resulting in a nonzero electronic coupling even at a large DA distance. The energies of these bridge units should be considerably larger than that of the donor/acceptor, so that the electron can tunnel through these empty, high-lying fragment orbitals of the bridge instead of a multi-step hopping. Thus,  $H_{\text{DA}}$  can be approximated by

$$H_{\text{DA}} = \frac{V_{\text{DB}} V_{\text{BA}}}{\Delta E_{\text{DB}}} \left( \frac{V_{\text{BB}}}{\Delta E_{\text{DB}}} \right)^{N-1}, \quad (2.5)$$

where  $\Delta E_{\text{DB}}$  is the energy difference between the donor and bridge.  $V_{\text{DB}}$  and  $V_{\text{BA}}$  are the electronic coupling matrix elements between the donor and bridge and between the bridge and acceptor, respectively.  $V_{\text{BB}}$  denotes the electronic coupling between adjacent bridge units. The electronic coupling,  $V_{ij}$ , between the adjacent  $\pi$ -conjugated units  $i$  and  $j$  correlates with their torsional angles by a  $\cos(\Phi)$  law[8]

$$V_{ij} = V_{ij}^0 \cos(\Phi), \quad (2.6)$$

where  $V_{ij}^0$  is the electronic coupling between the adjacent units  $i$  and  $j$  at  $\Phi = 0^\circ$ . Consequently,  $H_{\text{DA}}$  can be significantly influenced by the torsional motions.

In addition to its angular dependence, Equation (2.5) suggests  $H_{\text{DA}}$  is also distance-dependent provided that the DA distance is proportional to the number of bridge units. As a result of the exponential radial character of electronic wave functions,  $H_{\text{DA}}$  is expected to decay exponentially with increasing DA distance  $r_{\text{DA}}$  in the framework of superexchange model[9]:

$$H_{\text{DA}} = H_0 \exp\left(\frac{-\beta(r_{\text{DA}} - r_0)}{2}\right). \quad (2.7)$$

Here,  $H_0$  is the effective electronic coupling between the donor and acceptor at van der Waals contact distance  $r_0$ .  $\beta$  is the attenuation factor that characterizes the steepness of this exponential decay.

Note that Equation (2.5) only takes into account all the direct coupling between adjacent units through the DBA system, hence this approximation becomes unreliable when the indirect interaction between non-nearest neighbor sites and/or multiple transfer pathways plays an important role.

### 2.1.2. Assumptions and limitations

Any approximate model is derived based on a number of simplifying assumptions and Marcus–Hush theory is no exception. Under certain circumstances, one or more underlying assumptions may break down resulting in complications. Therefore, it is crucial to acknowledge the main assumptions and limitations before applying this theory to describe electron transfer phenomena.

#### High temperature limit

Marcus–Hush theory has shown impressive agreement with experiments at high temperatures ( $\hbar\omega \ll k_B T$ ) [10–12]. At low temperatures, however, the nuclear tunneling effect is no longer negligible [2, 13, 14]. That is, in addition to crossing the barrier, electron transfer by tunneling through the barrier accounts for a major part of  $k_{ET}$ . This nuclear tunneling process is enabled by the vibrational overlap between the vibrational levels associated with the initial and final states. In this case, quantum mechanical correction to Equation (2.2) is necessary. According to the so-called Marcus–Levich–Jortner model [15], when electron transfer is coupled to a single high-frequency vibrational mode at a relatively low temperature ( $k_B T \ll \hbar\omega$ ), non-adiabatic  $k_{ET}$  becomes

$$k_{ET} = \frac{2\pi}{\hbar} |H_{DA}|^2 \sqrt{\frac{1}{4\pi\hbar k_B T}} \sum_{n=0}^{\infty} \exp(-S) \frac{S^n}{n!} \exp\left(\frac{-(\Delta G^0 + \hbar\omega + n\hbar\omega)^2}{4\hbar k_B T}\right). \quad (2.8)$$

In Equation (2.8),  $\hbar\omega$  is the energy of the coupled vibrational mode and  $n$  is the quantum number of the vibrational level in the final state.  $S$  is the Huang-Rhys factor, expressed as  $S = \hbar\omega_i / \hbar\omega$ , where  $\hbar\omega_i$  the inner-sphere reorganization energy for this vibrational mode. This equation can be further generalized to include a continuous transition throughout the entire temperature range [15].

This quantum mechanical correction and its generalizations have important implications for temperature dependence. For instance, instead of a vanishing  $k_{ET}$  at 0K as predicted by Equation (2.2), the tunneling effect leads to temperature-independent  $k_{ET}$  at very low temperatures [16]. Another example is the overestimated temperature dependence in the inverted region by Equation (2.2). When the energy curve of the final state is embedded in that of the initial state (as in the inverted region), the overlap of vibrational wave functions below the top of the barrier is substantial. Consequently, an electron can tunnel through the barrier efficiently. Since further increase in the temperature will barely increase the vibrational overlap, a very weak temperature dependence is seen [17, 18]. In this way, the tunneling effect compensates for the exaggerated temperature dependence predicted by the classical model. In this thesis, all the electron transfer processes have been studied at the room temperature. Therefore, the high temperature limit always holds true.

### Weak coupling limit

A weak coupling between the donor and acceptor is essential for the non-adiabatic limit to be valid. In the non-adiabatic limit, the mixing of the initial and final states is so weak that their wave functions are localized on the donor and acceptor along the reaction coordinate. Hence, at the crossing point, two energy curves become degenerate, and the electron has to jump abruptly from the donor to the acceptor. When the electronic coupling is strong, the adiabatic limit applies, leading to a different situation at the crossing point. In this case, the barrier height at the crossing point is lowered by  $|H_{DA}|$  with respect to that in the non-adiabatic limit. Thus, the system becomes delocalized over the donor and acceptor, and it moves smoothly from the initial state to the final state while staying on the lowest potential energy curve.

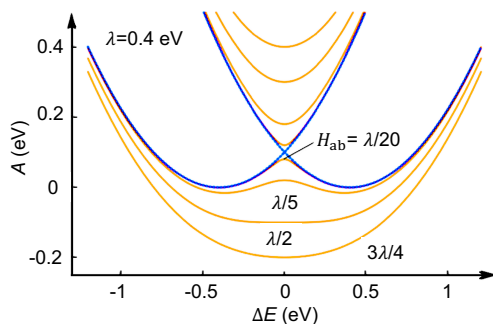


**Figure 2.2.** Free energy curves for different  $H_{DA}/\lambda$ . Adapted from ref[19]

Depending on the energy scales of the  $|H_{DA}|$  and  $\lambda$ , the degree of delocalization can be classified into three categories (at  $\Delta G^0 = 0$ ) [19]. First, when the coupling is much smaller than the reorganization energy ( $|H_{DA}| \ll \lambda$ ), the electron transfer occurs at a slow rate, and it can be considered as a non-adiabatic process. Second, when the coupling approaches half of the reorganization energy ( $0 \leq 2|H_{DA}| \leq \lambda$ ), treating the initial and final states as two separate states is inadequate, as additional optical and electronic properties due to the donor and acceptor interactions can be significant. Finally, when the coupling is larger than half of the reorganization energy ( $2|H_{DA}| \geq \lambda$ ), such a strong coupling will completely diminish the activation barrier, resulting in a minimum at the crossing point for the energy curve of the system (Figure 2.2).

### Condon approximation

Both Equation (2.2) and Equation (2.8) share an underlying assumption that the electronic coupling  $H_{DA}$  is independent of the nuclear configuration. This is commonly referred to as the Condon approximation, which is invoked in Fermi's golden rule for non-adiabatic electron transfer.

Consider a transition from  $\psi$  to  $\psi'$  by a perturbation  $H'$ , the probability of this

transition is given by Fermi's golden rule as:

$$T = \frac{2\pi}{\hbar} |\langle \psi | H' | \psi' \rangle|^2 \rho. \quad (2.9)$$

Under the Born–Oppenheimer approximation, nuclei are considered as stationary in the timescale of an electronic transition. Thus, the electronic wave functions can be separated from the nuclear wave functions in the general coupling matrix element:

$$|\langle \psi | H' | \psi' \rangle|^2 = |\langle \psi_n \psi_e | \hat{H}' | \psi'_e \psi'_{n'} \rangle|^2. \quad (2.10)$$

If the dependence of the matrix element on the nuclear configuration is disregarded (Condon approximation), then the general coupling matrix element can be written as a product of the electronic coupling matrix element and the nuclear overlap function:

$$|\langle \psi_n \psi_e | \hat{H}' | \psi'_e \psi'_{n'} \rangle|^2 = |\langle \psi_e | \hat{H}' | \psi'_e \rangle|^2 |\langle \psi_n \psi'_{n'} \rangle|^2. \quad (2.11)$$

The latter is also known as the Franck–Condon factor.

This Condon approximation clearly fails in some cases. Consequently, some phenomena of electron transfer predicted by the Marcus–Hush theory can be inconsistent with the experiments. For instance, it is known that the molecular orbital overlap depends on the molecular twisting as shown by Equation (2.6). When the electron tunneling occurs on the same timescale as the vibrational mode, such as the intramolecular torsional motion,  $H_{DA}$  will vary with this nuclear motion in the event of electron transfer, thereby breaking down the Condon approximation. As a result, the temperature dependence of  $k_{ET}$  can be dictated by the torsional motion through  $H_{DA}$ , leading to complex temperature dependence instead of the predicted Arrhenius-like behavior. Davis et al. have shown such non-Arrhenius temperature dependence of long-range electron transfer through flexible oligo-p-phenylenevinylene bridges due to the breakdown of the Condon approximation[20]. Apart from the temperature dependence, neither the distance dependence nor the free energy dependence of electron transfer is immune to the failure of the Condon approximation as shown by Franzen et al.[21]. They stressed the importance of taking into account the non-Condon effect when the energy of the bridge state approaches that of the transition state (i.e. the crossing point). Finally, it is important to note that the breakdown of one assumption often happens with the breakdown of others, as subtle changes in molecular structures can have significant influences on multiple parameters that govern the electron transfer process.

## 2.2. Experimental techniques

In 1985, Gérard Mourou and Donna Strickland succeeded in generating high-intensity, ultra-short laser pulses.<sup>1</sup> Since then, these powerful sharp beams have opened up new ways for deepening our understanding of the world. For spectroscopists, this invention is the key to observe ultrafast dynamics of transient species up to the femtosecond ( $10^{-15}$  s) regime. In this section, we introduce the basic principles and technical aspects of the femtosecond transient absorption (TA) spectroscopy, the main experimental technique used for this thesis. In Section 2.2.1, we briefly introduce the generation of the pump and probe beams as well as data collection and interpretation. In Section 2.2.2, we further introduce how to adapt the conventional TA setup to perform circularly polarized TA measurements.

### 2.2.1. Femtosecond transient absorption spectroscopy

Femtosecond TA spectroscopy is in essence a pump-probe technique: a powerful single-wavelength pulse pumping the sample from the ground state to the excited state followed by a weak white-light pulse probing the change of absorption in the excited sample at a certain time delay. A schematic representation of the TA setup is shown in Figure 2.3.

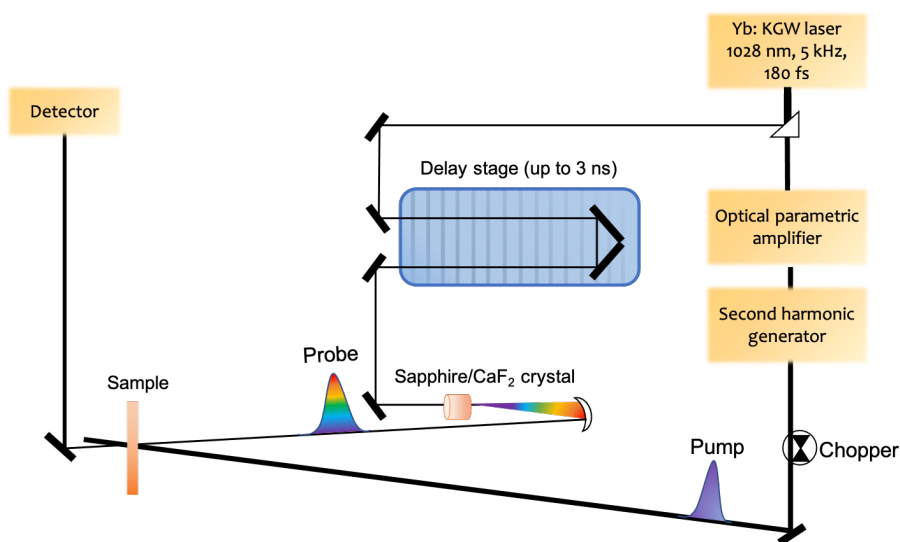


**Figure 2.3.** Schematic representation of the femtosecond transient absorption spectroscopy.

<sup>1</sup>The Nobel Prize in Physics 2018 was awarded "for groundbreaking inventions in the field of laser physics" with one half to Arthur Ashkin "for the optical tweezers and their application to biological systems", the other half jointly to Gérard Mourou and Donna Strickland "for their method of generating high-intensity, ultra-short optical pulses". <https://www.nobelprize.org/prizes/physics/2018/summary/>.

### Generation of fundamental laser pulse

To generate a femtosecond pump pulse with high-intensity, an ultrafast laser system generally consists of two main components: a seed oscillator and a regenerative amplifier with pulse stretcher/compressor modules. Specifically, the seed oscillator outputs low-intensity but ultrashort laser pulses, which is subsequently sent to the regenerative amplifier. To build up the pulse intensity, the seed pulses oscillate inside the regenerative amplifier cavity when passing through a pumped Yb:KGW crystal. To prevent damaging the Yb:KGW crystal, a stretcher broadens the temporal width of the seed pulse from  $\sim 170$  fs to 10-100 ps before feeding the pulse to the crystal. Once the high intensity has been achieved, the pulses are ejected from the cavity and sent into a compressor. The latter compresses the pulses to their initial temporal width (180-200 fs). The output pulse from the regenerative amplifier has an average power of 3 W, a repetition rate of 5 kHz and a center wavelength of 1028 nm. This output pulse is called the fundamental laser pulse.

### Generation of tunable pump pulse

The fundamental laser pulse is split into two beams using a beam splitter. About 90% of the fundamental laser pulse is sent to an optical parametric amplifier (OPA) to tune the pump wavelength. Different pump wavelengths can be generated using nonlinear crystals inside the OPA, because changing the incident angle on the nonlinear crystals results in different phase matching conditions. The OPA works based on a second-order nonlinear process, called difference frequency generation. During this process, a pump photon with a certain frequency is converted into two photons with different frequencies called *signal* and *idler*, respectively. The energy sum of these two photons equals the energy of the original pump photon:  $(h\nu_{pump} = h\nu_{signal} + h\nu_{idler})$ . Furthermore, the *signal* or *idler* will be used to generate pump beam at shorter wavelengths via second-harmonic generation (also called frequency doubling). Since multiple wavelengths are generated during the difference frequency generation, the output of OPA is sent through a wavelength separator, also known as a dichroic mirror, to filter out unwanted wavelengths.

### Generation of white-light probe pulse

One underlying assumption of the pump-probe technique is that the probe beam is so weak that its perturbation of the sample is negligible. For this reason, only 10% of the fundamental laser pulse is used for generating the probe beam. To capture the optical spectrum after the photoexcitation, the probe beam travels through a longer path length than the pump beam via a motorized delay stage in the probe path. This introduces a time delay between the pump and the probe pulses, the value of which is equal to the difference between two optical path lengths divided by the speed of light. By measuring the steady-state optical spectrum at each time point, the time-resolved optical spectra can be obtained by collecting all the optical spectra at different time delays. The *time zero* is



achieved when the time delay is equal to zero, meaning both pump and probe arrive at the sample position simultaneously. After travelling through the delay stage, the probe beam at 1028 nm is focused into a sapphire or a CaF<sub>2</sub> crystal to generate the white-light continuum via a third-order nonlinear process. Depending on the alignment, the resulting continuum typically spans from 350 nm to 900 nm for the CaF<sub>2</sub> crystal and from 460 nm to 900 nm for the thin sapphire crystal. This white-light probe pulse is subsequently focused on the sample by a parabolic mirror. To preclude the contribution from the rotational diffusion of molecules to the TA kinetics, the relative angle between the polarization planes of the pump and probe light should be set at the magic angle (54.7°)[22, 23]. Finally, the transmitted probe light is collected by the detector.

### Data collection and interpretation

In this thesis, all the TA spectra were collected in the transmission mode, meaning the detector records the change of the probe transmission due to the pump pulse. As a result, a TA spectrum is recorded as a difference absorption spectrum,  $\Delta A$ . And this difference absorption spectrum is related to the transmitted probe intensity by  $\Delta A = -\log(I_{\text{pump-on}}/I_{\text{pump-off}})$ . Typically,  $\Delta A$  can be interpreted as the absorption spectrum of the excited sample, from which the absorption spectrum of the sample in the ground state is subtracted,  $\Delta A = A_{\text{pump-on}} - A_{\text{pump-off}}$ . By further collecting the individual TA spectra at different delay times, a two-dimensional TA spectrum can be obtained, containing both time-resolved and wavelength-dependent information.

To properly interpret a TA spectrum at a specific time, it is necessary to understand possible contributions from various processes :

1. Ground state bleach (GSB): a negative signal in the  $\Delta A$  spectrum resembles a mirror image of the ground state absorption (blue solid line in Figure 2.4a). Upon photoexcitation, the number of molecules in the ground state decreases, resulting in a decrease of ground state absorption.
2. Excited state absorption (ESA), a positive signal in the  $\Delta A$  spectrum due to optical transitions to higher excited states in the excited sample (purple dashed line in Figure 2.4a).
3. Stimulated emission (SE): a negative signal in the  $\Delta A$  spectrum typically follows the fluorescence spectrum of the excited molecule (orange dashed line in Figure 2.4a). This process happens when a photon from the probe beam stimulates emission of another photon from the excited state to the ground state.

Apart from these three contributions, there can be positive signals arise from formed species due to photoinduced processes, such as the absorption of charge-separated states and triplet states. In addition, a change in the ground state absorption (GSA) will also influence the TA signal, as typically seen in semiconductor materials, such as metal halide perovskites[24]. In these

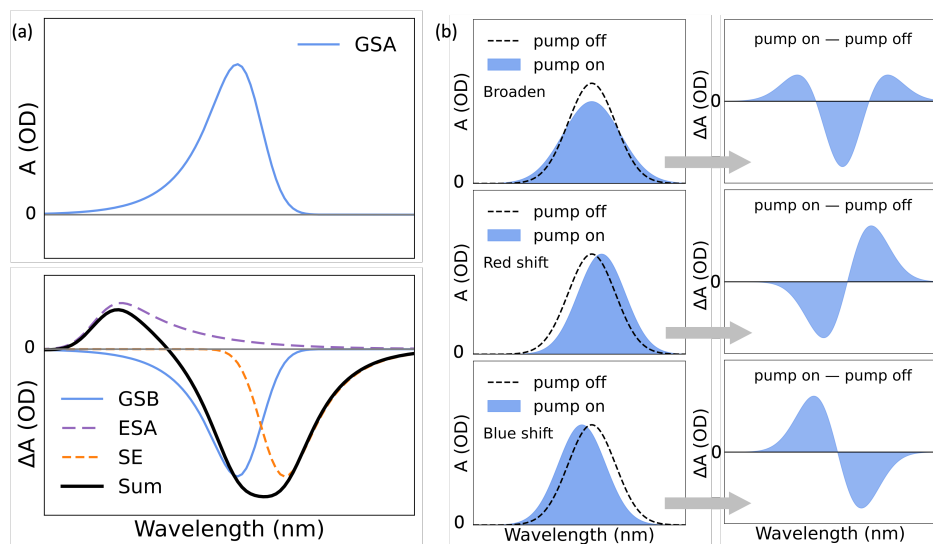


**Figure 2.4.** Possible contributions to a TA spectrum. (a) Examples of a ground state absorption (GSA) spectrum and the corresponding TA spectrum with contributions from ground state bleach (GSB), excited state absorption (ESA), stimulated emission (SE). (b) Effects of absorption spectral changes on the TA spectra, including broadening, red shift, and blue shift.

materials, the presence of photoinduced excitons or charge carriers may broaden or shift the GSA, resulting in additional TA signatures (Figure 2.4b).

### 2.2.2. Circularly polarized transient absorption spectroscopy

So far, we have only discussed the TA setup where pump and probe beams are linearly polarized, meaning the electric field of light oscillates in a single plane along its propagation direction. When this electric field rotates in a circle around the direction of propagation, the light becomes circularly polarized. According to spectroscopists' convention for circular polarization, the light is right-handed when it is circularly polarized clockwise from the receiver's point of view (Figure 2.5), and vice versa for the left circularly polarized light (CPL). Each left ( $\sigma^+$ ) or right ( $\sigma^-$ ) circularly polarized photon carries a spin angular momentum of  $+\hbar$  or  $-\hbar$  in the direction of their propagation. An efficient angular momentum transfer from a circularly polarized photon to an electron of the sample will allow us to study spin-dependent excited state dynamics using TA spectroscopy. More details on the working principle are provided in Chapter 6. In this section, we focus on the generation and verification of CPL.

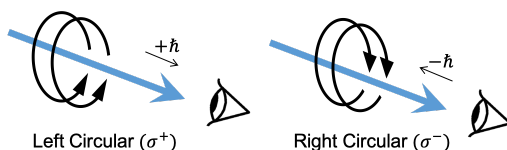


**Figure 2.5.** Definition of circularly polarized light.

### Generation of circularly polarized light

The generation of CPL requires a pair of a linear polarizer and a quarter-wave plate. As illustrated in Figure 2.6a, regardless of the polarization of the original light, the light transmitted through the linear polarizer becomes linearly polarized in the same direction as the polarization plane of the linear polarizer. When the polarization plane of this light is at  $45^\circ$  to the slow/fast axis of the subsequent quarter-wave plate, this linearly polarized light is then transformed to be circularly polarized by the quarter-wave plate. To understand its working principle, we can view a beam of CPL as an electric field composed of two orthogonal components that are of equal magnitude and are out of phase by one-quarter wavelength ( $90^\circ$ ). Depending on which component is leading in the phase, the sum of these two components will rotate clockwise or counter-clockwise in the direction of propagation. Thus, when the linearly polarized light passes through a quarter-wave plate at  $45^\circ$  to its slow/fast axis, the component parallel to the slow axis is retarded by a quarter of wavelength as compared to the one parallel to the fast axis, thereby generating the CPL. Practically, this can be achieved using a circular polarizer with a specific handedness or a combination of a linear polarizer and a quarter-wave plate. The former method typically offers high accuracy, while the latter offers the flexibility to change the handedness of generated CPL by rotating the quarter-wave plate by  $90^\circ$ .

### Verification of circularly polarized light

The circular polarization of the light generated with a circular polarizer can be verified using another circular polarizer with an opposite handedness. Since the CPL consists of two orthogonal electric field components with a quarter-wave phase shift, introducing an additional phase shift of quarter-wavelength in the same direction results in a total phase shift of half a wavelength. This is akin to sending the linearly polarized light through a half-wave plate, which rotates the linearly polarized light by twice the angle between its fast axis and the polarization plane of the incident light.

As illustrated in Figure 2.6b, when putting a left circular polarizer backwards after a right circular polarizer, the original unpolarized light will successively pass through a linear polarizer, two quarter-wave plates, and a linear polarizer. In a particular case where both quarter-wave plates and linear polarizers align at the same angle as shown in Figure 2.6b, the second quarter-wave plate will

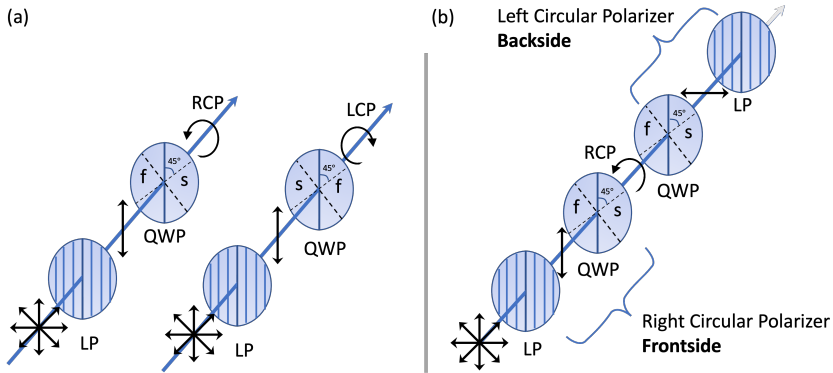


**Figure 2.6.** Schematic representation of (a) generating circularly polarized light and (b) verifying the circular polarization using circular polarizers. RCP: right circularly polarized light; LCP: left circularly polarized light; LP: linear polarizer; QWP: quarter-wave plate; f: fast axis; s: slow axis.

transform the right CPL to be linearly polarized at  $90^\circ$  to the polarization plane of both linear polarizers. Subsequently, this linearly polarized light will be blocked by the second linear polarizer due to their orthogonal polarization planes. Consequently, no light will emerge after the left circular polarizer. Obviously, for a circular polarizer, the angle between the polarization plane of its linear polarizer and the fast/slow axis of its quarter-wave plate is fixed at  $45^\circ$ . Therefore, the situation exemplified in Figure 2.6b can be generalized, meaning the CPL generated by a circular polarizer should always be blocked by its counterpart circular polarizer from the backside regardless of their relative angles.

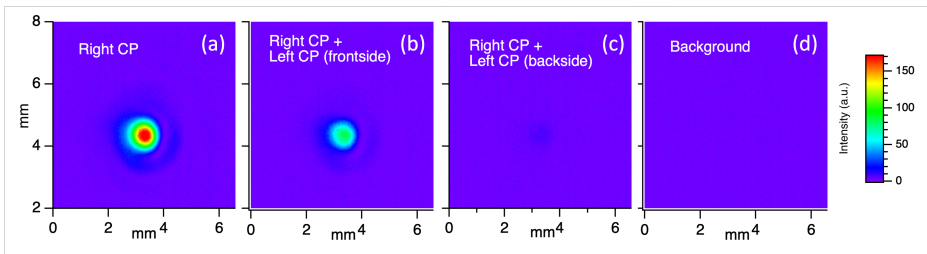


**Figure 2.7.** Verification of the circularly polarized pump beam at 488 nm. Beam profile of pump light transmitted through (a) a right circular polarizer, (b) a right circular polarizer and a left circular polarizer from the front side, and (c) a right circular polarizer and a left circular polarizer from the backside. (d) Background measurement with pump off.

This working principle was further employed to verify the circular polarization

of pump and probe beams. To verify whether the pump beam was circularly polarized, the beam intensity under different configurations was recorded by a camera beam profiler (BC106-VIS, ThorLabs). As demonstrated in Figure 2.7, the intensity of the pump beam, after passing through a right circular polarizer and then a left circular polarizer from the front side, was only marginally decreased (Figure 2.7b). In contrast, when passing through the same left circular polarizer from the backside, the beam intensity was nearly diminished to the background level as shown in Figure 2.7c. This is in line with the verification of CPL discussed above.

Similarly, the circularly polarized probe beam can be verified by measuring the probe spectra transmitted through one and two circular polarizers. To generate circularly polarized white light, we used a polymer film polarizer (CP42HE, Edmund optics) with a wavelength range of 400 - 700 nm. Noticeably, as displayed in Figure 2.8, the quality of the circular polarization is wavelength-dependent. This is because the broadband polarizer offers the best performance at 560nm and polarization may become more elliptical the further the deviation from this wavelength.

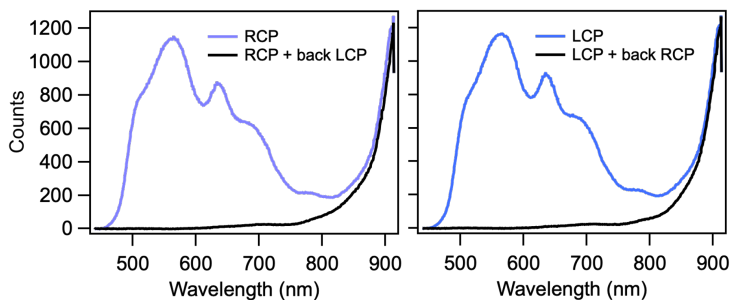


**Figure 2.8.** Verification of circularly polarized probe beam.

## References

1. Marcus, R. A. On the theory of oxidation-reduction reactions involving electron transfer. I. *The Journal of chemical physics* **24**, 966–978 (1956).
2. Marcus, R. A. & Sutin, N. Electron transfers in chemistry and biology. *Biochimica et Biophysica Acta (BBA)-Reviews on Bioenergetics* **811**, 265–322 (1985).
3. Hush, N. S. Adiabatic rate processes at electrodes. I. Energy-charge relationships. *The Journal of Chemical Physics* **28**, 962–972 (1958).
4. Hush, N. S. Adiabatic theory of outer sphere electron-transfer reactions in solution. *Transactions of the Faraday Society* **57**, 557–580 (1961).
5. Barbara, P. F., Meyer, T. J. & Ratner, M. A. Contemporary issues in electron transfer research. *The Journal of Physical Chemistry* **100**, 13148–13168 (1996).
6. Weller, A. Photoinduced electron transfer in solution: exciplex and radical ion pair formation free enthalpies and their solvent dependence. *Zeitschrift für Physikalische Chemie* **133**, 93–98 (1982).
7. McConnell, H. M. Intramolecular charge transfer in aromatic free radicals. *The Journal of Chemical Physics* **35**, 508–515 (1961).
8. Woitellier, S., Launay, J. & Joachim, C. The possibility of molecular switching: theoretical study of [(NH<sub>3</sub>)<sub>5</sub>Ru-4, 4'-bipy-Ru (NH<sub>3</sub>)<sub>5</sub>]<sup>5+</sup>. *Chemical physics* **131**, 481–488 (1989).
9. Gray, H. B. & Winkler, J. R. Long-range electron transfer. *Proceedings of the National Academy of Sciences* **102**, 3534–3539 (2005).
10. Closs, G. L. & Miller, J. R. Intramolecular long-distance electron transfer in organic molecules. *Science* **240**, 440–447 (1988).
11. Fox, L. S., Kozik, M., Winkler, J. R. & Gray, H. B. Gaussian free-energy dependence of electron-transfer rates in iridium complexes. *Science* **247**, 1069–1071 (1990).
12. Wasielewski, M. R., Niemczyk, M. P., Svec, W. A. & Pewitt, E. B. Dependence of rate constants for photoinduced charge separation and dark charge recombination on the free energy of reaction in restricted-distance porphyrin-quinone molecules. *Journal of the American Chemical Society* **107**, 1080–1082 (1985).
13. Moser, C. C., Keske, J. M., Warncke, K., Farid, R. S. & Dutton, P. L. Nature of biological electron transfer. *Nature* **355**, 796–802 (1992).
14. Bixon, M. & Jortner, J. Non-Arrhenius temperature dependence of electron-transfer rates. *The Journal of Physical Chemistry* **95**, 1941–1944 (1991).
15. Jortner, J. Temperature dependent activation energy for electron transfer between biological molecules. *The Journal of Chemical Physics* **64**, 4860–4867 (1976).
16. De Vault, D. & Chance, B. Studies of photosynthesis using a pulsed laser: I. Temperature dependence of cytochrome oxidation rate in chromatium. Evidence for tunneling. *Biophysical journal* **6**, 825–847 (1966).

17. Gunner, M. & Dutton, P. L. Temperature and  $\Delta G$  dependence of the electron transfer from BPh. to QA in reaction center protein from *Rhodobacter sphaeroides* with different quinones as QA. *Journal of the American Chemical Society* **111**, 3400–3412 (1989).
18. Smit, K. J., Warman, J. M., De Haas, M. P., Paddon-Row, M. N. & Oliver, A. M. Charge recombination kinetics of giant dipoles in saturated hydrocarbon solvents. *Chemical physics letters* **152**, 177–182 (1988).
19. Blumberger, J. Recent advances in the theory and molecular simulation of biological electron transfer reactions. *Chemical reviews* **115**, 11191–11238 (2015).
20. Davis, W. B., Ratner, M. A. & Wasielewski, M. R. Conformational Gating of Long Distance Electron Transfer through Wire-like Bridges in Donor- Bridge- Acceptor Molecules. *Journal of the American Chemical Society* **123**, 7877–7886 (2001).
21. Franzen, S., Goldstein, R. F. & Boxer, S. G. Distance dependence of electron-transfer reactions in organized systems: the role of superexchange and non-Condon effects in photosynthetic reaction centers. *The Journal of Physical Chemistry* **97**, 3040–3053 (1993).
22. Lessing, H. & Von Jena, A. Separation of rotational diffusion and level kinetics in transient absorption spectroscopy. *Chemical Physics Letters* **42**, 213–217 (1976).
23. Schott, S., Steinbacher, A., Buback, J., Nuernberger, P. & Brixner, T. Generalized magic angle for time-resolved spectroscopy with laser pulses of arbitrary ellipticity. *Journal of Physics B: Atomic, Molecular and Optical Physics* **47**, 124014 (2014).
24. Chen, Z., Dong, G. & Qiu, J. Ultrafast Pump-Probe Spectroscopy—A Powerful Tool for Tracking Spin-Quantum Dynamics in Metal Halide Perovskites. *Advanced Quantum Technologies* **4**, 2100052 (2021).

# 3

## Excited state dynamics of acceptor–donor–acceptor systems based on BODIPY

*Donor-bridge-acceptor systems based on boron dipyrromethene (BODIPY) are attractive candidates for bio-imaging and sensing applications because of their sensitivity to temperature, micro-viscosity and solvent polarity. The optimization of the properties of such molecular sensors requires detailed knowledge of the relation between the structure and the photophysical behavior in different environments. In this chapter, we will delve into the excited-state dynamics of three acceptor-donor-acceptor molecules based on benzodithiophene and BODIPY in solvents of different polarities using a combination of ultrafast spectroscopy and DFT-based electronic structure calculations. Transient absorption spectra show that upon photoexcitation an initial excited species with an induced absorption band in the near-infrared regime is formed independent of the solvent polarity. The subsequent photophysical processes strongly depend on the solvent polarity. In non-polar toluene, this initial excited state undergoes a structural relaxation leading to a delocalized state with partial CT character, while in the more polar tetrahydrofuran a fully charge separated state is formed. The results clearly show how factors such as donor-acceptor distance and restricted rotational motion by steric hindrance can be used to tune the excited state photophysics to optimize such systems for specific applications.*

---

§This chapter is based on: [Zimu Wei](#), Sushil Sharma, Abbey M. Philip, Sanchita Sengupta, Ferdinand C. Grozema, *Physical Chemistry Chemical Physics*, 2021, 23 (14), 8900-8907.



### 3.1. Introduction

Fluorescent molecular rotors that are sensitive to the temperature and micro-viscosity variations have been extensively explored for applications in sensing[1, 2], bio-imaging[3–5] and diagnosis[6, 7]. Applications of such molecular sensors can be further extended to detection of metal ions [8, 9], humidity detection[10] and opto-electronics[11], by incorporation of a donor–acceptor (DA) system. Upon photoexciting such a DA system it may either exhibit photoemission from the local excited (LE) state that is formed on photoexcitation, or it may emit at a longer wavelength from a charge transfer (CT) state where electrons and holes are spatially apart from each other. Depending on the equilibrium between the LE state formed upon the excitation and the CT state formed by the subsequent photoinduced CT, the molecules can exhibit dual emission with a large Stokes shift, resulting in a high sensor accuracy[12] and the emission of white light[13]. Both the emission probability and the rate of formation of the CT state are directly influenced by subtle variations in the molecular structure, and hence such variations can lead to significant changes in the excited state behavior. Therefore, understanding the underlying photophysical mechanisms governing the CT process is of crucial importance in optimizing the design of such systems.

The rational design of a DA system entails a proper selection of the electron-donating and electron-accepting moieties. Benzodithiophene (BDT) is well known for its remarkable performance as a building block in organic photovoltaics[14–16]. Recently, it has been reported to be a promising candidate as the donor unit in functional dyads and triads[17, 18]. On the other hand, boron dipyrromethene (BODIPY) derivatives have been widely used as fluorophores as well as electron acceptors in fluorescent molecular probes[19, 20] due to their large extinction coefficients[8, 21], long excited state lifetimes[22], high photostability[23], various modification possibilities[24] and their intrinsic electron-accepting ability. However, only a few red emissive BODIPY-based DA rotor molecules with large Stokes shifts have been reported[25–27], and their quantitative photophysical characterizations regarding solvent dependence and steric restrictions on the ultrafast time scale, to our knowledge, have not been studied.

To gain more insight into the relation between molecular conformation and photophysics, we have investigated the photophysical properties of a series of acceptor–donor–acceptor triads based on a BDT donor and two BODIPY acceptors (Figure 3.1) that are of interest for molecular temperature/viscosity sensors and optoelectronics. In these DA systems, two electron-accepting BODIPY units are connected to the BDT donor at the meso positions, with either one or two intervening phenyl groups to investigate the effect of DA separation on the photophysics. In addition, introducing four methyl groups at the 1-, 3-, 5-, and 7-positions in each BODIPY unit allows us to study the effect of the mutual rotation angle, and hence the electronic coupling between the donor and acceptor unit without changing the DA distance. We have used a combination of femtosecond time-resolved transient absorption (TA) spectroscopy and

time-dependent density functional theory (TDDFT) calculations. The results show an unanticipated delocalization of the initial excited state in **p-ADA** and **pp-ADA** that can initiate a fast CT process in polar solvents. In addition, we have elucidated the role of the steric hindrance in the photophysical properties of **Me-pp-ADA**. These results offer new insight into the relation between the photophysics of BODIPY-based fluorescent molecular rotor systems that will aid in the optimization of their properties for future applications.

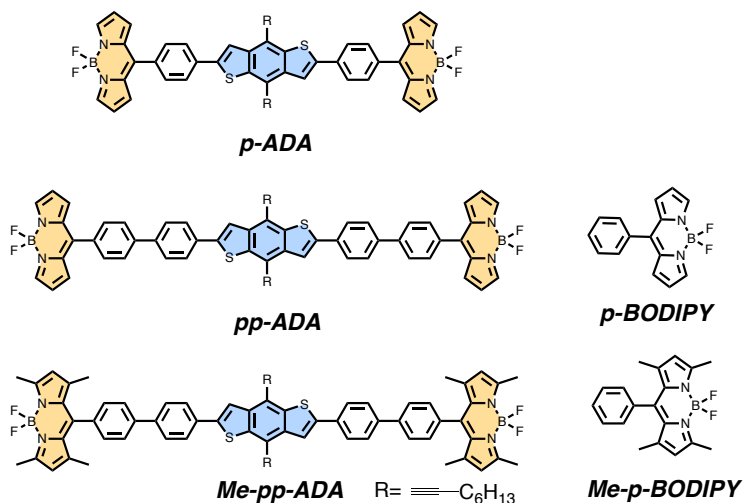


**Figure 3.1.** Chemical structures of ADA triads and their model acceptors.

## 3.2. Results and discussion

In this section, we will delve into the electronic structure/properties of three acceptor–donor–acceptor (ADA) molecules consisting of one BDT as the electron donor and two BODIPY cores as the electron acceptors, connected by either one or two intervening phenyl units (Figure 3.1). We have combined steady-state absorption and emission, time-resolved transient absorption, and electronic structure calculations to characterize and understand the effects of DA distance, geometric conformation (steric hindrance) and solvent polarity on the photophysics of these ADA triads.

### 3.2.1. Steady-state optical properties

A first indication of the electronic structure/properties can be obtained from steady-state absorption and emission spectra. In Figure 3.2a-c, the UV/Vis absorbance spectra of all three compounds in tetrahydrofuran (THF) are shown, together with those of the corresponding model donors and acceptors. All three compounds exhibit a dominant absorption peak at ~500 nm originating from an

$S_0 \rightarrow S_1$  transition on BODIPY[8]. The much weaker  $S_0 \rightarrow S_2$  transition on BODIPY below 400 nm is obscured by the strong absorption of BDT. The overlap between the spectra of ADA compounds and the acceptor units at 500 nm suggests that the electronic communication between the BODIPY acceptors and the BDT donor is very small in the ground state. Therefore, the photoexcitation at 500 nm is expected to result in a localized excited state on the BODIPY acceptor, generating a hole in the highest occupied fragment molecular orbital (HOFO) of BODIPY. On the other hand, compared to the absorption peak of the model BDT, a red-shifted broad peak at  $\sim 380$ – $400$  nm suggests a significant electronic interaction between BDT and the neighboring phenyl units.

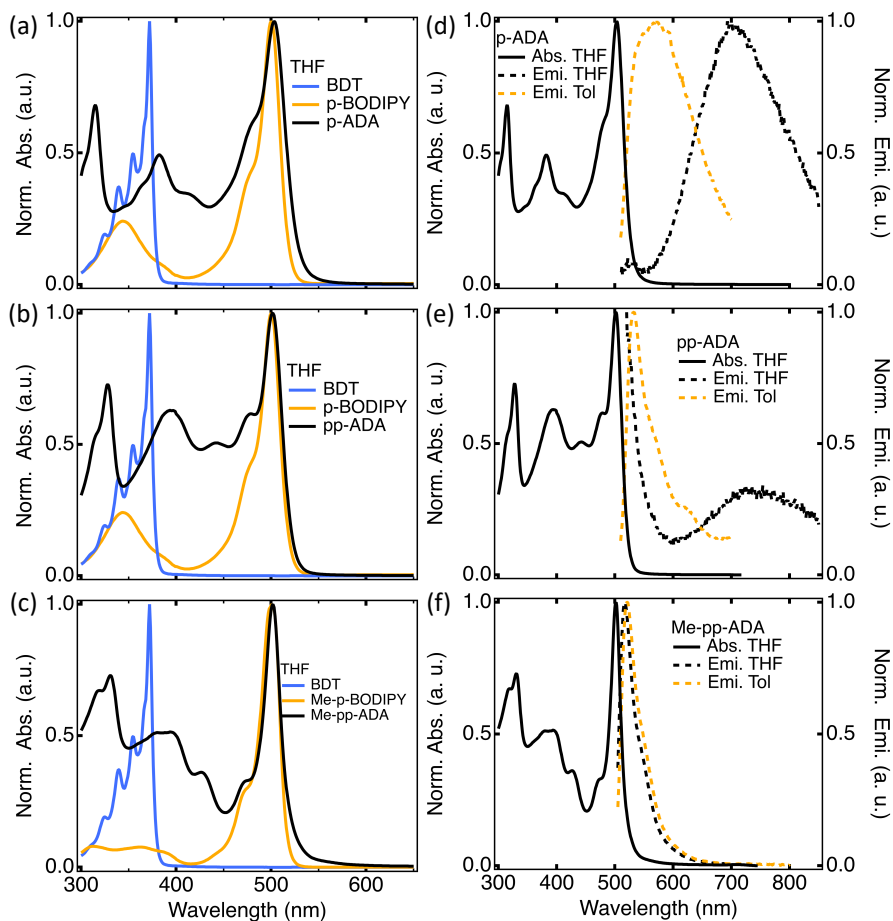


**Figure 3.2.** Steady-state spectra. (a)–(c) Normalized absorption spectra of ADA triads and their model compounds in THF. (d)–(f) Normalized emission spectra of ADA triads in THF and toluene. Normalized absorption spectra are replotted for comparisons.

The steady-state emission spectra for the three ADA compounds are shown in Figure 3.2d-f. In THF, an emission band with substantial Stokes shifts is observed in both **p-ADA** and **pp-ADA**, corresponding to the emission from the CT state. In the non-polar toluene, the emission band of **p-ADA** is blue-shifted by more than 100 nm compared to that in THF. Noteworthy, with the longer DA distance, the emission band of **pp-ADA** in toluene starts to resemble the characteristic emission of the model BODIPY acceptor more closely, indicating a more localized excited state on BODIPY acceptors. Finally, the sterically hindered **Me-pp-ADA** demonstrates a BODIPY-like emission band independent of the solvent polarity, indicating the absence of CT in this case.

### 3.2.2. Femtosecond transient absorption

To study the dynamics of the excited state on an ultrafast timescale, the TA spectra of three compounds in toluene and THF were measured. It is known that the CT process in DA molecules is affected by the polarity of the environment[28–30]. In a polar solvent, the highly dipolar CT state is stabilized by the relaxation of the dipolar solvent, thereby favoring the CT. In a non-polar solvent, the LE state is the dominant species upon excitation, since the CT state is not stabilized by the surroundings. Hence, this solvation effect allows us to study the absorption features of the LE state and CT state systematically.

In toluene, a non-polar solvent, upon photoexcitation of **p-ADA** at 500 nm (Figure 3.3a), a ground-state bleach (GSB) at ~500 nm and an induced absorption band in the near-infrared (NIR) range appear simultaneously (<0.4 ps, orange curve). The GSB at ~500 nm corresponds to the excited BODIPY acceptors. This GSB feature exhibits a fast initial decay immediately after the excitation pulse, which is accompanied by the further growth of the induced absorption band in the NIR as well as the formation of a small peak at 545 nm. The broad featureless NIR absorption band between 600 and 900 nm reaches a maximum after ~10 ps and eventually decays concurrently with the decay of the GSB at longer times (Figure A.1). Interestingly, the NIR absorption band becomes less pronounced in **pp-ADA** (Figure 3.3b) and completely disappears in **Me-pp-ADA** (Figure 3.3c). This shows that the steric hindrance introduced by the methyl groups decreases the electronic coupling with the BODIPY moiety to such an extent that the photophysics completely changes.

The absorption feature in the NIR regime can be found in other reported BODIPY derivatives with an analogous chemical structure[31, 32], but the origin of this absorption feature has hitherto escaped attention. Here, the formation of this absorption band should be associated with the ESA of the acceptor, because the CT process is expected to be suppressed in the nonpolar solvent, and the energy transfer to the donor is energetically impossible. Furthermore, in comparison with the TA spectra of the model compound **p-BODIPY** or **Me-p-BODIPY** (Figure A.2), where no induced absorption band was detected between 500 nm and 900 nm, it is plausible to conclude that the ESA in **p-ADA** and **pp-ADA** in the NIR regime originates from the ultrafast delocalization of the excited acceptors through the phenyl units onto the BDT donor to some extent,

concurrently resulting in a delocalized excited state with partial CT character. In **Me-pp-ADA**, this delocalization is completely hindered by the decoupling between the BODIPY core and the meso-phenyl unit, as evident by the absence of the absorption band in its TA spectrum.

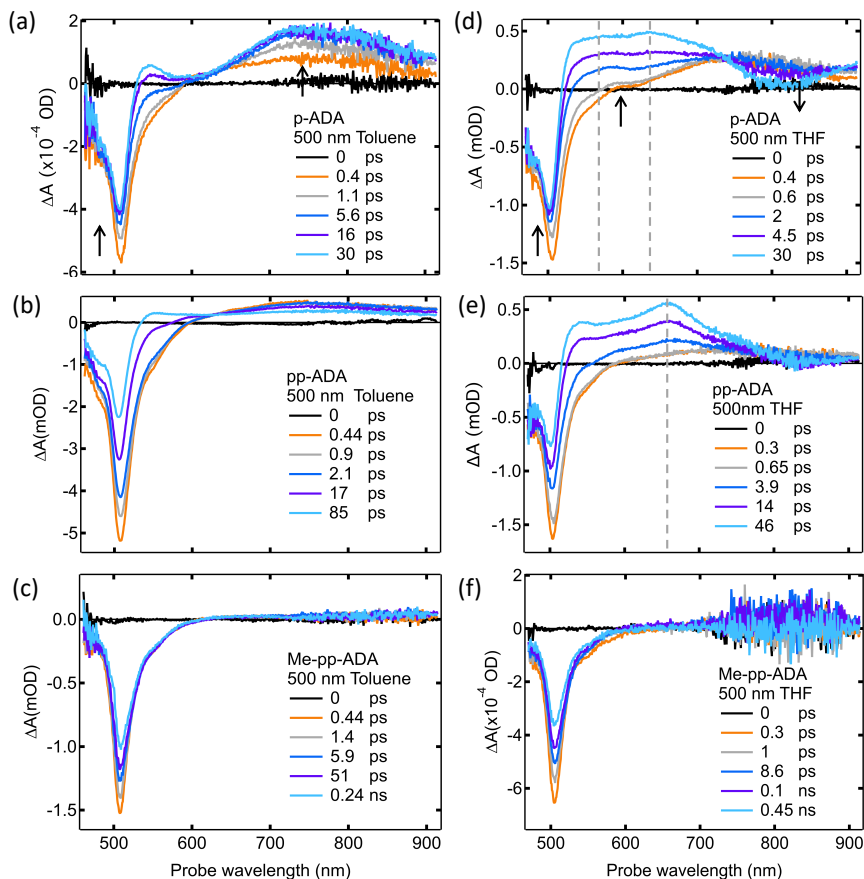


**Figure 3.3.** Transient absorption spectra (excited at 500 nm) of (a) **p-ADA**, (b) **pp-ADA** and (c) **Me-pp-ADA** in toluene and (d) **p-ADA**, (e) **pp-ADA** and (f) **Me-pp-ADA** in THF.

The photophysics of **p-ADA** in toluene discussed above change quite drastically when going to the more polar solvent THF. Upon photoexcitation at 500 nm, a similar ESA in the NIR regime is observed as in toluene but this feature decays in a few picoseconds, accompanied by the emergence of an absorption band with two maxima at around 580 nm and 635 nm (Figure 3.3d, grey dashed lines). This suggests the formation of a CT state stabilized by the solvent. The absorption feature at 580 nm is in accordance with the reported absorption spectra of radical anions of BODIPY analogues varying from 550–590

nm[11, 33]. Thus, the absorption feature at 635 nm is assigned to the BDT radical cation. Unfortunately, due to the novelty of incorporating BDT into DA molecules, the absorption feature of an analogous BDT radical cation has not been reported, to our best knowledge.

Similar to the observation for **p-ADA** in THF, a CT state is formed in **pp-ADA** with an absorption peak at 658 nm following the decay of the initial excited state (Figure 3.3e). The red-shift in the absorption wavelength and the sharper absorption feature is likely associated with the red-shifted absorption of the BODIPY radical anions due to the increasing number of phenyl units, as supported by TDDFT calculations shown in Figure A.3.

In the case of **Me-pp-ADA** (Figure 3.3f), even in the polar solvent, no absorption of the delocalized excited state or the formation of the CT state was observed, implying that the excited state is strictly localized on the BODIPY acceptors. This is consistent with the perpendicular geometry obtained from DFT geometry optimizations, resulting in a zero electronic coupling between BODIPY and the rest of the molecule. The absence of any electronic coupling also blocks the CT process. Moreover, DFT calculations also demonstrate that the adiabatic electron affinity for **Me-p-BODIPY** (1.75 eV) is lower than that for the model acceptor **p-BODIPY** (2.19 eV) (see Table A.1). This difference of 0.44 eV in the electron affinity shows that **Me-p-BODIPY** is a considerably weaker electron acceptor as compared with **p-BODIPY**. Therefore, the steric hindrance exerts a major impact on the photophysical properties of the ADA molecule through diminishing the electronic coupling across the molecule, which eventually prohibits CT process in **Me-pp-ADA**.

The TA spectra of the three compounds photoexcited at 380 or 400 nm are presented in Figure A.4 and Figure A.5. Generally, the TA spectra of **p-ADA** and **pp-ADA** are similar to those obtained on excitation at 500 nm, where the long-lived excited states are present in toluene, and the faster CT process is triggered in THF. Noticeable differences in the donor excitation arise from a slower formation of the GSB and a broader ESA band within 1 ps, indicating excitation energy transfer. However, it is nontrivial to disentangle the ESA of the donor from that of the acceptor and from coherent artifacts that are intrinsically present in the experiments to elucidate the excitation energy transfer on such an ultrafast timescale. In **Me-pp-ADA**, the excitation energy transfer is clearly evident in both toluene and THF as a result of the localized excited state on the acceptor. We have recently reported a more detailed analysis on the excitation energy transfer in **Me-pp-ADA**[34].

### 3.2.3. Global analysis

To extract the quantitative information on the photophysical processes occurring after photoexcitation, the full kinetic matrices of **p-ADA** and **pp-ADA** at acceptor excitation were fitted by global analysis. We found that the evolution of the TA spectra is sufficiently described by a two-step kinetic scheme. Using global analysis, we obtained the evolution-associated difference spectra (EADS) consisting of the spectra of transient species and their lifetimes. The relevant

photophysical processes are depicted in Figure 3.4c and f. Detailed lifetimes are tabulated in Table A.2. The quality of the fitting can be justified by the consistency between the fitted traces and the original TA data (Figure A.6).

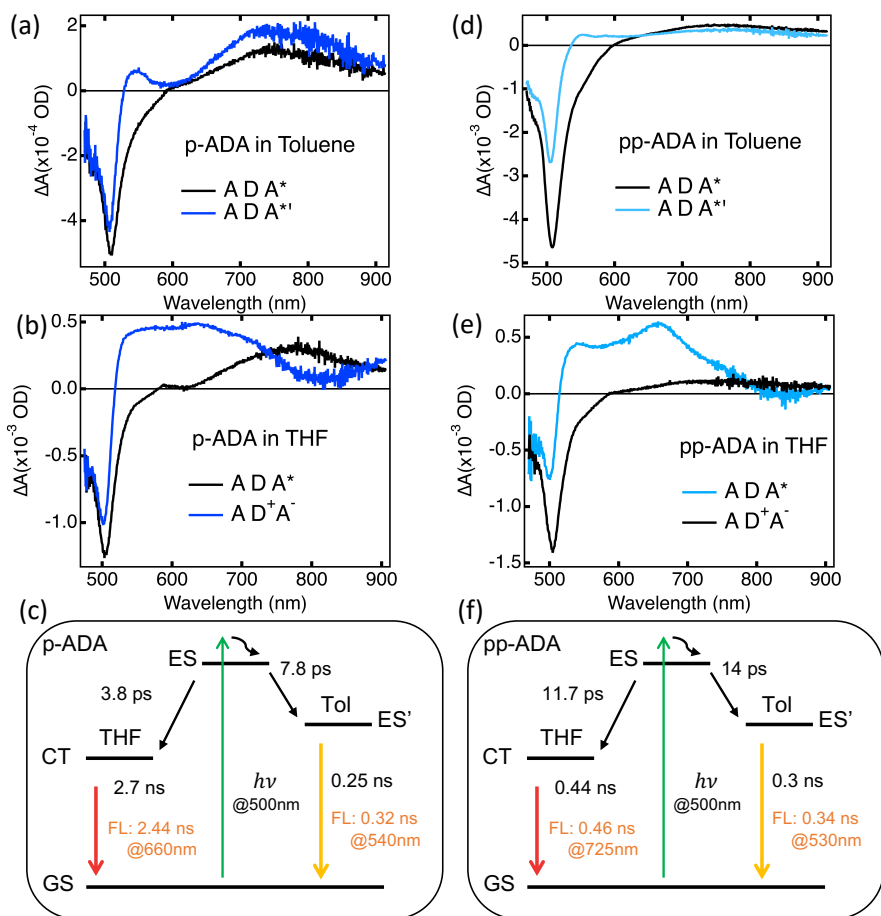


**Figure 3.4.** Evolution-associated difference spectra of transient species of **p-ADA** in (a) toluene and (b) THF, and of **pp-ADA** in (d) toluene and (e) THF, and schematic illustration of relevant photophysical processes after photoexcitation at 500 nm. Note that ADA<sup>+</sup>A<sup>-</sup> and ES' represent the delocalized excited state with the partial CT character.

As presented in Figure 3.4, the spectral signatures of EADS coincide with the photophysical processes discussed above. For **p-ADA** in both toluene and THF (Figure 3.4a and b), photoexcitation initially leads to an excited state (ADA\*) with the same spectral features (black curve), independent of the solvent polarity. This initial (vertical) excited state is characterized by a GSB feature at ~500 nm and a broad ESA in the NIR regime. The subsequent evolution of this excited

state strongly depends on the solvent.

In toluene, with a representative time of 7.8 ps, a second species is formed with a lifetime of 0.25 ns (dark blue curve) showing a loss of amplitude in the GSB and a rise with a similar amplitude in the broad ESA. The preserved absorption feature in the NIR regime suggests a structural relaxation process in the excited state, whereas the small peak at 545 nm can be ascribed to the partial CT character stemming from the relaxation-induced delocalization. Considering the similar fluorescence lifetime of 0.32 ns of the dominant species at 540 nm (Table A.2 and Figure A.7) and a featureless fluorescence emission band, we assign this second species in toluene to be a delocalized excited state with the partial CT character (ADA<sup>\*'</sup>). Hence, the initial excited state of **p-ADA** experiences a structural relaxation reaching a new electron density equilibrium in the presence of the solute–solvent interaction in toluene[35].

In THF, the spectrum of the initial excited state (ADA<sup>\*</sup>) is converted into the spectrum of the CT state (AD<sup>+</sup>A<sup>-</sup>) with a time constant of 3.8 ps. The CT state decays back to the ground state with a characteristic time of 2.68 ns as obtained from global analysis. This decay time closely matches the fluorescence lifetime of 2.44 ns at measured for the CT emission at 660 nm (Figure A.7).

In comparison with **p-ADA**, **pp-ADA** exhibits similar spectral characteristics (Figure 3.4d and e) and different rate constants for the charge transfer (11.65 ps) and charge recombination processes (0.44 ns). The slower CT rate upon lengthening the spacer is consistent with the attenuation of the rate expected for both the coherent tunneling and incoherent hopping mechanisms in DA systems[36, 37]. The faster decay rate of the CT state in **pp-ADA** can be explained by the additional deactivation pathways induced by intramolecular rotations[25, 31, 38].

### 3.2.4. Electronic structure calculations

In order to gain more insight into the nature of the initial (vertical) and relaxed excited states, we have performed electronic structure calculations. Geometry optimizations of the ground state (GS) and excited state (ES) were performed by TDDFT calculations using a CAM-B3LYP exchange-correlation functional with a DZP basis set. Details about calculations are described in the Section 3.4. The preliminary comparison between the excited **p-BODIPY** and **Me-p-BODIPY** pinpoints the limited conformational freedom in the ES posed by the steric hindrance (Figure A.8). Therefore, the ES geometry optimizations were focused on **p-ADA** and **pp-ADA** to study the effect of structural relaxation and different DA distances in ES behaviors.

Given the optimized GS geometry (Figure 3.5a), the major contributions to the lowest allowed vertical transition in **p-ADA** consist of transitions from occupied fragment molecular orbitals localized on the two BODIPY cores to the unoccupied orbitals on BODIPY cores (Figure A.9). As a result, the difference between the Mulliken charges in the lowest ES and GS is negligible as shown in Figure 3.5b (black bar). This indicates a highly localized vertical ES. Subsequently, the gradients of the lowest excitation energy were used to



optimize the geometry of the relaxed local excited (LE) state. When restricting the geometry to C(i) symmetry, the ES optimization results in a decrease of  $5.8^\circ$  in the torsion angles between the BODIPY core and the meso-phenyl (BODIPY-ph), accompanied by an increase of  $4.5^\circ$  in the torsion angles between the BDT donor and the phenyl units. These geometry rearrangements result in a slightly increased delocalization in the ES (Figure 3.5b, gray bar) and a lower  $S_1$  energy (Figure 3.5c).

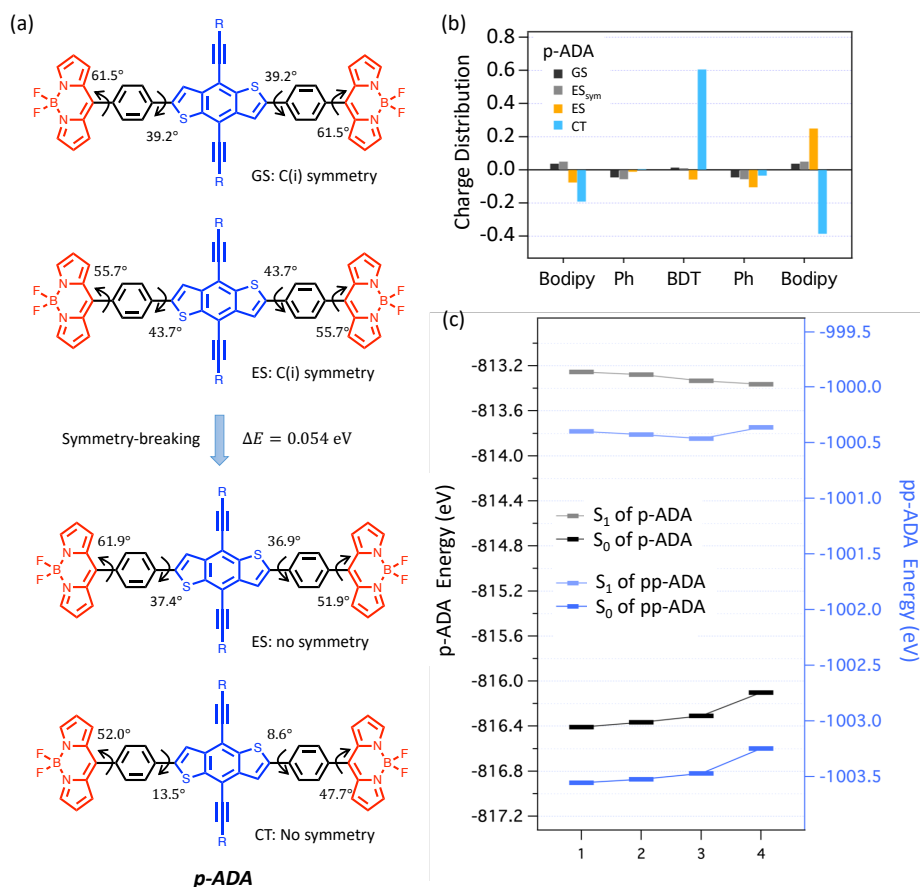


**Figure 3.5.** (a) Torsion angles in the geometry optimized ground state (GS), symmetrical excited state (ES<sub>sym</sub>), asymmetrical excited state (ES) and charge transfer state (CT) of **p-ADA**. (b) Geometry-dependent charge distribution of the excited state as compared to the ground state following the lowest vertical transition of **p-ADA**. (c) Energy levels of  $S_0$  and  $S_1$  corresponding to the geometries of GS, ES<sub>sym</sub>, ES and CT of **p-ADA** and **pp-ADA**.

When symmetry breaking is allowed, in the ES geometry optimization a

broken symmetry structure is obtained with an energy that is 0.054 eV lower than for the symmetric ES. As shown in Figure 3.5a, the symmetry-breaking structural relaxation in the ES yields a slightly reduced BODIPY-ph torsion angle of 51.9° and an increased BODIPY-ph torsion angle of 61.9°. Consequently, the BODIPY-phenyl electronic coupling is increased on one side and decreased on the other side, splitting the energy levels of the LUMO and LUMO+1 that are degenerate in the symmetrical geometry. Along with the reduced BDT-ph torsion angles, the delocalization of the LE state is enhanced by the symmetry-breaking as evident in Figure 3.5b (yellow bar) and Figure A.9. Similar ES symmetry-breaking and its solvent dependence have been seen in other ADA or DAD triads using time-resolved infrared spectroscopy[39] or broadband fluorescence upconversion spectroscopy[40].

Finally, the geometry of the CT state in **p-ADA** was optimized using the excitation energy gradients of the second lowest allowed transition, which mainly consists of transitions from the occupied fragment molecular orbital on the BDT donor to the unoccupied fragment molecular orbital on the BODIPY acceptors with a weight of 54%. Notably, the optimized geometry of the CT state is much more planar compared with that of the LE state (Figure 3.5a). The concomitant delocalization of the electron density is manifested in its LUMO as shown in Figure A.9. In this optimized CT geometry, the lowest vertical transition becomes CT-dominated, where the BDT-to-BODIPY transition accounts for 78% of the total transition. Accordingly, the CT character prevails in the lowest transition leading to a large charge redistribution as quantified in Figure 3.5b (blue bar). Moreover, the lowest transition energy based on the CT geometry leads to a lower  $S_1$  energy than the local ES geometry in spite of its higher  $S_0$  energy (Figure 3.5c). This energetically favorable CT character further substantiates the delocalized excited state suggested by the comparison between the TA spectrum of **p-ADA** with that of the model compound **p-BODIPY**.

Similarly, in **pp-ADA** the lowest allowed vertical transition corresponding to the GS geometry is mostly localized on BODIPY cores (Figure A.10). Driven by the symmetry-breaking geometry relaxation, the electron density becomes more delocalized in the  $S_1$  as indicated by its charge distribution in Figure A.11 (yellow bar). Compared with **p-ADA**, the longer DA distance causes a smaller overall delocalization in the excited state in **pp-ADA**. The weaker delocalization in the excited **pp-ADA** indicated by the calculations is consistent with the much weaker induced NIR absorption in the TA spectra as well as the more BODIPY-like emission spectrum in toluene. Furthermore, the TDDFT geometry optimization following the second lowest allowed transition was used to obtain the CT geometry. However, based on this optimized geometry, 66% of the lowest transition is made up of the transition from the occupied fragment molecular orbital on the BDT to the unoccupied fragment molecular orbital on the BDT (Figure A.10). Hence, the degree of CT character in **pp-ADA** is smaller than that in **p-ADA** as shown in Figure A.11. As a consequence, the  $S_1$  energy associated with this CT geometry is less favorable than the  $S_1$  energy of the LE state (Figure 3.5c). This attenuation in the CT character upon lengthening the DA

distance is concurrent with the slower CT rate in **pp-ADA** indicated by the global analysis.

Considering that the solvating effect on the molecule in the experiments such as the stabilization is not taken into account by the calculations in the gas phase, the COSMO solvation method was used in state-specific DFT calculations to estimate the solvent stabilization for the pure LE state and the CT state. As listed in Table A.3, the CT state is generally stabilized more than the LE state in the polar solvent, as expected. Moreover, the more delocalized LE state in **p-ADA** shows a slightly larger solvent stabilization than that in **pp-ADA**. Although the solvent stabilization of the pure CT state is larger in **pp-ADA**, it is plausible that the overall CT character in the excited **pp-ADA** is smaller due to the longer DA distance outweighs this larger solvent stabilization for the pure CT state.

### 3.3. Conclusions

In conclusion, we have examined the solvent-dependent ultrafast excited state dynamics of three ADA triads by combining femtosecond TA spectroscopy and complementary electronic structure (DFT/TDDFT) calculations. In toluene, the photoexcitation yields a delocalized vertical excited state in **p-ADA** and **pp-ADA**. This excited state undergoes structural relaxation that gives rise to an excited state with partial CT character. In THF, both red emissive **p-ADA** and **pp-ADA** triads show a fast CT process triggered by the same initial excited state, that is also formed in toluene. Increasing the DA distance leads to a slower CT and a less pronounced delocalization in the excited state as shown by global analysis and TDDFT calculations, respectively. Noteworthy, manipulation of the molecular conformation through steric hindrance strongly affects the photophysical properties of such triads. Forcing the BODIPY acceptor in a perpendicular conformation with respect to the conjugated spacer leads to a lowering of the electron affinity of the acceptor. In addition, it disrupts electronic coupling across the molecule and therefore prohibits the formation of the delocalized excited state, which in turn suppresses the CT process in **Me-pp-ADA**. These results show that by systematically varying the molecular structure, the balance between the population of the local excited state and the CT state can be tuned to a large extent. The improved understanding of the relation between molecular structure and the excited state processes will enable the design of the next generation of fluorescent molecular rotors based on BODIPY dyes for use in imaging and sensing applications.

## 3.4. Methods

### Materials

For all the spectroscopic measurements, spectroscopy-grade solvents were purchased from commercial suppliers and used as received. The model acceptor **Me-p-BODIPY** (1,3,5,7-tetramethyl-8-phenyl-4,4-difluoroboradiazaindacene) was purchased from Sigma-Aldrich. The model acceptor **p-BODIPY** was synthesized according to the previously reported procedure[41] and the characterization is presented in the [Figure A.12](#) and [Figure A.13](#). The synthesis of **p-ADA**, **pp-ADA** and **Me-pp-ADA** were published in ref [42] and [34].

### Optical characterization

All the spectroscopic measurements were carried out at room temperature. Steady-state absorption spectra were measured by PerkinElmer Lambda UV/Vis spectrophotometer using a quartz cuvette (1 cm path length). Steady-state emission spectra were measured using an Edinburgh FLS980 spectrometer excited at 500 nm. Fluorescence lifetimes were recorded using an Edinburgh LifeSpec-ps spectrometer with a fixed excitation wavelength of 404 nm.

### Femtosecond transient absorption

Transient absorption (TA) spectra were measured by a pump-probe transient absorption spectroscopy system at room temperature (25 °C). The generation of pump and probe is described in [Section 2.2.1](#). The white light (450–900 nm) was generated using a sapphire crystal. TA data were acquired using a commercial TA spectrometer (HELIOS, Ultrafast Systems) by subtracting the probe signal with pump off from that with pump on. To assure the stability of the pump pulse, the deviation of the pump power before and after each measurement was limited to 10%. All compounds were measured in a quartz cuvette with 2 mm path length. All spectra were corrected for the chirp of the white probe light and the polarization effect due to the diffusive reorientation.

TA spectra of **p-ADA** and **pp-ADA** were analyzed by global analysis using the open source software Glotaran[43]. In this method, the two-dimensional data were fitted by a sequential kinetic scheme with increasing lifetimes. This analysis yields a set of evolution-associated difference spectra (EADS), representing the spectral evolution of the excited species. The strength of the analysis can be assessed by the comparison between the original TA data and the fitted traces.

### DFT calculations

All electronic structure calculations were performed using the Amsterdam Density Functional (ADF) software package[44, 45], with the CAM-B3LYP functional and the double-zeta plus polarization (DZP) basis set consisting of Slater-type functions. The CAM-B3LYP functional was chosen since long-range corrected functionals are essential in accurately describing the energetics of excited states with substantial CT character[46, 47]. Density functional theory (DFT) was used for the geometry optimization of the ground state molecules, in

which both alkyl chains attached to the BDT unit were replaced by methyl groups. The optical transition spectra were calculated by time-dependent density functional theory (TDDFT)[48]. Unrestricted DFT and TDDFT with a spin polarization of 1 were used to optimize the geometry and the excitation spectra of charged molecules, respectively. It should be noted that it has been shown that the two-electron contributions to the excited state that are not included in TDDFT will introduce an overestimation of the excitation energies for BODIPY[49, 50], but this is prohibitive of the size of the molecules in this study.

To optimize the geometries of the excited states, the ground state gradients, together with the gradients of the TDDFT excitation energy were used to calculate the excited state gradients[51]. To simulate the excited state formed upon photoexcitation at 500 nm, the lowest vertical excited state from the ground state was optimized to obtain the relaxed geometry of the lowest excited state. The electronic structure of this relaxed excited state can then be compared to that of the vertical excited state corresponding to the ground state geometry. To allow the possibility of symmetry-breaking during the structural relaxation in the initial excited state, the excited state geometries of **p-ADA** and **pp-ADA** were optimized in both C(i) symmetry and without symmetry. Furthermore, the geometry optimization of the CT state was performed using the gradients of the second lowest allowed excitation that exhibits strong CT character in the ground state geometry.

The delocalization of the relaxed excited state and the degree of the CT character were quantified by calculating the difference in charge distribution between the ground state and the excited state. For a given geometry, the charge distribution in the ground state was derived from the Mulliken charges on the donor, the acceptors and the phenyl units. The charge distribution in the excited state was summed over the different contributions to the excited state including single orbital transitions with a contribution >1%.

Finally, in order to elucidate the solvent stabilization effect in THF, the Conductor like Screening Model (COSMO)[52] was used as the solvation method in state-specific single point calculations. The pure LE and CT state were calculated by specifying the corresponding electron occupation numbers based on the optimized geometries of relaxed LE state and CT state, respectively. Subsequently, the stabilization energy due to solvation for a specific state was determined by subtracting the solvent stabilization energy for its ground state from that for this specific state.

## References

1. Athanasiadis, A., Fitzgerald, C., Davidson, N. M., Giorio, C., Botchway, S. W., Ward, A. D., Kalberer, M., Pope, F. D. & Kuimova, M. K. Dynamic viscosity mapping of the oxidation of squalene aerosol particles. *Physical Chemistry Chemical Physics* **18**, 30385–30393 (2016).
2. Haidekker, M. A., Akers, W., Lichlyter, D., Brady, T. P. & Theodorakis, E. A. Sensing of flow and shear stress using fluorescent molecular rotors. *Sensor Letters* **3**, 42–48 (2005).
3. López-Duarte, I., Vu, T. T., Izquierdo, M. A., Bull, J. A. & Kuimova, M. K. A molecular rotor for measuring viscosity in plasma membranes of live cells. *Chemical Communications* **50**, 5282–5284 (2014).
4. Kuimova, M. K., Yahioglu, G., Levitt, J. A. & Suhling, K. Molecular rotor measures viscosity of live cells via fluorescence lifetime imaging. *Journal of the American Chemical Society* **130**, 6672–6673 (2008).
5. Kuimova, M. K., Botchway, S. W., Parker, A. W., Balaz, M., Collins, H. A., Anderson, H. L., Suhling, K. & Ogilby, P. R. Imaging intracellular viscosity of a single cell during photoinduced cell death. *Nature chemistry* **1**, 69–73 (2009).
6. Haidekker, M. A., Tsai, A. G., Brady, T., Stevens, H. Y., Frangos, J. A., Theodorakis, E. & Intaglietta, M. A novel approach to blood plasma viscosity measurement using fluorescent molecular rotors. *American Journal of Physiology-Heart and Circulatory Physiology* **282**, H1609–H1614 (2002).
7. Wu, Y.-Y., Yu, W.-T., Hou, T.-C., Liu, T.-K., Huang, C.-L., Chen, I.-C. & Tan, K.-T. A selective and sensitive fluorescent albumin probe for the determination of urinary albumin. *Chemical communications* **50**, 11507–11510 (2014).
8. Kollmannsberger, M., Rurack, K., Resch-Genger, U. & Daub, J. Ultrafast charge transfer in amino-substituted boron dipyrromethene dyes and its inhibition by cation complexation: a new design concept for highly sensitive fluorescent probes. *The Journal of Physical Chemistry A* **102**, 10211–10220 (1998).
9. Rurack, K., Kollmannsberger, M., Resch-Genger, U. & Daub, J. A selective and sensitive fluoroionophore for HgII, AgI, and CuII with virtually decoupled fluorophore and receptor units. *Journal of the American Chemical Society* **122**, 968–969 (2000).
10. Cheng, Y., Wang, J., Qiu, Z., Zheng, X., Leung, N. L., Lam, J. W. & Tang, B. Z. Multiscale humidity visualization by environmentally sensitive fluorescent molecular rotors. *Advanced Materials* **29**, 1703900 (2017).
11. Hattori, S., Ohkubo, K., Urano, Y., Sunahara, H., Nagano, T., Wada, Y., Tkachenko, N. V., Lemmetyinen, H. & Fukuzumi, S. Charge separation in a nonfluorescent donor- acceptor dyad derived from boron dipyrromethene dye, leading to photocurrent generation. *The Journal of Physical Chemistry B* **109**, 15368–15375 (2005).

12. McLaurin, E. J., Bradshaw, L. R. & Gamelin, D. R. Dual-emitting nanoscale temperature sensors. *Chemistry of Materials* **25**, 1283–1292 (2013).
13. Li, D., Hu, W., Wang, J., Zhang, Q., Cao, X.-M., Ma, X. & Tian, H. White-light emission from a single organic compound with unique self-folded conformation and multistimuli responsiveness. *Chemical Science* **9**, 5709–5715 (2018).
14. Yao, H., Ye, L., Zhang, H., Li, S., Zhang, S. & Hou, J. Molecular design of benzodithiophene-based organic photovoltaic materials. *Chemical reviews* **116**, 7397–7457 (2016).
15. Ye, L., Zhang, S., Zhao, W., Yao, H. & Hou, J. Highly efficient 2D-conjugated benzodithiophene-based photovoltaic polymer with linear alkylthio side chain. *Chemistry of Materials* **26**, 3603–3605 (2014).
16. Ye, L., Zhang, S., Huo, L., Zhang, M. & Hou, J. Molecular design toward highly efficient photovoltaic polymers based on two-dimensional conjugated benzodithiophene. *Accounts of chemical research* **47**, 1595–1603 (2014).
17. Sengupta, S., Pandey, U. K. & Athresh, E. U. Regioisomeric donor–acceptor–donor triads based on benzodithiophene and BODIPY with distinct optical properties and mobilities. *RSC advances* **6**, 73645–73649 (2016).
18. Aswathy, P., Sharma, S., Tripathi, N. P. & Sengupta, S. Regioisomeric BODIPY benzodithiophene dyads and triads with tunable red emission as ratiometric temperature and viscosity sensors. *Chemistry—A European Journal* **25**, 14870–14880 (2019).
19. Sunahara, H., Urano, Y., Kojima, H. & Nagano, T. Design and synthesis of a library of BODIPY-based environmental polarity sensors utilizing photoinduced electron-transfer-controlled fluorescence ON/OFF switching. *Journal of the American Chemical Society* **129**, 5597–5604 (2007).
20. Gabe, Y., Urano, Y., Kikuchi, K., Kojima, H. & Nagano, T. Highly sensitive fluorescence probes for nitric oxide based on boron dipyrromethene chromophore rational design of potentially useful bioimaging fluorescence probe. *Journal of the American Chemical Society* **126**, 3357–3367 (2004).
21. Ulrich, G., Ziessel, R. & Harriman, A. The chemistry of fluorescent bodipy dyes: versatility unsurpassed. *Angewandte Chemie International Edition* **47**, 1184–1201 (2008).
22. Karolin, J., Johansson, L. B.-A., Strandberg, L. & Ny, T. Fluorescence and absorption spectroscopic properties of dipyrrometheneboron difluoride (BODIPY) derivatives in liquids, lipid membranes, and proteins. *Journal of the American Chemical Society* **116**, 7801–7806 (1994).
23. Pavlopoulos, T. G., Shah, M. & Boyer, J. H. Laser action from a tetramethylpyrromethene-BF<sub>2</sub> complex. *Applied Optics* **27**, 4998–4999 (1988).
24. Loudet, A. & Burgess, K. BODIPY dyes and their derivatives: syntheses and spectroscopic properties. *Chemical reviews* **107**, 4891–4932 (2007).
25. Hu, R., Lager, E., Aguilar-Aguilar, A., Liu, J., Lam, J. W., Sung, H. H., Williams, I. D., Zhong, Y., Wong, K. S., Pena-Cabrera, E., et al. Twisted intramolecular charge transfer and aggregation-induced emission of BODIPY derivatives. *The Journal of Physical Chemistry C* **113**, 15845–15853 (2009).

26. Zhang, D., Martín, V., García-Moreno, I., Costela, A., Pérez-Ojeda, M. E. & Xiao, Y. Development of excellent long-wavelength BODIPY laser dyes with a strategy that combines extending  $\pi$ -conjugation and tuning ICT effect. *Physical Chemistry Chemical Physics* **13**, 13026–13033 (2011).
27. Buck, J. T., Wilson, R. W. & Mani, T. Intramolecular long-range charge-transfer emission in donor–bridge–acceptor systems. *The Journal of Physical Chemistry Letters* **10**, 3080–3086 (2019).
28. Weller, A. Photoinduced electron transfer in solution: exciplex and radical ion pair formation free enthalpies and their solvent dependence. *Zeitschrift für Physikalische Chemie* **133**, 93–98 (1982).
29. Inan, D., Dubey, R. K., Jager, W. F. & Grozema, F. C. Tailoring photophysical processes of perylene-based light harvesting antenna systems with molecular structure and solvent polarity. *The Journal of Physical Chemistry C* **123**, 36–47 (2018).
30. Zhu, H., Li, M., Hu, J., Wang, X., Jie, J., Guo, Q., Chen, C. & Xia, A. Ultrafast investigation of intramolecular charge transfer and solvation dynamics of tetrahydro [5]-helicene-based imide derivatives. *Scientific Reports* **6**, 24313 (2016).
31. Suhina, T., Amirjalayer, S., Woutersen, S., Bonn, D. & Brouwer, A. M. Ultrafast dynamics and solvent-dependent deactivation kinetics of BODIPY molecular rotors. *Physical Chemistry Chemical Physics* **19**, 19998–20007 (2017).
32. Whited, M. T., Patel, N. M., Roberts, S. T., Allen, K., Djurovich, P. I., Bradforth, S. E. & Thompson, M. E. Symmetry-breaking intramolecular charge transfer in the excited state of meso-linked BODIPY dyads. *Chemical Communications* **48**, 284–286 (2012).
33. Mangham, B., Hanson-Heine, M. W., Davies, E. S., Wriglesworth, A., George, M. W., Lewis, W., Kays, D. L., McMaster, J., Besley, N. A. & Champness, N. R. Influence of molecular design on radical spin multiplicity: characterisation of BODIPY dyad and triad radical anions. *Physical Chemistry Chemical Physics* **22**, 4429–4438 (2020).
34. Sharma, S., Wei, Z., Grozema, F. C. & Sengupta, S. Structure–property relationships in multi-stimuli responsive BODIPY-biphenyl-benzodithiophene TICT rigidochromic rotors exhibiting (pseudo-) Stokes shifts up to 221 nm. *Physical Chemistry Chemical Physics* **22**, 25514–25521 (2020).
35. Kim, T., Kim, W., Mori, H., Osuka, A. & Kim, D. Solvent and structural fluctuations induced symmetry-breaking charge transfer in a porphyrin triad. *The Journal of Physical Chemistry C* **122**, 19409–19415 (2018).
36. Winters, M. U., Pettersson, K., Mårtensson, J. & Albinsson, B. Competition between Superexchange-Mediated and Sequential Electron Transfer in a Bridged Donor–Acceptor System. *Chemistry—A European Journal* **11**, 562–573 (2005).
37. McConnell, H. M. Intramolecular charge transfer in aromatic free radicals. *The Journal of Chemical Physics* **35**, 508–515 (1961).
38. Kee, H. L., Kirmaier, C., Yu, L., Thamyongkit, P., Youngblood, W. J., Calder, M. E., Ramos, L., Noll, B. C., Bocian, D. F., Scheidt, W. R., et al. Structural control of the photodynamics of boron-dipyrin complexes. *The journal of physical chemistry B* **109**, 20433–20443 (2005).
39. Dereka, B., Rosspeintner, A., Stężycki, R., Ruckebusch, C., Gryko, D. T. & Vauthey, E. Excited-state symmetry breaking in a quadrupolar molecule visualized in time and space. *The journal of physical chemistry letters* **8**, 6029–6034 (2017).



40. Beckwith, J. S., Rosspeintner, A., Licari, G., Lunzer, M., Holzer, B., Fröhlich, J. & Vauthey, E. Specific monitoring of excited-state symmetry breaking by femtosecond broadband fluorescence upconversion spectroscopy. *The journal of physical chemistry letters* **8**, 5878–5883 (2017).
41. Toliautas, S., Dodonova, J., Žvirblis, A., Čiplies, I., Polita, A., Devižis, A., Tumkevičius, S., Šulskus, J. & Vyšniauskas, A. Enhancing the Viscosity-Sensitive Range of a BODIPY Molecular Rotor by Two Orders of Magnitude. *Chemistry—A European Journal* **25**, 10342–10349 (2019).
42. Sengupta, S. & Pandey, U. K. Dual emissive bodipy–benzodithiophene–bodipy TICT triad with a remarkable Stokes shift of 194 nm. *Organic & Biomolecular Chemistry* **16**, 2033–2038 (2018).
43. Snellenburg, J. J., Laptенок, S., Seger, R., Mullen, K. M. & van Stokkum, I. H. Glotaran: A Java-based graphical user interface for the R package TIMP. *Journal of Statistical Software* **49**, 1–22 (2012).
44. Te Velde, G. t., Bickelhaupt, F. M., Baerends, E. J., Fonseca Guerra, C., van Gisbergen, S. J., Snijders, J. G. & Ziegler, T. Chemistry with ADF. *Journal of Computational Chemistry* **22**, 931–967 (2001).
45. Baerends, E., Ellis, D. & Ros, P. Self-consistent molecular Hartree–Fock–Slater calculations I. The computational procedure. *Chemical Physics* **2**, 41–51 (1973).
46. Pedone, A. Role of solvent on charge transfer in 7-aminocoumarin dyes: new hints from TD-CAM-B3LYP and state specific PCM calculations. *Journal of Chemical Theory and Computation* **9**, 4087–4096 (2013).
47. Yanai, T., Tew, D. P. & Handy, N. C. A new hybrid exchange–correlation functional using the Coulomb-attenuating method (CAM-B3LYP). *Chemical physics letters* **393**, 51–57 (2004).
48. Van Gisbergen, S., Snijders, J. & Baerends, E. Implementation of time-dependent density functional response equations. *Computer Physics Communications* **118**, 119–138 (1999).
49. Le Guennic, B. & Jacquemin, D. Taking up the cyanine challenge with quantum tools. *Accounts of chemical research* **48**, 530–537 (2015).
50. Momeni, M. R. & Brown, A. Why do TD-DFT excitation energies of BODIPY/aza-BODIPY families largely deviate from experiment? Answers from electron correlated and multireference methods. *Journal of chemical theory and computation* **11**, 2619–2632 (2015).
51. Seth, M., Mazur, G. & Ziegler, T. Time-dependent density functional theory gradients in the Amsterdam density functional package: geometry optimizations of spin-flip excitations. *Theoretical Chemistry Accounts* **129**, 331–342 (2011).
52. Klamt, A. & Schüürmann, G. COSMO: a new approach to dielectric screening in solvents with explicit expressions for the screening energy and its gradient. *Journal of the Chemical Society, Perkin Transactions 2*, 799–805 (1993).

# A

## Appendix to Chapter 3

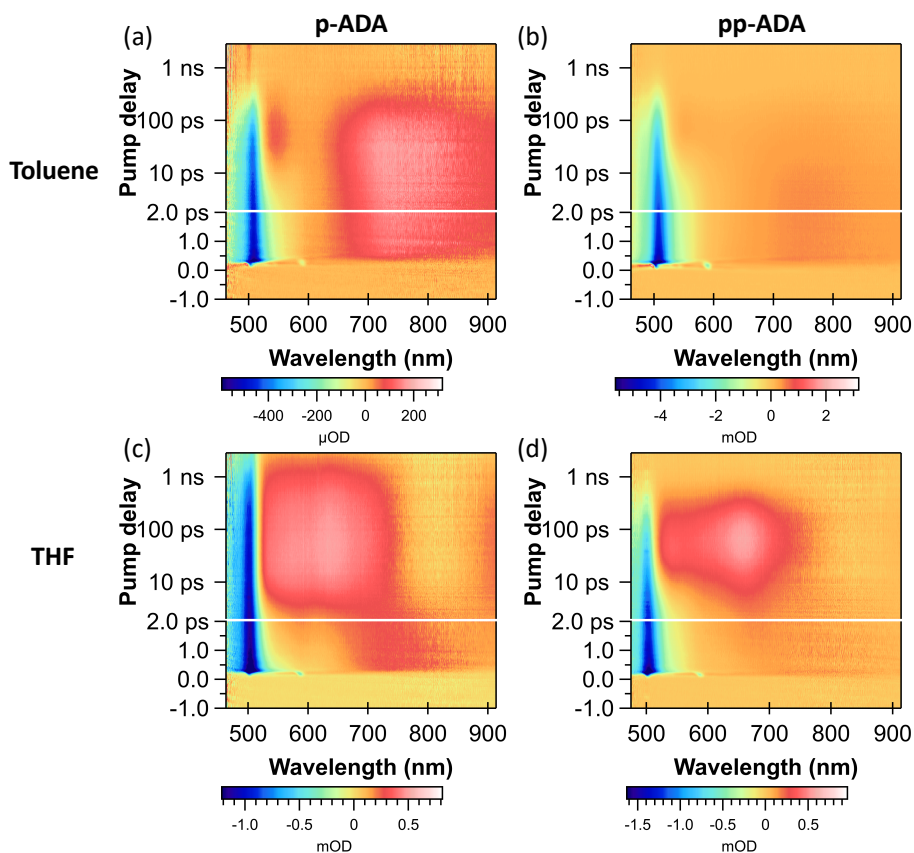


**Figure A.1.** Contour plots of the transient absorption spectra of **p-ADA** and **pp-ADA** in toluene and THF with photoexcitation at 500 nm.

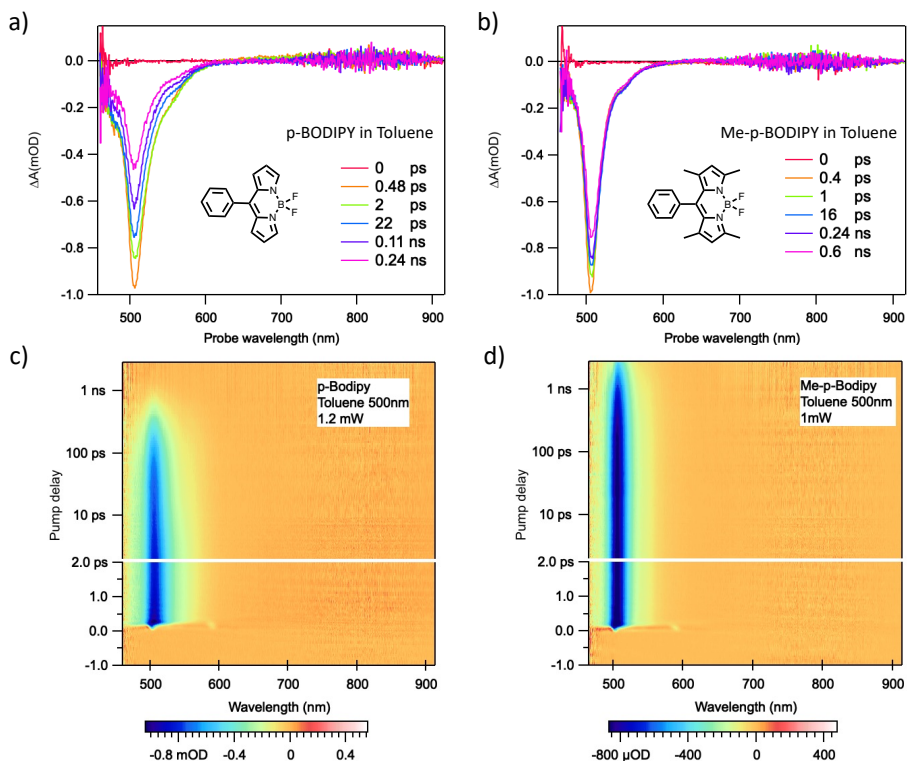


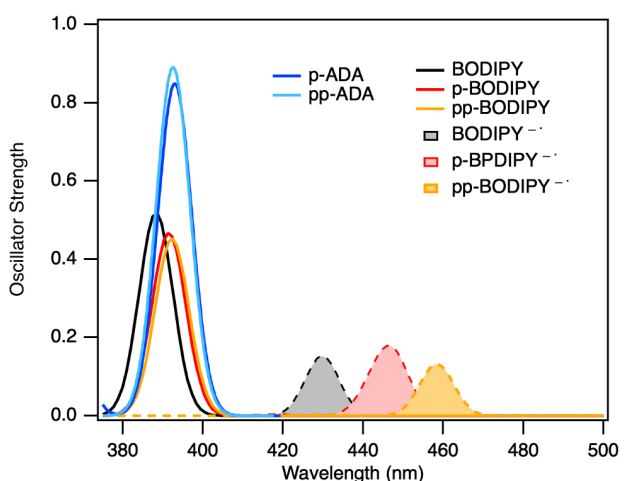
**Figure A.2.** Transient absorption spectra and their contour plots of a), c) **p-BODIPY** and b), d) **Me-p-BODIPY** in toluene with photoexcitation at 500 nm.

Geometries of the neutral molecule and the negatively charged molecule were optimized by DFT calculations with CAM-B3LYP/DZP to obtain the total bonding energy,  $E_{\text{bonding}}$ , of the molecules. The adiabatic electron affinity,  $E_{\text{EA}}$ , is calculated by  $E_{\text{EA}} = E_{\text{bonding}}(\text{neutral}) - E_{\text{bonding}}(\text{negative})$ .

**Table A.1.** Calculated electron affinity of **p-BODIPY** and **Me-p-BODIPY**

	$E_{\text{bonding}}$ (neutral)	$E_{\text{bonding}}$ (negative)	$E_{\text{EA}}$
<b>p-BODIPY</b>	-290.0297 eV	-292.2175 eV	2.19 eV
<b>Me-p-BODIPY</b>	-380.3387 eV	-382.0885 eV	1.75 eV

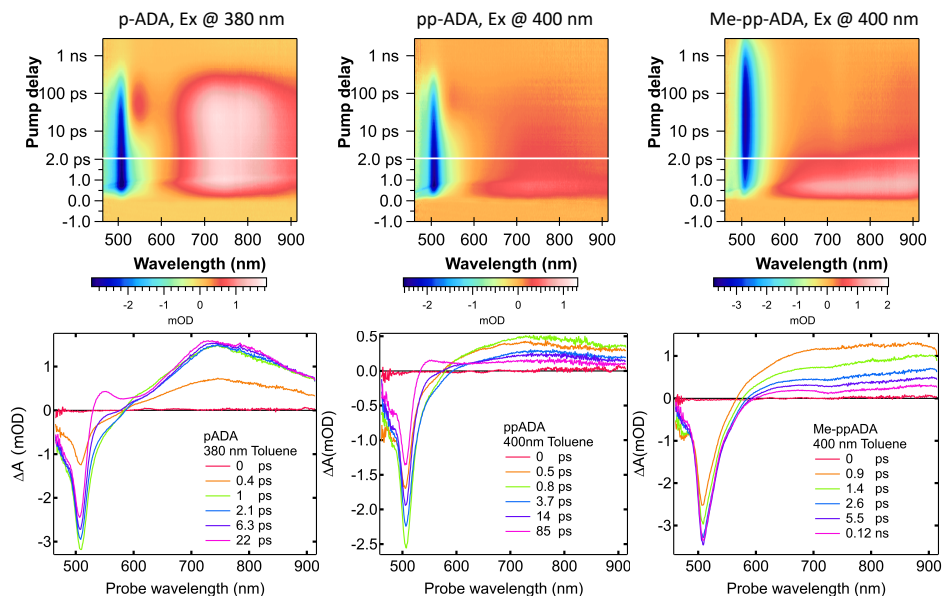
According to the TDDFT calculations, the lowest allowed transitions in both **p-ADA** and **pp-ADA** are located at  $\sim 393$  nm. Their oscillator strengths are nearly twice as large as these of the individual acceptors, in line with the incorporation of two acceptors in triad molecules. **p-ADA**, **pp-ADA** and **p-BODIPY** show similar vertical transition energies, which is consistent with their overlapping experimental absorption spectra, showing the strength of the calculations. For



**Figure A.3.** Vertical transition energies calculated by TDDFT with CAM-B3LYP/DZP.

the neutral BODIPY molecules, increasing the number of phenyl units has a small impact on the lowest excitation energy. For the negatively charged BODIPY molecules, the excitation energy is systematically red-shifted by dozens of nanometers with the increasing the number of phenyl units. This possibly associated with the transformation of the two broad absorption features at 580 nm and 635 nm of the CT state in **p-ADA** into the one sharp absorption peak at 658 nm of that in **pp-ADA**.

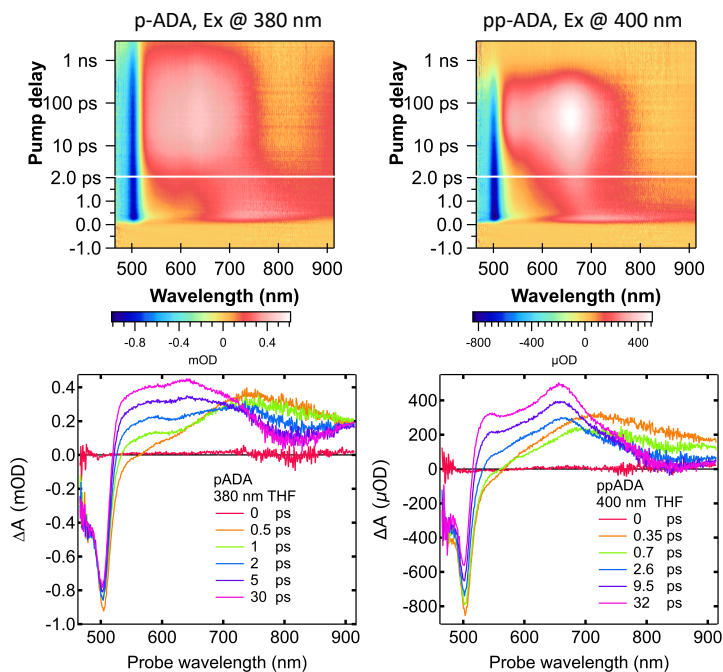
In general, the TA spectrum of **p-ADA** in toluene (Figure A.4a) is similar to that at the excitation of acceptor (Figure A.1a). Nevertheless, in the first picosecond, the GSB at  $\sim 500$  nm is growing to the maximum instead of simultaneously reaching the maximum upon the photoexcitation. Meanwhile, the broad ESA band experiences a narrowing in the band width and a growth in the amplitude, giving rising to the spectral signature of the excited acceptor. These features indicate an ultrafast excitation energy transfer from the BDT donor to the BODIPY acceptor. In **pp-ADA**, the absorption band between 650 nm and 900 nm is less pronounced than that in **p-ADA**, consistent with the weaker ESA of acceptor in **pp-ADA**. Since no ESA of acceptor is observed in **Me-pp-ADA** as indicated in Figure 3.3c, Figure A.4f further demonstrates that the broad absorption band presented upon the excitation is associated with the absorption of the excited donor.



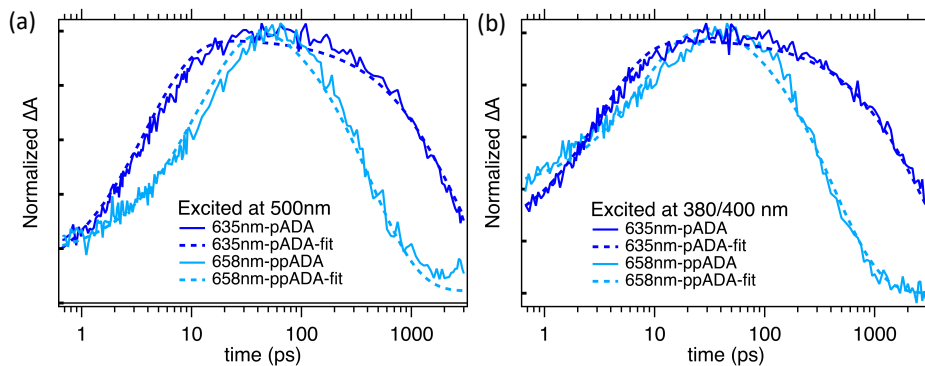
**Figure A.4.** Transient absorption spectra and their contour plots of triads in toluene with photoexcitation at 380/400 nm.

**Table A.2.** Time constants of global analysis of fluorescence lifetime

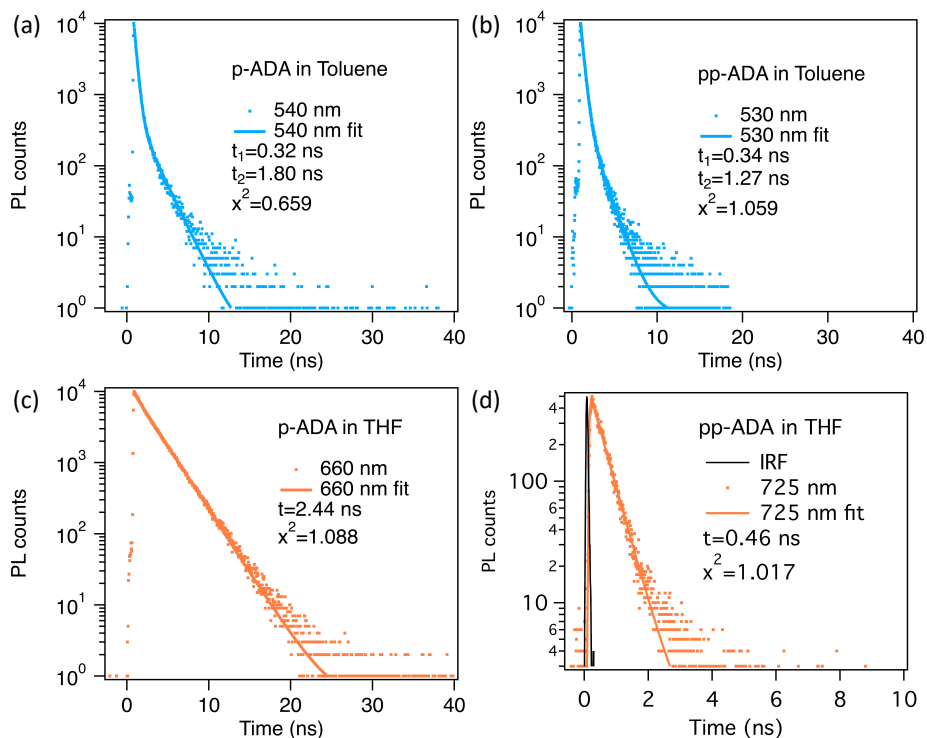
		THF		Toluene	
		<b>p-ADA</b>	<b>pp-ADA</b>	<b>p-ADA</b>	<b>pp-ADA</b>
Excited at 500 nm	$t_2$	3.83 ps	11.65 ps	7.83 ps	14.0 ps
	$t_2$	2.68 ns	0.44 ns	0.25 ns	0.3 ns
Excited at 380/400 nm	$t_1$	3.24 ps	8.38 ps	11.1 ps	14.5 ps
	$t_2$	2.80 ns	0.42 ns	0.27 ns	0.26 ns
Excited at 404 nm	$t_{FL}$	2.44 ns	0.46 ns	0.32 ns (76%)	0.34 ns (80%)
		@660 nm	@725 nm	1.80 ns (24%) @540 nm	1.27 ns (20%) @530 nm



**Figure A.5.** Transient absorption spectra and their contour plots of triads in THF with photoexcitation at 380/400 nm.



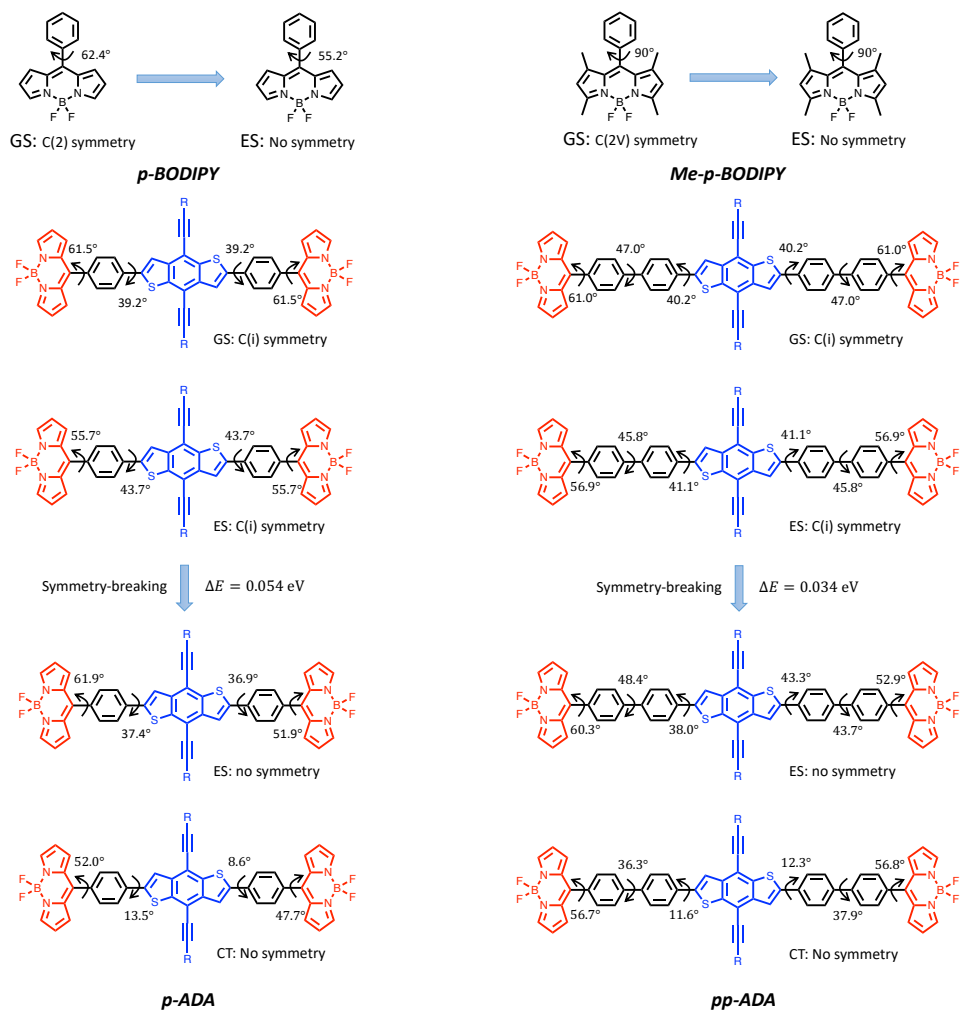
**Figure A.6.** Selected time traces (solid lines) and fits (dashed lines) at the characteristic wavelengths of the charge transfer state for **p-ADA** (dark blue) and **pp-ADA** (light blue).



**Figure A.7.** Fluorescence lifetime recorded at different wavelengths excited at 404 nm for **p-ADA** a) in toluene and c) in THF, and for **pp-ADA** b) in toluene and d) in THF.

**Table A.3.** State-specific solvent stabilization of the local excited state and charge-transfer state in **p-ADA** and **pp-ADA**.

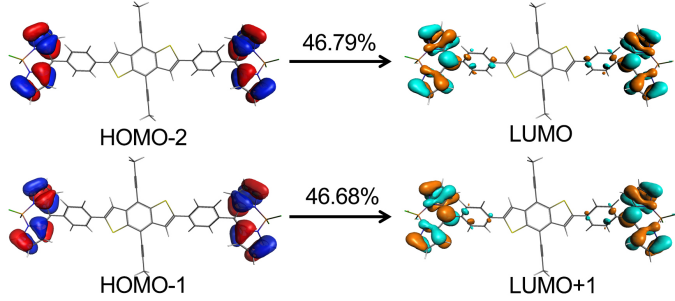
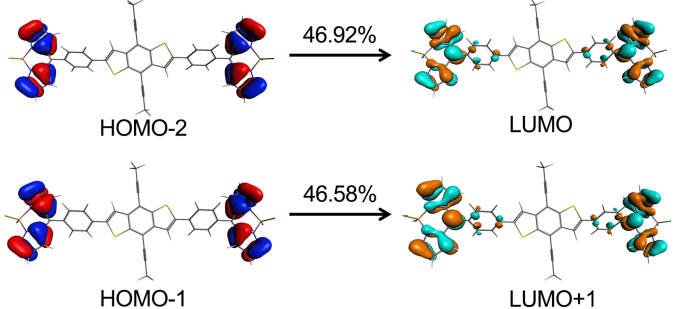
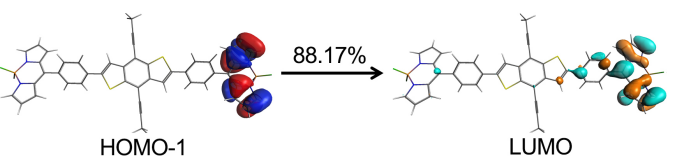
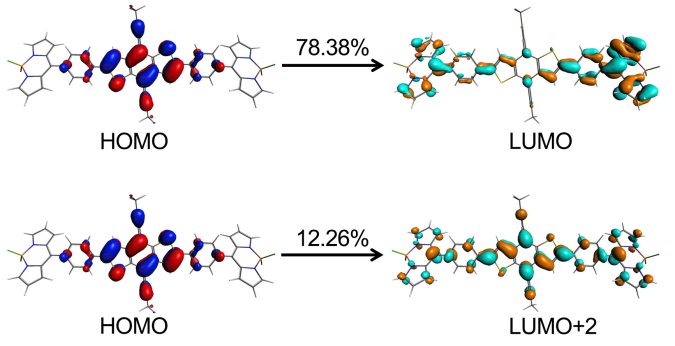
		<b>p-ADA</b>			
		$E_{\text{vacuum}}$ (eV)	$E_{\text{THF}}$ (eV)	$\Delta E$ (eV)	$E_{\text{solvent}}$ (eV)
ES geometry	GS	-816.3083	-816.9700	0.662	0.053
	HOMO-1->LUMO	-813.4458	-814.1607	0.715	
CT geometry	GS	-816.1006	-816.7846	0.684	0.735
	HOMO->LUMO	-813.628	-815.0474	1.419	
		<b>pp-ADA</b>			
		$E_{\text{vacuum}}$ (eV)	$E_{\text{THF}}$ (eV)	$\Delta E$ (eV)	$E_{\text{solvent}}$ (eV)
ES geometry	GS	-1003.4718	-1004.1925	0.721	0.022
	HOMO-1->LUMO	-1000.5769	-1001.3203	0.743	
CT geometry	GS	-1003.2479	-1003.9853	0.737	1.252
	HOMO->LUMO	-999.8068	-1001.7956	1.989	



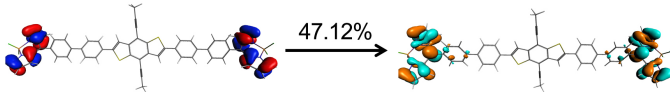
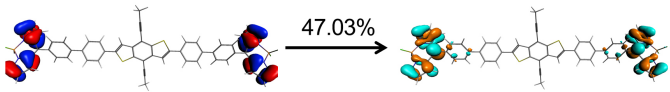
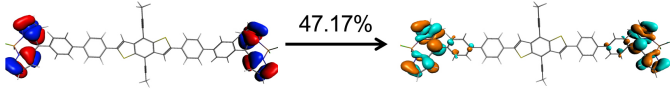
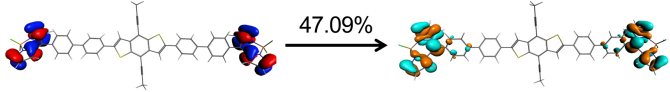
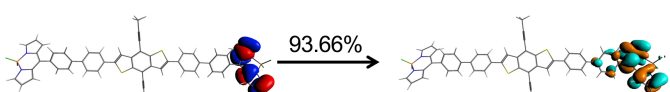
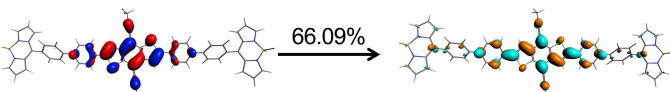
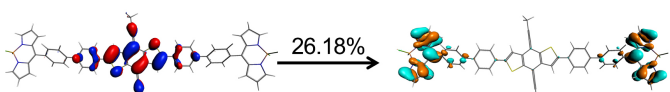
**Figure A.8.** Torsion angles in the geometry optimized ground state (GS), symmetrical excited state (ESSym), asymmetrical excited state (ES) and charge transfer state (CT) of **p-ADA** and **pp-ADA** and BODIPY-Ph torsion angles in GS and ES of **p-BODIPY** and **Me-p-BODIPY**.



A

Geometry	Excitation Energy/ Oscillator Strength	Major MO $\rightarrow$ MO transitions for the lowest allowed excitation
GS	3.155 eV/ 0.85	
ES <sub>sym</sub>	3.089 eV/ 0.80	
ES	2.977 eV/ 0.35	
CT	2.737 eV/ 1.62	

**Figure A.9.** Major single orbital transitions for the lowest allowed transition of **p-ADA** with geometries of optimized ground state (GS), symmetrical excited state (ES<sub>sym</sub>), asymmetrical excited state (ES) and charge transfer state (CT).

Geometry	Excitation Energy/ Oscillator Strength	Major MO $\rightarrow$ MO transitions for the lowest allowed excitation
GS	3.159 eV/ 0.89	 HOMO-2 $\xrightarrow{47.12\%}$ LUMO+1  HOMO-1 $\xrightarrow{47.03\%}$ LUMO
ES <sub>sym</sub>	3.096 eV/ 0.84	 HOMO-2 $\xrightarrow{47.17\%}$ LUMO+1  HOMO-1 $\xrightarrow{47.09\%}$ LUMO
ES	3.008 eV/ 0.38	 HOMO-1 $\xrightarrow{93.66\%}$ LUMO
CT	2.885 eV/ 2.03	 HOMO $\xrightarrow{66.09\%}$ LUMO+2  HOMO $\xrightarrow{26.18\%}$ LUMO

**Figure A.10.** Major single orbital transitions for the lowest allowed transition of **pp-ADA** with geometries of optimized ground state (GS), symmetrical excited state (ES<sub>sym</sub>), asymmetrical excited state (ES) and charge transfer state (CT).

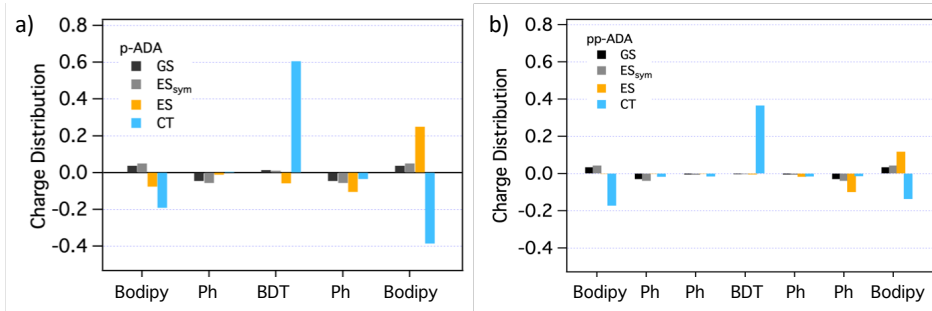


**Figure A.11.** Geometry-dependent charge distribution over the BODIPY acceptors, the individual phenyl units and the BDT donor of the excited state as compared to the ground-state corresponding to the lowest vertical transition for a) **p-ADA** and b) **pp-ADA**. Only the single orbital transitions with contribution larger than 1% are taken into account.

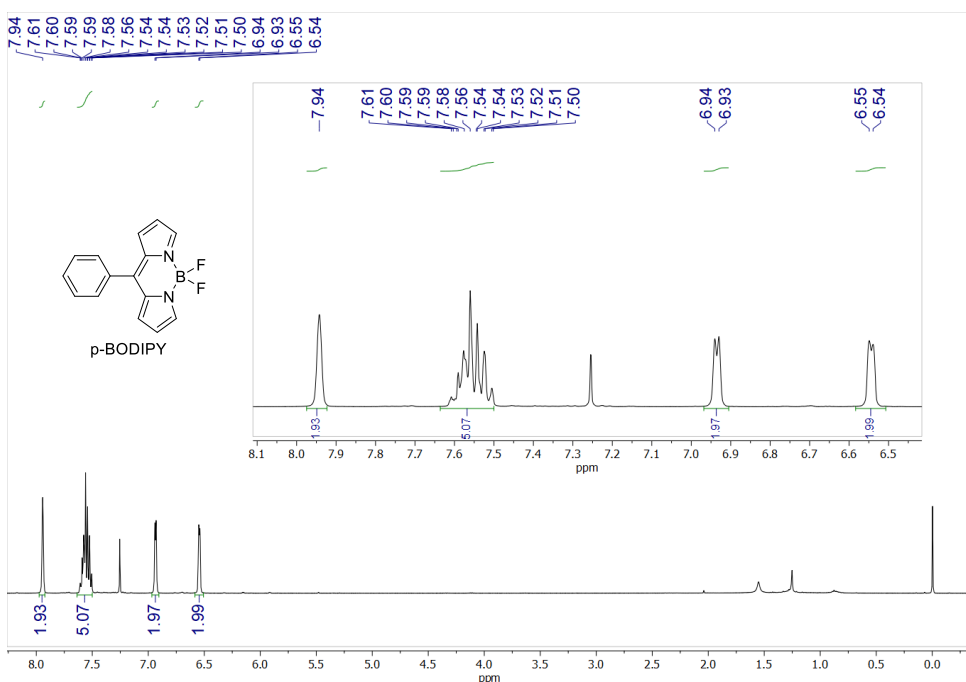


**Figure A.12.** <sup>1</sup>H NMR spectrum of **p-BODIPY** in CDCl<sub>3</sub>.

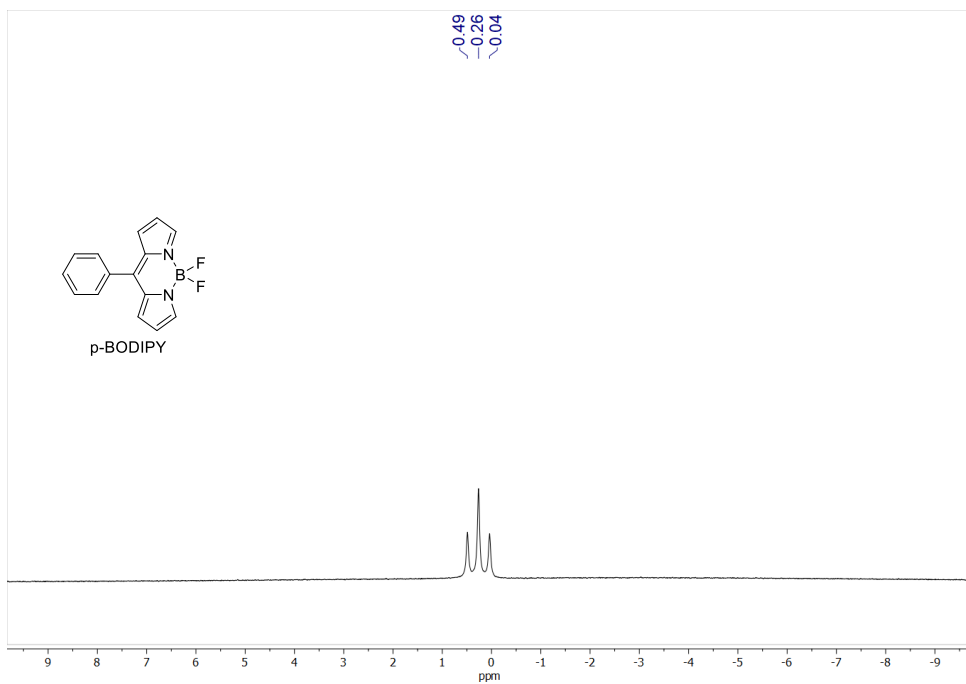


**Figure A.13.**  $^{11}\text{B}$  NMR spectrum of **p-BODIPY** in  $\text{CDCl}_3$ .



# 4

## Fast charge separation driven by relaxation of hot excited state

*In this chapter, we present a comprehensive experimental and computational investigation of the photoinduced charge separation (CS) in a series of three perylenemonoimide-*p*-oligophenylene-dimethylaniline molecular dyads. This study reveals a clear demarcation concerning the nature of the CS accessed at shorter (bridgeless) and longer DA distances. At the shortest distance, strong DA interaction and ground-state charge delocalization populate a hot excited state (ES) with prominent charge transfer (CT) character, via Franck-Condon vertical excitation. The presence of such CT polarized hot ES enables a subpicosecond CS in the bridgeless dyad. The incorporation of *p*-oligophenylene bridge effectively decouples the donor and the acceptor units in the ground state and consequentially suppresses the CT polarization in the hot ES. Theoretically, this should render a slower CS at longer distances. However, the transient absorption measurement reveals a fast CS process even at a longer distance, contrary to the anticipated exponential distance dependence of the CS rates. A closer look into the excited state dynamics suggests that the hot ES undergoes ultrafast geometry relaxation ( $\tau < 1$  ps) to create a relaxed ES. As compared to a decoupled, twisted geometry in the hot ES, the geometry of the relaxed ES exhibit a more planar conformation of the *p*-oligophenylene bridges. Planarization of the bridge endorses an increased charge delocalization and a prominent CT character in the relaxed ES and forms the origin for the evident fast CS at the longest distance. Thus, the relaxation of the hot ES and the concomitantly enhanced charge delocalization adds a new caveat to the classic nature of distance-dependent CS in artificial DBA chromophores and recommends a cautious treatment of the attenuation factor ( $\beta$ ) while discussing anomalous CS trends.*

---

<sup>†</sup>This chapter is based on: Zimu Wei<sup>#</sup>, Abbey M. Philip<sup>#</sup>, Wolter F. Jager, Ferdinand C. Grozema, The Journal of Physical Chemistry C, 2022, 126 (45), 19250-19261. <sup>#</sup>Authors contributed equally.

## 4.1. Introduction

Inspired by nature, there is a strong interest in developing artificial systems for driving photochemical reactions, producing electrical output, or deriving stimulus-responsive photoswitches[1–6]. In these natural[7] and artificial systems[2, 4, 8], charge transfer (CT) processes play a quintessential role and thus draw major interest from a scientific and technological perspective[9]. To tailor the CT properties for a specific application[10, 11], it is crucial to understand the fundamental nature of the excited state (ES), the precursor state for a CT process. Many such examples of synthetic control over the nature of the ES have been achieved by artificial donor–bridge–acceptor (DBA) chromophores that combine electron-donating and electron-accepting groups with complementary (opto)electronic character[3, 10, 11].

In a typical DBA system, the photoinduced charge separation (CS) is dictated by the thermodynamic[12] and kinetic[13] parameters including the free energy ( $\Delta G_{\text{CS}}^0$ ), reorganization energy ( $\lambda$ ) and electronic coupling ( $H_{\text{DA}}$ ). The thermodynamic feasibility ( $\Delta G_{\text{CS}}^0$ ) for efficient CS relies on the redox potentials of the donor and acceptor, molecule distances ( $R_{\text{DA}}$ ), and solvent polarity[12]. The latter two also influence the reorganization energy ( $\lambda$ ). The electronic coupling ( $H_{\text{DA}}$ ) strongly depends on the nature of the molecular bridge, the donor, the acceptor, their relative spatial orientation[14–17], and distances ( $R_{\text{DA}}$ )[13, 18–21]. Because of the exponential radial character of electronic wave functions, the electronic coupling ( $H_{\text{DA}}$ ) is expected to decay exponentially with increasing DA distances ( $R_{\text{DA}}$ ).

Consequently, the CS kinetic rates ( $k_{\text{CS}}$ ) in DBA systems generally follow an exponential distance dependence in the tunneling regime at short distances ( $<20 \text{ \AA}$ )[22],  $k_{\text{CS}} = k_0 e^{-\beta R_{\text{DA}}}$  wherein  $k_0$  is a kinetic prefactor and  $\beta$  is the attenuation factor that characterizes the capability of the intervening bridge to transfer charge. The attenuation factor  $\beta$  has been perceived to be a bridge-dependent parameter, and the reported values of the attenuation factor span a wide range between fully conducting ( $\beta < 0.1 \text{ \AA}^{-1}$ )[23–25] and highly insulating ( $\beta > 0.5 \text{ \AA}^{-1}$ ) bridges[26, 27]. It has been observed that for the same  $\pi$ -conjugated bridge,  $\beta$  values can be considerably dissimilar in different DBA systems, and many mechanisms have been proposed to account for the anomalous distance dependence observed experimentally[28, 29]. For instance, it is widely recognized that switching from coherent tunneling (superexchange) to incoherent hopping is responsible for the shallow distance dependence and small  $\beta$  values at a long DA distance (up to  $40 \text{ \AA}$ )[19, 30]. In the frame of the superexchange mechanism, nonexponential distance dependence has been observed and attributed to a crossover from the inverted to normal CS regime, owing to high reorganization energy with an increasing distance[31, 32]. At short DA distances ( $<20 \text{ \AA}$ ), however, a sharp decrease in the CS rate with the distance is generally expected[33]. Only a few exceptions have been reported mostly due to system-specific mechanisms, such as the initial state delocalization[34], strong solvent polarity[35], and resonant bridge states[36]. Therefore, a comprehensive understanding on mechanisms for an anomalous

CS trend at a short distance will pave the way to customize DBA chromophores for specific applications with a broad choice of molecular lengths.

Herein, we explore the nature of the distance-dependent CS in a series of short DBA dyads (**P0**, **P1**, and **P2**) wherein a perylenemonoimide (**PMI**) acceptor is connected to a dimethylaniline (**DMA**) donor via intervening p-oligophenylene bridges ( $n = 0, 1, \text{ and } 2$ , **Figure 4.1a**). The excited-state photodynamics within the DBA compounds was evaluated using steady-state optical, ultrafast transient absorption, and theoretical investigations. Evidence from the comprehensive experimental and computational studies indicates an anomalous deviation from the exponential attenuation of the CS rates at longer distances (for **P2**) as compared to the shorter distances (**P0** and **P1**). The origin of the deviation was rationalized by comparing the charge delocalization in the excited states (hot and relaxed ES)<sup>1</sup> as compared to the ground-state geometries. The comparison suggests that the geometry relaxation of the hot ES results in a more planar and electronically coupled relaxed ES in **P2** that exhibits an enhanced charge delocalization and CT character. This, in turn, increases the rate of charge separation from the relaxed ES and creates a deviation from the anticipated nature of distance dependence of CS rates at longer distances. Thus, charge delocalization adds a new caveat to the nature of distance-dependent charge separation and stresses the importance of treating the attenuation factor  $\beta$  as a system-specific parameter while interpreting anomalous CS trends in distant DBA architectures.

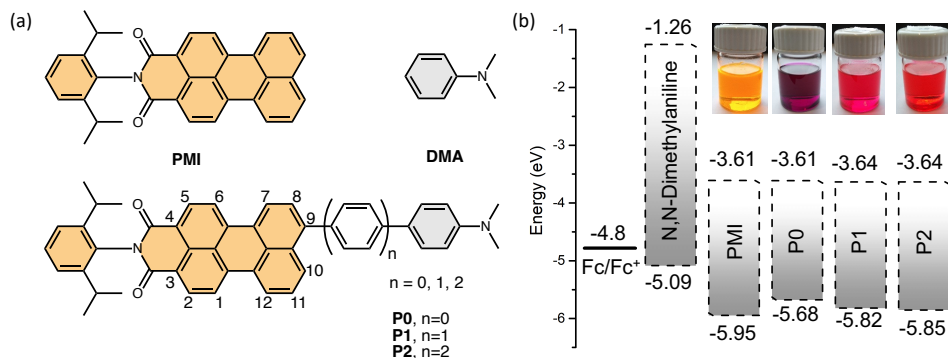


**Figure 4.1.** (a) Molecular structures of **PMI**, **DMA** and DBA derivatives (**P0-P2**). (b) Energy levels of the reference (**PMI**) and DBA derivatives (**P0**, **P1**, and **P2**) against vacuum.

<sup>1</sup>The term “hot” excited state refers to the first singlet excited state that is populated via Franck–Condon vertical excitation. The term “relaxed” excited state refers to the singlet state accessed by the relaxation of the “hot” excited state.



## 4.2. Results and discussion

Perylenemonoimide (**PMI**) belongs to the family of rylene chromophores, which are widely known for their promising optical features, excellent photo(chemical) stability, and electron-deficient nature[37–39]. **PMI** was chosen as the electron acceptor owing to its facile, scalable syntheses and the ease of direct functionalization at the 9-position as reported earlier (Figure 4.1a) [40–47]. N,N-Dimethylaniline (**DMA**) was utilized as the electron donor owing to its strong electron-donating nature as well as its proton sensitivity. To construct the DBA scaffolds, **PMI** and **DMA** were directly connected at the 9-position with an intervening p-oligophenylene bridge of varying lengths. A direct connection with a rigid bridge not only defines the distance but also affords sufficient electronic coupling between the distant D/A units. Additionally, the substitution at the 9-position of **PMI** renders a minimal steric block between D and A units, as opposed to the large steric congestion at the bay region. Herein, unsubstituted perylenemonoimide (**PMI**) acts as a model reference for **P0** (no bridge), **P1** (phenyl bridge), and **P2** (biphenyl bridge) DBA derivatives. Though **PMI** and **DMA** units are connected via a rigid, nonfunctionalized p-oligophenylene bridge, the DBA compounds possess adequate solubility in weakly polar toluene, moderately polar tetrahydrofuran (THF), and polar benzonitrile (Bzn) solvents used for the spectroscopic studies. The derivatives **P0** exhibited sufficient solubility in nonpolar hexane as compared to **P1** and **P2**, which were insoluble in that solvent.

The standard values of the redox potentials are reported in Tables B.1 and B.2, Figures B.1 and B.2 along with the HOMO/LUMO energy levels versus vacuum in Figure 4.1b. The reference **PMI** exhibits a first reduction at ca. -1.38 V and oxidation at ca. 0.98 V[48]. The electrochemical reduction of the perylene core in the DBA derivatives becomes gradually more facile as the distance between **DMA** and the perylene core increases in **P0** (ca. -1.39 V), **P1** (ca. -1.38 V), and **P2** (ca. -1.36 V) (Table B.1), and a reverse trend is observed for the oxidation of the perylene core. The observed changes in the redox properties translate into HOMO-LUMO energy gap ( $E_g$ ) tuning. The  $E_g$  of **P0** is 0.27 eV smaller than the unsubstituted **PMI**, implying a strong ground-state interaction among the **PMI** and **DMA** donor[49]. The HOMO-LUMO energy gap increases as the **PMI** and **DMA** groups are further separated in **P1/P2**, and this is clearly reflected in the systematic tuning of the optical color of the solutions (Figure 4.1b).

### 4.2.1. Steady-state optical properties

To probe the photoexcited-state properties and their distance dependence, steady-state UV-vis absorption and fluorescence (Figure 4.2) of the DBA compounds were measured in solvents of varying polarities (Table 4.1 and Figures B.3 to B.9). The UV-vis absorption of the **PMI** in toluene is characterized by typical singlet  $\pi - \pi^*$  transitions of the perylene chromophore in the 400-550 nm range and depicts negligible change with the increasing solvent polarity (Figure B.4)[50]. The DBA derivative **P0** exhibits a broad, structureless UV-vis absorption in toluene and a concomitant bathochromic shift upon increasing the

solvent polarity (Figure 4.2a). The broad, featureless UV-vis absorption in **P0** as compared to the reference **PMI** and the strong solvent polarity dependence suggest that the Franck–Condon (FC) vertical excitation is accompanied by a partial charge transfer (CT) from the D to A unit. Thus, the hot excited state (ES) in **P0**, formed upon FC vertical excitation, is delocalized showing CT character[51]. Upon introducing the p-oligophenylene bridge between the **PMI** and **DMA** groups, a UV-vis absorption with vibronic signature is observed in **P1** and **P2**, analogous to **PMI** in toluene. Although the UV-vis absorption of the **P1** and **P2** still deviates from that of **PMI** (Figure B.3), the deviation becomes much smaller than that of **P0**, implying that the degree of delocalization in hot ES is gradually suppressed with the increasing bridge length. This is evidently observed in the form that the magnitude of the solvatochromic bathochromic shift in **P1/P2** is minuscule as compared to **P0**. This further suggests that the CT polarization in the hot ES of **P1/P2** is small and diminished for longer bridge lengths.

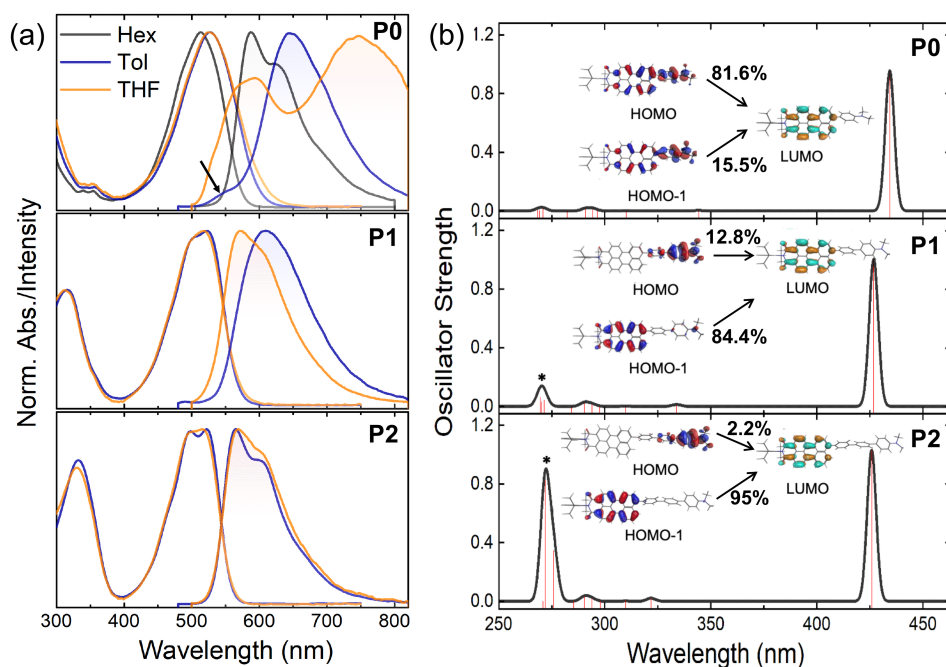


**Figure 4.2.** (a) Normalized UV-vis absorbance (solid lines) and fluorescence emission (dashed lines, Ex @ 490 nm) spectra in solvents of varying polarities and (b) simulated optical excitation for **P0** (top), **P1** (middle), and **P2** (bottom) calculated using TD-DFT with CAM-B3LYP/DZP. The arrow in the emission spectra of **P0** highlights the diffuse emission band in toluene. \*Bands appearing at high energies indicate the mixed transition involving the p-oligophenylene bridge.

To gain a more detailed picture of the hot ES of the DBA compounds, DFT

calculations were performed using the Amsterdam Density Functional (ADF) theory package using the range-separated CAM-B3LYP functional with the double-zeta plus polarization (DZP) basis set (Figure 4.2 and Table B.4)[52]. The simulated absorption spectra of the reference **PMI** reveal a dominant HOMO→LUMO (~416 nm) transition localized on the perylene core ( $\pi - \pi^*$ ) as the main band with a considerable oscillator strength (Figure B.10). For DBA compounds, the nature of the excited states exhibits a marked distance dependence as compared to **PMI**. In **P0**, the principal band at 434 nm has prominent contributions from HOMO→LUMO (81.6%) and HOMO-1→LUMO (15.5%) CT-type transitions. In **P1**, the fundamental absorption at 427 nm mainly consists of  $\pi - \pi^*$ -type HOMO-1→LUMO (84.4%) and a much smaller CT-type HOMO→LUMO (12.8%) transition. This trend is further apparent in **P2**, wherein a further reduction in the CT character (HOMO-1→LUMO; 2.2%) is observed for the fundamental absorption band at 426 nm. Additionally, with the increasing length of the bridge in **P1** and **P2**, a new band (with considerable oscillator strengths) emerges in the near-UV region, similar to that observed in UV-vis spectra. These high-energy absorption bands in **P1** and **P2** arise from complex mixed transitions involving the p-oligophenylene bridge (see Figure B.11).

The distance-dependent CT character of the hot ES in DBA derivatives is established from the UV-vis experiments and molecular simulations. The nature of the relaxed ES and its distance dependence can further be established from the fluorescence measurements in solvents of varying polarities (Figure 4.2a and Figures B.3 to B.9). The fluorescence spectrum of the reference **PMI** in toluene, THF, and Bzn centers around 500-750 nm with a mirror image symmetry to the UV-vis absorption. Marginal solvent dependence of radiative emission for **PMI** suggests a low impact of the solvent environment on the bright local ES and a small dipole moment change upon FC vertical excitation (Figure B.4 and Table B.3)[53]. Contrarily, **P0** depicts an interesting and complex emission profile with respect to the solvent continuum. **P0** in nonpolar hexane depicts a characteristic **PMI**-like emission with a high quantum efficiency ( $\Phi_F \approx 0.81$ ). Changing the solvent to weakly polar toluene renders a dual emission character at 550 (weak band) and 644 nm (intense and broad) with a considerable Stokes shift ( $\Delta\lambda = 117$  nm) and a moderate decrease in quantum yields ( $\Phi_F \approx 0.60$ ). Increasing the polarity to THF leads to a clear dual emission with an increased Stokes shift ( $\Delta\lambda = 221$ ) for the long-wavelength band as well as a low fluorescence quantum yield ( $\Phi_F \approx 0.12$ )[41, 54]. Increasing the solvent polarity to Bzn further quenches the fluorescence emission for **P0** ( $\Phi_F \approx 0.05$ ). Herein, the redshifted band becomes diffuse, and the residual emission becomes prominent from the relaxed ES with minor CT polarization. To assess the dipole moment difference between the ground and excited state, the solvatochromic method was utilized (see Chapter B for details)[55, 56]. The assessment of the ground- ( $\mu_g = 2.92$  D) and excited-state dipole ( $\mu_e = 21.24$  and 30.04 D) moments for **P0** reveal (i) a large dipole moment difference ( $\Delta\mu = 18.32$  and 27.48 D) between the ground and excited state and (ii) at least two different dipole moments for the ES indicating the presence of excited states

**Table 4.1.** Optical properties of **PMI** and **P0-P2** in solvents of varying polarity.

	Solvent	$\lambda_{abs}$ (nm)	$\lambda_{em}$ (nm)	Stokes Shift <sup>a</sup> [ $\Delta\lambda$ ](nm)	$\phi_F^b$	$\phi_F^c$	FE	$\tau_F$ ( ns) <sup>f</sup>
<b>PMI</b>	Toluene	507	530	23	0.88	--- <sup>d</sup>	--- <sup>d</sup>	4.54
	THF	502	536	34	0.91	--- <sup>d</sup>	--- <sup>d</sup>	4.87
	Bzn	511	550	39	0.83	--- <sup>d</sup>	--- <sup>d</sup>	4.93
<b>P0</b>	Hexane	513	587	74	0.81	--- <sup>d</sup>	--- <sup>d</sup>	3.92
	Toluene	527	553 <sup>e</sup> , 644	117	0.60	--- <sup>d</sup>	--- <sup>d</sup>	3.44 <sup>g</sup>
	THF	527	593,748	221	0.12	0.86	7.2	3.35, <sup>h</sup> 0.76
	Bzn	545	611,778 <sup>e</sup>	233	0.05	0.84	16.8	3.89 <sup>i</sup>
<b>P1</b>	Toluene	523	608	85	0.70	--- <sup>d</sup>	--- <sup>d</sup>	3.55
	THF	518	572	54	0.027	0.86	32	3.77
	Bzn	529	590	61	0.018	0.81	45	4.18
<b>P2</b>	Toluene	522	566	44	0.78	--- <sup>d</sup>	--- <sup>d</sup>	3.55
	THF	516	569	53	0.055	0.839	16.2	3.67
	Bzn	526	591	65	0.015	0.76	51	4.04

<sup>a</sup>Stokes shifts with respect to the red-shifted band. Fluorescence quantum yield in <sup>b</sup>neutral and <sup>c</sup>protonated state (using 48 % HBr solution), <sup>d</sup>no protonation attempted, <sup>e</sup>diffuse band. FE = fluorescence enhancement in protonated versus non-protonated state, excitation at 404 nm. The emission lifetime was monitored around the emission maxima unless otherwise mentioned; emission monitored at <sup>g</sup>640, <sup>h</sup>600, <sup>i</sup>750, and <sup>j</sup>610 nm. Photophysical measurements of **PMI**, **P1** and **P2** in hexane were not possible owing to the low solubility.

with a distinct nature of charge distribution[57, 58].

The longer DBA derivatives, **P1** ( $\Phi_F \approx 0.70$ ,  $\Delta\lambda = 85$  nm) and **P2** ( $\Phi_F \approx 0.78$ ,  $\Delta\lambda = 44$  nm), in toluene exhibit an intense fluorescence emission and a narrow Stokes shift as compared to **P0**. With the increasing solvent polarity, **P1/P2** (THF and Bzn) exhibits a marginal solvatochromic shift but a significantly quenched fluorescence emission (Figure 4.2a). The marginal solvatochromic change suggests a smaller dipole moment change upon FC vertical excitation for **P1** ( $\Delta\mu = 16.34$ ) and **P2** ( $\Delta\mu = 15.17$  D) as compared to **P0** (Table B.3). Notably, all three compounds exhibit much larger changes in the dipole moment than the reference **PMI** ( $\Delta\mu = 7.24$  D), indicating a larger degree of delocalization in the relaxed ES of these DBA derivatives.

Accounting for the solvent polarity, **P0-P2** exhibit a very systematic fluorescence trend with marginal quenching in weakly polar toluene (see Figure B.3b and Table 4.1). Since the free energy for charge separation ( $\Delta G_{CS}^0 >$

0) is not favorable for the DBA derivatives in toluene (see Table B.5), the systematic fluorescence quenching can be explained by the partial CT polarization in the relaxed ES of **P0–P2** that changes as a function of the distance. Contrarily, the fluorescence emission of **P0–P2** in (moderately) polar THF/Bzn exhibits drastic quenching (Figure 4.2a and Figure B.3d) and can arise from an interplay of partial and full CS processes, which becomes favorable ( $\Delta G_{CS}^0 < 0$ ) in polar solvents (see Table B.5).

The ground-state CT mixing and its extent can be further confirmed by the UV–vis absorption and fluorescence emission under protonated conditions. Protonation of the dimethylamino group counters the electron-donating nature of the dimethylamino group and thereby ceases the CT and CS processes. The protonation of **P0–P2** in THF/Bzn gives rise to a more **PMI**-like absorption with a distinct hypsochromic shift as compared to the neutral state (Figure B.12). The magnitude of the hypsochromic shift in the UV–vis absorption of the protonated compounds scales as the distance between **PMI** and **DMA**, with **P0** exhibiting the most prominent change, **P1** exhibiting moderate change, and **P2** the least change as a function of the DA distance. This observation confirms the distance-dependent CT polarization in **P0–P2**, in line with the UV–vis absorption and TD-DFT simulations. Concurrently, the fluorescence emission for protonated **P0–P2** is activated from the bright excited state with quantum efficiencies similar to **PMI** (Figure B.12). The recovery of the fluorescence emission upon protonation for **P0–P2** suggests that the quenched fluorescence emission in highly polar solvents stems from the formation of radical ion-pair intermediates by photoinduced CS.

#### 4.2.2. Femtosecond transient absorption

To gain insights into the dynamics of the excited state in **P0–P2**, their femtosecond transient absorption (TA) spectra were measured upon predominantly exciting the **PMI** acceptor at 530 nm for **P0** or at 500 nm for **P1** and **P2**. To distinguish the ES from the CS state in THF, the spectral features of the ES were determined by the TA spectra in nonpolar hexane or acidic solution, where the formation of the CS state is expected to be nonexistent. The TA spectra of **P0** in hexane, toluene, and THF along with the inverted steady-state absorption and emission spectra are depicted in Figure 4.3a and Figure B.13a. After photoexcitation at 530 nm, the TA spectrum in hexane (Figure B.13a) is dominated by the local excited (LE) state **PMI\*** as expected and exhibits the long-lived features of the ground-state bleach (GSB, at ~515 nm), stimulated emission (SE, at ~585 nm), and strong induced absorption, peaked at 690 nm due to the  $S_1 \rightarrow S_n$  excited-state absorption (ESA) of **PMI\***[59].

Upon increasing the solvent polarity to weakly polar toluene, additional spectral features emerge as a positive shoulder between 590 and 640 nm and a minor negative signal at ~800 nm (Figure 4.3a). Both features become much more pronounced in THF on an ultrafast timescale (<1 ps). It has been reported that the absorption maximum of the perylenemonoimide radical anion (**PMI<sup>-</sup>**) ranges from 588[60] to 640 nm[61, 62]. Thus, the induced absorption between

590 and 640 nm is ascribed to the formation of  $\text{PMI}^-$ . It is plausible that the fast relaxation of the ES of  $\text{PMI}^*$  in toluene leads to polarization and creation of a partial CT character, whereas a full CS radical ion-pair state is not observed owing to the unfavorable free energy for charge separation ( $\Delta G_{\text{CS}}^0 > 0$ , Table B.5). Contrarily, a concurrent formation of a well-defined CS state with redshifted stimulated emission and a radical anion ( $\text{PMI}^-$ ) is apparent in THF as the free energy is favorable for charge separation ( $\Delta G_{\text{CS}}^0 < 0$ ). The emissive nature of the CS state apparently suggests that the degree of charge separation in **P0** is fractional and does not reach unity in moderately polar THF[58]. A larger degree of CS is expected in more polar solvents, and partial evidence comes from the measurements of steady-state fluorescence emission in highly polar Bzn/DMSO where a near-quantitative quenching of the redshifted emission is observed (Figures B.5 and B.8)[63].

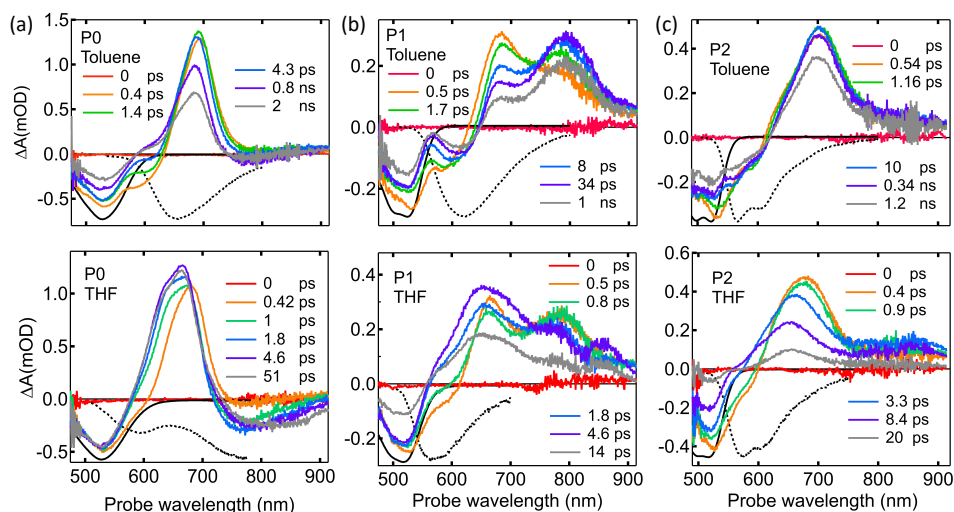


**Figure 4.3.** Transient absorption spectra of (a) **P0** (Ex @ 530 nm), (b) **P1** (Ex @ 500 nm), and (c) **P2** (Ex @ 500 nm) in toluene (top) and THF (bottom). The inverted steady-state absorption spectra and emission spectra are included as a black solid line and a black dotted line, respectively.

To understand the excited-state dynamics in **P1** and **P2**, the TA spectra were measured in toluene, neutral, and protonated THF solutions (Figure 4.3b,c and Figure B.13b,c). As shown in Figure 4.3b, the TA spectrum of **P1** in toluene at 0.5 ps displays the GSB ( $\sim 530$  nm), SE ( $\sim 580$  nm), and ESA ( $\sim 680$  nm) of perylene excited-state  $\text{PMI}^*$  as well as an additional absorption peak at  $\sim 790$  nm. Subsequently, the decay of  $\text{PMI}^*$  leads to the further growth of the additional absorption peak along with a redshift ( $\sim 30$  nm) in the SE. Herein, only a marginal CT polarization and no CS processes are anticipated for **P1** in toluene as established by the steady-state optical measurements and the unfavorable

free energy for CS, respectively. Therefore, the absorption peak at  $\sim 790$  nm can be attributed to the CT polarization since the delocalization of the ES of **PMI\*** may extend onto the phenyl bridge and the **DMA** donor leading to additional absorption features. Accordingly, this relaxation of the initial excited state gives rise to the redshift in the SE.

With the increased solvent polarity, the TA spectrum of **P1** in THF shows that the absorption peaks of both the initial and delocalized excited states of **PMI** transform into the absorption of the radical anion **PMI<sup>-</sup>** within a few picoseconds (Figure 4.3b). As a result, the SE of **PMI\*** at  $\sim 600$  nm is no longer observable at 1.8 ps. Since the **DMA** radical cation (**DMA<sup>+</sup>**) absorbs at 475 nm[51], the small peak at  $\sim 850$  nm is likely to be associated with the long-wavelength absorption of **PMI<sup>-</sup>** as reported earlier by spectroelectrochemistry[60]. Following the fast CS process, the charge recombination (CR) process and the return to the ground state occur rapidly in tens of picoseconds. We noticed that no residual signal was observed in the TA measurements on the nanosecond timescale. This is seemingly inconsistent with the nanosecond fluorescence lifetime in Table 4.1. We believe this to be associated with a very small fraction of aggregation in THF that is dominating the fluorescence measurements. However, such a small contribution is not detectable in the TA measurements. As a control experiment, the TA spectra of **P1** under protonated conditions were also recorded where the CS processes are blocked and a long-lived ESA is perceived corresponding to the LE state of **PMI\*** (Figure B.13b).

Figure 4.3c shows the TA spectrum of **P2** in toluene excited at 500 nm. When compared to the reference **PMI** (Figure B.14), the spectrum contains all the features expected for the perylene excited-state **PMI\***, including the long-lived GSB ( $\sim 520$  nm), SE ( $\sim 560$  nm), and ESA ( $\sim 700$  nm). The slightly broadened and redshifted ESA of **P2** in toluene likely originates from the inhomogeneous distribution of the molecular conformations and extended  $\pi$  conjugation by the incorporation of p-oligophenylene linkers. Interestingly, the long-wavelength absorption of the delocalized excited state at 790 nm in **P1** disappears in **P2**, suggesting that the further separation of **PMI** and **DMA** by an extra phenyl linker limits the oscillator strength of the ESA that is prominent at a shorter distance. Furthermore, **P2** in THF exhibits an unambiguous CS process (Figure 4.3c), as supported by the blueshift in ESA caused by **PMI<sup>-</sup>** absorption, fast recovery of SE, and an overall shortened lifetime of the ESA suggesting a fast recombination process. Similar to **P1**, the CS process in **P2** is also prohibited by protonating the **DMA** donor. As a result, only the spectral features of the LE state of **PMI\*** and SE are shown upon photoexcitation (Figure B.13c).

### 4.2.3. Global and target analysis

To deconvolute the spectral components and further extract the kinetic rates for the complex excited-state dynamics, global and target analyses were performed with Glotaran[64]. With this method, the temporal evolutions at all wavelengths were globally fitted to analyze the kinetic profiles (see Section 4.4 for details).

Global analysis with a sequential model is used to analyze the TA spectrum of



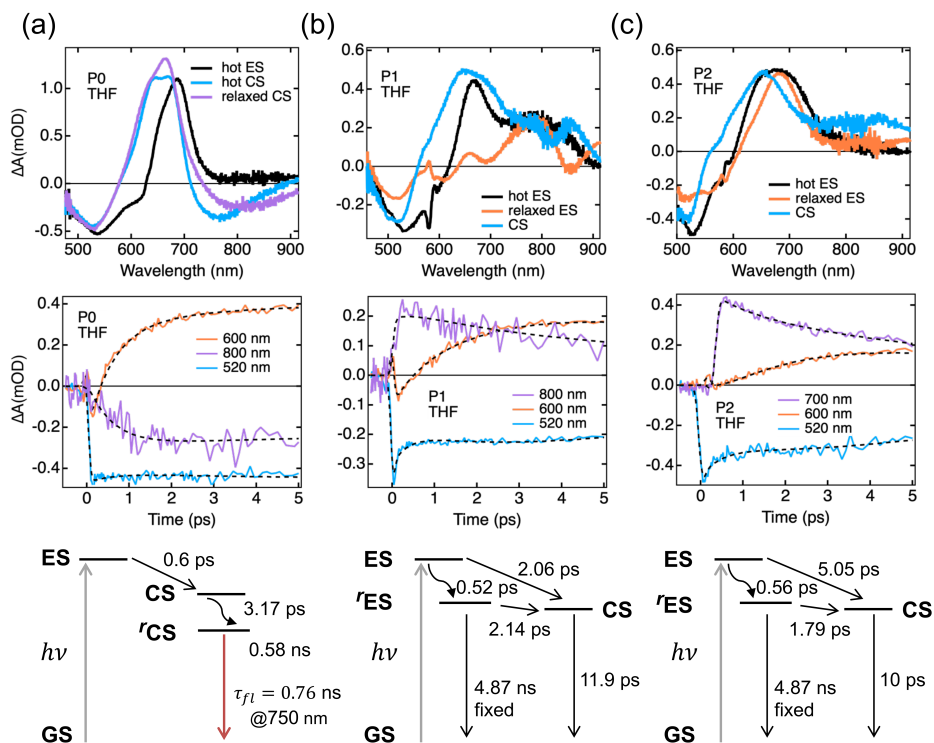


**Figure 4.4.** Global (**P0**) and target (**P1/P2**) analysis of femtosecond transient absorption (TA) data for (a) **P0**, (b) **P1**, and (c) **P2** derivatives in THF. First row: EADS (**P0**) and SADS (**P1/P2**) obtained from global/target analysis; second row: kinetic profiles of TA data at selected wavelengths and their fits (up to 5 ps); \*coherent artifacts affect the kinetics of **P1** and **P2** at initial times (<1 ps). Third row: kinetic scheme for the photodynamics charted with the global and target analysis.

**P0** in THF. The resulting evolution-associated difference spectra (EADS) are shown in Figure 4.4a, where three decay components are found, with time constants of 0.6, 3.2, and 580 ps. The first component (0.6 ps) is assigned to the hot excited-state **PMI\***, as it is formed simultaneously upon excitation and resembles the spectral features of **PMI\***, analogous to **P0** in hexane (Figure B.13a). Following the rapid decay of the hot **PMI\***, the second component (3.2 ps) displays the characteristics of a CS state, namely, the **PMI<sup>-</sup>** absorption at ~600 nm and the redshifted SE at long wavelengths. The third component (580 ps) retains the spectral features of the second component with a slight difference in amplitude, suggesting a relaxation process. Thus, we assign the second and third components to be the hot and relaxed CS states, akin to **PMI<sup>-</sup>**,



respectively. Since the charge separation is extremely fast ( $<1$  ps), as indicated by the lifetime of the hot **PMI\***, it is possible that the initially formed hot CS state (**PMI<sup>-</sup>**) relaxes in a few picoseconds due to vibrational/solvent reorganization processes[65, 66]. The kinetic traces and global fits of **P0** at three selected wavelengths are shown in Figure 4.4, and the strength of global analysis and the reliability of the kinetic rate are justified by the compelling fits (dotted lines) at characteristic wavelengths. As the emission from the CS state grows at 800 nm, the SE at 600 nm is rapidly overshadowed by the rising **PMI<sup>-</sup>** absorption within 1 ps, whereas the ground state is still bleached. This means that virtually no **PMI\*** decays back to the ground state while the CS state is formed. The charge recombination time (0.58 ns) obtained from the global analysis is in line with the major component of the fluorescence lifetime recorded at 750 nm (Figure 4.4a, third row). Calculating the CS rate constant ( $k_{CS}$ ) for **P0** in moderately polar THF renders a fast rate of  $\sim 1.66$  ps<sup>-1</sup> for the charge separation.

To disentangle the true spectra of the individual excited species and describe the ES dynamics in **P1** and **P2**, target analysis with a specific model is used. As demonstrated in Figure 4.4b,c, the used model considers two pathways for the CS process: (i) direct CS from the hot ES and (ii) CS from the relaxed ES. The obtained species-associated difference spectra (SADS) of **P1** and **P2** are presented in Figure 4.4b,c (first row). Despite the contamination of coherent artifacts at  $\sim 580$  nm (at  $<1$  ps), the spectral signatures of hot and relaxed excited states of both **P1** and **P2** are well-described by the black and orange SADS, respectively. The first two components of the SADS for **P1/P2** in THF corresponding to the localized and the delocalized states display the GSB, ESA, and SE signatures analogous to the ES seen in toluene (Figure B.15). The third SADS component corresponding to the nonradiative CS state in both the compounds is represented by the blue curves, representing a **PMI** radical anion (**PMI<sup>-</sup>**).

To further illustrate the fate of the ES and CS states in **P1** and **P2**, kinetic traces and their fits from target analysis at three selected wavelengths are shown in Figure 4.4b,c (second row). Despite the overlap between the absorption bands of the **PMI\*** and **PMI<sup>-</sup>**, the hole transfer from **PMI\*** to the **DMA** donor is evident from the increasing characteristic absorption of **PMI<sup>-</sup>** at 600 nm and the concurrently decreasing excited-state absorption of **PMI\*** at longer wavelengths. Meanwhile, the slight decrease in the GSB at 520 nm is indicative of the fast charge recombination. Notably, although the DA distance is longer in **P2**, there is a striking similarity between the CS rates in **P1** and **P2**. This similarity is further illustrated in Figure 4.4b,c (third row), wherein a similar kinetic model for the target analysis is depicted for **P1** and **P2**. Alternative models were assessed and then discarded based on the quality of the fits and/or physical interpretability of the estimated rate constants and SADS. In the kinetic model shown in Figure 4.4b,c, the initially formed hot ES branches to the relaxed ES and the CS state with different rates. In addition to the decay to the ground state, the relaxed ES undergoes charge separation. The CS state subsequently undergoes CR and decay to the ground state in several picoseconds. In both

models, the decay of the relaxed ES to the ground state was constrained to be equal to the lifetime of the isolated **PMI\*** in THF. As a result, the target analysis yields similar relaxation lifetimes of the hot ES in **P1** (0.52 ps) and **P2** (0.56 ps). Interestingly, the direct charge separation from the hot ES is about 2 times slower in **P2**, whereas the charge separation from the relaxed ES is faster in **P2**. As a result, the overall CS rate constants are determined to be 0.47 and 0.45  $\text{ps}^{-1}$  in **P1** and **P2**, respectively (see Figure B.16).

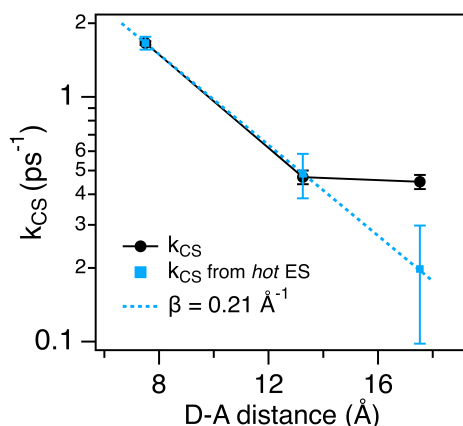


**Figure 4.5.** Logarithmic plots of the charge separation rate constants versus the donor–acceptor distance for **P0–P2**. Black dots represent the overall rate constants, and blue squares represent the rate constants of charge transfer from the hot excited state. The blue line is an exponential fit to the distance dependence with the attenuation parameter  $\beta$ .

Based on the obtained kinetic rate constants, the distance dependence of the CS rates in **P0–P2** is plotted on a logarithmic scale in Figure 4.5. As derived from the target analysis, the formation of the CS state is surprisingly fast in **P2**, resulting in a minuscule attenuation of the overall CS rate from **P1** to **P2** (black dots). According to the coherent tunneling (superexchange) mechanism[67], upon elongation of the bridge, the CS rate is expected to drop exponentially with an attenuation factor ( $\beta$ ) not less than  $0.2 \text{ \AA}^{-1}$ [68]. On the other hand, the incoherent hopping mechanism[69, 70] is only expected to set in with longer p-oligophenylene spacers ( $n > 3$ )[33, 71]. Thus, a shallow distance dependence cannot be ascribed to either of the mechanisms. However, we notice that the direct CS from the hot ES conforms to the exponential distance dependence with a  $\beta$  value of  $0.21 \text{ \AA}^{-1}$  (Figure 4.5, blue squares). This indicates that the CS from the relaxed ES is responsible for the deviation from the exponential distance dependence for the overall CS rate.

Noticeably, CR rates also show anomalous distance dependence with **P0** ( $k_{CR}=1.7 \times 10^9 \text{ s}^{-1}$ ), **P1** ( $k_{CR}= 8.4 \times 10^{10} \text{ s}^{-1}$ ), and **P2** ( $k_{CR}= 1.0 \times 10^{11} \text{ s}^{-1}$ ). Indeed, other factors may play a role in the observed anomalous distance

dependence such as distance dependence of the outer-sphere reorganization energy ( $\lambda_o$ )[72]. Derived from the dielectric continuum model by Marcus and Sutin[13],  $\lambda_o$  is predicted to increase with increasing  $R_{DA}$ . Such an effect could result in a larger electron transfer rate at a longer DA distance in the inverted regime[31, 73]. Based on the dielectric continuum model, the value of  $\lambda_o$  for **P0-P2** in THF is estimated to increase moderately from 1.1 to 1.4 eV (Chapter B). Given the estimated free energy (Table B.5), the charge separation and charge recombination are expected to occur in the normal and inverted regimes, respectively. Therefore, although the distance dependence of  $\lambda_o$  may contribute to the anomalous CR rates, it cannot explain the unusual distance dependence of the CS rates. However, we note that it is the CR rate for **P0** that is distinct from **P1** and **P2**, while the CR rates for **P1** and **P2** show similar distance independence to their CS rates. To rationalize this anomalous CR rate for **P0**, a hint can be taken from its distinct nature of CR through radiative emission. A more comprehensive picture of photophysics for **P0** is provided in the following subsection.

4

#### 4.2.4. Electronic structure calculations

To shed more light on the unexpected distance-dependent kinetic rates, we performed the electronic structure calculations to investigate the nature of the hot and relaxed excited states. With TD-DFT calculations, the hot and relaxed excited states were studied based on the lowest vertical transition corresponding to the optimized geometries of the ground state and the excited state, respectively (see Section 4.4).

It has been previously reported by our group that electron transfer through oligophenylene bridges can be almost distance-independent due to the effect of initial state distribution[74]. In this case, the vertical excitation of the electron donor involves a direct transition to the bridges[34]. According to the TD-DFT calculations, the vertical excitation of the **PMI** acceptor in **P0-P2** reveals a strong distance-dependent CT character as discussed in the earlier section (Figure 4.2b and Figure B.17 (left panel)). The fundamental (vertical) excitation in **P0** involves a CT-type transition (from HOMO and HOMO-1 to LUMO). The incorporation of p-oligophenylene bridges in **P1** and **P2** renders a highly localized HOMO-1 to LUMO transition localized on the perylene core. To quantify the charge delocalization in the hot ES, the difference of Mulliken charge distribution in the excited state with respect to the ground state was summed for the **DMA** donor, the **PMI** acceptor, and each phenyl unit (Figure 4.6a). In **P0**, the lowest vertical transition leads to substantial charge redistribution over **DMA** and **PMI** units, indicating that CT in **P0** can be triggered instantaneously upon photoexcitation. Such a strong CT character upon vertical excitation is thus postulated to aid the ultrafast CS in **P0** that is seen experimentally[63]. Subsequently, the degree of partial CT character decreases significantly with an increasing distance among the **PMI** and **DMA** units. As a result, the difference between the Mulliken charges in the lowest vertical excited state and that in the ground state is negligible for **P1** and **P2**, suggesting a highly localized hot ES.

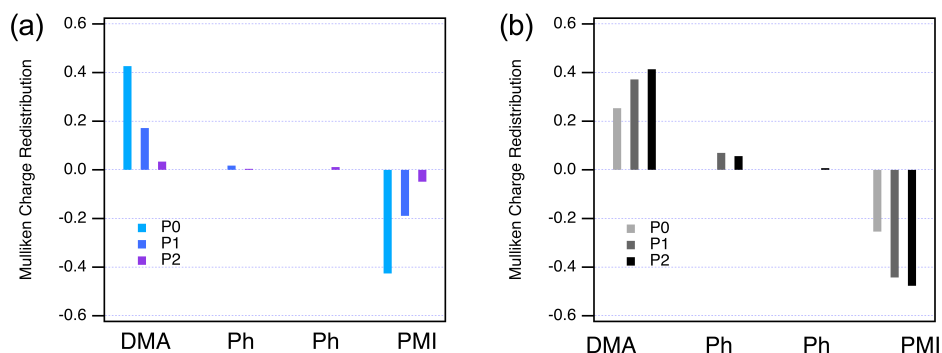


**Figure 4.6.** Mulliken charge distribution of the excited state as compared to the ground state for (a) ground-state geometry and (b) excited-state geometry.

To substantiate the extent of ES geometric relaxation and its effect on the CS rates, geometries of the relaxed ES in **P0-P2** were optimized. Since it is recognized that the conformational effect can play an important role in determining the  $\pi$  conjugation through the system[75], we first assessed the conformational changes upon geometry relaxation in the excited state by comparing the dihedral angles between adjacent fragments. As displayed in Figure B.18, the conformation of the relaxed ES has a propensity for more planarity, especially between **PMI** and its adjacent phenyl unit when compared to the hot ES and the ground-state geometries, where they are identically more twisted. The relaxation timescale of  $\sim 0.5$  ps found by target analysis is in line with the subpicosecond torsional relaxation leading to delocalized CT character observed in donor- $\pi$ -acceptor copolymers[76, 77]. Indeed, as a result of the favored planar structure, the HOMO and HOMO-1 charge densities in the relaxed ES of **P0-P2** are widely distributed over the entire molecule suggesting substantial charge delocalization (Figure B.17, right panel). It is recognized that the conformations optimized from the calculations in vacuum are not the best representative of the conformations in an ensemble of many molecules in solution. Therefore, to demonstrate the trend for planarity in the excited state, the relative potential energy surfaces (PES) of the ground state ( $S_0$ ) and the lowest excited state ( $S_1$ ) in **P0** along with the solvent stabilization energy were calculated and are plotted in Figure B.19. The PES of  $S_0$  suggests a large degree of rotational freedom in the ground state at room temperature (0.025 eV), varying from 50 to 135°. In contrast, the same energy barrier only allows rotational freedom of  $\sim 10^\circ$  around the PES minimum ( $\sim 45^\circ$ ) in  $S_1$  regardless of the solvent effect. Hence, it is reasonable to expect that randomly distributed conformations in the ground state are mostly replaced by more planar arrangements in the relaxed excited state. Accordingly, the planar relaxed ES exhibits a higher degree of charge delocalization and higher CT character at the longer DA distance, as illustrated in Figure 4.6b. This explains how the relaxed

ES exhibits a stronger CT character due to bridge planarization and in turn accelerates the charge separation at a longer distance.

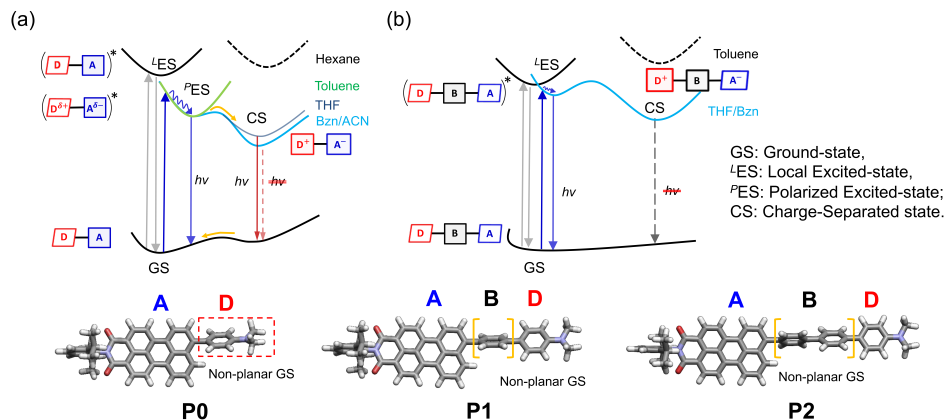


**Figure 4.7.** Comprehensive narration of the photoexcited-state processes in (a) **P0** and (b) **P1/P2** in nonpolar (highlighted black) and polar solvents (highlighted blue). Geometry-optimized structures (CAM-B3LYP/DZP) of the ground state for **P0–P2** are shown for reference.

A careful inspection of the solvent-dependent steady-state spectroscopic results, TD-DFT, TA experiments, and global/target analysis suggests that **P0–P2** exhibit a distinct ES character as a function of the DA distances and solvent polarity. The DA separation dictates the ground-state electronic interaction and determines where the initial charge density in the ground state gets redistributed after the FC vertical transition, whereas the solvent polarity commands the subsequent photodynamics from the ES. For **P0**, the direct coupling between **PMI** and **DMA** renders a strong charge delocalization in the hot ES upon FC vertical excitation. The subsequent de-excitation process now becomes solvent-dependent, and complex photodynamics is obtained depending on the solvent polarity (Figure 4.7a). Herein, in nonpolar hexane, the relaxed ES is formed with the characteristic of a normal LE state, whereas in weakly polarizing toluene, a polarized relaxed ES is created with a redshifted CT-like emission and a substantial Stokes shift (see Figure 4.2a, Figure 4.7a, Figure B.8, and Table 4.1). In moderately polar THF, **P0** exhibits dual emission characteristics owing to the access to at least two different emitting states: (i) a (CT) polarized ES ( $\mu_e = 21.24$  D) and (ii) CS state ( $\mu_e = 30.04$  D) (Figure 4.7a and Table B.4). Since the point dipole approximation<sup>2</sup> estimates  $1 \text{ D} = 0.208 \text{ e\AA}$ ,  $\mu_e$

<sup>2</sup>The solvatochromic method estimates the dipole moments for excited states based on the observable spectral shifts and cannot track the states that are nonemissive. As a result, the estimated degree of charge separation using solvatochromic shifts represents only the lower limits. The actual degree of charge separation could be much higher and is evident from the near-quantitative fluorescence quenching and the gradual disappearance of the redshifted emission of **P0** in polar Bzn and DMSO.

values of 21.24 and 30.04 D over a distance of 8.93 Å for **P0** translate to a moderate (0.49 e) and a fractional degree of CT (0.70 e) for the polarized ES and the CS states, respectively[51, 63]. The emissive nature of the CS state in THF suggests that the charge separation is fractional here, and perhaps, a remarkable degree of charge separation can occur in a more polar solvent[63]. This is further confirmed by the gradual quenching of the redshifted emission from the CS state in more polar solvents such as Bzn and DMSO (Figure B.8)[63]. Thus, **P0** is a remarkable molecule that due to the charge delocalization in the ground state has the propensity to populate a (non)polarized excited state depending on the solvent polarity. This is evident as a creation of (i) a nonpolarized (local) ES in nonpolar hexane, (ii) a polarized ES in weakly polar toluene, (iii) a polarized ES and CS state (fractional CS) in moderately polar THF, and (iv) a polarized ES and CS state (near-quantitative CS) in highly polar solvents (Figure 4.7a)[63]. The current observation is in line with the seminal reports on the charge separation that happens via an intermediate partial CT state in organic DA chromophores[63, 78–80]. Additionally, the geometric reorganization and the solvatochromic excited-state character in the dyad **P0** can be compared to the twisted intramolecular charge transfer (TICT) chromophores[58, 78, 81].

The introduction of the p-oligophenylene bridge between the **PMI** and **DMA** units breaks the coupling of D/A chromophores in the ground state for **P1/P2** (Figure 4.7b) as evident from the marginal solvatochromic effect and the limited charge delocalization in the hot ES upon FC vertical excitation. Furthermore, the polar solvent opens the access to a CS state for **P1/P2** as confirmed by the presence of the **PMI** radical anion in the TA experiments. Thus, the ultrafast charge separation for **P0** in THF is facilitated by the instantaneous population of an intermediate (CT) polarized excited state upon vertical excitation. Meanwhile, in **P1/P2**, the charge separation occurs directly from the hot ES and the relaxed ES (polarized) in polar solvents, albeit with different rates. Herein, not only the nature and the mode of the charge separation vary as a function of the distance in **P0** and **P1/P2**, but also, the extracted kinetic rates also add a new caveat to the classic distance dependence for CS rates.

### 4.3. Conclusions

Herein, we report a detailed investigation of the factors that adds a new caveat to the classic nature of the distance-dependent charge separation in **PMI**-p-oligophenylene-**DMA** (**P0–P2**) compounds. A combined experimental and computational investigation of the charge separation photodynamics reveals that deviation from the distance dependence originates from the relative changes in charge delocalization and CT character in the ES that scales as a function of bridge separation in **P0–P2**. At shorter bridge separation (**P0**), a substantial ground-state D/A electronic interaction and charge delocalization in polar solvents render the population of a strong (CT) polarized ES upon vertical excitation. The creation of a polarized ES further aids in an ultrafast charge

separation as well as exhibits a high solvent-controlled ES character for **P0**. The effect of ground-state orbital mixing and the polarization of the ES gradually fades with the increasing distance between D/A units in **P1/P2**. However, the observed CS kinetic rates in **P2** are much faster than anticipated and represent a deviation from the expected exponential distance-dependent attenuation of CS rates in DBA chromophores. A detailed kinetic analysis suggests two pathways for forming the charge-separated state: one from the initially formed hot excited state and the other one via the relaxed excited state. While the former shows an attenuation factor of  $\beta = 0.21 \text{ \AA}^{-1}$ , the latter shows a large deviation leading to an overall shallow distance dependence for charge separation. To understand the origin of the two distance dependences, we further provided compelling theoretical evidence to demonstrate the distinct nature of the initial states for these two charge transfer pathways. Upon increasing the DA distances, a significant increase of the charge delocalization is apparent in the relaxed excited state. This leads to a substantial charge transfer character and a fast charge separation from the relaxed excited state in **P2** than anticipated and compensates for the slower charge separation from the highly localized hot excited state. These findings highlight that the exponential expression for describing the distance dependence at a short DA distance should be used with caution as the charge delocalization along the  $\pi$ -conjugated systems may play an important role in determining the charge separation rates.

## 4.4. Methods

### Experimental methods

The synthesis and electrochemical characterization were performed by Abbey M. Philip. The synthesis scheme and the complete characterization can be found in the supporting information of the publication[82]. The cyclic voltammetry (V vs Fc/Fc<sup>+</sup>) of **PMI** and the DBA derivatives was carried out in a chloroform:acetonitrile (2:3) mixture. Absorption spectra were acquired using a PerkinElmer Lambda 40 UV-vis spectrophotometer. The photoluminescence measurements were performed with a Horiba Jobin Yvon SPEX Fluorolog 3 spectrophotometer. Fluorescence lifetimes were recorded on an Edinburgh LifeSpec-ps spectrometer with a fixed excitation wavelength of 404 nm. For quantum yield measurements, the formula for optically dilute solutions ( $OD \leq 0.10$ ) was used[83]. Fluorescence quantum yields of the **PMI** and DBA compounds were determined using N,N'-bis(1-hexylheptyl)-perylene-3,4,9,10-tetracarboxy bisimide ( $\Phi_F = 0.99$  in CHCl<sub>3</sub>) as a reference[84, 85]. During fs-TA measurements, the samples were first excited with a pump beam. Subsequently, a broadband white light (460–915 nm) was used to probe the transient absorption of the excited sample at a series of delay times. The generation of pump and probe is described in Section 2.2.1. With a commercial TA spectrometer (HELIOS, Ultrafast Systems), the change in the absorption spectrum,  $\Delta A$ , was recorded as a function of time.

### Global and target analysis

The two-dimensional TA data were analyzed by global and target analysis using Glotaran[64]. With this method, the 2D data matrix,  $\Psi(\lambda, t)$ , is modeled as linear combinations of  $n$  components given by the equation:

$$\Psi(\lambda, t) = \sum_{l=1}^n c_l(t)\varepsilon(\lambda) \quad (4.1)$$

Each component has its own spectrum,  $\varepsilon(\lambda)$ , that following a certain concentration profile,  $c_l(t)$ . To be specific, with global analysis a sequential kinetic model is used to describe the evolution of one component into the other with increasing time constants. In addition to the rate constants, each component is characterized by its own evolution associated difference spectrum (EADS). Although the EADS may reflect mixtures of excited species due to the simplicity of the sequential model, the global analysis does provide important information on the temporal evolution of the system. For more complex systems, that following non-sequential kinetics, the target analysis with a specific kinetic model should be used. The resulting species associated difference spectra (SADS) represents the true spectra of the individual excited species based on the used kinetic model.

### Theoretical calculations

Molecular and electronic structure calculations were performed using the Amsterdam Density Functional (ADF) software package[52]. All calculations were computed at the density functional theory (DFT) level of theory using a range-separated CAM-B3LYP functional with the double-zeta plus polarization (DZP) basis set in vacuum if not specified otherwise. The CAM-B3LYP functional was chosen because it offers a good description for the energetics of excited states when handling charge transfer states and related Coulomb interactions[86, 87]. With time-dependent density functional theory (TDDFT), the optimized ground-state geometries were used to calculate the vertical absorption spectra. Based on such spectra, the hot excited states corresponding to the vertical excitation of the PMI acceptor were derived. To further study the relaxed excited states, the excited-state geometries were optimized using the ground-state gradients and the gradients of the TDDFT excitation energy for the lowest allowed transition[88]. To quantify the charge delocalization in the hot and relaxed excited states, the difference in charge distribution between the ground state and the excited state for a given geometry was calculated. In detail, the charge distribution in the ground state was derived from the Mulliken[89] charges on the donor, the acceptor, and each intervening phenyl unit. The charge distribution in the excited state was summed over the different contributions to the excited state from all single orbital transitions with a contribution larger than 2%.





## References

1. Lim, G. N., Obondi, C. O. & D'Souza, F. A High-Energy Charge-Separated State of 1.70 eV from a High-Potential Donor–Acceptor Dyad: A Catalyst for Energy-Demanding Photochemical Reactions. *Angewandte Chemie* **128**, 11689–11693 (2016).
2. Wasielewski, M. R. Self-assembly strategies for integrating light harvesting and charge separation in artificial photosynthetic systems. *Accounts of chemical research* **42**, 1910–1921 (2009).
3. Dubey, R. K., Inan, D., Sengupta, S., Sudhölter, E. J., Grozema, F. C. & Jager, W. F. Tunable and highly efficient light-harvesting antenna systems based on 1, 7-perylene-3, 4, 9, 10-tetracarboxylic acid derivatives. *Chemical Science* **7**, 3517–3532 (2016).
4. Dogutan, D. K. & Nocera, D. G. Artificial photosynthesis at efficiencies greatly exceeding that of natural photosynthesis. *Accounts of Chemical Research* **52**, 3143–3148 (2019).
5. Imahori, H., Guldi, D. M., Tamaki, K., Yoshida, Y., Luo, C., Sakata, Y. & Fukuzumi, S. Charge separation in a novel artificial photosynthetic reaction center lives 380 ms. *Journal of the American Chemical Society* **123**, 6617–6628 (2001).
6. Escudero, D. Revising intramolecular photoinduced electron transfer (PET) from first-principles. *Accounts of Chemical Research* **49**, 1816–1824 (2016).
7. Blankenship, R. E. *Molecular Mechanisms of Photosynthesis*. Wiley 2013.
8. Gust, D., Moore, T. A. & Moore, A. L. Mimicking photosynthetic solar energy transduction. *Accounts of Chemical Research* **34**, 40–48 (2001).
9. Brédas, J.-L., Norton, J. E., Cornil, J. & Coropceanu, V. Molecular understanding of organic solar cells: the challenges. *Accounts of chemical research* **42**, 1691–1699 (2009).
10. Chen, X.-K., Coropceanu, V. & Brédas, J.-L. Assessing the nature of the charge-transfer electronic states in organic solar cells. *Nature communications* **9**, 5295 (2018).
11. Coropceanu, V., Chen, X.-K., Wang, T., Zheng, Z. & Brédas, J.-L. Charge-transfer electronic states in organic solar cells. *Nature Reviews Materials* **4**, 689–707 (2019).
12. Weller, A. Photoinduced electron transfer in solution: exciplex and radical ion pair formation free enthalpies and their solvent dependence. *Zeitschrift für Physikalische Chemie* **133**, 93–98 (1982).
13. Marcus, R. A. & Sutin, N. Electron transfers in chemistry and biology. *Biochimica et Biophysica Acta (BBA)-Reviews on Bioenergetics* **811**, 265–322 (1985).

14. Aghamohammadi, M., Fernandez, A., Schmidt, M., Perez-Rodriguez, A., Goñi, A. R., Fraxedas, J., Sauthier, G., Paradinas, M., Ocal, C. & Barrena, E. Influence of the relative molecular orientation on interfacial charge-transfer excitons at donor/acceptor nanoscale heterojunctions. *The Journal of Physical Chemistry C* **118**, 14833–14839 (2014).
15. Olguin, M., Zope, R. R. & Baruah, T. Effect of geometrical orientation on the charge-transfer energetics of supramolecular (tetraphenyl)-porphyrin/C60 dyads. *The Journal of Chemical Physics* **138**, 074306 (2013).
16. Schneider, S., Jäger, W., Lauteslager, X. & Verhoeven, J. Conformational Dynamics of Semirigidly Bridged Electron Donor- Acceptor Systems As Revealed by Stationary and Time-Resolved Fluorescence Spectroscopies at Higher Pressures. *The Journal of Physical Chemistry* **100**, 8118–8124 (1996).
17. Holman, M. W., Yan, P., Ching, K.-C., Liu, R., Ishak, F. I. & Adams, D. M. A conformational switch of intramolecular electron transfer. *Chemical physics letters* **413**, 501–505 (2005).
18. Lewis, F. D., Wu, T., Zhang, Y., Letsinger, R. L., Greenfield, S. R. & Wasielewski, M. R. Distance-dependent electron transfer in DNA hairpins. *Science* **277**, 673–676 (1997).
19. Davis, W. B., Svec, W. A., Ratner, M. A. & Wasielewski, M. R. Molecular-wire behaviour in p-phenylenevinylene oligomers. *Nature* **396**, 60–63 (1998).
20. Albinsson, B., Eng, M. P., Pettersson, K. & Winters, M. U. Electron and energy transfer in donor–acceptor systems with conjugated molecular bridges. *Physical Chemistry Chemical Physics* **9**, 5847–5864 (2007).
21. Wenger, O. S. How donor- bridge- acceptor energetics influence electron tunneling dynamics and their distance dependences. *Accounts of Chemical Research* **44**, 25–35 (2011).
22. Paddon-Row, M. N. Investigating long-range electron-transfer processes with rigid, covalently linked donor-(norbornylogous bridge)-acceptor systems. *Accounts of chemical research* **27**, 18–25 (1994).
23. Gunasekaran, S., Hernangómez-Pérez, D., Davydenko, I., Marder, S., Evers, F. & Venkataraman, L. Near length-independent conductance in polymethine molecular wires. *Nano letters* **18**, 6387–6391 (2018).
24. Giacalone, F., Segura, J. L., Martín, N. & Guldi, D. M. Exceptionally small attenuation factors in molecular wires. *Journal of the American Chemical Society* **126**, 5340–5341 (2004).
25. Osuka, A., Tanabe, N., Kawabata, S., Yamazaki, I. & Nishimura, Y. Synthesis and intramolecular electron-and energy-transfer reactions of polyene-or polyene-bridged diporphyrins. *The Journal of Organic Chemistry* **60**, 7177–7185 (1995).
26. Hanss, D. & Wenger, O. S. Tunneling barrier effects on photoinduced charge transfer through covalent rigid rod-like bridges. *Inorganic chemistry* **48**, 671–680 (2009).
27. Sachs, S. B., Dudek, S. P., Hsung, R. P., Sita, L. R., Smalley, J. F., Newton, M. D., Feldberg, S. W. & Chidsey, C. E. Rates of interfacial electron transfer through  $\pi$ -conjugated spacers. *Journal of the American Chemical Society* **119**, 10563–10564 (1997).

28. Wiberg, J., Guo, L., Pettersson, K., Nilsson, D., Ljungdahl, T., Mårtensson, J. & Albinsson, B. Charge recombination versus charge separation in donor-bridge-acceptor systems. *Journal of the American Chemical Society* **129**, 155–163 (2007).
29. Atienza, C., Martín, N., Wielopolski, M., Haworth, N., Clark, T. & Guldi, D. M. Tuning electron transfer through p-phenyleneethynylene molecular wires. *Chemical communications*, 3202–3204 (2006).
30. Goldsmith, R. H., Sinks, L. E., Kelley, R. F., Betzen, L. J., Liu, W., Weiss, E. A., Ratner, M. A. & Wasielewski, M. R. Wire-like charge transport at near constant bridge energy through fluorene oligomers. *Proceedings of the National Academy of Sciences* **102**, 3540–3545 (2005).
31. Kuss-Petermann, M. & Wenger, O. S. Electron transfer rate maxima at large donor-acceptor distances. *Journal of the American Chemical Society* **138**, 1349–1358 (2016).
32. Kuss-Petermann, M. & Wenger, O. S. Unusual distance dependences of electron transfer rates. *Physical Chemistry Chemical Physics* **18**, 18657–18664 (2016).
33. Weiss, E. A., Ahrens, M. J., Sinks, L. E., Gusev, A. V., Ratner, M. A. & Wasielewski, M. R. Making a molecular wire: charge and spin transport through p-ara-phenylene oligomers. *Journal of the American Chemical Society* **126**, 5577–5584 (2004).
34. Gorczak, N., Tarkuç, S., Renaud, N., Houtepen, A. J., Eelkema, R., Siebbeles, L. D. & Grozema, F. C. Different mechanisms for hole and electron transfer along identical molecular bridges: the importance of the initial state delocalization. *The Journal of Physical Chemistry A* **118**, 3891–3898 (2014).
35. Luo, Y., Barthelmes, K., Wächtler, M., Winter, A., Schubert, U. S. & Dietzek, B. Increased Charge Separation Rates with Increasing Donor-Acceptor Distance in Molecular Triads: The Effect of Solvent Polarity. *The Journal of Physical Chemistry C* **121**, 9220–9229 (2017).
36. Zieleniewska, A., Zhao, X., Bauroth, S., Wang, C., Batsanov, A. S., Krick Calderon, C., Kahnt, A., Clark, T., Bryce, M. R. & Guldi, D. M. Resonance-Enhanced Charge Delocalization in Carbazole-Oligoynone-Oxadiazole Conjugates. *Journal of the American Chemical Society* **142**, 18769–18781 (2020).
37. Zhan, X., Facchetti, A., Barlow, S., Marks, T. J., Ratner, M. A., Wasielewski, M. R. & Marder, S. R. Rylene and related diimides for organic electronics. *Advanced Materials* **23**, 268–284 (2011).
38. Würthner, F., Saha-Möller, C. R., Fimmel, B., Ogi, S., Leowanawat, P. & Schmidt, D. Perylene bisimide dye assemblies as archetype functional supramolecular materials. *Chemical reviews* **116**, 962–1052 (2016).
39. Li, C. & Wonneberger, H. Perylene imides for organic photovoltaics: yesterday, today, and tomorrow. *Advanced Materials* **24**, 613–636 (2012).
40. Zagranyski, Y., Chen, L., Zhao, Y., Wonneberger, H., Li, C. & Müllen, K. Facile transformation of perylene tetracarboxylic acid dianhydride into strong donor-acceptor chromophores. *Organic letters* **14**, 5444–5447 (2012).
41. Li, C., Schöneboom, J., Liu, Z., Pschirer, N. G., Erk, P., Herrmann, A. & Müllen, K. Rainbow perylene monoimides: easy control of optical properties. *Chemistry—A European Journal* **15**, 878–884 (2009).

42. Weil, T., Wiesler, U. M., Herrmann, A., Bauer, R., Hofkens, J., De Schryver, F. C. & Müllen, K. Polyphenylene dendrimers with different fluorescent chromophores asymmetrically distributed at the periphery. *Journal of the American Chemical Society* **123**, 8101–8108 (2001).
43. Mandal, A. K., Diers, J. R., Niedzwiedzki, D. M., Hu, G., Liu, R., Alexy, E. J., Lindsey, J. S., Bocian, D. F. & Holten, D. Tailoring Panchromatic Absorption and Excited-State Dynamics of Tetrapyrrole–Chromophore (Bodipy, Rylene) Arrays—Interplay of Orbital Mixing and Configuration Interaction. *Journal of the American Chemical Society* **139**, 17547–17564 (2017).
44. Weingarten, A. S., Kazantsev, R. V., Palmer, L. C., McClendon, M., Koltonow, A. R., Samuel, A. P., Kiebalá, D. J., Wasielewski, M. R. & Stupp, S. I. Self-assembling hydrogel scaffolds for photocatalytic hydrogen production. *Nature chemistry* **6**, 964–970 (2014).
45. Kazantsev, R. V., Dannenhoffer, A. J., Aytun, T., Harutyunyan, B., Fairfield, D. J., Bedzyk, M. J. & Stupp, S. I. Molecular control of internal crystallization and photocatalytic function in supramolecular nanostructures. *Chem* **4**, 1596–1608 (2018).
46. Zheng, D., Oskouei, M. R., Sanders, H. J., Qian, J., Williams, R. M. & Brouwer, A. M. Photophysics of perylene monoimide-labelled organocatalysts. *Photochemical & Photobiological Sciences* **18**, 524–533 (2019).
47. Creissen, C. E., Warnan, J., Antón-García, D., Farré, Y., Odobel, F. & Reisner, E. Inverse opal CuCrO<sub>2</sub> photocathodes for H<sub>2</sub> production using organic dyes and a molecular Ni catalyst. *ACS catalysis* **9**, 9530–9538 (2019).
48. Lee, S. K., Zu, Y., Herrmann, A., Geerts, Y., Müllen, K. & Bard, A. J. Electrochemistry, spectroscopy and electrogenerated chemiluminescence of perylene, terrylene, and quaterylene diimides in aprotic solution. *Journal of the American Chemical Society* **121**, 3513–3520 (1999).
49. Edvinsson, T., Li, C., Pschirer, N., Schöneboom, J., Eickemeyer, F., Sens, R., Boschloo, G., Herrmann, A., Müllen, K. & Hagfeldt, A. Intramolecular charge-transfer tuning of perylenes: spectroscopic features and performance in dye-sensitized solar cells. *The Journal of Physical Chemistry C* **111**, 15137–15140 (2007).
50. Dubey, R. K., Efimov, A. & Lemmetyinen, H. 1, 7-And 1, 6-regioisomers of diphenoxy and dipyrrolidinyl substituted perylene diimides: Synthesis, separation, characterization, and comparison of electrochemical and optical properties. *Chemistry of Materials* **23**, 778–788 (2011).
51. Banerji, N., Angulo, G., Barabanov, I. & Vauthey, E. Intramolecular charge-transfer dynamics in covalently linked perylene- dimethylaniline and cyanoperylene- dimethylaniline. *The Journal of Physical Chemistry A* **112**, 9665–9674 (2008).
52. Te Velde, G. t., Bickelhaupt, F. M., Baerends, E. J., Fonseca Guerra, C., van Gisbergen, S. J., Snijders, J. G. & Ziegler, T. Chemistry with ADF. *Journal of Computational Chemistry* **22**, 931–967 (2001).
53. Maity, B., Chatterjee, A. & Seth, D. Photophysics of a coumarin in different solvents: use of different solvatochromic models. *Photochemistry and Photobiology* **90**, 734–746 (2014).
54. Mathew, S. & Imahori, H. Tunable, strongly-donating perylene photosensitizers for dye-sensitized solar cells. *Journal of Materials Chemistry* **21**, 7166–7174 (2011).

55. Lippert, E. v. Spektroskopische Bestimmung des Dipolmomentes aromatischer Verbindungen im ersten angeregten Singulettzustand. *Zeitschrift für Elektrochemie, Berichte der Bunsengesellschaft für physikalische Chemie* **61**, 962–975 (1957).
56. Kowski, A. On the estimation of excited-state dipole moments from solvatochromic shifts of absorption and fluorescence spectra. *Zeitschrift für Naturforschung A* **57**, 255–262 (2002).
57. Gustavsson, T., Coto, P. B., Serrano-Andrés, L., Fujiwara, T. & Lim, E. C. Do fluorescence and transient absorption probe the same intramolecular charge transfer state of 4-(dimethylamino) benzonitrile? *The Journal of chemical physics* **131**, 031101 (2009).
58. Grabowski, Z. R., Rotkiewicz, K. & Rettig, W. Structural changes accompanying intramolecular electron transfer: focus on twisted intramolecular charge-transfer states and structures. *Chemical reviews* **103**, 3899–4032 (2003).
59. Ik, Y. S., Lammi, R. K., Prathapan, S., Miller, M. A., Seth, J., Diers, J. R., Bocian, D. F., Lindsey, J. S. & Holten, D. Synthesis and excited-state photodynamics of perylene-porphyrin dyads Part 3. Effects of perylene, linker, and connectivity on ultrafast energy transfer. *Journal of Materials Chemistry* **11**, 2420–2430 (2001).
60. Gosztola, D., Niemczyk, M. P., Svec, W., Lukas, A. S. & Wasielewski, M. R. Excited doublet states of electrochemically generated aromatic imide and diimide radical anions. *The Journal of Physical Chemistry A* **104**, 6545–6551 (2000).
61. Lor, M., Thielemans, J., Viaene, L., Cotlet, M., Hofkens, J., Weil, T., Hampel, C., Müllen, K., Verhoeven, J. W., Van der Auweraer, M., et al. Photoinduced electron transfer in a rigid first generation triphenylamine core dendrimer substituted with a peryleneimide acceptor. *Journal of the American Chemical Society* **124**, 9918–9925 (2002).
62. Kirmaier, C., Yang, S. I., Prathapan, S., Miller, M. A., Diers, J. R., Bocian, D. F., Lindsey, J. S. & Holten, D. Synthesis and excited-state photodynamics of perylene-porphyrin dyads. 4. Ultrafast charge separation and charge recombination between tightly coupled units in polar media. *Research on chemical intermediates* **28**, 719–740 (2002).
63. Kim, T., Kim, W., Vakuliuk, O., Gryko, D. T. & Kim, D. Two-step charge separation passing through the partial charge-transfer state in a molecular dyad. *Journal of the American Chemical Society* **142**, 1564–1573 (2019).
64. Snellenburg, J. J., Laptinok, S., Seger, R., Mullen, K. M. & van Stokkum, I. H. Glotaran: A Java-based graphical user interface for the R package TIMP. *Journal of Statistical Software* **49**, 1–22 (2012).
65. Schweitzer, G., Gronheid, R., Jordens, S., Lor, M., De Belder, G., Weil, T., Reuther, E., Müllen, K. & De Schryver, F. C. Intramolecular directional energy transfer processes in dendrimers containing perylene and terrylene chromophores. *The Journal of Physical Chemistry A* **107**, 3199–3207 (2003).
66. Akbarimoosavi, M., Rohwer, E., Rondi, A., Hankache, J., Geng, Y., Decurtins, S., Hauser, A., Liu, S.-X., Feuerer, T. & Cannizzo, A. Tunable Lifetimes of Intramolecular Charge-Separated States in Molecular Donor-Acceptor Dyads. *The Journal of Physical Chemistry C* **123**, 8500–8511 (2019).
67. McConnell, H. M. Intramolecular charge transfer in aromatic free radicals. *The Journal of Chemical Physics* **35**, 508–515 (1961).

68. Berlin, Y. A., Grozema, F. C., Siebbeles, L. D. & Ratner, M. A. Charge transfer in donor-bridge-acceptor systems: Static disorder, dynamic fluctuations, and complex kinetics. *The Journal of Physical Chemistry C* **112**, 10988–11000 (2008).
69. Berlin, Y. A., Hutchison, G. R., Rempala, P., Ratner, M. A. & Michl, J. Charge hopping in molecular wires as a sequence of electron-transfer reactions. *The Journal of Physical Chemistry A* **107**, 3970–3980 (2003).
70. Berlin, Y. A., Burin, A. L. & Ratner, M. A. Elementary steps for charge transport in DNA: thermal activation vs. tunneling. *Chemical physics* **275**, 61–74 (2002).
71. Weiss, E. A., Tauber, M. J., Kelley, R. F., Ahrens, M. J., Ratner, M. A. & Wasielewski, M. R. Conformationally gated switching between superexchange and hopping within oligo-p-phenylene-based molecular wires. *Journal of the American Chemical Society* **127**, 11842–11850 (2005).
72. Brunschwig, B. S., Ehrenson, S. & Sutin, N. The distance dependence of electron transfer reactions: rate maxima and rapid rates at large reactant separations. *Journal of the American Chemical Society* **106**, 6858–6859 (1984).
73. Kuss-Petermann, M. & Wenger, O. S. Increasing Electron-Transfer Rates with Increasing Donor-Acceptor Distance. *Angewandte Chemie International Edition* **55**, 815–819 (2016).
74. Skourtis, S. & Nitzan, A. Effects of initial state preparation on the distance dependence of electron transfer through molecular bridges and wires. *The Journal of chemical physics* **119**, 6271–6276 (2003).
75. Schubert, C., Wielopolski, M., Mewes, L.-H., de Miguel Rojas, G., Van Der Pol, C., Moss, K. C., Bryce, M. R., Moser, J. E., Clark, T. & Guldi, D. M. Precise Control of Intramolecular Charge-Transport: The Interplay of Distance and Conformational Effects. *Chemistry—A European Journal* **19**, 7575–7586 (2013).
76. Roy, P., Jha, A., Yasarapudi, V. B., Ram, T., Puttaraju, B., Patil, S. & Dasgupta, J. Ultrafast bridge planarization in donor- $\pi$ -acceptor copolymers drives intramolecular charge transfer. *Nature Communications* **8**, 1716 (2017).
77. Hwang, I., Beaupré, S., Leclerc, M. & Scholes, G. D. Ultrafast relaxation of charge-transfer excitons in low-bandgap conjugated copolymers. *Chemical Science* **3**, 2270–2277 (2012).
78. Sasaki, S., Drummen, G. P. & Konishi, G.-i. Recent advances in twisted intramolecular charge transfer (TICT) fluorescence and related phenomena in materials chemistry. *Journal of Materials Chemistry C* **4**, 2731–2743 (2016).
79. Mauck, C. M., Bae, Y. J., Chen, M., Powers-Riggs, N., Wu, Y.-L. & Wasielewski, M. R. Charge-transfer character in a covalent diketopyrrolopyrrole dimer: implications for singlet fission. *ChemPhotoChem* **2**, 223–233 (2018).
80. Liu, L., Liu, Q., Li, R., Wang, M.-S. & Guo, G.-C. Controlled photoinduced generation of “visual” partially and fully charge separated states in viologen analogues. *Journal of the American Chemical Society* **143**, 2232–2238 (2021).
81. Grabowski, Z. R. Electron transfer and the structural changes in the excited state. *Pure and applied chemistry* **64**, 1249–1255 (1992).
82. Wei, Z., Philip, A. M., Jager, W. F. & Grozema, F. C. Fast Charge Separation in Distant Donor-Acceptor Dyads Driven by Relaxation of a Hot Excited State. *The Journal of Physical Chemistry C* **126**, 19250–19261 (2022).

83. Crosby, G. A. & Demas, J. N. Measurement of photoluminescence quantum yields. Review. *The Journal of Physical Chemistry* **75**, 991–1024 (1971).
84. SEYBOLD, P. G., GOUTERMAN, M. & CALLIS, J. Calorimetric, photometric and lifetime determinations of fluorescence yields of fluorescein dyes. *Photochemistry and photobiology* **9**, 229–242 (1969).
85. Taniguchi, M. & Lindsey, J. S. Database of absorption and fluorescence spectra of > 300 common compounds for use in photochem CAD. *Photochemistry and photobiology* **94**, 290–327 (2018).
86. Wiggins, P., Williams, J. & Tozer, D. J. Excited state surfaces in density functional theory: a new twist on an old problem. *The Journal of chemical physics* **131** (2009).
87. Yanai, T., Tew, D. P. & Handy, N. C. A new hybrid exchange–correlation functional using the Coulomb-attenuating method (CAM-B3LYP). *Chemical physics letters* **393**, 51–57 (2004).
88. Seth, M., Mazur, G. & Ziegler, T. Time-dependent density functional theory gradients in the Amsterdam density functional package: geometry optimizations of spin-flip excitations. *Theoretical Chemistry Accounts* **129**, 331–342 (2011).
89. Wiberg, K. B. & Rablen, P. R. Comparison of atomic charges derived via different procedures. *Journal of Computational Chemistry* **14**, 1504–1518 (1993).





# B

## Appendix to Chapter 4

### Electrochemical analysis

The electrochemical behavior of the compounds was studied by cyclic voltammetry (CHI 600D electrochemical analyzer) in a three-electrode single-compartment cell consisting of a platinum electrode as the working electrode, a Ag/AgCl wire as the reference electrode, and a Pt wire as the counter electrode (scan rate = 50 mV/s). The cell was connected to the computer controlled potentiostat (CH Instruments Inc. 600D). A predried mixture of chloroform : acetonitrile (2:3) containing 0.1 M tetrabutylammonium hexafluorophosphate was used as solvent. The samples were degassed via nitrogen purging prior to the experiment and the concentration of the prepared samples were ca. 0.5 mM. Under these experimental conditions, the oxidation potential for ferrocene (external reference) was observed at 0.43 V (vs. Ag/AgCl).

**Table B.1.** Electrochemical redox potential (vs. Fc/Fc<sup>+</sup>) and electronic energy levels (vs. vacuum) of the reference and the DBA derivatives in chloroform:acetonitrile (2:3) mixture.

	$E_{ox}^1$ (V) <sup>a</sup>	$E_{ox}^2$ (V) <sup>a</sup>	$E_{red}^1$ (V) <sup>a</sup>	$E_{red}^2$ (V) <sup>a</sup>	$E_g$ (eV) <sup>c</sup>	$E_{LUMO}$ (eV) <sup>d</sup>	$E_{HOMO}$ (eV)
<b>DMA</b>	0.365 <sup>b</sup>	—	—	—	3.83	-1.26 <sup>f</sup>	-5.09
<b>PMI</b>	0.98	—	-1.377	—	2.33	-3.61	-5.95
<b>P0</b>	0.399	0.828	-1.388	—	2.06	-3.61	-5.68
<b>P1</b>	0.387 <sup>b</sup>	0.906	-1.376	—	2.18	-3.64	-5.82
<b>P2</b>	0.367 <sup>b</sup>	0.902	-1.362	—	2.22	-3.64	-5.85

<sup>a</sup>scan rate = 50mVs<sup>-1</sup> and the potentials are reported as  $E_{1/2}^a (= (E_p^a + E_p^c) / 2)$  unless otherwise specified. <sup>b</sup> $E_p$  (peak potential). <sup>c</sup> Optical bandgap ( $E_g = 1240/\hat{\lambda}_{ac}$ ); where  $\hat{\lambda}_{ac}$  denotes the absorption edge wavelength in nm.  
<sup>d</sup> $E_{LUMO} = -(E_{red}^{onset} + 4.8)$  eV. <sup>e</sup> $E_{HOMO} = (E_{LUMO} - E_g)$  eV;

**Table B.2.** Onset redox potential (vs.  $\text{Fc}/\text{Fc}^+$ ) of the reference and the DBA derivatives in chloroform:acetonitrile (2:3) mixture.

	$E_{\text{onset,ox}}(\text{V})^a$	$E_{\text{onset,red}}(\text{V})^a$
<b>DMA</b>	0.286	—
<b>PMI</b>	0.859	-1.188
<b>P0</b>	0.308	-1.185
<b>P1</b>	0.254	-1.162
<b>P2</b>	0.240	-1.164

<sup>a</sup>scan rate=50 m Vs<sup>-1</sup>.

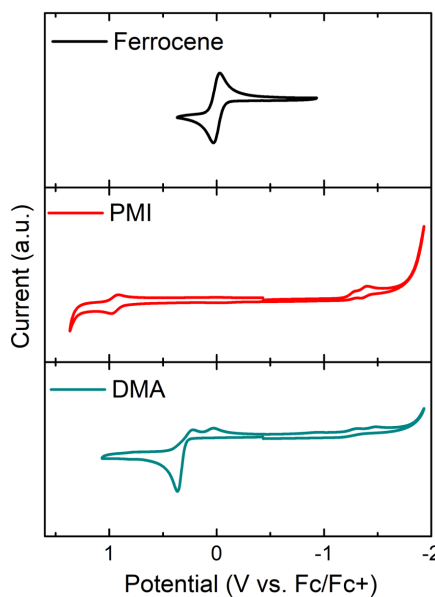


**Figure B.1.** Cyclic voltammograms (vs  $\text{Fc}/\text{Fc}^+$ ) of the reference compounds in chloroform:acetonitrile (2:3) mixture.

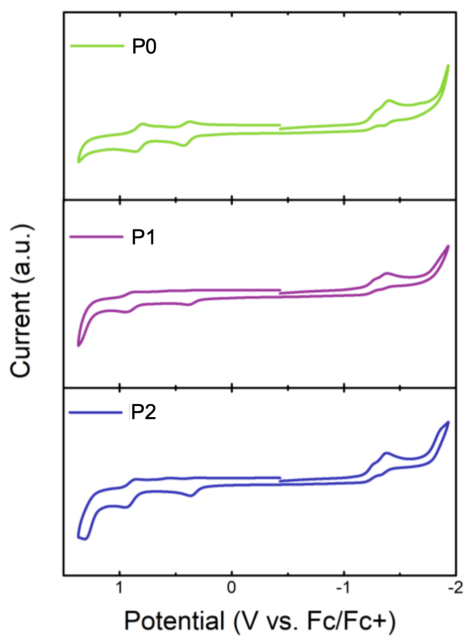


**Figure B.2.** Cyclic voltammograms (vs Fc/Fc<sup>+</sup>) of the DBA derivatives **P0**, **P1**, and **P2** in chloroform:acetonitrile (2:3) mixture.

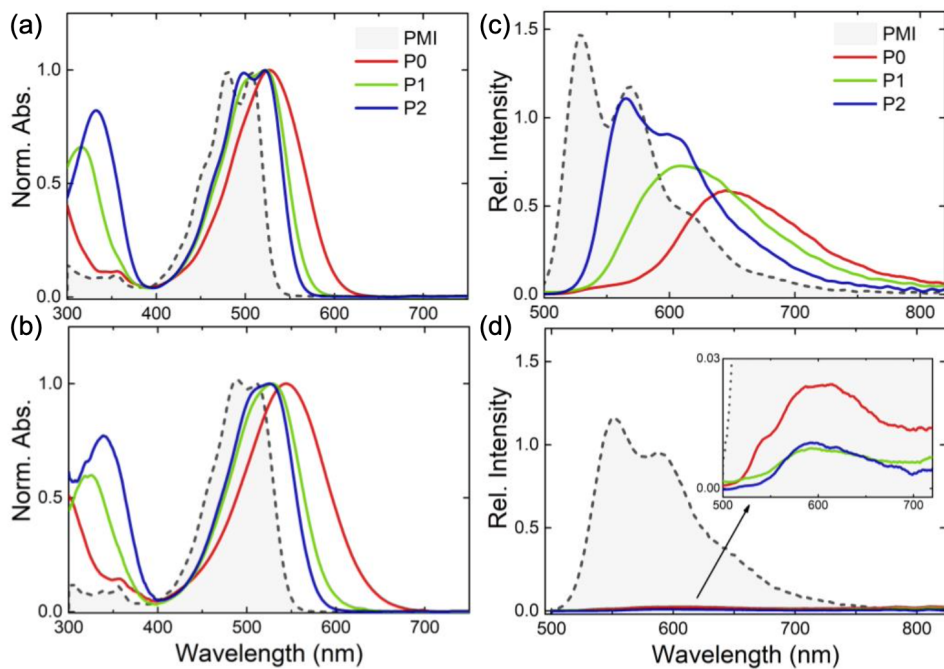


**Figure B.3.** UV-Vis absorption (left) and fluorescence emission (right) spectra of **PMI** and **P0-P2** in toluene (a,b) and Bzn (c, d).

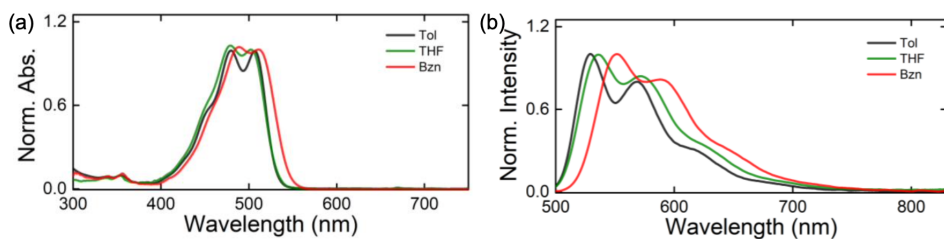


**Figure B.4.** UV-Vis absorption and (b) fluorescence emission spectra of **PMI** in solvents of varying polarity.

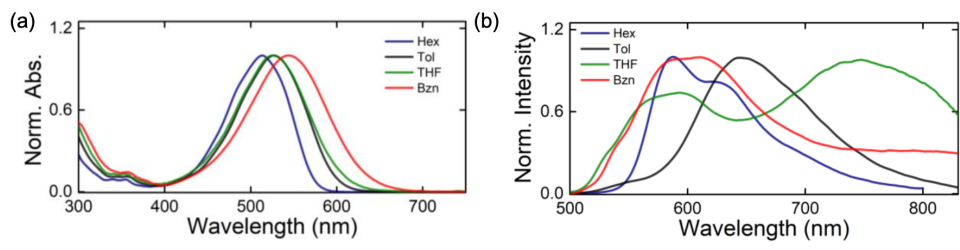


**Figure B.5.** UV-Vis absorption and (b) fluorescence emission spectra of **P0** in solvents of varying polarity.

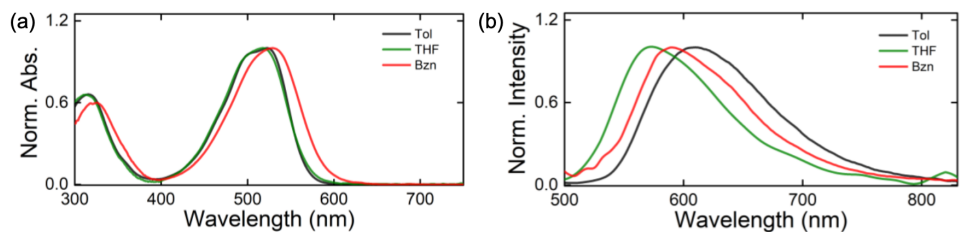


**Figure B.6.** UV-Vis absorption and (b) fluorescence emission spectra of **P1** in solvents of varying polarity.

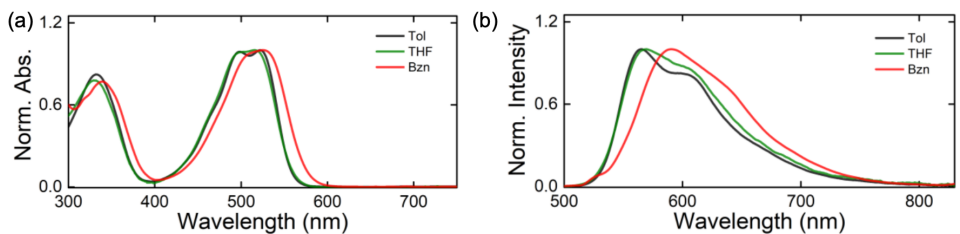


**Figure B.7.** UV-Vis absorption and (b) fluorescence emission spectra of **P2** in solvents of varying polarity.

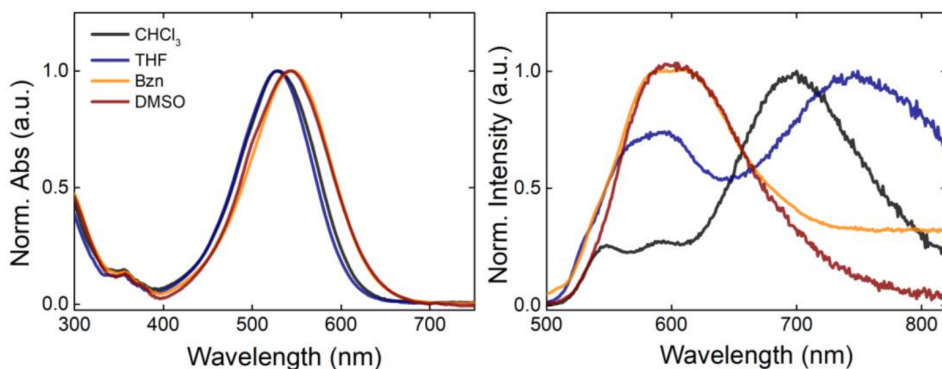


**Figure B.8.** UV-vis absorption (left) and fluorescence emission (right) spectra of **PO** in solvent of increasing polarity (CHCl<sub>3</sub> ( $\epsilon = 4.81$ ); THF ( $\epsilon = 7.60$ ); Bzn ( $\epsilon = 25.90$ ); DMSO ( $\epsilon = 46.70$ )).

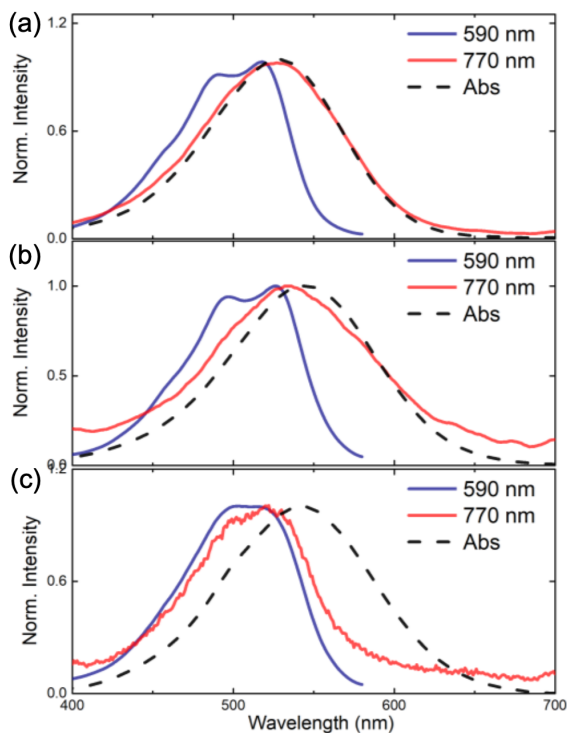


**Figure B.9.** Excitation spectra of **PO** in (a) THF, (b) Bzn and (c) DMSO monitored at the short and long emission wavelengths. For comparison the UV-vis absorption of **PO** (dashed lines) in corresponding solvent is plotted along with the excitation spectra.

### Solvatochromic method for dipole moment calculations[1–3]

Solvent polarity dependent UV-vis absorption and fluorescence emission provide a convenient and facile method to probe the change in the dipole moment between the ground and the excited-state of a fluorophore. Herein, the fluorophore is considered as a spherical point-dipole placed at the centre of a continuous medium with a uniform dielectric medium. The interaction between the fluorophore and the dielectric solvent medium creates a change in the energetics of the ground and the excited-state and as a result the dipole moment associated with them. This approximation neglects the effect of the dispersive interactions caused by the Van de Waals forces and is valid only when the dispersive forces are quite weaker as compared to the dipolar interaction between the fluorophore and the dielectric solvent medium. The difference in the dipole moment associated with the ground and the excited states can be described as a function of refractive index ( $n$ ) and the dielectric medium ( $\varepsilon$ ) under consideration. To calculate both the ground and the excited state dipole moments, a generalized linear correlation can be utilized:

$$\begin{aligned}\tilde{\nu}_a - \tilde{\nu}_f &= m_1 f(\varepsilon, n) + \text{constant} \\ \tilde{\nu}_a + \tilde{\nu}_f &= -m_2 \varphi(\varepsilon, n) + \text{constant}\end{aligned}$$

$$\text{where } m_1 = \frac{2(\mu_e - \mu_g)^2}{hca^3} \quad (\text{B.1})$$

$$m_2 = \frac{2(\mu_e^2 - \mu_g^2)^2}{hca^3}$$

Herein,  $\mu_g$  and  $\mu_e$  are the ground and excited state dipole moments of the solute;  $f(\varepsilon, n)$  is a function of the solvent dielectric constant ( $\varepsilon$ ) and its refractive index ( $n$ );  $g(n) = \frac{n^2-1}{2n^2+1}$  is a function of the refractive index;  $h$  is Planck's constant;  $c$  is the speed of light in vacuum;  $a$  is the spherical Onsager cavity radius of the solute molecule.

$m_1$  and  $m_2$  can be determined from the slopes of the linear plots of  $(\tilde{\nu}_a - \tilde{\nu}_f)$  versus  $f(\varepsilon, n)$  and  $(\tilde{\nu}_a + \tilde{\nu}_f)$  versus  $\varphi(\varepsilon, n)$ , respectively. The solvent polarity parameter  $f(\varepsilon, n)$  and  $\varphi(\varepsilon, n)$  are defined as follows (ignoring the polarizability of solute):

$$\begin{aligned}f(\varepsilon, n) &= \frac{\varepsilon - 1}{2\varepsilon + 1} - \frac{n^2 - 1}{2n^2 + 1} \\ \varphi(\varepsilon, n) &= f(\varepsilon, n) + 2g(n) \quad (\text{B.2}) \\ \varphi(\varepsilon, n) &= \frac{\varepsilon - 1}{2\varepsilon + 1} + \frac{n^2 - 1}{2n^2 + 1}\end{aligned}$$

Considering that the symmetry of the solute molecule remains unchanged upon an electronic transition, the ground and excited state dipole moments can be calculated from the following equations:



$$\begin{aligned}\mu_g &= \frac{m_2 - m_1}{2} \left[ \frac{hca^3}{2m_1} \right]^{1/2} \\ \mu_e &= \frac{m_1 + m_2}{2} \left[ \frac{hca^3}{2m_1} \right]^{1/2}\end{aligned}\tag{B.3}$$

Thus,

$$\mu_e = \frac{m_1 + m_2}{m_2 - m_1} \mu_g\tag{B.4}$$

B

**Table B.3.** Electrochemical redox potential (vs. Fc/Fc<sup>+</sup>) and electronic energy levels (vs. vacuum) of the reference and the DBA derivatives in chloroform:acetonitrile (2:3) mixture.

	Solvent	$f(\epsilon, n)$	$\phi(\epsilon, n)$	$\nu_a$ (cm <sup>-1</sup> )	$\nu_f$ (cm <sup>-1</sup> )	$(\nu_a - \nu_f)$ (cm <sup>-1</sup> )	$(\nu_a + \nu_f)$ (cm <sup>-1</sup> )	$m_1$	$m_2$	$\mu_g$ (D)	${}^a\mu_e$ (D)	${}^b\mu_e$ (D)	${}^{c,d}\Delta\mu$ (D)
<b>PMI</b>	Toluene	0.0132	0.4660	19724	18868	856	38592						
	CHCl <sub>3</sub>	0.1482	0.5692	19646	18553	1093	38199						
	DCM	0.2171	0.6237	19724	18382	1342	38106	2343	3499	1.78	9.02	9.02	7.24
	THF	0.2096	0.6047	19920	18657	1263	38577						
	Bzn	0.2361	0.7070	19569	18182	1387	37751						
	DMF	0.2744	0.6852	19802	18018	1784	37820						
<b>P0</b>	Hexane	0.00027	0.3721	19493	17036	2457	36529						
	Toluene	0.0132	0.4660	18975	15528	3447	34503						
	CHCl <sub>3</sub>	0.1482	0.5692	18939	14286	4653	33225	12942	17068	2.92	30.04	21.24	27.48 <sup>c</sup> , 18.32 <sup>d</sup>
	THF	0.2096	0.6047	18975	13369	5606	32344						
	Bzn <sup>e</sup>	0.2361	0.7070	18349	12853	5495	31202						
	Toluene	0.0132	0.4660	19120	16447	2673	35567						
<b>P1</b>	CHCl <sub>3</sub>	0.1482	0.5692	19011	17762	1249	36773						
	THF	0.2096	0.6047	19305	17482	1823	36787	7600	9582	2.13	18.47	18.47	16.34
	acetone	0.2842	0.6450	19380	17331	2049	36711						
	Bzn	0.2361	0.7070	18904	16949	1955	35853						
	ACN	0.3054	0.6550	19380	16920	2460	36300						
	Toluene	0.0132	0.4660	19157	17668	1489	36825						
<b>P2</b>	CHCl <sub>3</sub>	0.1482	0.5692	19120	17544	1576	36664						
	THF	0.2096	0.60471	19380	17575	1805	36955	6465	9982	4.12	19.29	19.29	15.17
	Bzn	0.2361	0.7070	19011	16920	2091	35931						
	ACN	0.3054	0.6550	19455	16863	2592	36318						

$${}^a\mu_e = \frac{m_1 + m_2}{2} \left[ \frac{hcc\epsilon^3}{2m_1} \right]^{1/2}; {}^b\mu_e = \frac{m_1 + m_2}{m_2 - m_1} \mu_g; {}^c\Delta\mu = {}^a\mu_e - \mu_g; {}^d\Delta\mu = {}^b\mu_e - \mu_g.$$

<sup>e</sup>The diffuse red-shifted component was selected as emission band.

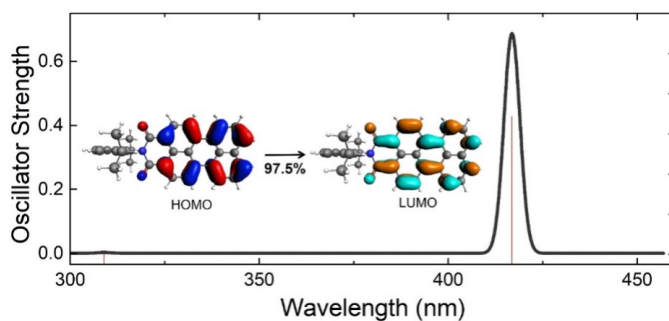


**Figure B.10.** Optical transition of **PMI** calculated by TD-DFT with DZP/CAM-B3LYP.

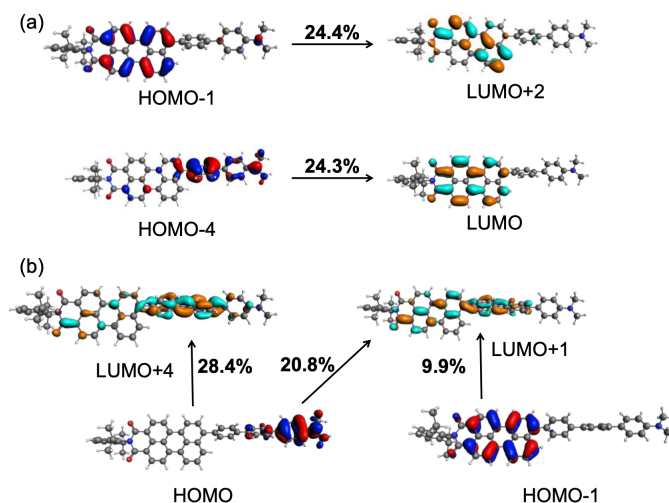


**Figure B.11.** Orbital transitions involved in the high energy absorption band of (a) **P1** (271 nm,  $f = 0.046$ ) and (b) **P2** (272 nm,  $f = 0.82$ ) calculated using TD-DFT with DZP/CAM-B3LYP.

**Table B.4.** Dipole moment, excitation energies, oscillator strengths and main contributions to the excited state of the DBA molecules.

Molecule	$E_{\text{ex}}(\text{eV})$	$\lambda(\text{nm})$	$f$	Main contribution
<b>PMI</b>	2.97	416	0.687	97.5%(H $\rightarrow$ L)
	4.66	265	0.006	51.3%(H - 2 $\rightarrow$ L) 42.2%(H $\rightarrow$ L + 1)
<b>P0</b>	2.85	434	0.956	81.6%(H $\rightarrow$ L) 15.5%(H - 1 $\rightarrow$ L)
	3.60	334	0.004	15.5%(H - 1 $\rightarrow$ L)
	4.58	270	0.018	35.4%(H - 1 $\rightarrow$ L + 1)
<b>P1</b>	2.90	427	1.00	84.4%(H - 1 $\rightarrow$ L) 12.8%(H $\rightarrow$ L)
	3.71	333	0.013	79.4%(H $\rightarrow$ L) 12.3%(H - 1 $\rightarrow$ L)
	4.56	271	0.046	24.4%(H - 1 $\rightarrow$ L + 2) 24.3%(H - 4 $\rightarrow$ L)
<b>P2</b>	2.91	426	1.03	95.0%(H - 1 $\rightarrow$ L) 2.2%(H $\rightarrow$ L)
	3.85	321	0.021	89.97%(H $\rightarrow$ L) 5.3%(H - 3 $\rightarrow$ L)
	4.56	272	0.82	28.4%(H $\rightarrow$ L + 4) 20.8%(H $\rightarrow$ L + 1) 9.9%(H - 1 $\rightarrow$ L + 1)

### Distance-dependent protonation

The UV-vis absorption and emission experiments under protonated condition were carried out using 48% HBr as the proton source. A small amount of the acid (2-2.5 microliter) was added to the solution of the DBA samples in THF/Bzn. The DBA compounds **P0-P2** exhibit a distance-dependent fluorescence emission in weakly polar toluene (Figure B.3), whereas a dramatic quenching is observed in polar THF/Bzn (Figure B.3) from the different deexcitation processes. To simplify the photoexcited state properties and nullify the complication arising from the CT and CS processes, we attempted protonation of **P0-P2** derivatives in Bzn with hydrobromic acid (HBr, Figure B.12). Protonation of the dimethylamino group reduces its electron-donating nature and blocks all the complex CT processes that render a nonradiative deexcitation in polar solvents. The protonation experiments in THF/Bzn reveal a distinct hypsochromic shift in the UV-vis absorption as a function of the distance between **PMI** and **DMA** units for the DBA compounds (Figure B.12a, Figure B.12c, and Figure B.12e). The nature and the magnitude of the hypsochromic shift in the UV-vis absorption of the protonated compounds proves the distance-dependent CT polarization in **P0-P2**, as earlier proved by the UV-vis absorption and TD-DFT calculations. Concurrently, the fluorescence emission for protonated **P0-P2** is synchronously activated from the bright LE state with spectral character similar to unsubstituted **PMI** and a remarkably enhanced quantum yields. The magnitude of the fluorescence enhancement (FE) upon protonation depends on the DBA distances and the solvent polarity (Table 4.1, Figure B.12). The FE upon protonation is high (**P1/P2**) and moderate (**P0**) when the fluorescence quenching is high and moderate in the neutral state. The red-shift of the emission band in the protonated state reveal a trend of most increased shift in **P2**, then **P1** and the least in **P0**. This observation suggests that the charge delocalization in the excited state of **P2** is more as compared to **P1** and **P0**.

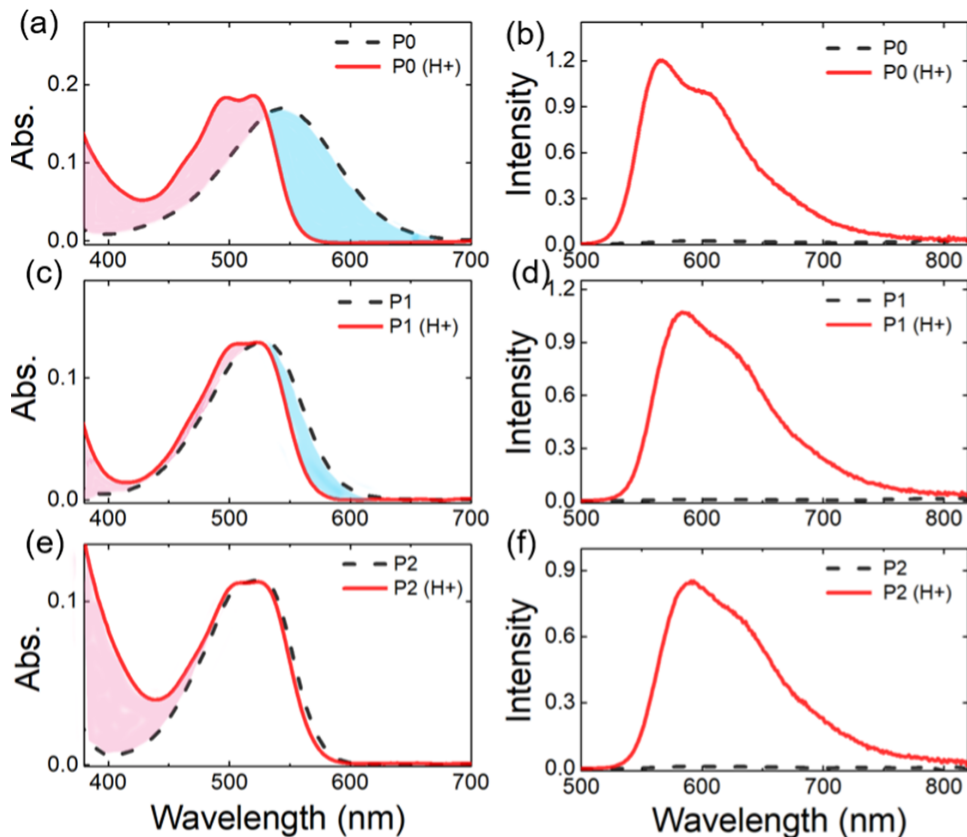


**Figure B.12.** UV-vis absorption (a, c, e) and fluorescence emission (b, d, f) in neutral (dashed black lines) and protonated (bold red line) state for **P0** (1st row); **P1** (2nd row); **P2** (3rd row) in Bzn. Protonation experiments were performed by adding a small amount of HBr (48%) to the solutions containing the DBA compound in Bzn. Shaded area highlight the magnitude of change in UV-vis absorption under protonated and neutral condition.

B

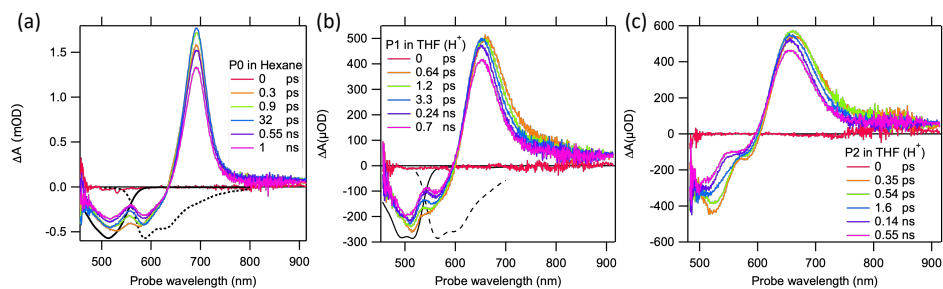


**Figure B.13.** TA spectra of (a) **P0** in hexane upon excitation at 530 nm. TA spectra of protonated (b) **P1** and (c) **P2** in THF upon excitation at 500 nm.

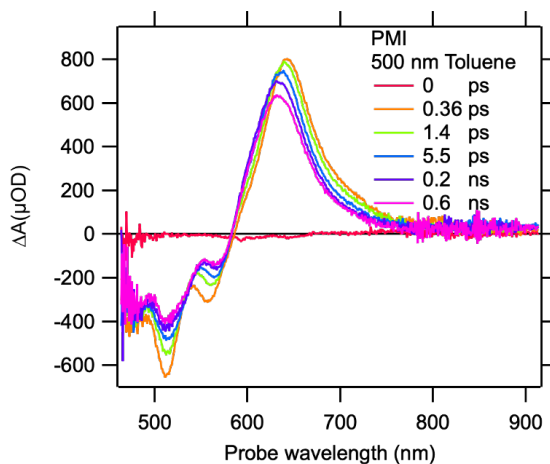


**Figure B.14.** Transient absorption spectra of **PMI** in toluene upon excitation at 500 nm.

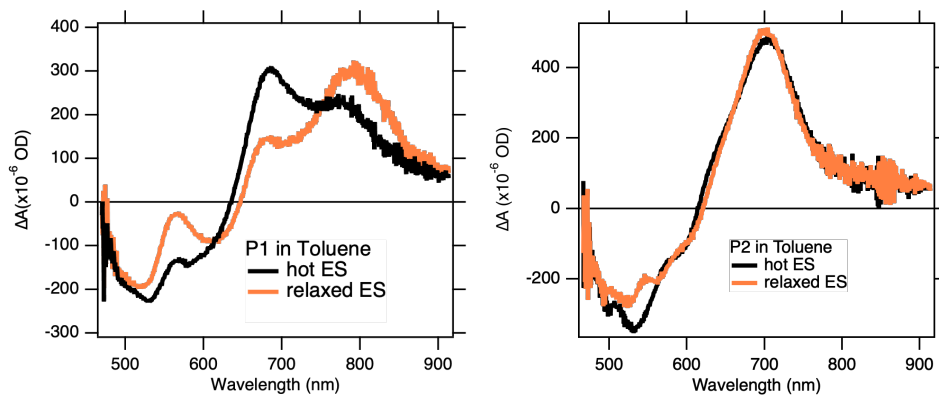


**Figure B.15.** Evolution-associated difference spectra (EADS) of **P1** and **P2** in toluene.

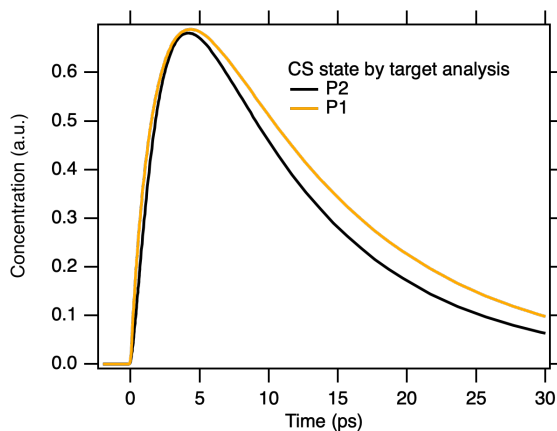


**Figure B.16.** Comparison of the concentration profiles of CS state for **P1** and **P2** in THF.



## Rehm-Weller analyses and dielectric continuum model[4–7]

$$\Delta G_{CS}^{\circ} = E_{ox}(D) - E_{red}(A) - E_{0,0}(D/A) - \Delta G_S$$

$$\Delta G_{CR}^{\circ} = -E_{ox}(D) + E_{red}(A) + \Delta G_S$$

(B.5)

$$\text{where } \Delta G_S = \frac{e^2}{4\pi\epsilon_0 r_{DA} \epsilon_S} - \frac{e^2}{8\pi\epsilon_0} \left( \frac{1}{2r_D} + \frac{1}{2r_A} \right) \left( \frac{1}{\epsilon_S} - \frac{1}{\epsilon_{ref}} \right)$$

In Equation (B.5),  $E_{ox}(D)$  and  $E_{red}(A)$  are the oxidation potential of the donor and the reduction potential of the acceptor, while  $E_{0,0}(D/A)$  is the spectroscopic excited state energy of the donor/acceptor. In this equation  $r_D$  and  $r_A$  are the ionic radii of the donor and acceptor radical ions,  $r_{DA}$  is the donor-acceptor distance, while  $\epsilon_{ref}$  and  $\epsilon_S$  are the dielectric constants of the reference solvent and the chosen solvent for spectroscopy, respectively. Using the Rehm-Weller equation is a rather crude approximation, as it assumes the formation of spherical ions and approaches the charge separation energy by point charges at the center to center distance between the chromophores  $r_{DA}$ . The charge separation distance for **P0** ( $r_{DA} = 8.93 \text{ \AA}$ ), **P1** ( $r_{DA} = 13.03 \text{ \AA}$ ) and **P2** ( $r_{DA} = 17.46 \text{ \AA}$ ) were computed from the DFT optimized geometries (CAM-DA B3LYP/DZP in ADF package). The ionic radius of the perylene acceptor  $r_A = 6.08 \text{ \AA}$ , and dimethylaniline donor  $r_D = 2.10 \text{ \AA}$  was estimated from the DFT optimized geometries employing *volume* function in Gaussian09 Rev. B.01 (B3LYP/6-31g(d,p)). It is obvious that in the apolar solvent toluene, the margins of error in the calculated charge separation energies are significant, whereas the values calculated for Bzn are more accurate.  $\Delta G_{CS}^{\circ}$  and  $\Delta G_{CR}^{\circ}$  are free energies for charge separation and recombination, respectively.

**Table B.5.** Rehm-Weller driving force for charge separation ( $\Delta G_{CS}^{\circ}$ ) and recombination ( $\Delta G_{CR}^{\circ}$ ) for the DBA derivatives.

	$\Delta G_{CS}^{\circ}(\text{Tol})$	$\Delta G_{CS}^{\circ}(\text{THF})$	$\Delta G_{CS}^{\circ}(\text{Bzn})$	$\Delta G_{CR}^{\circ}(\text{Tol})$	$\Delta G_{CR}^{\circ}(\text{THF})$	$\Delta G_{CR}^{\circ}(\text{Bzn})$
<b>P0</b>	0.93	-0.30	-0.65	-3.32	-2.08	-1.68
<b>P1</b>	1.22	-0.23	-0.64	-3.61	-2.15	-1.69
<b>P2</b>	1.43	-0.13	-0.56	-3.75	-2.17	-1.67

To roughly estimate the outer-sphere reorganization energy ( $\lambda_o$ ) for **P0-P2** in THF ( $\eta = 1.41$ ,  $\epsilon_s = 7.58$ ), the dielectric continuum model in Equation (2.3) was used. We used the same values of radii and distance as mentioned above. As a result, we obtained **P0** = 1.1 eV, **P1** = 1.3 eV and **P2** = 1.4 eV.

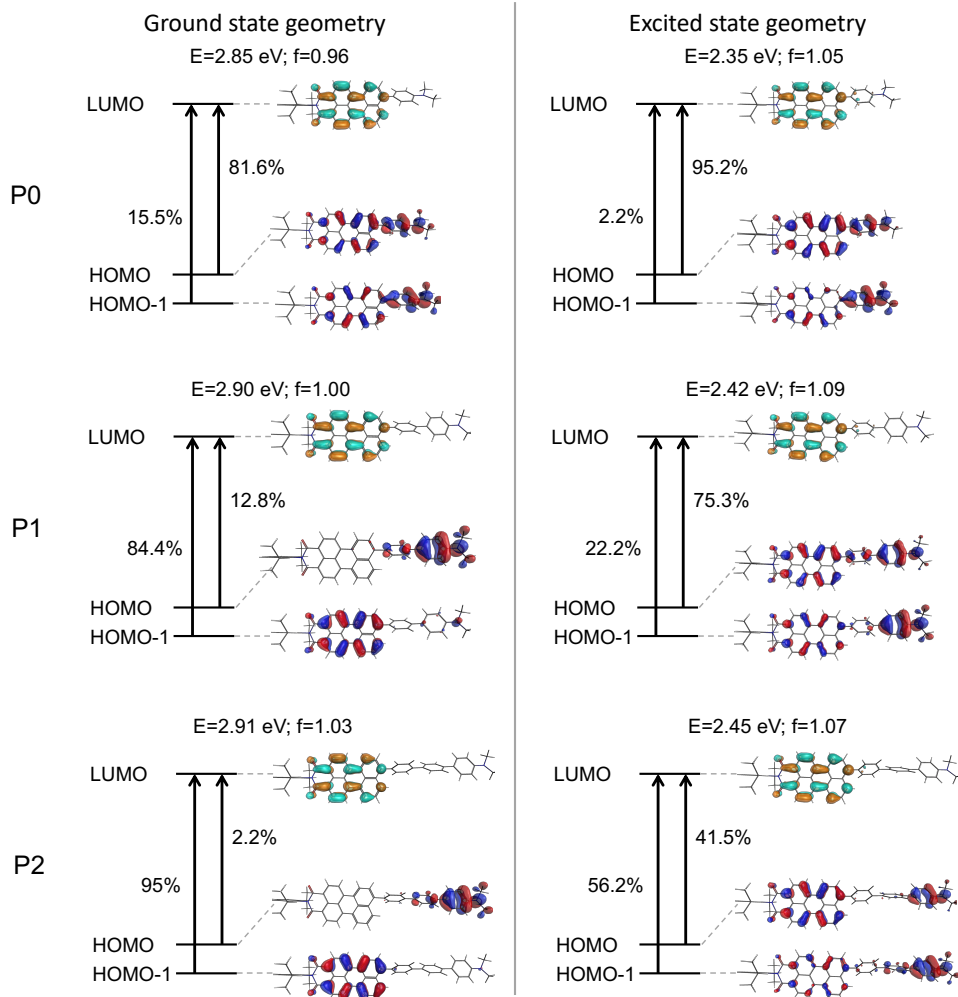


**Figure B.17.** Contributions of single orbital transitions to the lowest vertical excitation in **P0**–**P2** based on the ground state geometry (left) and excited state geometry (right) calculated using TD-DFT with CAM-B3LYP/DZP. Only the contribution larger than 2% is shown.

### Theoretical calculations

Relative potential energy surface (PES) of  $S_0$  in **P0** was calculated by fixing the dihedral angle between the **PMI** and **DMA**, while leaving the rest of the geometry to optimize freely. Based on the PES of  $S_0$ , the PES of  $S_1$  in  $P_0$  was then built up by adding the lowest vertical transition energy for the corresponding ground state (GS) geometry. To demonstrate the effect of solvent stabilization by THF on the PES of  $S_1$ , the Conductor like Screening Model (COSMO)[8] was used as the solvation method. For a given geometry, the single-determinant states were specified by setting the corresponding electron occupation numbers explicitly. The solvent stabilization energy of a specific state was then calculated by subtracting its total bonding energy calculated in THF from that calculated in vacuum. Therefore, the solvent stabilization energy for the GS,  $S_0$ , was directly obtained by calculating the difference between the total bonding energy in THF and that in vacuum based on single point calculations. For the first excited state  $S_1$ , the overall solvent stabilization energy was calculated as a linear combinations of stabilization energies for the dominant determinants that making up the ES.

	Ground state geometry			Excited state geometry		
	$\Phi_1$	$\Phi_2$	$\Phi_3$	$\Phi_1$	$\Phi_2$	$\Phi_3$
P <sub>0</sub>	63.4°	-	-	45.8°	-	-
P <sub>1</sub>	69.0°	42.4°	-	51.2°	39.1°	-
P <sub>2</sub>	71.0°	46.1°	43.5°	55.1°	44.7°	45.3°

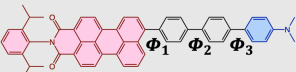


**Figure B.18.** Dihedral angles of the geometry optimized GS and ES.

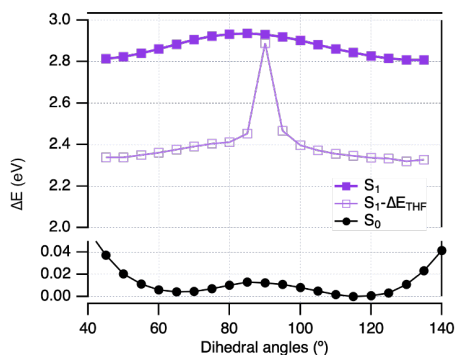


**Figure B.19.** Relative potential energy surfaces (PES) of  $S_0$  and  $S_1$  in vacuum and  $S_1$  in THF *versus* the dihedral angle between **PMI** and **DMA** in  $P_0$  calculated with CAM-B3LYP/DZP.  $\Delta E_{\text{THF}}$  is the amount of energy stabilized by THF in the ES with respect to the GS. The PES of the CT state is not shown for the clarity.

# 5

## Functional molecules on the surface of perovskite nanoplatelets

Understanding the interplay between the kinetics and energetics of photophysical processes in perovskite-chromophore hybrid systems is crucial for realizing their potential in optoelectronics, photocatalysis, and light-harvesting applications. In this chapter, we will discuss the mechanism of interfacial charge transfer (CT) between colloidal CsPbBr<sub>3</sub> nanoplatelets (NPLs) and surface-anchored perylene derivatives and explore the possibility of controlling the CT rate by tuning the driving force. The CT driving force was tuned systematically by attaching acceptors with different electron affinities and by varying the bandgap of NPLs via thickness-controlled quantum confinement. Our results show that the charge-separated state is formed by selectively exciting either the electron donors or acceptors in the same system. Upon exciting attached acceptors, hole transfer from perylene derivatives to CsPbBr<sub>3</sub> NPLs takes place on a picosecond timescale, showing an energetic behavior in line with the Marcus-normal regime. Interestingly, such energetic behavior is absent upon exciting the electron donor, suggesting the dominant CT mechanism is energy transfer followed by ultrafast hole transfer. Our findings not only elucidate the photophysics of perovskite-molecule systems but also provide guidelines for tailoring such hybrid systems for specific applications.

---

§This chapter is based on: [Zimu Wei](#), Jence T. Mulder, Rajeev K. Dubey, Wiel H. Evers, Wolter F. Jager, Arjan J. Houtepen, Ferdinand C. Grozema, *The Journal of Physical Chemistry C*, 2023, 127 (31), 15406–15415.

## 5.1. Introduction

In recent years, strenuous synthetic efforts towards colloidal perovskite nanomaterials have unlocked the potential of perovskite nanoplatelets (NPLs) for LEDs[1–3], lasers[4, 5], luminescent solar concentrators[6], photovoltaics[7] and photocatalysis[8, 9]. They can be synthesized with thicknesses smaller than their exciton Bohr radius, showing strong quantum and dielectric confinement[10, 11]. Hence, they exhibit unique thickness-dependent absorption and emission with narrow linewidth and large exciton binding energy (i.e., 200–400 meV)[12, 13]. The latter benefits the light-emitting properties of NPLs but limits their potential for photovoltaics and photo-detectors by hampering the charge separation process[14]. Our group has previously shown that efficient charge separation can be achieved by attaching strongly electron-accepting chromophores onto the surface of colloidal CsPbBr<sub>3</sub> NPLs[15]. To further control and optimize charge separation in those hybrid systems towards specific applications, understanding the kinetics and energetics of charge transfer (CT) between the chromophoric molecules and perovskite nanomaterials is essential.

Despite some recent interest in perovskite–molecule hybrid systems[16–18], photophysical understanding of such systems remains underdeveloped and sometimes disputed[19, 20]. In particular, systematic studies on how to control the CT rate by tuning the driving force are lacking. Most studies of perovskite–molecule systems focused on relatively large perovskite nanocrystals with bulk-like electronic structures. In this weakly quantum confined regime, it becomes questionable to approximate the conduction band and valence band of NCs by two single levels when evaluating the interfacial CT. This problem can be alleviated by the strong quantum confinement in NPLs[21]. Through precise control over the number of monolayers, the bandgap energy of NPLs can be varied accordingly, thereby tuning the CT driving force. On the other hand, the CT driving force can be tuned by customizing the redox potential of molecules. By attaching different molecules to the NPLs synthesized in the same batch, we can study the effect of energetics while averting the reproducibility issue of nanomaterials.

In this work, we investigate the mechanism of interfacial CT between colloidal 2D CsPbBr<sub>3</sub> NPLs (3 and 4 monolayers) and surface-anchored perylene derivatives, with a focus on the effect of driving force on the CT rate. Through the combination of steady-state optical characterizations and transient absorption measurement, we have established a detailed picture of the photophysical processes upon selectively exciting either the electron donor or acceptor in the same system. Upon exciting attached acceptor molecules, we demonstrate hole transfer from perylene derivatives to CsPbBr<sub>3</sub> NPLs on a picosecond timescale. By only varying the electron affinity of the perylene derivatives, we show that the hole transfer rate increases with increasing driving force. Strikingly, this energetic effect is absent when varying the NPLs bandgap, which is an indirect consequence of a concomitant change in their lateral sizes. Upon exciting CsPbBr<sub>3</sub> NPLs, our data suggest the driving force

dependence of CT rate is incompatible with electron transfer in the Marcus normal regime. We conclude that the photoexcitation of NPLs predominately leads to energy transfer from NPLs to acceptor molecules followed by ultrafast hole transfer to produce triplet states in the molecules. Our findings deepen the fundamental understanding of the photophysics of perovskite–molecule hybrid systems and pave the way for tailoring those hybrid systems for various light-harvesting applications.

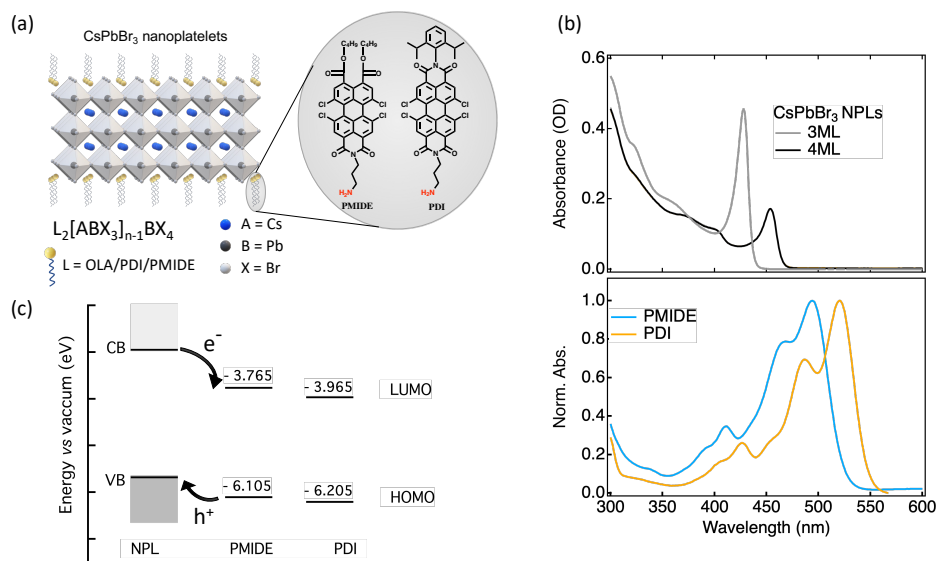


**Figure 5.1.** System design of perovskite–chromophore hybrids. (a) Schematic representation of CsPbBr<sub>3</sub> nanoplatelets (NPLs)–perylene derivative hybrids. (b) Absorption spectra of CsPbBr<sub>3</sub> NPLs with different thicknesses in hexane and normalized absorption spectra of perylene monoimide diester (PMIDE) and of perylene diimide (PDI) in dichloromethane (DCM). (c) Estimated energy levels of CsPbBr<sub>3</sub> NPLs and molecular acceptors. Arrows indicate interfacial electron transfer and hole transfer pathways.

## 5.2. Results and discussion

### 5.2.1. System design

To design a proper donor–acceptor system, suitable energetic and spectroscopic properties are essential. Therefore, we chose a system consisting of CsPbBr<sub>3</sub> NPLs functionalized with either perylene diimide derivatives (PDI) or perylene monoimide diester derivatives (PMIDE) (Figure 5.1a). Details of syntheses are provided in the Supporting Information. Both chromophores are excellent electron acceptors but with different electron accepting abilities[22]. As both

molecules are terminated with the same alkylamine group at the imide position, it allows us to study the effect of driving force on CT without changing the anchoring group or the CT distance. On the other hand, the CT driving force can be tuned by varying the bandgap of CsPbBr<sub>3</sub> NPLs via thickness-controlled quantum confinement[11, 23]. By controlling the synthesis conditions, colloidal CsPbBr<sub>3</sub> NPLs with monodispersed thickness are obtained[24]. Their thickness-dependent absorption properties are shown in Figure 5.1b. Based on the TEM images (Figure C.1), their sharp absorption peaks at 428 nm (2.90 eV) and 454 nm (2.73 eV) are assigned to the excitonic absorption of 3-monolayer (~1.7 nm) and 4-monolayer (~2.5 nm) NPLs[25], respectively. 3ML and 4ML NPLs were chosen because of their relatively good stability and minimized spectral overlap with the absorption of PDI and PMIDE (Figure 5.1b). In this way, we can selectively excite both components at different wavelengths to explore the effect of driving force on both electron transfer from NPLs to PDI/PMIDE and hole transfer from PDI/PMIDE to NPLs.

The estimated energy diagram of the perovskite–chromophore system is shown in Figure 5.1c. The energy levels of HOMO and LUMO of PMIDE and PDI are determined based on the electrochemical characterization (Figure C.2). Experimental details regarding the cyclic voltammetry are described in the Section 5.4. Unfortunately, it is impracticable to use the same method to determine the band edge positions for CsPbBr<sub>3</sub> NPLs due to their poor electrochemical stability. Although there have been some attempts to estimate the energy levels of conduction and valence band of CsPbBr<sub>3</sub> NPLs[16], a large uncertainty, on the order of hundreds of meV, is typically expected. However, it is still possible to make a few qualitative estimations that can reflect the energetic environment in our hybrid system. Firstly, based on the reported VB edge positions (-5.4 eV) of ~10 nm CsPbBr<sub>3</sub> nanocrystals[26], strongly quantum-confined CsPbBr<sub>3</sub> NPLs are expected to have a deeper VB level. This gives rise to an upper limit of 0.8 eV for the driving force of hole transfer. Secondly, since the hole transfer from PDI/PMIDE to CsPbBr<sub>3</sub> NPLs is energetically favored as evident in our previous report[15] and results in this work, the lower limit of the VB energy level is -6.1 eV. Finally, the energy difference between the CB and VB should be larger than the energy of the exciton peak. As a result, the driving force for electron transfer is at least 0.4 eV and 0.6 eV for 4ML NPLs and 3ML NPLs, respectively. Therefore, the hybrid system should possess a type II energy level alignment, as shown in Figure 5.1c.

### 5.2.2. Steady-state optical properties

Hybrid systems of NPLs and acceptor molecules were produced by adding the PDI or PMIDE stock solutions in DCM to the CsPbBr<sub>3</sub> NPLs solution in hexane. With this ligand exchange process, the PDI or PMIDE molecules were attached to the NPLs surfaces presumably via the alkylammonium group. The direct proof of the attachment via the alkylammonium group is shown by the TA measurements in Section 5.2.3. Considering the possible instability of CsPbBr<sub>3</sub> NPLs in the polar solvent, the same amount of DCM was added to the CsPbBr<sub>3</sub> NPLs solution in

hexane to be used as the reference NPLs solution. Figure C.3 clearly shows that the addition of DCM has a negligible impact on the optical properties of NPLs except for a minor reduction in the PL quantum yield, which is likely due to the dissolution of some surface ligands. As shown in Figure 5.2a and d, upon the addition of the acceptor molecules, the absorption spectrum of the hybrid system is basically a linear combination of the individual spectra of the two components. This suggests a minimal electronic coupling between the donor and acceptor in the ground state. Thus, no CT-like complex is formed in the ground state. Based on the extinction coefficients of PDI and PMIDE (Figure C.4), the concentrations of both are estimated to be  $\sim 5\mu\text{M}$  in the mixed solution.

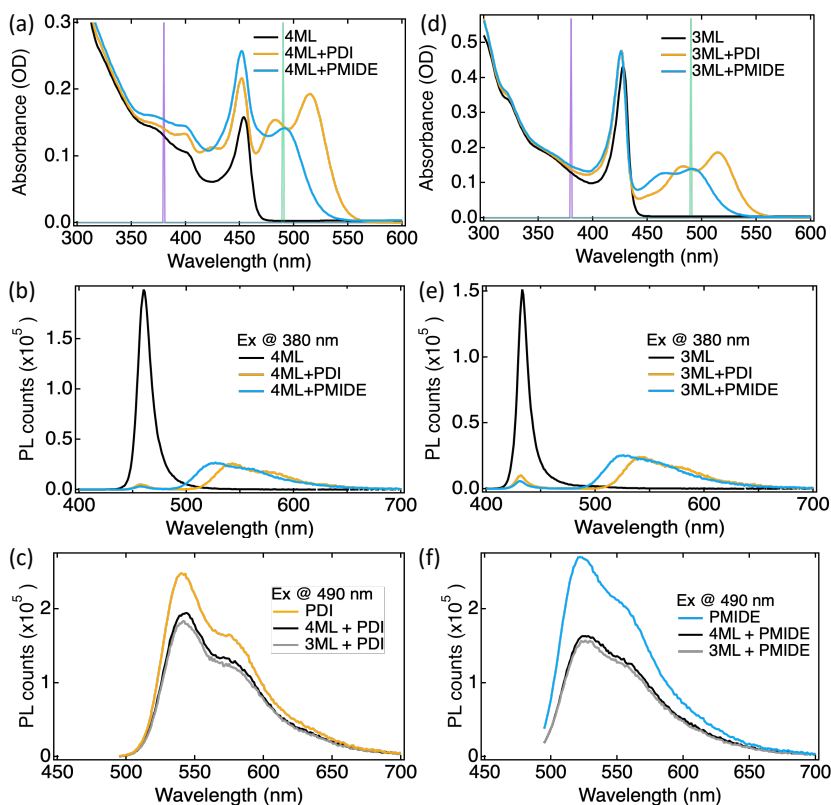


**Figure 5.2.** Optical absorption and photoluminescence emission spectra in Hex:DCM (18:1) mixture with  $c_{\text{PDI/PMIDE}} \approx 5\mu\text{M}$ . (a), (d) Absorption spectra of CsPbBr<sub>3</sub> NPLs, NPLs + PDI and NPLs + PMIDE (4 ML in (a) and 3ML in (d)). (b), (e) Emission spectra of NPLs, NPLs + PDI, NPLs + PMIDE excited at 380 nm. (c) Emission spectra of PDI and NPLs + PDI excited at 490 nm. (f) Emission spectra of PMIDE and NPLs + PMIDE excited at 490 nm. Purple and green lines indicate the excitation wavelengths (380 nm and 490 nm).

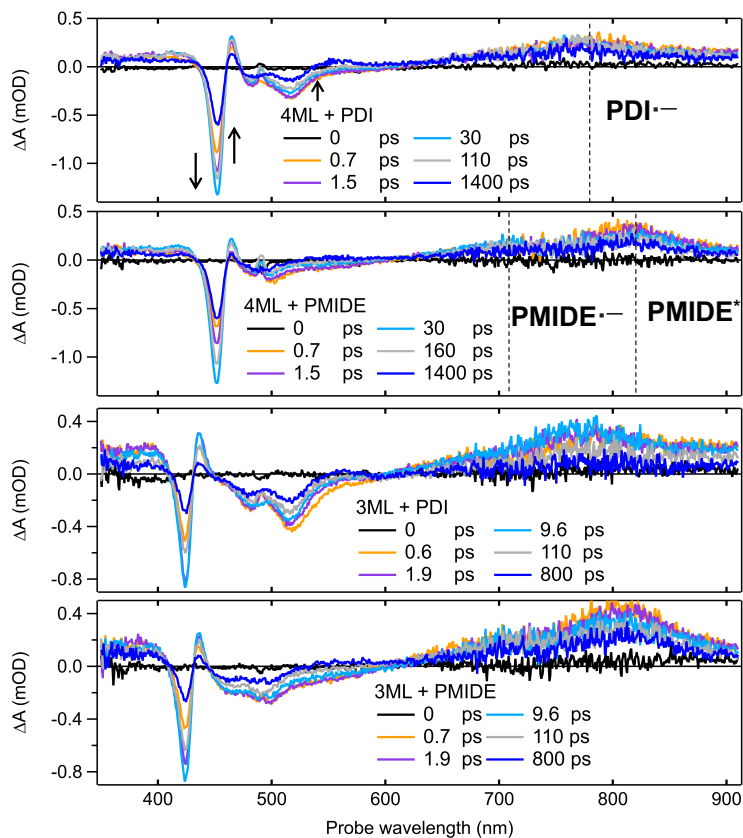


Figure 5.2b and e show the PL spectra of NPLs and the hybrid systems. Notably, the PL of both 3ML and 4ML NPLs is almost entirely quenched in the presence of acceptor molecules. In addition to the reduced PL quantum yield, their PL decays significantly faster upon the addition of acceptor molecules (Figure C.5). This is a strong indication of either electron transfer or energy transfer from the NPLs to PDI or PMIDE. To evaluate the possibility of energy transfer, PL excitation spectra were measured for the 4ML + PDI and 4ML + PMIDE hybrid systems. By monitoring the emission intensity at 550 nm while scanning the excitation wavelength from 350 to 545 nm, we can clarify the origin of the PDI/PMIDE emission in the hybrid systems. If this emission originates from the energy transfer from 4ML NPLs, the spectral feature of NPLs absorption is expected to present in the PL excitation spectrum. However, no such response was observed for either of the hybrid systems, as the excitation spectra of hybrid systems nicely overlap with the absorption spectra of reference PDI/PMIDE molecules in solution (Figure C.6a). Considering a less likely energy transfer from 3ML NPLs due to a smaller overlap between the PL of 3ML NPLs and the absorption of PDI/PMIDE (Figure C.6b), the PDI/PMIDE emission in Figure 5.2b and Figure 5.2e should only stem from the photoexcited PDI/PMIDE instead of the energy transfer from NPLs to PDI/PMIDE. Furthermore, upon excitation at 490 nm (Figure 5.2c and Figure 5.2f), PDI/PMIDE emission in the hybrid systems is also quenched, indicating hole transfer from the PDI/PMIDE to NPLs. Note that although no evidence of energy transfer from NPLs to PDI/PMIDE was found based on their steady-state optical properties, it is impossible to exclude the possibility of energy transfer followed by hole transfer from PDI/PMIDE to NPLs on an ultrafast time scale.

### 5.2.3. Photoexcitation at 490 nm

To investigate whether there is hole transfer from PDI/PMIDE to the NPLs and how it may be affected by the driving force, the excited state dynamics of the hybrid systems were measured by femtosecond transient absorption (TA) spectroscopy, exciting at 490 nm (see Section 5.4 for details). Since the photon energy of the pump pulses was below the bandgap of the NPLs, only the acceptor molecules were excited. To rule out the possibility of sub-bandgap absorption, we measured the TA spectra of a reference 4ML NPLs solution excited at 490 nm under different pump fluences, covering the pump fluence used for the main text. Indeed, apart from the common coherent artifact during the pump-probe overlap ( $< 0.5$  ps), no TA signal was detected for the reference NPLs (Figure C.7).

The TA spectra of the hybrid systems upon photoexcitation at 490 nm are shown in Figure 5.3. For the 4ML NPLs + PDI system (Figure 5.3a), immediately after the photoexcitation (at 0.7 ps), we observe the ground-state bleach (GSB) of PDI molecules at  $\sim 520$  nm. The broad induced absorption centered at  $\sim 760$  nm signals the presence of PDI anion ( $\text{PDI}^-$ ), which is known to be blue-shifted with respect to the absorption of its excited state ( $\text{PDI}^*$ ) at  $\sim 800$  nm (Figure C.8a)[27]. The TA spectrum between 350 nm and 470 nm exhibits typical features for  $\text{CsPbBr}_3$  NPLs (also see in Figure 5.5a), namely a sharp



**Figure 5.3.** Transient absorption spectra of perovskite–chromophore hybrid systems upon photoexcitation at 490 nm ( $1.1 - 1.6 \times 10^{13}$  photons/cm<sup>2</sup>/pulse). TA spectra of (a) 4ML NPLs + PDI, (b) 4ML NPLs + PMIDE, (c) 3ML NPLs + PDI, and (d) 3ML NPLs + PMIDE.

exciton bleach at  $\sim 450$  nm and two nearby induced absorption features[13, 16]. These spectral features are clear evidence of the hole transfer from HOMO of PDI to the VB of NPLs, forming PDI anions and the hole bleach in the NPLs as illustrated in Figure 5.4a. With increasing time, we see the further growth of the NPLs exciton bleach and its ns-lifetime (Figure C.9), indicating the formation of long-lived charges in the NPLs. Such hole transfer clearly also takes place in the 4ML NPLs + PMIDE system (Figure 5.3b), despite the fact that the PMIDE is a weaker electron acceptor. In this case, the two induced absorption bands are visible in the TA spectra. As compared to the TA spectra of the reference PMIDE (Figure C.8b), the absorption band at  $\sim 810$  nm can be ascribed to the absorption of the PMIDE excited state (PMIDE\*). Accordingly, we assign the absorption band at  $\sim 700$  nm to be the PMIDE anion (PMIDE<sup>-</sup>) absorption[28]. The red-shifted

PMIDE<sup>-</sup> absorption as compared to the literature likely arises from the twisting of the perylene core due to the introduction of chlorides in the bay area. Similar to the 4ML NPLs, the hole transfer processes from both acceptor molecules to the 3ML NPLs are also neatly captured in their TA spectra (Figure 5.3c and Figure 5.3d), including the formation of hole bleach of 3ML NPLs at ~425 nm and the absorption of PDI and PMIDE anions. To verify whether the alkylammonium group functions as the anchoring group in attaching molecules to the NPLs surface, we performed TA measurements with a reference PDI molecule, in which the propylamine group at the imide position is substituted by a diisopropylphenyl group. As evident in Figure C.10, hole transfer from PDI to NPLs diminishes in the absence of a proper anchoring group. Based on this, we conclude that the acceptor molecules are attached to the NPLs surface via the alkylammonium group.

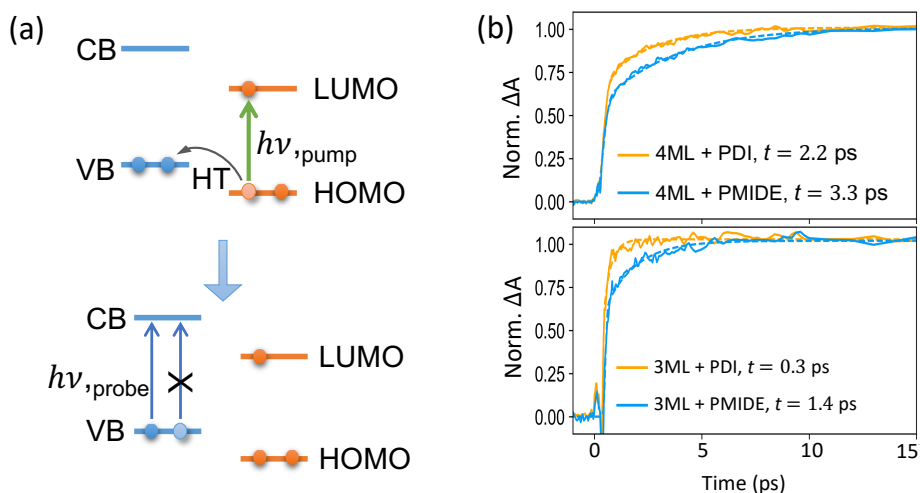


**Figure 5.4.** (a) Schematic of NPLs exciton bleach induced by hole transfer upon photoexciting acceptor molecules. (b) Normalized kinetics at the wavelength of exciton bleach for NPLs and their fits in the time window of the hole transfer process.

Since hole transfer takes place in all four hybrid systems, the next step is to quantify the hole transfer rate and to understand how it is influenced by the driving force. Considering the partial overlap between the absorption of PDI<sup>-</sup>/PMIDE<sup>-</sup> and PDI\*/PMIDE\* and the concurrent absorption from unattached PDI/PMIDE molecules in solution, the formation of the NPLs hole bleach is a reliable indicator to reflect the hole transfer rate. Figure 5.4b shows the normalized single-wavelength fitting of the formation of NPLs bleach due to hole transfer. Details of the fitting procedure can be found in Section 5.4. Overall, the hole transfer rates in all hybrid systems take place on the order of a picosecond. For both 4ML and 3ML systems, the hole transfer from the stronger electron

acceptor, PDI, is faster than that from the weaker electron acceptor, PMIDE. In this comparison, both molecules are attached to the same NPLs via the same anchoring group. Therefore, other factors, such as the electronic coupling and the CT distance, should not play any role in determining the hole transfer rate. In addition, the effect of the energetic distribution of band states in NPLs is insignificant due to the strong quantum confinement. This is supported by the calculations on band structures of CsPbBr<sub>3</sub> NPLs, where the energy difference between the first and second confined energy levels is considerably large already for the 4ML[21]. Furthermore, the fact that the spectra of formed NPLs bleach do not change in shape over the entire time (Figure C.11) is consistent with the formation of holes in the NPLs directly at the band-edge of the VB without subsequent relaxation. Hence, the increasing hole transfer rate with the increasing driving force conforms to CT in the Marcus normal regime[29].

Interestingly, such Marcus-normal behavior does not pertain to the comparison between 4ML and 3ML systems for the same acceptor molecules. By reducing the thickness of NPLs, the VB of 3ML NPLs is expected to be lower than that of the 4ML NPLs due to quantum confinement, thereby lowering the CT driving force. To estimate the difference in the bandgap energy between 3ML and 4ML, we obtained the exciton energy and the exciton binding energy from their optical absorption spectra (Figure C.12). Using this bandgap, we estimate the difference in the HT driving force between 3ML and 4ML to be approximately 95 meV (See Chapter C for detailed estimations). Nevertheless, hole transfer from acceptor molecules to the 3ML NPLs is much faster than to the 4ML NPLs as demonstrated in Figure 5.4b. Given that hole transfer is expected to happen in the Marcus-normal regime as described above, other factors unrelated to energetics must play a role. We have noticed that the average lateral sizes of the 3ML NPLs are almost 30 times larger than that of the 4ML NPLs, as indicated by their TEM images (Figure C.13). Such a large difference in lateral sizes can have several consequences on the CT rate. Firstly, the electronic coupling ( $H_{DA}$ ) in the Marcus theory is known to be surface-area-dependent in semiconductor nanoparticle–molecule systems[30]. However, a smaller CT rate for a larger surface area is generally reported due to a more delocalized wave function for larger sizes[30, 31]. Hence, the surface-area dependence of the electronic coupling is unlikely to be the reason for the faster hole transfer to 3ML NPLs. The second one is the reorganization energy. Although the reorganization energy of NPLs ( $\lambda_{NPLs}$ ) should be size-dependent, we expect the total reorganization energy of the hybrid systems ( $\lambda$ ) to be dominated by the reorganization of the acceptor molecules ( $\lambda_{PDI/PMI}$ ), given the much larger sizes and more delocalized orbitals in NPLs. Hence, the total reorganization energy is expected to be similar for hybrid systems with the same chromophore. Finally, unlike conventional donor–acceptor systems, the CT rate in a nanoparticle–molecule system is expected to be proportional to the average number of molecules attached on each NPL[16, 18]. As a result of much larger lateral sizes, the average number of molecules attached to 3ML NPLs is estimated to be 15 times larger than that of 4ML NPLs (Detailed estimation in Chapter C). Unfortunately, controlling the

lateral dimensions of perovskite NPLs still remains challenging in the field[10]. By tentatively plotting how the hole transfer rate may scale with a pre-factor in the context of Marcus theory (Figure C.14), we reason that the abnormal driving-force dependence of hole transfer from the same molecules to 3ML/4ML NPLs is dominated by the different number of molecules attached as a consequence of very different lateral sizes.

### 5.2.4. Photoexcitation at 380 nm

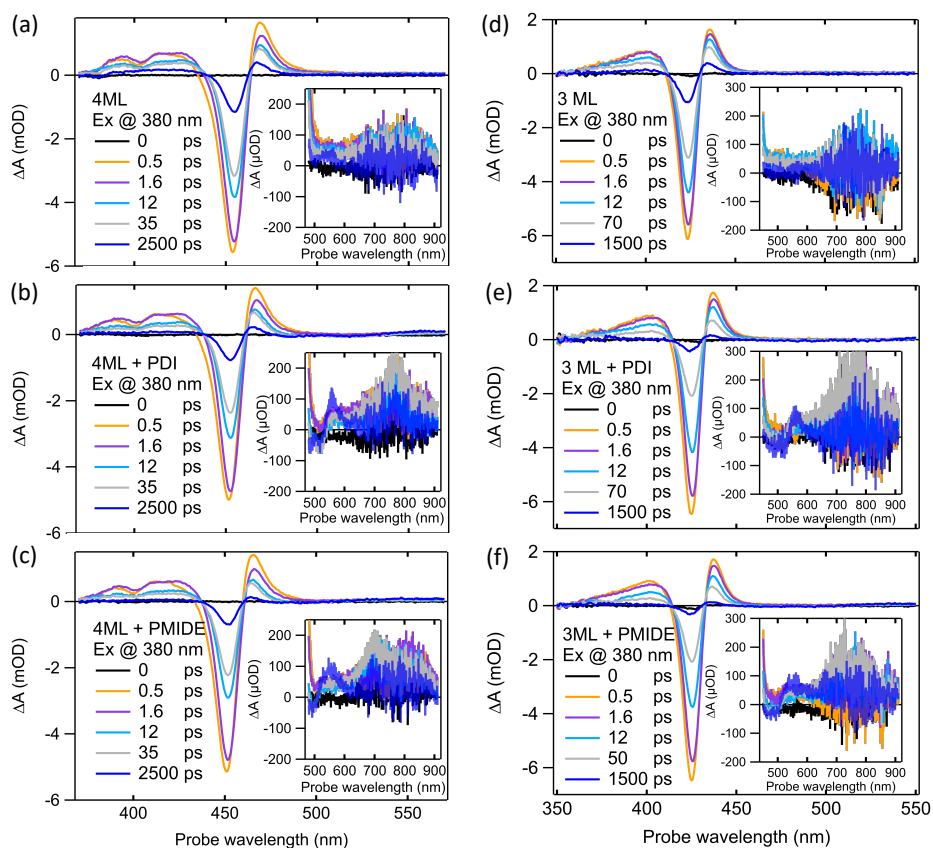


**Figure 5.5.** Transient absorption spectra of upon photoexcitation at 380 nm ( $\sim 5 \times 10^{12}$  photons/cm<sup>2</sup>). TA spectra of (a) 4ML NPLs, (b) 4ML NPLs + PDI, (c) 4ML NPLs + PMIDE, (d) 3ML NPLs, (e) 3ML NPLs + PDI, and (f) 3ML NPLs + PMIDE. Insets are enlarged plots of TA spectra in the near-IR region.

To determine whether PL quenching of NPLs is indeed due to electron transfer from NPLs to acceptor molecules and its driving force dependence, their TA spectra were measured upon photoexcitation at 380 nm. At this wavelength, the

direct excitation of acceptor molecules is negligible given the similar absorbance of hybrid systems and reference NPLs (Figure 5.2a and d). All TA experiments were performed under sufficiently low pump fluences ( $\sim 5 \times 10^{12}$  photons/cm<sup>2</sup>) to avoid multiexciton generation and photodegradation as much as possible. As shown in Figure 5.5a and d, the TA spectra of reference NPLs exhibit characteristics of photoexcited CsPbBr<sub>3</sub> NPLs as reported in the literature[13, 16], including the main exciton bleach due to the state filling of band-edge excitons ( $\sim 450$  nm for 4ML,  $\sim 425$  nm for 3ML) and two absorption features on the blue and red sides of the exciton bleach. Upon attachment of acceptor molecules, three drastic changes are seen in their TA spectra (Figure 5.5b-c and e-f). The obvious one is the much faster recovery of NPLs bleach in hybrid systems. This is in good agreement with the quenched PL quantum yield and the shortened PL lifetime of NPLs as shown in Figure 5.2 and Figure C.5. The second change is observed in the near-IR region, where the GSB of PDI/PMIDE and their anion absorption (PDI<sup>-</sup>/PMIDE<sup>-</sup>) appear after tens of picoseconds, indicating the formation of the charge-separated (CS) state. Finally, on the nanosecond timescale, the absorption of PDI<sup>-</sup>/PMIDE<sup>-</sup> decays accompanied by the growth of an induced absorption peaked at  $\sim 550$  nm, while the GSB of PDI/PMIDE almost remains the same. Since the  $T_1 \rightarrow T_n$  transition of PDI triplet has been reported to have a characteristic absorption at 555 nm[32], we attribute this induced absorption to the triplet state of the acceptor molecules. Given the high reactivity of the triplet state with oxygen molecules to generate singlet oxygen, a reactive species for photocatalysis, this intriguing finding demonstrates the potential of such hybrid systems for catalyst applications[33]. Based on these observations, the sequence of photophysical processes upon excitation at 380 nm can be summarized as follows: (1) the photogeneration of excitons in NPLs, (2) the formation of a CS state, and (3) the triplet formation during the charge recombination. Therefore, the faster decay of the excitons in NPLs is indeed associated with the CT process. Nonetheless, it is still difficult to determine whether the CS state is formed due to the direct electron transfer from the CB of NPLs to the LUMO of PDI/PMIDE or due to the energy transfer from NPLs to PDI/PMIDE, followed by the ultrafast hole transfer process, because both pathways are energetically favorable and give rise to the same final products.

To further understand the photophysics upon excitation at 380 nm and to quantify the rate constants of the relevant photophysical processes, the TA spectra were fitted with global and target analysis using the open source software Glotaran[34]. This method was used because the single-wavelength fitting of PDI/PMIDE anion absorption was inadequate to obtain reliable CT rates due to the noise in the near-infrared part of the spectra. With global and target analysis, the full 2D TA data were fitted to a pre-defined kinetic model, resulting in a series of spectra corresponding to species used in the kinetic model and their lifetimes (details are described in Chapter C). The global analysis of reference 4ML (3ML) NPLs yields three decay components with time constants of 0.62 (0.64) ps, 14 (29) ps and 2.48 (1.62) ns (Table C.1). The first sub-picosecond time constant is in line with the reported cooling rates of hot

carriers/excitons in 2D perovskite nanoplatelets (0.2-0.9 ps)[35, 36]. Since photoexcitation at 380 nm is well above the bandgap of the NPLs, we assign the first decay component to the fast cooling of the hot excitons. This is followed by a decay component on the order of tens of picoseconds, which should correspond to fast trapping due to surface defects on perovskite NPLs[12]. Lastly, the nanosecond component is comparable to the PL lifetime of the NPLs excitons (Figure C.5).

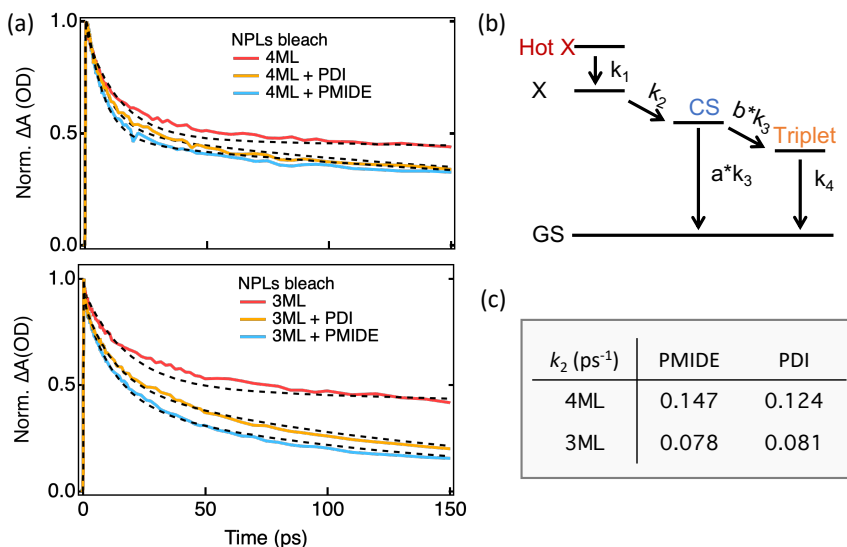


**Figure 5.6.** Global and target analysis of transient absorption spectra. (a) Normalized kinetics of exciton bleach of NPLs and their fits. (b) Kinetic model of target analysis for perovskite–chromophore systems. (c) Charge separation rates of all perovskite–chromophore systems excited at 380 nm.

Upon the addition of acceptor molecules, the faster decay of NPLs bleach is clearly evident in the comparison of their normalized kinetics as shown in Figure 5.6a. Notably, the bleach of the NPLs recovers faster with the weaker acceptor PMIDE than with the stronger acceptor PDI for both 4ML and 3ML NPLs. This can be an indication of the occurrence of energy transfer from NPLs to PDI/PMIDE, as the spectral overlap is larger for the PMIDE molecules than for the PDI molecules (Figure C.6b). On the other hand, it can also be a result of electron transfer from NPLs to PDI/PMIDE taking place in the Marcus-inverted region, where the electron transfer rate decreases with the increasing driving force[29]. However, this is unlikely to be the responsible mechanism due to the Auger-assisted mechanism that can effectively bypass the inverted region of electron transfer by dissipation of energy through intra-band excitation, rather than by coupling to the vibrational density of states[37–39]. In fact, despite extensive studies of CT from colloidal semiconductor nanomaterials to adsorbed



molecules using time-resolved spectroscopy, the inverted region was never observed for the charge transfer involving Coulomb-coupled charges (i.e. excitons)[40]. This is precisely the case for electron transfer from NPLs to acceptor molecules studied in this work. To further validate this interpretation, the TA data of hybrid systems were fitted by the target analysis using the kinetic model illustrated in Figure 5.6b and Figure C.15. According to this model, the hot exciton in NPLs is generated upon photoexcitation, followed by rapid cooling to the band edge. Subsequently, the relaxed exciton undergoes charge transfer, forming a charge-separated (CS) state. Finally, the CS state can either decay back to the ground state or form the triplet state.

The obtained rate constants of the different processes are summarized in Table C.2. The validity of this analysis can be assessed by the comparison between the temporal kinetics and their fits at selected wavelengths and the resulting species-associated spectra. The former is an indicator of the fitting quality, while the interpretability of the latter should agree with the kinetic model used. Overall, the fitting quality is reasonable at various wavelengths in all the samples (Figures C.16 to C.19). In the species-associated spectra, the evolution of the second species (relaxed exciton) to the third species (CS state) shows the emergence of PDI/PMIDE anion absorption at 760/700 nm, in line with a CT process from NPLs to PDI/PMIDE acceptors. Hence, the second rate constant ( $k_2$ ) should correctly reflect the CT rate. Although  $k_2$  is possibly influenced by the fast trapping in the NPLs, such effect should be similar, if not identical, when comparing CT from the same NPLs to different molecules. As displayed in Figure 5.6c, the target analysis suggests the CT rate from 4ML NPLs to PMIDE is indeed faster than that to PDI, consistent with the faster decay of NPLs bleach with PMIDE. Nonetheless, in spite of a larger difference in the decay of NPLs bleach, such trend becomes obscure for CT from 3ML NPLs, as both CT rates to PDI and to PMIDE are virtually the same. This seems to imply a slower energy transfer from 3ML NPLs to PDI compensated by the following faster hole transfer from PDI to 3ML NPLs. Although we acknowledge that the target analysis fits to the hybrid systems with 3ML NPLs are not as satisfactory as the 4ML due to the noisiness in the NIR region, it is still possible to discern a generally faster rate for CT from 4ML NPLs than from 3ML NPLs as indicated by the faster GSB formation of PDI/PMIDE for 4ML NPLs (Figure C.20). This is interesting because an opposite trend has been demonstrated for the hole transfer, for which the smaller CT driving force for 3ML NPLs is overcompensated by a much larger number of molecules attached as compared to the 4ML NPLs. Since the electron transfer in the Marcus-inverted region should also be proportional to the number of acceptors attached, a faster CT rate is expected for the 3ML NPLs. However, in the case of energy transfer followed by hole transfer, the PL of 3ML NPLs indeed has a lower quantum yield (Figure 5.2b and e) as well as a smaller spectral overlap with the absorption of acceptor molecules (Figure C.6b), thereby limiting the overall CT rate. Therefore, it is plausible that the energy transfer followed by hole transfer is the dominant pathway for forming the CS state upon excitation at 380nm.



### 5.3. Conclusions

In conclusion, we have systematically explored the mechanism of CT between CsPbBr<sub>3</sub> perovskite NPLs and perylene derivatives, especially to understand how we can control the CT rate by tuning the driving force. The CT driving force has been tuned by attaching acceptor molecules with different electron affinities and by varying the bandgap of NPLs via thickness-controlled quantum confinement. The transient absorption data unambiguously show the necessity of an anchoring group for achieving charge separation. For perylene derivatives ended with the alkylammonium group, CS states are formed by selectively exciting either the electron donors or acceptors in the same system. This offers direct insight into the band edge positions of perovskite NPLs that cannot be determined electrochemically owing to their notorious instability. Upon exciting acceptors at 490 nm, the stronger acceptor indeed leads to a faster hole transfer from the acceptors to the perovskite NPLs. For NPLs with different bandgaps, the effect of the driving force on hole transfer is overshadowed by the difference in the number of attached molecules due to the different lateral sizes of NPLs. Upon exciting NPLs at 380 nm, we found the CT mechanism is distinct from a direct electron transfer from NPLs to acceptors in the Marcus normal regime. By carefully examining the TA data for all hybrid systems, we conclude that the dominant mechanism for CT is energy transfer from NPLs to acceptors followed by an ultrafast hole transfer from acceptors to NPLs. These results highlight how the nature of CT between inorganic NPLs and molecular acceptors can be unraveled by systematic variation. In addition to elucidating the photophysical picture in perovskite–chromophore systems, we have demonstrated the potential of such hybrid systems for triplet sensitization. With these results, we envision that functionalizing the surface of 2D perovskite nanomaterials is not only a successful strategy for deepening the fundamental understanding of intermolecular CT in such systems. This increased understanding is of great relevance to the development of new materials for photocatalysis, photon up-conversion and optoelectronics where charge separation and the formation of triplet excited states play essential roles.

## 5.4. Methods

### Chemicals

Cesium carbonate ( $\text{Cs}_2\text{CO}_3$ , 99%, Sigma Aldrich), lead(II) bromide ( $\text{PbBr}_2$ , 99.999%, Sigma Aldrich), oleic acid (OA, Extra Pure, Thermo Scientific Chemicals), oleylamine (OLA, approximate C18-content 80-90%, Thermo Scientific Chemicals), acetone (ACS reagent,  $\geq 99.5\%$ , Sigma Aldrich), hexane (suitable for HPLC,  $\geq 95\%$ , Sigma Aldrich), toluene, dichloromethane (for spectroscopy Uvasol, Sigma Aldrich). All chemicals were used as received.

### Synthesis of $\text{CsPbBr}_3$ NPLs

$\text{CsPbBr}_3$  NPLs were synthesized following a procedure modified from a procedure described by Bohn et al[24]. The Cs-oleate precursor solution was prepared by adding 0.2 mmol  $\text{Cs}_2\text{CO}_3$  powder in 20 mL oleic acid. The  $\text{PbBr}_2$  precursor solution was prepared by adding 0.5 mmol  $\text{PbBr}_2$  powder with 500  $\mu\text{L}$  oleylamine and 500  $\mu\text{L}$  oleic acid in 50 mL toluene. Both precursor solutions were stirred continuously at 100 °C until all the powders were dissolved. 150  $\mu\text{L}$  Cs-oleate precursor solution was added into  $\text{PbBr}_2$  precursor solution (1.5 mL for 4 ML and 3 mL for 3 ML) under vigorous stirring. After 5 s, 2 mL acetone was quickly added. After 1 min, the solution was centrifuged at 4000 rpm for 3 min. The precipitate was redispersed in hexane. All  $\text{CsPbBr}_3$  NPLs were synthesized at room temperature and under ambient conditions.

### Preparation of sample solutions (NPLs+PDI/PMIDE)

Synthesis of PDI and PDI-D have been published in ref [15, 41]. And the synthesis of PMIDE is provided in Chapter C. The diluted NPLs solution in hexane was added into three cuvettes, each containing 2.7 mL. Subsequently, 150  $\mu\text{L}$  of  $10^{-4}$  M PDI or PMIDE in DCM was added to form NPLs–chromophore hybrids at room temperature. For the reference NPLs solution, 150  $\mu\text{L}$  DCM was added into the cuvette. The same sample solution was used for absorption, PL, PL lifetime and TA measurement on the same day. The mixed solution was filtered and sonicated for 2 min before the TA measurement.

### Cyclic Voltammetry

The electrochemical behavior of the compounds was studied using cyclic voltammetry (Autolab PGSTAT128N potentiostat) in a three-electrode single-compartment cell consisting of a platinum sheet, evaporated on quartz, as the working electrode, a silver wire as pseudo reference electrode, and a platinum sheet as the counter electrode. The cell was connected to the computer controlled potentiostat (Autolab PGSTAT128N potentiostat). Anhydrous DCM containing 0.1 M tetrabutylammonium hexafluorophosphate was used as the electrolyte solution. The measurements were inside a nitrogen filled glovebox. The concentration of the prepared samples was sufficiently low. Under these experimental conditions, the ferrocene oxidation was observed at 0.455 (PDI) / 0.43 (PMIDE) V. The potentials of all the reversible peaks are

reported as  $E_{1/2} = (E_p^a + E_p^c)/2$  in V vs. Fc/Fc<sup>+</sup> and quoted to the nearest 0.01 V. The measurements were carried out at 0.01 V s<sup>-1</sup> scan rate. The energy level of LUMO was calculated by  $E_{\text{LUMO}} = -(E_{1\text{red}} + 4.8 \text{ eV})$ . The energy level of HOMO was calculated by  $E_{\text{HOMO}} = E_{\text{LUMO}} - E_g$ . Optical band gap,  $E_g$ , was estimated from the absorption onset wavelength  $E_g = 1240/\lambda$ .

### Transmission electron microscopy

Transmission electron microscopy (TEM) images were acquired using JEOL JEM-1400 plus TEM microscopy operating at 120 kV. TEM samples were prepared by drop-casting NPLs hexane solution onto a carbon-coated Cu TEM grid. High-resolution TEM (HR-TEM) images were acquired using a JEOL JEM-3200 FSC operating at 300 kV and using a Gatan K2 camera operating in counting mode. The images were taken at zero loss with a slit width of 20 eV.

### Optical spectroscopy

Absorption spectra were measured by PerkinElmer Lambda 365 UV-vis spectro-photometer. PL spectra were measured by Edinburgh Instruments FLS980 spectro-fluorimeter with a xenon lamp as the excitation source. PL lifetimes were recorded on an Edinburgh LifeSpec-ps spectrometer with a fixed excitation wavelength of 404 nm. For the fs-TA measurement, the generation of the pump pulse is described in Section 2.2.1. The probe beam was generated by focusing a small fraction of the fundamental beam in a CaF<sub>2</sub> crystal, producing a broadband continuum spectrum (350 - 910 nm). The sample solution was measured in a 2 mm quartz cuvette under vigorous stirring at the magic angle (54.7°). The pump power stayed stable during each measurement with a deviation smaller than 2% before and after each measurement. To assure the sample stability, at least 3 scans were performed for each measurement, and no degradation was detected during the TA measurement.

## References

1. Ling, Y., Yuan, Z., Tian, Y., Wang, X., Wang, J. C., Xin, Y., Hanson, K., Ma, B. & Gao, H. Bright light-emitting diodes based on organometal halide perovskite nanoplatelets. *Advanced materials* **28**, 305–311 (2016).
2. Kumar, S., Jagielski, J., Kallikounis, N., Kim, Y.-H., Wolf, C., Jenny, F., Tian, T., Hofer, C. J., Chiu, Y.-C., Stark, W. J., et al. Ultrapure green light-emitting diodes using two-dimensional formamidinium perovskites: achieving recommendation 2020 color coordinates. *Nano letters* **17**, 5277–5284 (2017).
3. Cui, J., Liu, Y., Deng, Y., Lin, C., Fang, Z., Xiang, C., Bai, P., Du, K., Zuo, X., Wen, K., et al. Efficient light-emitting diodes based on oriented perovskite nanoplatelets. *Science Advances* **7**, eabg8458 (2021).
4. Zhang, Q., Su, R., Du, W., Liu, X., Zhao, L., Ha, S. T. & Xiong, Q. Advances in small perovskite-based lasers. *Small Methods* **1**, 1700163 (2017).
5. Li, G., Che, T., Ji, X., Liu, S., Hao, Y., Cui, Y. & Liu, S. Record-Low-Threshold Lasers Based on Atomically Smooth Triangular Nanoplatelet Perovskite. *Advanced Functional Materials* **29**, 1805553 (2019).
6. Wei, M., de Arquer, F. P. G., Walters, G., Yang, Z., Quan, L. N., Kim, Y., Sabatini, R., Quintero-Bermudez, R., Gao, L., Fan, J. Z., et al. Ultrafast narrowband exciton routing within layered perovskite nanoplatelets enables low-loss luminescent solar concentrators. *Nature Energy* **4**, 197–205 (2019).
7. Ha, S. T., Liu, X., Zhang, Q., Giovanni, D., Sum, T. C. & Xiong, Q. Synthesis of organic-inorganic lead halide perovskite nanoplatelets: towards high-performance perovskite solar cells and optoelectronic devices. *Advanced optical materials* **2**, 838–844 (2014).
8. Schanze, K. S., Kamat, P. V., Yang, P. & Bisquert, J. Progress in perovskite photocatalysis. *ACS Energy Letters* **5**, 2602–2604 (2020).
9. Liu, Z., Yang, H., Wang, J., Yuan, Y., Hills-Kimball, K., Cai, T., Wang, P., Tang, A. & Chen, O. Synthesis of lead-free Cs<sub>2</sub>AgBiX<sub>6</sub> (X= Cl, Br, I) double perovskite nanoplatelets and their application in CO<sub>2</sub> photocatalytic reduction. *Nano Letters* **21**, 1620–1627 (2021).
10. Otero-Martínez, C., Ye, J., Sung, J., Pastoriza-Santos, I., Pérez-Juste, J., Xia, Z., Rao, A., Hoye, R. L. & Polavarapu, L. Colloidal Metal-Halide Perovskite Nanoplatelets: Thickness-Controlled Synthesis, Properties, and Application in Light-Emitting Diodes. *Advanced Materials* **34**, 2107105 (2022).
11. Weidman, M. C., Goodman, A. J. & Tisdale, W. A. Colloidal halide perovskite nanoplatelets: an exciting new class of semiconductor nanomaterials. *Chemistry of Materials* **29**, 5019–5030 (2017).

12. Bodnarchuk, M. I., Boehme, S. C., Ten Brinck, S., Bernasconi, C., Shynkarenko, Y., Krieg, F., Widmer, R., Aeschlimann, B., Günther, D., Kovalenko, M. V., et al. Rationalizing and controlling the surface structure and electronic passivation of cesium lead halide nanocrystals. *ACS energy letters* **4**, 63–74 (2018).
13. Vale, B. R., Socie, E., Burgos-Caminal, A., Bettini, J., Schiavon, M. A. & Moser, J.-E. Exciton, biexciton, and hot exciton dynamics in CsPbBr<sub>3</sub> colloidal nanoplatelets. *The Journal of Physical Chemistry Letters* **11**, 387–394 (2019).
14. Straus, D. B. & Kagan, C. R. Electrons, excitons, and phonons in two-dimensional hybrid perovskites: connecting structural, optical, and electronic properties. *The Journal of physical chemistry letters* **9**, 1434–1447 (2018).
15. Gélvez-Rueda, M. C., Fridriksson, M. B., Dubey, R. K., Jager, W. F., Van der Stam, W. & Grozema, F. C. Overcoming the exciton binding energy in two-dimensional perovskite nanoplatelets by attachment of conjugated organic chromophores. *Nature Communications* **11**, 1901 (2020).
16. Li, Q. & Lian, T. Ultrafast charge separation in two-dimensional CsPbBr<sub>3</sub> perovskite nanoplatelets. *The Journal of Physical Chemistry Letters* **10**, 566–573 (2019).
17. Luo, X., Lai, R., Li, Y., Han, Y., Liang, G., Liu, X., Ding, T., Wang, J. & Wu, K. Triplet energy transfer from CsPbBr<sub>3</sub> nanocrystals enabled by quantum confinement. *Journal of the American Chemical Society* **141**, 4186–4190 (2019).
18. Wu, K., Liang, G., Shang, Q., Ren, Y., Kong, D. & Lian, T. Ultrafast interfacial electron and hole transfer from CsPbBr<sub>3</sub> perovskite quantum dots. *Journal of the American Chemical Society* **137**, 12792–12795 (2015).
19. Luo, X., Liang, G., Han, Y., Li, Y., Ding, T., He, S., Liu, X. & Wu, K. Triplet energy transfer from perovskite nanocrystals mediated by electron transfer. *Journal of the American Chemical Society* **142**, 11270–11278 (2020).
20. DuBose, J. T. & Kamat, P. V. Directing energy transfer in halide perovskite–chromophore hybrid assemblies. *Journal of the American Chemical Society* **143**, 19214–19223 (2021).
21. Saporì, D., Kepenekian, M., Pedesseau, L., Katan, C. & Even, J. Quantum confinement and dielectric profiles of colloidal nanoplatelets of halide inorganic and hybrid organic–inorganic perovskites. *Nanoscale* **8**, 6369–6378 (2016).
22. Dubey, R. K., Westerveld, N., Sudhölter, E. J., Grozema, F. C. & Jager, W. F. Novel derivatives of 1, 6, 7, 12-tetrachloroperylene-3, 4, 9, 10-tetracarboxylic acid: synthesis, electrochemical and optical properties. *Organic Chemistry Frontiers* **3**, 1481–1492 (2016).
23. Sichert, J. A., Tong, Y., Mutz, N., Vollmer, M., Fischer, S., Milowska, K. Z., García Cortadella, R., Nickel, B., Cardenas-Daw, C., Stolarczyk, J. K., et al. Quantum size effect in organometal halide perovskite nanoplatelets. *Nano letters* **15**, 6521–6527 (2015).
24. Bohn, B. J., Tong, Y., Gramlich, M., Lai, M. L., Döblinger, M., Wang, K., Hoye, R. L., Müller-Buschbaum, P., Stranks, S. D., Urban, A. S., et al. Boosting tunable blue luminescence of halide perovskite nanoplatelets through postsynthetic surface trap repair. *Nano letters* **18**, 5231–5238 (2018).

25. Akkerman, Q. A., Motti, S. G., Srimath Kandada, A. R., Mosconi, E., D'Innocenzo, V., Bertoni, G., Marras, S., Kamino, B. A., Miranda, L., De Angelis, F., et al. Solution synthesis approach to colloidal cesium lead halide perovskite nanoplatelets with monolayer-level thickness control. *Journal of the American Chemical Society* **138**, 1010–1016 (2016).
26. Mulder, J. T., Du Fossé, I., Alimoradi Jazi, M., Manna, L. & Houtepen, A. J. Electrochemical p-doping of CsPbBr<sub>3</sub> perovskite nanocrystals. *ACS Energy Letters* **6**, 2519–2525 (2021).
27. Gorczak, N., Tarkuç, S., Renaud, N., Houtepen, A. J., Eelkema, R., Siebbeles, L. D. & Grozema, F. C. Different mechanisms for hole and electron transfer along identical molecular bridges: the importance of the initial state delocalization. *The Journal of Physical Chemistry A* **118**, 3891–3898 (2014).
28. Zhao, Y., Sukhanov, A. A., Duan, R., Elmali, A., Hou, Y., Zhao, J., Gurzadyan, G. G., Karatay, A., Voronkova, V. K. & Li, C. Study of the spin–orbit charge transfer intersystem crossing of perylenemonoimide–phenothiazine compact electron donor/acceptor dyads with steady-state and time-resolved optical and magnetic spectroscopies. *The Journal of Physical Chemistry C* **123**, 18270–18282 (2019).
29. Marcus, R. A. & Sutin, N. Electron transfers in chemistry and biology. *Biochimica et Biophysica Acta (BBA)-Reviews on Bioenergetics* **811**, 265–322 (1985).
30. Diroll, B. T., Fedin, I., Darancet, P., Talapin, D. V. & Schaller, R. D. Surface-area-dependent electron transfer between isoenergetic 2D quantum wells and a molecular acceptor. *Journal of the American Chemical Society* **138**, 11109–11112 (2016).
31. Shang, Q., Kaledin, A. L., Li, Q. & Lian, T. Size dependent charge separation and recombination in CsPbI<sub>3</sub> perovskite quantum dots. *The Journal of Chemical Physics* **151**, 074705 (2019).
32. Yu, Z., Wu, Y., Peng, Q., Sun, C., Chen, J., Yao, J. & Fu, H. Accessing the Triplet State in Heavy-Atom-Free Perylene Diimides. *Chemistry—A European Journal* **22**, 4717–4722 (2016).
33. Liu, M., Wang, J., Liang, G., Luo, X., Zhao, G., He, S., Wang, L., Liang, W., Li, J. & Wu, K. Spin-enabled photochemistry using nanocrystal-molecule hybrids. *Chem* **8**, 1720–1733 (2022).
34. Snellenburg, J. J., Laptinok, S., Seger, R., Mullen, K. M. & van Stokkum, I. H. Glotaran: A Java-based graphical user interface for the R package TIMP. *Journal of Statistical Software* **49**, 1–22 (2012).
35. Villamil Franco, C., Trippé-Allard, G., Mahler, B., Cornaggia, C., Lauret, J.-S., Gustavsson, T. & Cassette, E. Exciton Cooling in 2D Perovskite Nanoplatelets: Rationalized Carrier-Induced Stark and Phonon Bottleneck Effects. *The Journal of Physical Chemistry Letters* **13**, 393–399 (2022).
36. Hintermayr, V. A., Polavarapu, L., Urban, A. S. & Feldmann, J. Accelerated carrier relaxation through reduced coulomb screening in two-dimensional halide perovskite nanoplatelets. *ACS nano* **12**, 10151–10158 (2018).
37. Zhu, H., Yang, Y., Hyeon-Deuk, K., Califano, M., Song, N., Wang, Y., Zhang, W., Prezhdo, O. V. & Lian, T. Auger-assisted electron transfer from photoexcited semiconductor quantum dots. *Nano letters* **14**, 1263–1269 (2014).

38. Olshansky, J. H., Ding, T. X., Lee, Y. V., Leone, S. R. & Alivisatos, A. P. Hole transfer from photoexcited quantum dots: the relationship between driving force and rate. *Journal of the American Chemical Society* **137**, 15567–15575 (2015).
39. Zhu, H., Yang, Y., Wu, K. & Lian, T. Charge transfer dynamics from photoexcited semiconductor quantum dots. *Annual review of physical chemistry* **67**, 259–281 (2016).
40. Wang, J., Ding, T., Gao, K., Wang, L., Zhou, P. & Wu, K. Marcus inverted region of charge transfer from low-dimensional semiconductor materials. *Nature Communications* **12**, 6333 (2021).
41. Dubey, R. K., Westerveld, N., Grozema, F. C., Sudhölter, E. J. & Jager, W. F. Facile synthesis of pure 1, 6, 7, 12-tetrachloroperylene-3, 4, 9, 10-tetracarboxy bisanhydride and bisimide. *Organic letters* **17**, 1882–1885 (2015).

# C

## Appendix to Chapter 5

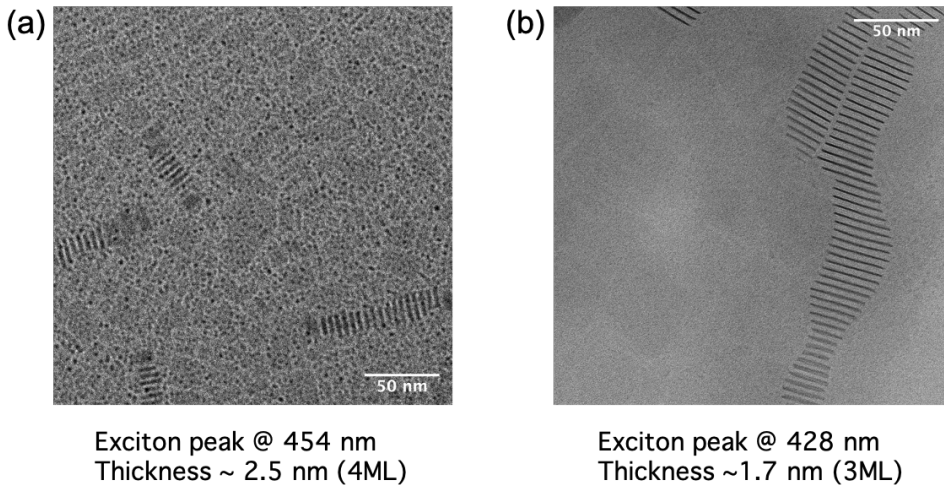


**Figure C.1.** TEM/HR-TEM images of NPLs thickness. (a) TEM image of NPLs with exciton peak absorption at 454 nm. (b) HR-TEM image of NPLs with exciton peak absorption at 428 nm. Note that the black dots in (a) are likely to be reduced lead due to the beam sensitivity of the sample.

**Table C.1.** Fitting parameters of global analysis

	4ML NPLs	3ML NPLs
$k_c$ ( $\tau_c$ in ps)	1.61 (0.62)	1.57 (0.64)
$k_T$ ( $\tau_T$ in ps)	0.071 (14.0)	0.034 (29.4)
$k_{rad}$ ( $\tau_{rad}$ in ps)	0.00040 (2.48)	0.00062 (1.62)



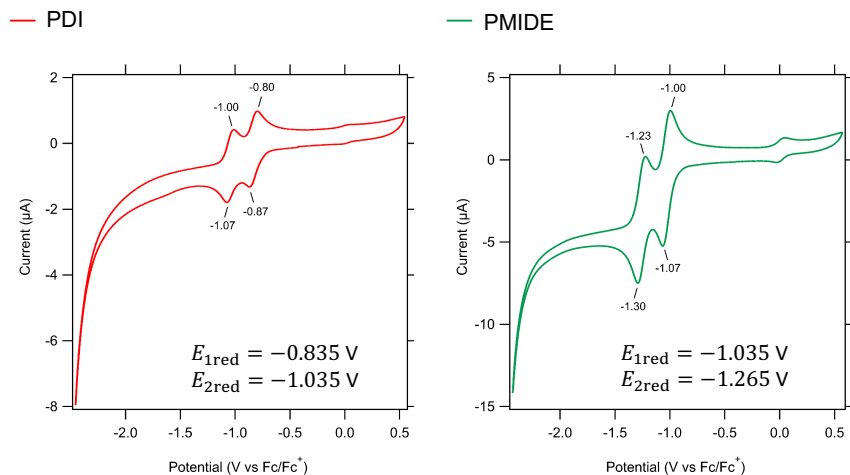


**Figure C.2.** Cyclic voltammograms (vs  $\text{Fc}/\text{Fc}^+$ ) of PDI and PMIDE in DCM with 0.1M  $\text{TBAPF}_6$ . Note that a small amount of ferrocene is added to these measurements (the small signal at 0 V) as internal standard/calibration.

**Table C.2.** Fitting parameters of target analysis

	4ML+PDI	4ML+PMIDE	3ML+PDI	3ML+PMIDE
$k_1$ ( $\tau_1$ in ps)	2.12 (0.47)	2.08 (0.48)	2.81 (0.35)	2.73 (0.36)
$k_2$ ( $\tau_2$ in ps)	0.124 (8.08)	0.147 (6.78)	0.0847 (11.73)	0.0846 (11.83)
$k_3$ ( $\tau_3$ in ps)	0.0066 (151)	0.0064 (156)	0.0085 (118)	0.0094 (107)
$k_4$ ( $\tau_4$ in ps)	0.00019 (5196)	0.00021 (4701)	0.00021 (4825)	0.00016 (6250)
a	0.2	0.2	0.25	0.25
b	0.8	0.8	0.75	0.75

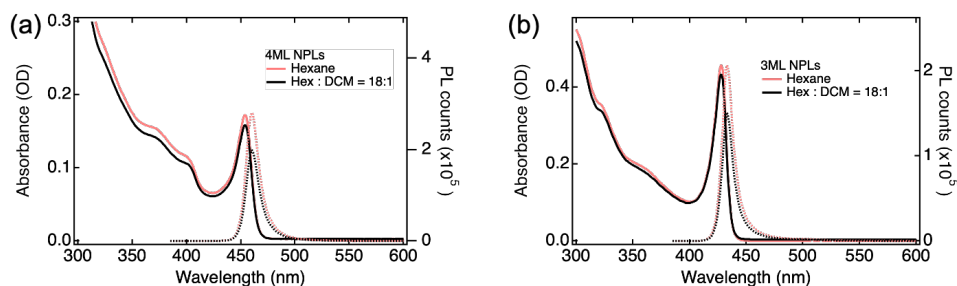


**Figure C.3.** Optical absorption and photoluminescence emission spectra of reference NPLs before and after the addition of 150  $\mu\text{L}$  DCM. PL spectra were measured with excitation at 380 nm.

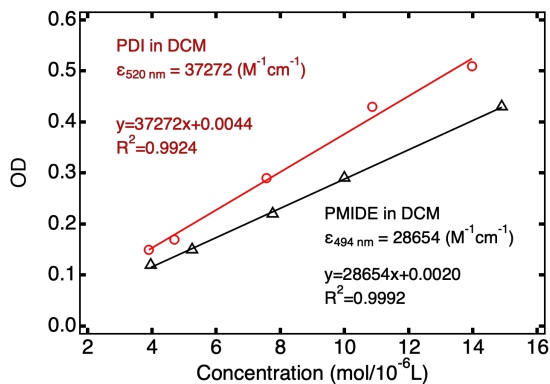


**Figure C.4.** Extinction coefficients of PDI and PMIDE measured in DCM.

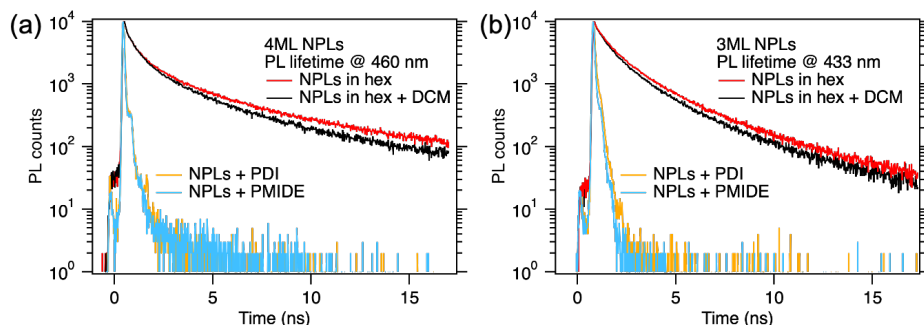


**Figure C.5.** PL lifetime of (a) 4ML NPLs and (b) 3ML NPLs with excitation at 404 nm.

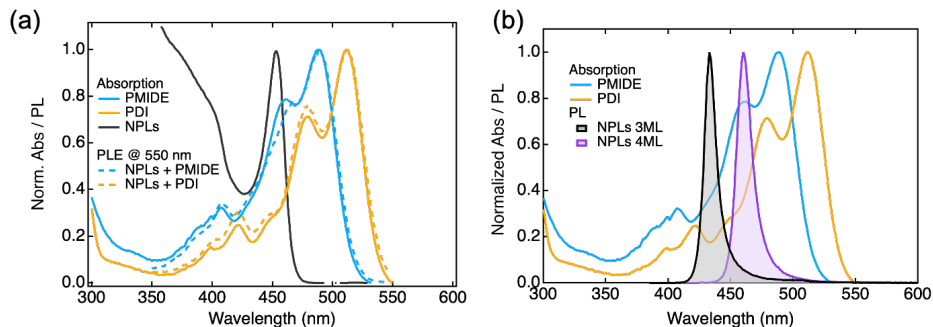


**Figure C.6.** Normalized absorption spectra of 4ML NPLs, PDI and PMIDE in Hex/DCM mixture and photoluminescence excitation spectra of 4ML NPLs + PDI/PMIDE hybrids monitored at 550 nm. (b) Normalized photoluminescence emission spectra of NPLs and absorption spectra of PDI/PMIDE in Hex/DCM mixture.

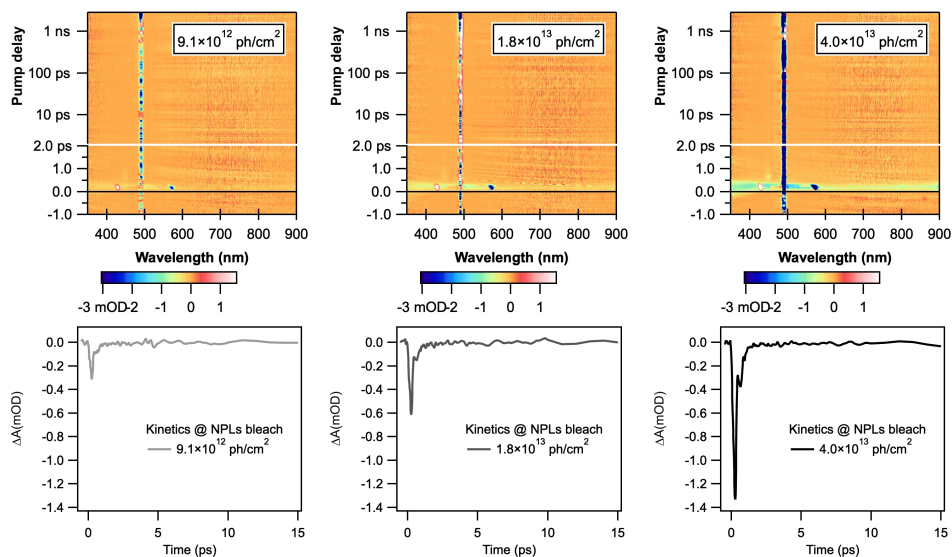


**Figure C.7.** TA spectra of reference 4ML NPLs Hex:DCM (18:1) mixture excited at 490 nm. Upper panel: 2D TA spectra recorded at different photon fluences:  $9.1 \times 10^{12}$  ph/cm<sup>2</sup>/pulse,  $1.8 \times 10^{13}$  ph/cm<sup>2</sup>/pulse and  $4.0 \times 10^{13}$  ph/cm<sup>2</sup>/pulse. Lower panel: TA kinetics due to coherent artifacts at exciton bleach for corresponding photon fluences.

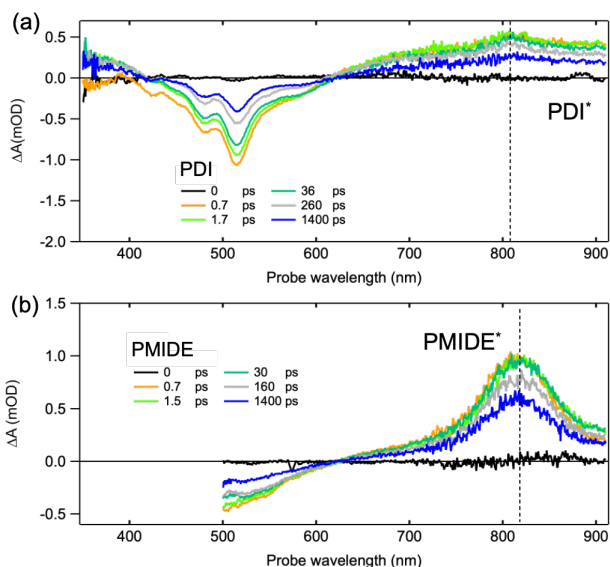


**Figure C.8.** TA spectra of reference acceptor molecules in Hex/DCM mixture. (a) PDI excited at 510 nm and (b) PMIDE excited at 490 nm.

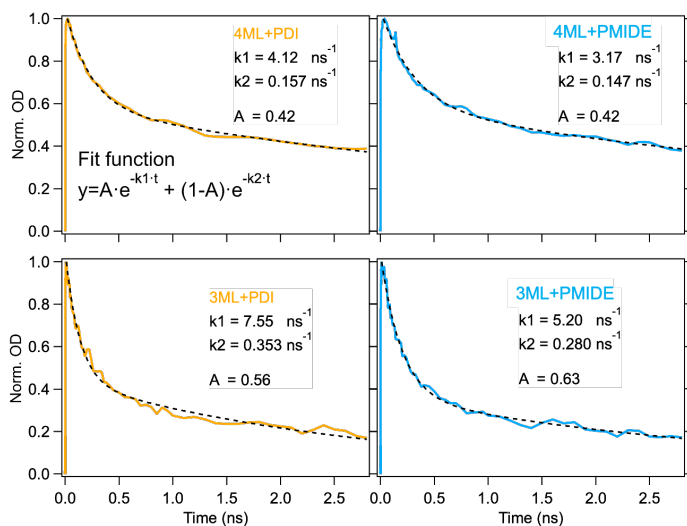


**Figure C.9.** Normalized bleach kinetics of NPLs and their single-wavelength fits excited at 490 nm.

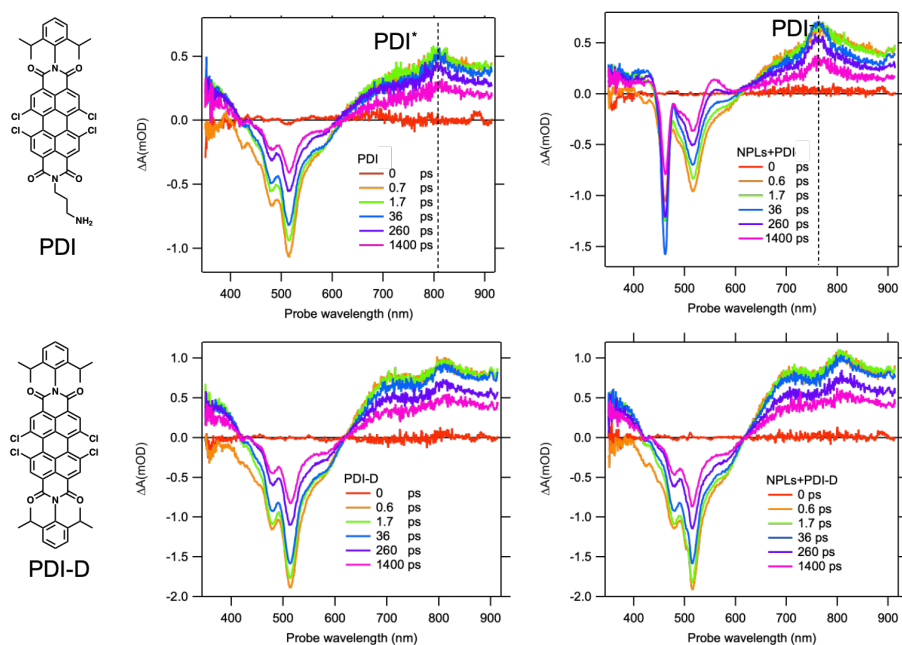


**Figure C.10.** Transient absorption spectra excited at 510 nm. Upper panel: molecular structure of PDI (PDI used in the main text), TA spectra of PDI and of NPLs + PDI. Lower panel: molecular structure of reference PDI-D, TA spectra of PDI-D and of NPLs + PDI-D.

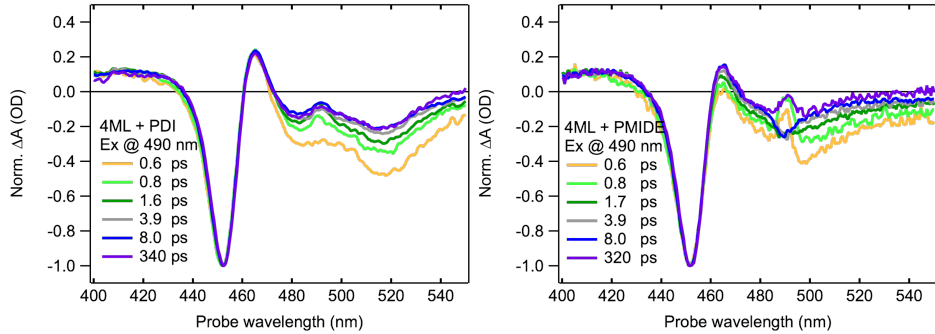


**Figure C.11.** TA spectra normalized to the bleach of 4ML NPLs upon excitation at 490 nm in hybrid systems.

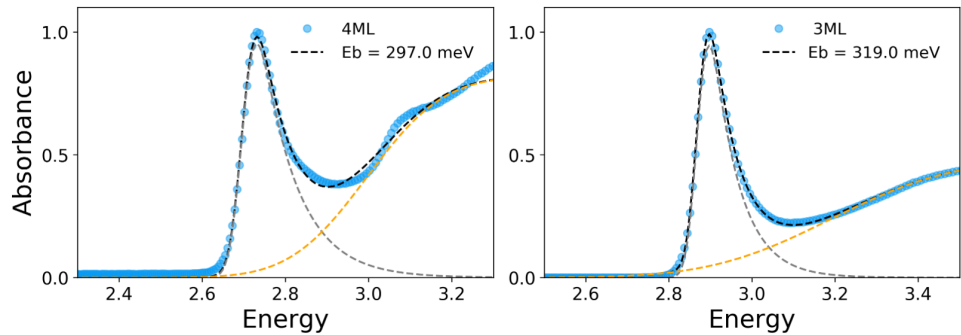


**Figure C.12.** Normalized absorption spectra of 4ML and 3ML NPLs (blue spheres) and their fits. The black line is the fitted model, and the gray and orange lines are the exciton and continuum contributions, respectively.

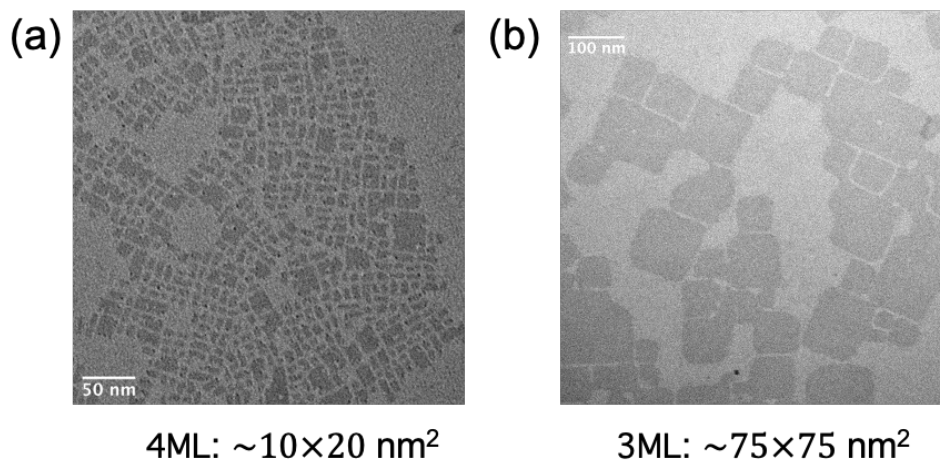


**Figure C.13.** TEM images of NPLs lateral size drop-casted on the day of TA measurement. (a) TEM image of 4ML NPLs. (b) TEM image of 3ML NPLs.

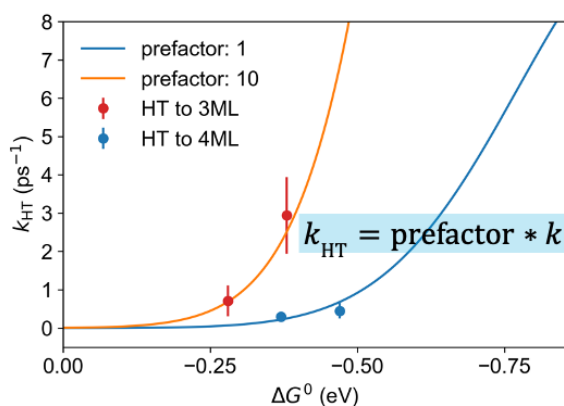


**Figure C.14.** An example of driving force dependence of hole transfer rate for different prefactors. Red and blue dots represent hole transfer rates obtained by kinetic fitting. The relative difference in the HT driving force was calculated based on the VB shift between 3ML and 4ML and the difference in HOMO between PDI and PMIDE. Due to the uncertainty of VB energy levels for NPLs, the absolute value of driving force is set arbitrarily with an upper limit of 0.8 eV. The values used:  $\hbar = 1 \text{ eV}$ ,  $H = 200 \text{ cm}^{-1}$ .

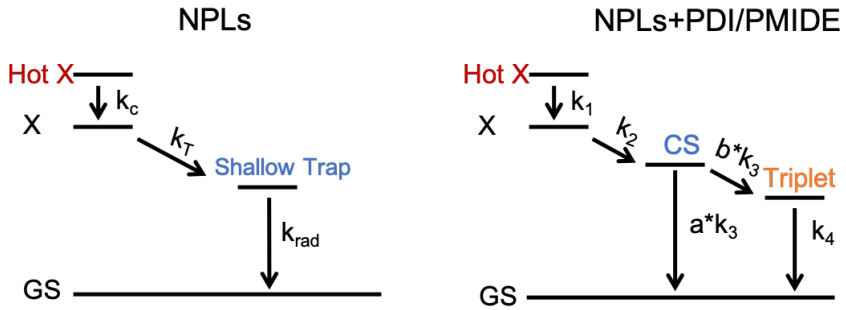


**Figure C.15.** Global and target analysis models.

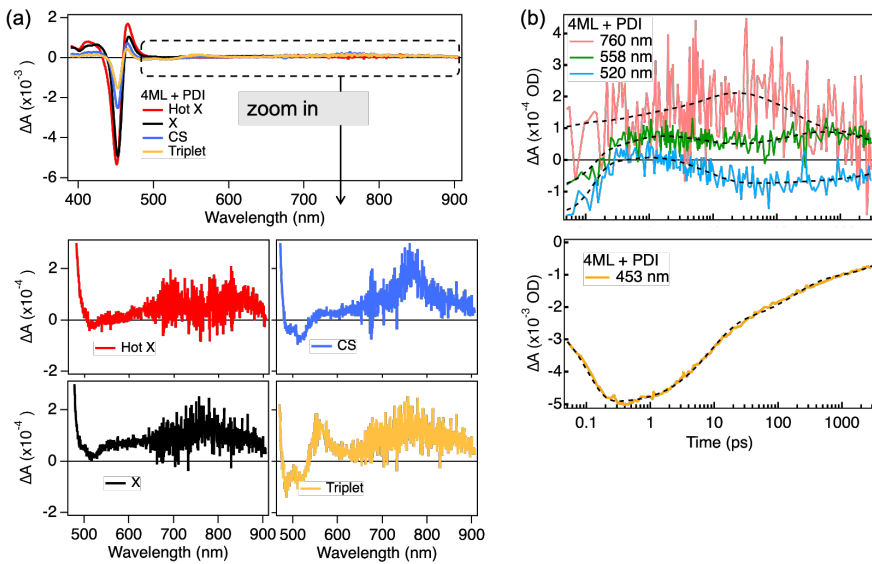
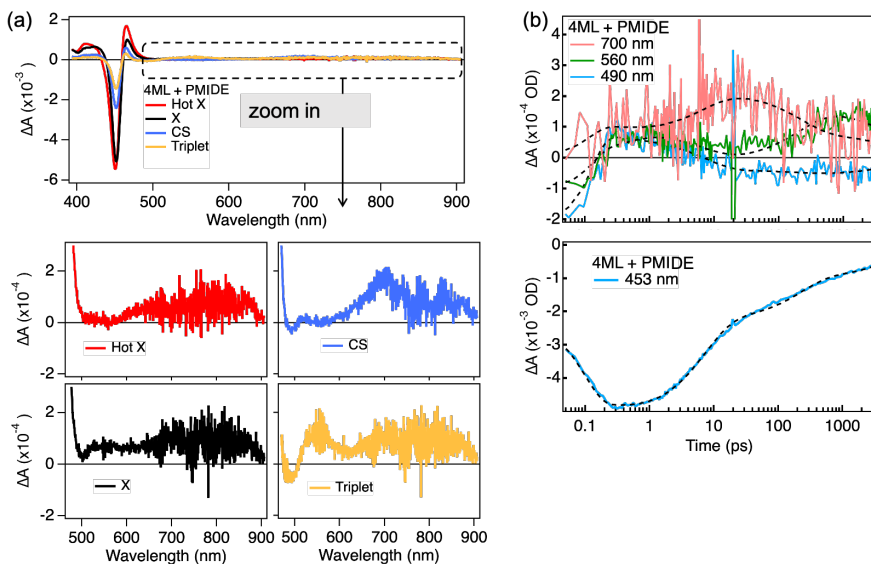


**Figure C.16.** Target analysis of TA spectra for 4ML + PDI excited at 380 nm. (a) Species-associated spectra (b) Temporal kinetics and fits at different wavelengths.



C

**Figure C.17.** Target analysis of TA spectra for 4ML + PMIDE excited at 380 nm. (a) Species-associated spectra (b) Temporal kinetics and fits at different wavelengths.

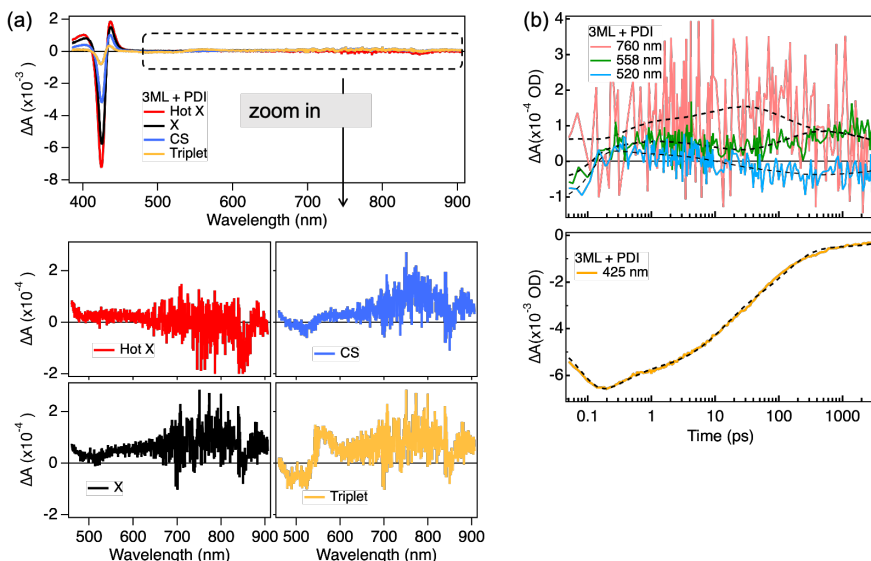


**Figure C.18.** Target analysis of TA spectra for 3ML + PDI excited at 380 nm. (a) Species-associated spectra (b) Temporal kinetics and fits at different wavelengths.



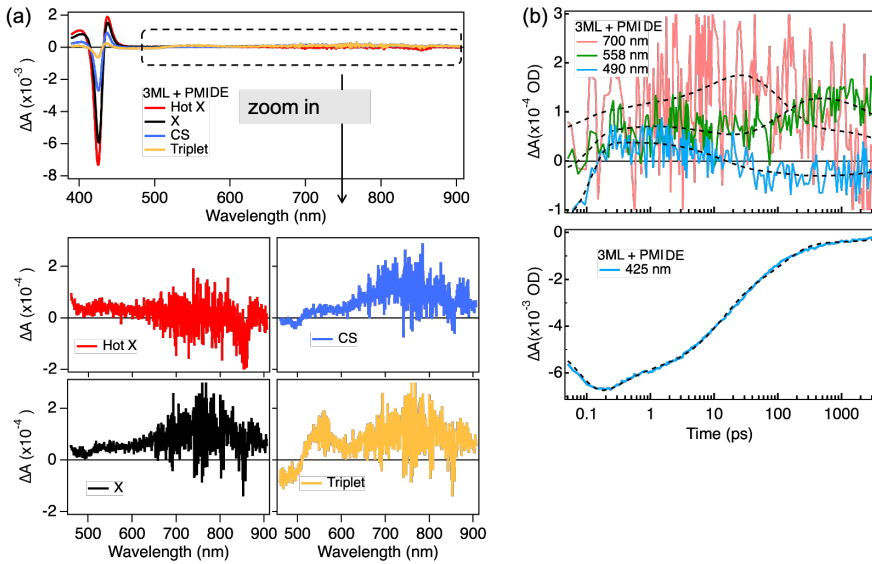


**Figure C.19.** Target analysis of TA spectra for 3ML + PMIDE excited at 380 nm. (a) Species-associated spectra (b) Temporal kinetics and fits at different wavelengths.

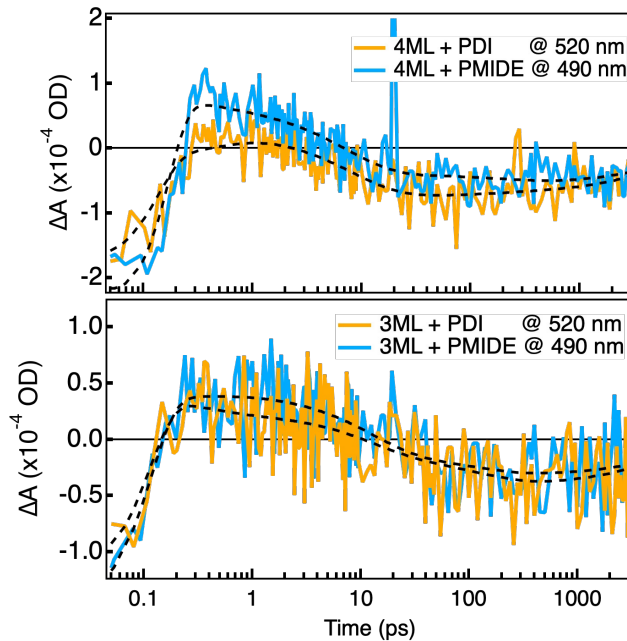


**Figure C.20.** Comparison of the GSB kinetics for PDI and PMIDE in hybrid systems.

## Synthesis of PMIDE

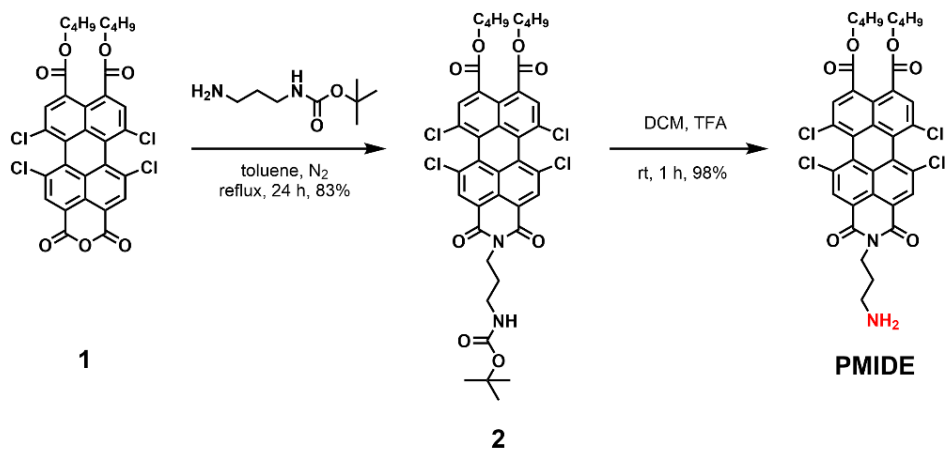


**Figure C.21.** Syntheses of PMIDE

Synthesis of N-(Boc-3-aminopropyl) -1,6,7,12-tetrachloroperylene -3,4,9,10-tetracarboxy monoimide dibutylester **2**:

A mixture of 1,6,7,12-tetrachloroperylene monoanhydride dibutylester[9] **1** (0.50 g, 0.76 mmol, 1 eq.) and N-Boc-1,3-propanediamine (0.40 g, 2.27 mmol, 3 eq.) was taken in a round-bottom flask (50 ml) equipped with a water condenser. To this mixture, toluene (14 ml) was added. The combined mixture was refluxed for 24 h under argon atmosphere and then cooled to room temperature. Toluene was evaporated under vacuum and the solid residue was washed with water and methanol. Subsequently, the solid residue was dried and chromatographed on silica, with  $\text{CH}_2\text{Cl}_2$  to afford the desired product (0.51 g, 83%) as an orange powder.  $^1\text{H}$  NMR (400 MHz,  $\text{CDCl}_3$ ):  $\delta$  = 8.62 (s, 2H), 8.12 (s, 2H), 5.14 (br s, 1H), 4.41-4.32 (m, 4H), 4.28 (t,  $J$  = 8.0 Hz, 2H), 3.23-3.11 (m, 2H), 1.97-1.89 (m, 2H), 1.80 (q,  $J$  = 8.0 Hz, 4H), 1.53-1.46 (m, 4H), 1.44 (s, 9H), 1.00 ppm (t,  $J$  = 8.0 Hz, 6H).  $^1\text{H}$  NMR spectrum of compound **2** in  $\text{CDCl}_3$  is shown below.

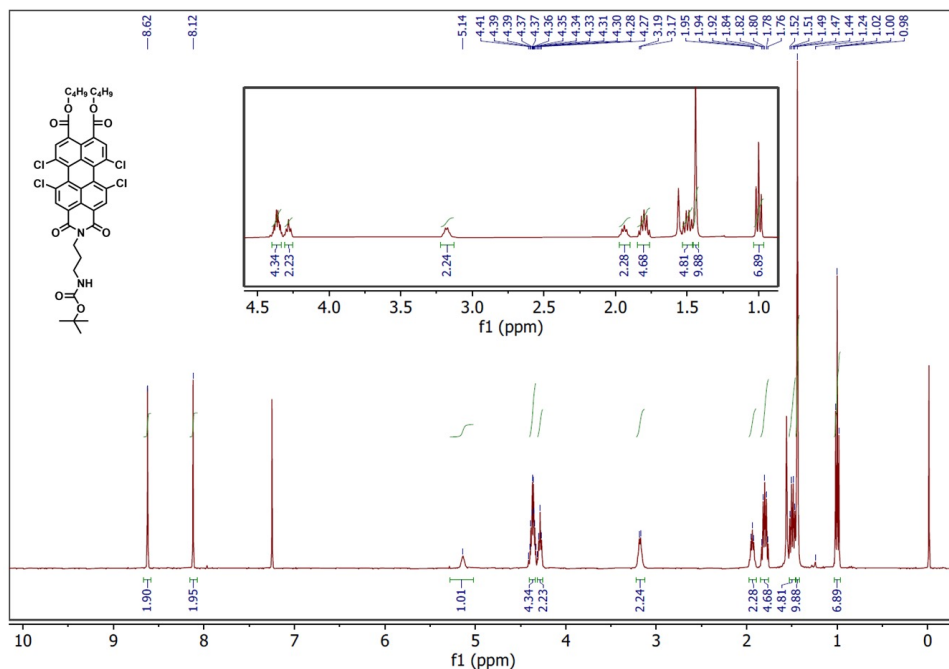


**Figure C.22.**  $^1\text{H}$  NMR spectrum of compound **2**

Synthesis of N-(3-aminopropyl)-1,6,7,12-tetrachloroperylene-3,4,9,10-tetracarboxy monoimide dibutylester (PMIDE):

Compound **2** (0.50 g, 0.61 mmol) was dissolved in DCM (10 mL) in a round-bottom flask (50 mL). Trifluoroacetic acid (3 mL) was added to this solution. The combined reaction mixture was stirred for 1 h at room temperature. The progress of the reaction was thoroughly followed by TLC analysis of removed aliquots (50:1 DCM-EtOH). After the complete consumption of the starting material, more DCM (50 mL) was added. The resultant solution was washed first with aqueous  $\text{K}_2\text{CO}_3$  and then with water. The organic phase was collected and concentrated. The crude product was then chromatographed on silica with 20:1 DCM-EtOH mixture to yield the pure product (0.43 g, 98%) as an orange powder.  $^1\text{H}$  NMR (400 MHz,  $\text{CDCl}_3$ ):  $\delta = 8.62$  (s, 2H), 8.12 (s, 2H), 4.43-4.25 (m, 6H), 2.80 (br s, 2H), 1.95-1.86 (m, 2H), 1.85-1.74 (q,  $J = 8.0$  Hz, 4H), 1.53-1.43 (m, 6H), 1.00 ppm (t,  $J = 8.0$  Hz, 6H).  $^1\text{H}$  NMR spectrum of compound PMIDE in  $\text{CDCl}_3$  is shown below (Note: the multiplet at ca. 1.5 ppm overlaps with the water peak.).

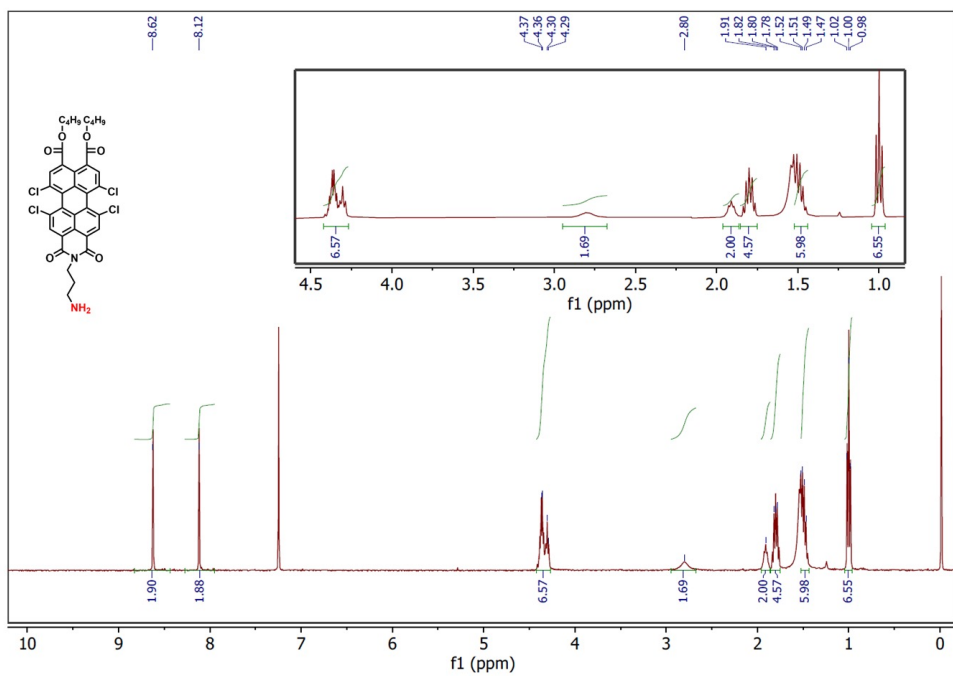


**Figure C.23.**  $^1\text{H}$  NMR spectrum of compound PMIDE in  $\text{CDCl}_3$

### Estimation of the exciton binding energy and difference in CT driving force

To have an approximate estimation of the exciton binding energy of NPLs, their absorption spectra in hexane were normalized and fitted with a quantum-well absorption model[10, 11], which has been widely used for extracting exciton binding energy in CsPbBr<sub>3</sub> NPLs[12–14]. According to this model, the absorption spectrum  $A(E)$  is described as a sum of the exciton peak absorption,  $X(E)$  and continuum band absorption  $Con(E)$ :

$$A(E) = X(E) + Con(E), \quad (C.1)$$

where

$$X(E) = \frac{1}{2\eta} \left[ \operatorname{erf} \left\{ \frac{E - E_0}{\gamma_x} - \frac{\gamma_x}{2\eta} \right\} \exp \left( \frac{\gamma^2}{4\eta^2} - \frac{E - E_0}{\eta} \right) \right], \quad (C.2)$$

and

$$Con(E) = \frac{H_c}{2} \left[ \operatorname{erf} \left\{ \frac{E - E_0 - E_b}{\gamma_c} \right\} + 1 \right]. \quad (C.3)$$

$E_0, E_b, \gamma_x, \gamma_c, \eta,$  and  $H_c$  represent absolute exciton energy, exciton binding energy, exciton peak width, continuum edge width, asymmetric broadening of exciton peak and the step height of continuum edge, respectively.

As shown in Figure C.12, the fitting results in the exciton binding energies of  $300 \pm 30$  meV for 4ML NPLs and  $320 \pm 20$  meV for 3ML NPLs, which agree with reported values ranging from 260 to 350 meV[13, 14].

With estimated exciton binding energies,  $E_b$ , and exciton energy,  $E_x$ , obtained from absorption spectra, the energy shift in VB and CB from 4ML to 3ML NPLs was calculated according to[15]:

$$\Delta E_{VB} = \frac{m_e}{m_e + m_h} [(E_{x,3ML} + E_{b,3ML}) - (E_{x,4ML} + E_{b,4ML})], \quad (C.4)$$

and

$$\Delta E_{CB} = \frac{m_h}{m_e + m_h} [(E_{x,3ML} + E_{b,3ML}) - (E_{x,4ML} + E_{b,4ML})], \quad (C.5)$$

where  $m_e$  and  $m_h$  represent the effective mass for electron and hole of CsPbBr<sub>3</sub> NPLs. Since similar effective mass has been reported for electron and hole of CsPbBr<sub>3</sub> NPLs regardless of their thickness[16]. The CB and VB shift from 4ML to 3ML is estimated to be the same at 95 meV.

### Estimation of the average number of molecules on each NPLs

It has been reported that at high photon energies, the intrinsic absorption coefficient of CsPbBr<sub>3</sub> nanocrystals is size-independent[17]. This means that based on the absorbance of NPLs at high photon energies, such as at 335 nm, the total volume of NPLs in a solution can be estimated. With the average lateral size and thickness of NPLs obtained from TEM measurements, the total number of 4ML NPLs is estimated to be 15 times larger than that of 3ML NPLs. Since both NPLs lead to similar PLQY for each acceptor molecule (Figure 5.2c and f), it is

reasonable to assume that the total amount of molecules attached is similar for both NPLs. Accordingly, the average number of molecules attached on 3ML NPLs should be 15 times larger than that of 4ML NPLs.

### Single-wavelength fitting for the growth of NPLs bleach excited at 490 nm

As the formation rate of the NPLs bleach directly represents the hole transfer rate, the dynamics at the wavelengths of the main exciton bleach for NPLs were fitted to extract the hole transfer rate. Specifically, the obtained dynamics are considered as a convolution of the real dynamics of the sample by the Instrument Response Function (IRF) of the setup. Hence, to extract the rates from the real dynamics, the TA data was fitted by an analytical form for the convolution of a function describing hole transfer by a function describing the IRF[18].

The IRF function was described by a Gaussian function:

$$IRF(t, t_0, \sigma) = e^{-\frac{(t-t_0)^2}{2\sigma^2}}. \quad (C.6)$$

The NPL growth was described by a step-function multiplied by an exponential ingrowth of a fraction of the signal:

$$NPL(t, t_0, \tau, f_a) = \vartheta(t, t_0) \left( 1 - f_a \cdot \exp\left(-\frac{t-t_0}{\tau}\right) \right), \quad (C.7)$$

where  $\vartheta$  is the Heaviside function and  $(1 - f_a)$  accounts for the initial signal at  $t_0$  due to coherent artifact (Figure C.7).

The convolution of these two functions yields:

$$F(t, t_0, \sigma, \tau, f_a, A) = \frac{A}{2} \left( 1 + \operatorname{erf}\left(\frac{t-t_0}{\sqrt{2}\sigma}\right) - f_a \cdot \exp\left(\frac{\sigma^2}{2\tau^2} - \frac{t-t_0}{\tau}\right) \cdot \left( 1 + \operatorname{erf}\left(\frac{t-t_0}{\sqrt{2}\sigma} - \frac{\sigma}{\sqrt{2}\tau}\right) \right) \right), \quad (C.8)$$

where  $A$  is a fitting parameter for normalizing the bleach amplitude.

### Global and Target analysis

The two-dimensional TA data were analyzed by global and target analysis using Glotaran[19]. With this method, the 2D data matrix,  $\Psi(\hat{\lambda}, t)$ , is modeled as a linear combination of  $n$  components given by the equation:

$$\Psi(\hat{\lambda}, t) = \sum_{l=1}^n c_l(t) \varepsilon_l(\hat{\lambda}). \quad (C.9)$$

Each component has its own spectrum,  $\varepsilon_l(\hat{\lambda})$ , that follows a certain concentration profile,  $c_l(t)$ . To be specific, with global analysis, a sequential kinetic model is used to describe the evolution of one component into the other with increasing time constants. In addition to the rate constants, each component is characterized by its own evolution associated difference spectrum

(EADS). Although the EADS may reflect mixtures of excited species due to the simplicity of the sequential model, the global analysis does provide important information on the temporal evolution of the system. For more complex systems, that follow non-sequential kinetics, the target analysis with a specific kinetic model was used. The resulting species associated difference spectra (SADS) should represent the true spectra of the individual excited species based on the used kinetic model.

#### Global analysis of CsPbBr<sub>3</sub> NPLs excited at 380 nm:

In order to adequately fit the excited state kinetics of CsPbBr<sub>3</sub> NPLs, a three-step sequential model was used (Figure C.15). Based on this model, upon photoexcitation above the band gap of NPLs, the hot exciton relaxes to form the band-edge exciton with a cooling rate constant,  $k_c$ . Subsequently, the short lifetime on the order of tens of picoseconds is assigned to the shallow trapping,  $k_T$ , followed by a longer lifetime of a few nanoseconds as the radiative recombination lifetime,  $k_{rad}$ . Fitting parameters are listed in Table C.1.

#### Target analysis of NPLs+PDI/PMIDE systems excited at 380 nm:

To model the excited state kinetics of the hybrid systems, we assume each NPL is attached with a PDI/PMIDE as the concentration of acceptor molecules is much higher than the concentration of NPLs. In order to keep the kinetic model as simple as possible, a four-step sequential model was first used: Hot X → X → CS state → triplet state → GS state. However, with this sequential model, the characteristics of PDI/PMIDE anion absorption were found in the decay-associated spectra of the triplet state. In order to obtain better species associated spectra of the triplet state, a branched model (target analysis) was used (Figure C.15). In this model, a small fraction of CS state is allowed to decay directly to the ground state without forming the triplet states. The spectra of the second and fourth species in the NIR region are forced to be the same, in order to reduce the contamination of anion absorption in the triplet spectra. Despite the difference in the global and target analysis models, the first (cooling of hot exciton) and second (formation of CS state) rate constants are very similar in both sequential and branched models. Note that the second rate constant ( $k_2$ ) will not only be influenced by the charge transfer rate but also, to some extent, by the fast trapping in the NPLs. In the case of energy transfer followed by the ultrafast hole transfer,  $k_2$  should reflect the total contribution of both processes. Fitting parameters are listed in Table C.2.

# 6

## Towards probing chirality-induced spin selectivity

*Chiral molecules, non-superimposable on their mirror images, are ubiquitous in biology. Spin, on the other hand, is an intrinsic property of the electron that is essential to the structure and function of matter. Recent discoveries have underpinned an intriguing relationship between chirality and spin orientation, termed chirality-induced spin selectivity (CISS). This phenomenon shows that the chirality of molecules can induce spin polarization in electrons propagated through the chiral system. Over the past decade, the CISS effect has rapidly garnered tremendous attention due to its significant importance in physics, chemistry and biology. However, a comprehensive understanding of this phenomenon still remains elusive. In this chapter, we explore the possibility to study the CISS effect using donor-(bridge)-acceptor systems, where spin polarization can be generated or detected using circularly polarized light.*



## 6.1. Introduction

The recently discovered chirality-induced spin selectivity (CISS) effect demonstrates that electrons transmitted through chiral molecules (or materials) can have a preferred spin orientation depending on the chirality of the molecule[1–3]. In a qualitative picture, the CISS effect can be viewed as an asymmetric electron scattering process in a chiral potential[4]. As an electron propagates along a chiral molecule, it experiences an effective magnetic field that stems from the symmetry breaking in the chiral molecule and leads to an energy splitting of the two spin states of the electron[3]. As a result, one spin state is more stabilized than the other one, giving rise to spin-polarized electrons after passing through a chiral structure.

Since the major breakthrough in 2011[5], CISS has been observed in a variety of chiral molecular systems, including double-stranded DNA[6–8], supramolecular assemblies[9, 10], helicene molecules[11, 12] and stereogenic molecules with no helicity[13]. This intriguing relationship between the chirality of a molecule and spin orientation opens new possibilities for manipulating electron spins in the absence of a magnetic field. It is particularly noteworthy that this effect has been repeatedly observed even at room temperature and ambient conditions. Hence, the CISS effect has profound implications for spintronics[14–16], enantiomer separations[17, 18] and biological functions[19].

While the importance of the CISS effect received unanimous recognition within the scientific community, its exact origin remains highly debated. This primarily arises from the lack of a unifying mechanism that can quantify the relation between various molecular and environmental parameters and the observed CISS effect. The theoretical efforts to establish such a framework are confounded by the plethora of parameters potentially influencing experimental observables, making it difficult to disentangle their individual contributions. Therefore, a deeper understanding of CISS pivots on systematic investigations that can isolate and identify specific influences.

Hitherto, to validate CISS experimentally, one can either directly measure the spin polarization of electrons transmitted through chiral molecules or demonstrate how the chirality determines spin-dependent observables. The former typically refers to the photoemission studies, where a Mott detector is used to explicitly measure the spin orientation of photoelectrons transmitted from a metal substrate through monolayers of chiral molecules[5, 11, 20]. As demonstrated by Göhler *et al* [5], unpolarized electrons ejected from the gold substrate with linearly polarized light become spin-polarized after transmitted through monolayers of double-stranded DNA, yielding an impressive spin polarization close to 60%. Following this pioneering work, many different experimental configurations emerged, mostly demonstrating CISS based on the second concept of measuring spin-dependent observables. Typical examples include magnetic conductive atomic force microscopy[21, 22], magnetoresistance[23, 24], and electrochemistry[25, 26]. In most of these experiments, ferromagnetic substrates or electrodes are used, in order to generate or detect spin-polarized electrons. Consequently, magnetic exchange

interactions may significantly influence the molecular response[27, 28], obscuring the effects solely from the chirality. In addition, the effect arising from the molecule–electrode interface may also contribute to experimental observables, as many experiments require contacting of chiral molecules to metallic electrodes or substrates, often with large spin-orbit coupling[13, 29].

Alternatively, using circularly polarized light (CPL) to generate or detect the spin polarization allows us to study spin-dependent electron transfer in an electrodeless way. This optical approach fundamentally precludes certain possible contributions to the size of CISS effect and effectively circumvents certain limitations, such as the requirement of a broken time-reversal symmetry[30–32]. An interesting example is spin-dependent electron transfer in DBA assemblies based on quantum dots (QDs) linked with chiral ligands[33]. In this study, Bloom *et al* used CPL to generate a spin-polarized excited state in an achiral CdTe QD. The subsequent electron transfer to the CdSe QD capped with L- or D- cysteine ligands exhibited different lifetimes by changing the incident light between left- and right-handed circular polarization. They interpreted this handedness-dependent electron transfer as a result of CISS in photoinduced electron transfer. Furthermore, they claimed that the coherence of the spin-polarized excited state in CdTe QDs survived the electron transfer lifetime, which was quantified to be on the order of a few hundred picoseconds. Nonetheless, they indirectly observed the lifetime of electron transfer by monitoring the photoluminescence decay of CdTe QDs, i.e. no direct confirmation of charge separation, for instance, no transient absorption (TA) measurement was given. Therefore, in this work, we aim to use circularly polarized TA to study photoinduced charge transfer in a chiral DBA or DA system, where spin polarization can be generated or detected with CPL.

In this chapter, we present the current progress and propose an experimental design for further studies to advance our understanding of CISS. In Section 6.2, we first introduce the basic working principles underlying the spin injection using CPL. Subsequently, we analyze the results of optical spin injection in three system candidates: chiral DBA molecule, perovskite thin film and perovskite nanoplatelets. Based on these results, we propose the design of a chiral DA system in Section 6.3 and discuss how this system can be used for optically probing CISS in an electrodeless way. Finally, we address the potential challenges associated with implementing the proposed experiment and outline additional measurements to further elucidate the outcomes.

## 6.2. Optical spin injection

The process to generate spin polarization using CPL is called "optical spin injection", also known as "optical spin orientation". In this process, the angular momentum of an absorbed circularly polarized photon is transferred to the material, leading to spin polarization. In this section, the working principle of optical spin injection will be explained, followed by the results and discussion on generating spin-polarization using CPL in three materials.

### 6.2.1. Working principle

To explain how optical spin injection works, we start from the concept of total angular momentum and how it depends on the spin-orbit coupling (SOC). For an electron orbiting around an atom, it has orbital angular momentum,  $\mathbf{L}$ , and spin angular momentum,  $\mathbf{S}$ . And the sum of the two is its total angular momentum,  $\mathbf{J}$ , where  $\mathbf{J} = \mathbf{L} + \mathbf{S}$ . In the presence of strong SOC,  $\mathbf{L}$  and  $\mathbf{S}$  will undergo a precessional motion, meaning the orientation of each depends on the orientation of the other. As a result, their sum,  $\mathbf{J}$ , is moving around a z-axis with a fixed magnitude  $J$  and a fixed component  $J_z$  projected on the z-axis. Furthermore,  $J$  and  $J_z$  are typically specified by the total angular momentum quantum number,  $j$ , and the total magnetic quantum number,  $m_j$ , respectively. Analogously, the z-components of  $l$  and  $s$  are specified by magnetic quantum number,  $m_l$ , and spin magnetic quantum number,  $m_s$ , respectively. Regardless of the SOC,  $m_j = m_l + m_s$  will hold. Figure 6.1a illustrates an example of a state with an orbital angular momentum quantum number  $l = 2$ , a total angular momentum quantum number  $j = 5/2$ , and a total magnetic quantum number  $m_j = 3/2$ .

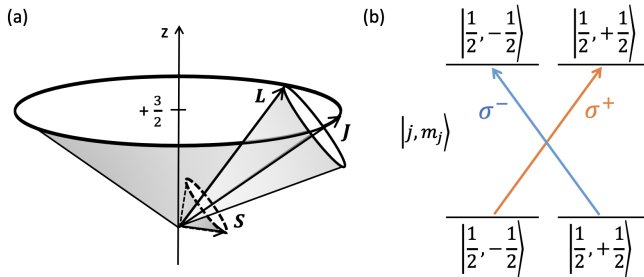


**Figure 6.1.** (a) Schematic illustration of angular momentum vectors  $\mathbf{L}$ ,  $\mathbf{S}$ , and  $\mathbf{J}$  for a state with  $l=2$ ,  $j=5/2$ ,  $m_j=3/2$ . (b) Principle of optical spin injection.

According to the conservation of total angular momentum, the absorption of a left ( $\sigma^+$ ) or a right ( $\sigma^-$ ) circularly polarized photon along the z-axis will raise or lower  $m_j$  by 1. Hence, as shown in Figure 6.1b, the absorption of a  $\sigma^+$  photon can excite an electron from spin-down ( $m_s = -1/2$ ) to spin-up ( $m_s = +1/2$ ) and vice versa. A prerequisite for this to happen is the presence of SOC. In this case, the selective excitation of one spin-state only works when  $m_j$  equals  $m_s$ , meaning  $m_l$

is zero in both initial and final states. Note that such a transition still follows the optical selection rule, such as a transition from  $m_l = 0, l = 0$  to  $m_l = 0, l = 1$ . Given the possible values of  $m_l$  in a degenerate state of  $l = 1$  can be  $-1, 0, 1$ , there is a theoretical limit to the spin polarization that can be generated by optical spin injection. This limit further depends on the probability of the involved optical transitions. Consequently, the efficiency of optical spin injection significantly depends on the photon energy, as it determines which states are accessible and which transitions will be involved.

### 6.2.2. Chiral donor–bridge–acceptor molecule

The initial idea was to study spin-dependent charge transfer in a donor–bridge–acceptor system with a chiral bridge. Specifically, by selectively exciting the electron donor (acceptor) with CPL, the electron (hole) transfer with a well-defined spin orientation is triggered. Thus, when the bridge is chiral, the CISS effect should favor the transfer of one spin over the other.

To this purpose, Abbey Philip has synthesized a DBA molecule with (S)-2,2'-Dimethyl-1,1'-binaphthyl as a chiral bridge. The synthetic route of this molecule is provided in Figure D.1. As shown in Figure 6.2a, the electron donor and acceptor connected to the chiral binaphthyl bridge are dimethylaniline (DMA) and perylenemonoimide (PMI), respectively. The chirality of this molecule can be confirmed by its circular dichroism spectrum (Figure 6.2b), where the optical activity is preserved at the wavelength corresponding to the bridge absorption at around 300 nm (Figure D.2).

Once the chirality of the molecule is confirmed, the next step is to initialize the spin-dependent charge transfer in the molecule, which firstly requires the generation of a spin-polarized excited state. Therefore, we have further investigated the possibility of generating a spin-polarized excited state in this system using circularly polarized pump–probe spectroscopy.

In principle, for a material allowing optical spin injection, the generated spin-polarized excited state should be detectable via the same optical selection rule. As a result, different absorption features may be observed for different pump–probe configurations. However, the normalized TA spectra of different pump–probe configurations share the same spectral shape as shown by the overlaid TA spectra at 0.4 ps in Figure 6.2c. This overlap in the spectral shape is observed throughout the entire time window of TA measurement (Figure D.3), showing no sign of the presence of spin-polarized excited state or spin-dependent dynamics. On the other hand, upon spin-selective excitation with a  $\sigma^+$  pump, a large ground-state bleach (GSB) followed by a rapid bleach recovery is expected for the  $|+1\rangle$  excited state probed by a  $\sigma^+$  photon, while a bleach formation is expected for  $\sigma^-$  probe due to the spin relaxation of the excited state. Once again, the same GSB kinetics was obtained for different pump–probe configurations Figure 6.2d, suggesting that the optical spin injection in this system is too inefficient to be detectable.

Although the failure to observe optical spin injection in this DBA molecule can be associated with several reasons, the main reason is likely to be its weak SOC

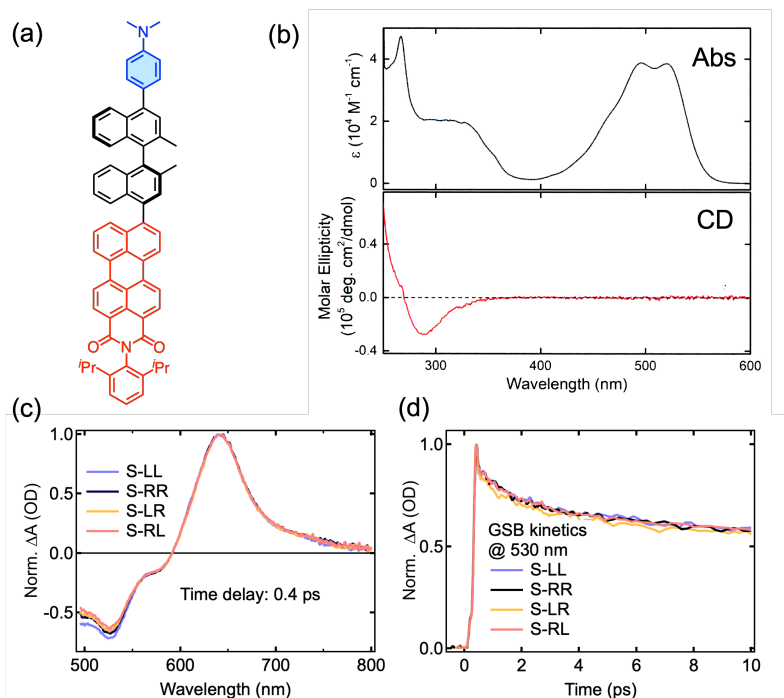


**Figure 6.2.** (a) Molecular structure of a chiral DBA molecule with a chiral bridge: (S)-2,2'-Dimethyl-1,1'-binaphthyl. (b) Absorption spectrum and circular dichroism spectrum of this molecule. (c) Normalized TA spectra at time delay of 2 ps for different pump and probe polarization. (d) Normalized TA kinetics at 530 nm (GSB) for different pump and probe polarization. LL: left pump + left probe; RR: right pump + right probe; LR: left pump + right probe; RL: right pump + left probe. All optical measurements were performed in chloroform.

strength. In general, the SOC strength is proportional to the fourth-power of the atomic number of the elements in the system[34]. Thus, an organic molecule consisting of light elements in the second row of the periodic table (i.e. C, H, O, N) typically possesses very weak SOC strength. Although a weak SOC strength can be beneficial for improving spin lifetime, it also directly limits the angular momentum transfer from the absorbed circularly polarized photon to the electron spin, thereby suppressing the optical spin injection[35].

Since the generation of a spin-polarized excited state in the DBA molecule is not possible by exciting with CPL, no difference in the CT rate is found between chiral and racemic DBA molecules as expected (Figure D.4). Therefore, it can be concluded that this DBA system is not suitable for testing the CISS effect on electron transfer using circularly polarized pump-probe spectroscopy.

### 6.2.3. Bulk perovskite thin film

The possibility of generating a spin-polarized excited state via optical spin injection was further explored in metal halide perovskite thin film, a family of semiconductors well-known for its strong SOC strength due to the presence of heavy atoms[36, 37]. The spin-coated  $\text{CH}_3\text{NH}_3\text{PbBr}_3$  thin film studied in this section was provided by Jiashang Zhao. Details regarding sample preparation and characterization can be found in ref [38].

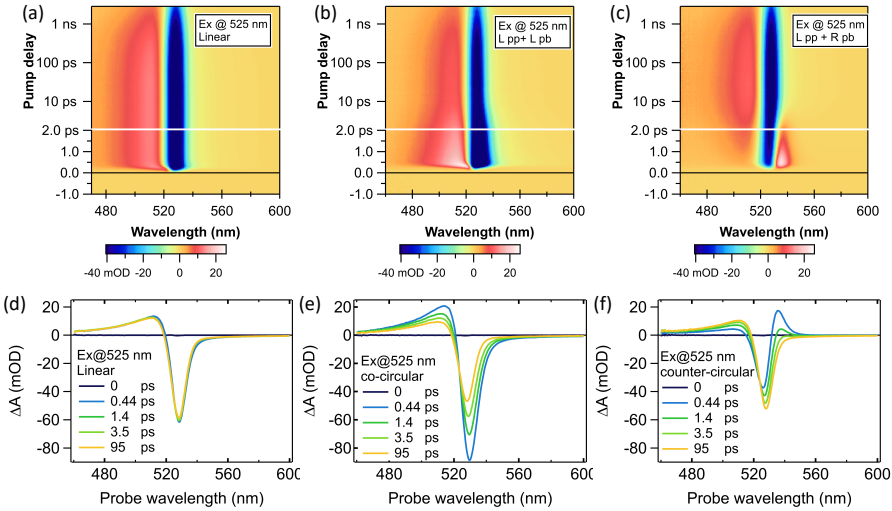


**Figure 6.3.** Upper part: 2D contour plots of TA spectra for  $\text{CH}_3\text{NH}_3\text{PbBr}_3$  thin film excited at 525 nm with (a) linearly polarized light, (b) Left circularly polarized pump and left circularly polarized probe, and (c) Left circularly polarized pump and right circularly polarized probe. Lower part: Corresponding TA spectra with (d) linearly polarized light, (e) co-circularly polarized pump and probe, and (f) counter-circularly polarized pump and probe.

Figure 6.3 displays the TA spectra of  $\text{CH}_3\text{NH}_3\text{PbBr}_3$  thin film measured with different pump-probe configurations. To maximize the effect of optical spin injection, the pump wavelength is set at 525 nm, resonant with the band edge exciton peak. For linearly polarized pump and probe beams (Figure 6.3a and Figure 6.3d), the TA spectra contains an exciton bleach at  $\sim 528$  nm and an induced absorption between 460 nm and 520 nm. Although the origin of the bleach has been unanimously assigned to the band-edge filling by photogenerated excitons, the origin of the induced absorption can be disputed. The most intuitive explanation would be the excited state absorption to higher lying states[39, 40], while the photoinduced changes in the refractive index has also been proposed to be the main contributor[41–44]. Nevertheless, it is clear that this induced absorption feature is associated with the band-edge excitons, as both absorption and bleach features show very similar lifetimes.

Upon photoexcitation with the CPL, the TA spectra on the long timescale are the same regardless of light polarization, as demonstrated by the complete overlap for normalized TA spectra at 95 ps in [Figure D.5](#). However, on the short timescale ( $t < 10$  ps), the TA spectra vary dramatically depending on the handedness of the circularly polarized pump and probe, indicating the success of spin-selective excitation. As shown in [Figure 6.3b](#) and [Figure 6.3e](#), when the pump and probe are circularly polarized with same handedness (co-circular), the formation of the photoinduced bleach is accompanied by an induced absorption feature at shorter wavelengths. This is similar to the spectral features obtained with linearly polarized light. Noticeably, both bleach and absorption are slightly red-shifted and show much larger amplitude than those from the linear TA measurement. For counter-circularly polarized pump and probe ([Figure 6.3c](#) and [Figure 6.3f](#)), the initial amplitude of the photoinduced bleach becomes much smaller, accompanied by a blue-shift in the peak wavelength. Concurrently, there is a reduction in the amplitude of the induced absorption at shorter wavelengths. In addition to these two spectral changes, a new absorption feature emerges, showing a pronounced positive signal peaked at  $\sim 535$  nm.

Although similar TA features have been reported for bulk perovskite thin films measured by circularly polarized transient absorption[45–47], different mechanisms also have been proposed to describe the origin of polarization-dependent TA features. For instance, Giovanni *et al* proposed a model, where the optical transitions involving different spin-polarized excited states result in absorption at different wavelengths [46]. To be specific, if a left circularly polarized ( $\sigma^+$ ) pump photon only populates the  $|+1\rangle$  excited state according to the conservation of total angular momentum, this  $|+1\rangle$  excited state should further absorb a left circularly polarized ( $\sigma^+$ ) probe photon to the  $|+2\rangle$  state or a right circularly polarized ( $\sigma^-$ ) probe photon to the  $|0\rangle$  state, leading to different absorption features for different pump-probe configurations. Later, Bourelle *et al* proposed that the different TA features with co-circular and counter-circular configurations are associated with a blue-shift and a red-shift in the absorption after optical excitation, respectively [47]. This spectral shift has been attributed to the shift in the exciton levels as a result of interactions between photogenerated excitons.

Fortunately, regardless of the origin of induced absorption, the decay in the spectral difference unambiguously reflects the spin relaxation process. This is particularly clear at the wavelength of exciton bleach. As illustrated in [Figure 6.4a](#), in the ideal case of an optical spin injection with 100% efficiency, the populated  $|+1\rangle$  state by  $\sigma^+$  pump will lead to a strong bleach signal for the  $\sigma^+$  probe due to state-filling. On the other hand, the unpopulated  $|-1\rangle$  state can still absorb  $\sigma^+$  probe, leading to the absence of a bleach signal. When the spin flips, the  $|+1\rangle$  state relaxes to be the  $|-1\rangle$  state. And this will simultaneously lead to a decay of the  $\sigma^+$  bleach and a formation of the  $\sigma^-$  bleach. Finally, TA signals for different configurations merge together, meaning the spin polarization is completely relaxed in the system. [Figure 6.4b](#) shows the photogenerated excitons are no longer spin-polarized after 15 ps, similar to reported timescales

for  $\text{CH}_3\text{NH}_3\text{PbBr}_3$  thin films at room temperature[48, 49].

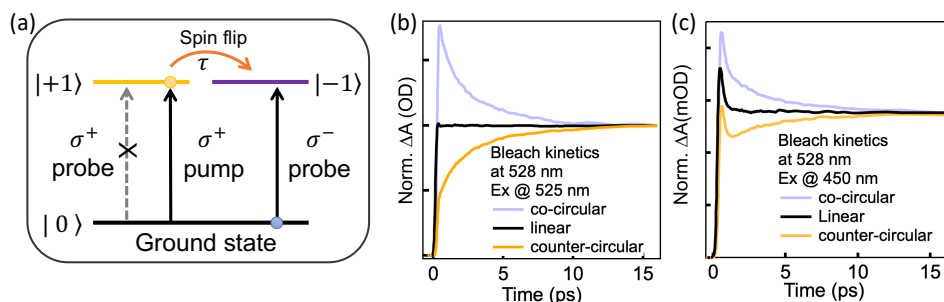


**Figure 6.4.** (a) Optical spin dynamics in a  $\text{CH}_3\text{NH}_3\text{PbBr}_3$  thin film measured by circularly polarized pump–probe spectroscopy. (b) Principle of spin relaxation measurements using circularly polarized pump–probe spectroscopy.

Interestingly, the optical spin injection also works with photoexcitation above the exciton peak at 450 nm, as evident in Figure D.6. As compared to the TA spectra excited at the exciton peak, additional features can be observed due to the presence of hot carriers. The cooling process of hot carriers is captured by the ultrafast decay within 1 ps in the bleach kinetics (Figure 6.4c). Notably, the spin-dependent TA features become less prominent with off-resonant excitation, as demonstrated by the smaller difference between co-circular and counter-circular configurations. This has been ascribed to the spin relaxation due to efficient carrier-phonon and carrier-carrier scattering during cooling of the hot carriers cooling by Zhao *et al*[45]. Hence, some charge carriers lose their spin polarization before forming excitons. Nonetheless, it should be noted that photoexcitation above the bandgap involves interband transitions beyond the band edge[50], possibly leading to less efficient spin selectivity to begin with. Remarkably, following the cooling of the hot carriers, the spin polarization lifetime of the excitons is almost the same (possibly even longer, see in Figure D.7) as compared to those excited at the exciton peak. Therefore, photoexcitation above the bandgap will reduce the efficiency of optical spin injection, while leaving the spin lifetime of excitons intact.

Given the successful optical spin injection in perovskite thin film, one can imagine using it as a source of spin-polarized charges to test the CISS process by studying the spin-dependent charge transport through or to a chiral transport layer. This would be a feasible idea only if the charge extraction rate can compete with the spin relaxation rate. Unfortunately, this is difficult to achieve in a bulk thin film considering that the charge carriers need to diffuse to the interface before they can be injected into the transport layer. This idea has been tested by measuring charge extraction from the  $\text{CH}_3\text{NH}_3\text{PbBr}_3$  thin film to a hole transport layer by circularly polarized TA. Indeed, the spin polarization has fully relaxed long before the charge extraction starts (Figure D.8). Surprisingly, alternative examples of CISS-based spin-polarized charge injection from a 2D



chiral perovskite layer have been reported. For instance, the spin-polarized carriers were claimed to be injected from a 200 nm-thick (S-MBA)<sub>2</sub>PbI<sub>4</sub> perovskite layer to a monolayer of WSe<sub>2</sub>[51]. As a result, circular polarization with a degree of 13% was observed in the light emission. Similarly, strong circularly polarized photoluminescence was reported for CdSe/ZnS QDs interfaced with a 2D chiral perovskite layer[52]. These results indicate that the lifetime of injected spin polarization is longer or at least comparable with the lifetime of radiative recombination. However, we should note that these studies were mainly based on the PL measurement. Therefore, there was no direct observation of spin-polarized carriers with circularly polarized TA measurement.

### 6.2.4. Perovskite nanoplatelets

As demonstrated in the Chapter 5, the photoinduced charge transfer between perovskite nanoplatelets (NPLs) and surface-anchored electron acceptors takes place on the picosecond time scale. Such fast charge transfer rates make this model system promising for studying spin-dependent charge transfer. Hence, the optical spin injection in CsPbBr<sub>3</sub> perovskite NPLs (4ML, thickness~2.4 nm) was further studied, and the results will be discussed in this section. CsPbBr<sub>3</sub> perovskite NPLs were synthesized using the same method as described in the Chapter 5.

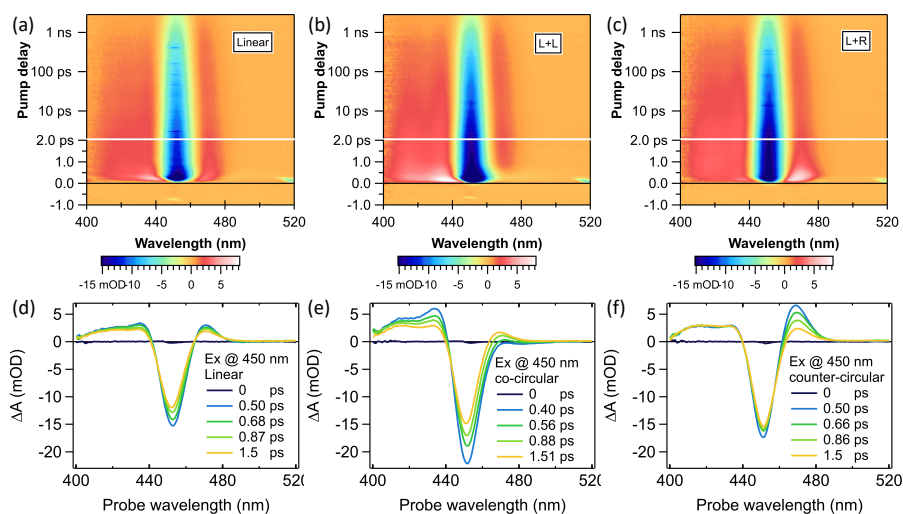


**Figure 6.5.** Upper part: 2D contour plots of TA spectra for CsPbBr<sub>3</sub> nanoplatelets in hexane excited at 450 nm with (a) linearly polarized light, (b) left circularly polarized pump and left circularly polarized probe, and (c) left circularly polarized pump and right circularly polarized probe. Lower part: Corresponding TA spectra for CsPbBr<sub>3</sub> nanoplatelets with (d) linearly polarized light, (e) co-circularly polarized pump and probe, and (f) counter-circularly polarized pump and probe.

Figure 6.5 shows the TA spectra of CsPbBr<sub>3</sub> NPLs in hexane measured with different pump-probe configurations. To ensure the efficiency of optical spin injection, the samples were excited at the exciton peak (450 nm). With linear polarization (Figure 6.5a and Figure 6.5d), the typical TA features of CsPbBr<sub>3</sub> NPLs were obtained, namely a strong exciton bleach at ~450 nm and two positive shoulders on the red and blue sides of the bleach. Although the bleach clearly stems from the band-edge filling by the photogenerated excitons similar to the bulk perovskite films, the refractive index change on the surface of the films cannot be responsible for the observed blue-side absorption in solution. Rossi *et al* have observed a similar absorption feature in perovskite QDs and assigned this absorption to exciton-activated forbidden transitions in strongly quantum confined perovskite nanostructures[53]. Recently, Villamil Franco *et al* have rationalized this signal in terms of exciton-induced stark effect in perovskite NPLs, where the probed optical transitions shift in energy due to local fields originating from the presence of photogenerated excitons[54].

With CPL, spin-dependent TA signals were obtained (Figure 6.5b-c and Figure 6.5e-f). Similar to the bulk perovskite films, the co-circular TA spectra of perovskite NPLs show a pronounced exciton bleach and strong high-energy absorption. The induced absorption at lower energies becomes weaker than that obtained with linear configuration. On the other hand, the counter-circular TA spectra show a strong positive signal at the low-energy side (~470 nm). Similar low-energy absorption for counter-circular polarization has also been observed for CsPbBr<sub>3</sub> and CsPbI<sub>3</sub> QDs, where this feature was explained by a red-shift due to a biexciton interaction between the exciton generated by the  $\sigma^+$  ( $\sigma^-$ ) pump and the exciton measured by the  $\sigma^-$  ( $\sigma^+$ ) probe[55].

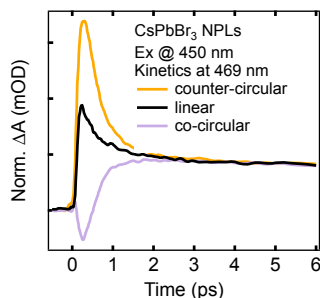


**Figure 6.6.** Optical spin dynamics in CsPbBr<sub>3</sub> NPLs (4ML) dispersed in hexane measured by circularly polarized pump-probe spectroscopy.

Notably, the spin relaxation is much faster in perovskite NPLs as compared to that in the bulk perovskite film. As illustrated by the kinetics at a probe wavelength of 469 nm in Figure 6.6, spin-dependent TA features disappear after 2 ps. This is understandable as different mechanisms will prevail at bulk and nanometer scales. In comparison with their bulk counterparts, the quantum confinement in nanostructures may suppress the carrier-phonon scattering (the

Elloitt–Yafet mechanism)[49]. On the other hand, a much smaller volume and much larger surface-to-volume ratio could open additional spin relaxation pathways, such as electron-hole exchange interaction[56] and surface effects[55, 57]. The short spin lifetime obtained in CsPbBr<sub>3</sub> NPLs is consistent with reported results in CsPbBr<sub>3</sub> QDs, where the polarization-dependent TA signals merge together within 5 ps[55]. Although the optical spin lifetime of perovskite nanocrystals has been reported to increase with increasing size due to a smaller surface-to-volume ratio, this improvement is limited as listed in Table D.1. This improvement can be further enhanced by replacing Br with I, however, the underlying reason is unclear. Strikingly, the game changing strategy turns out to be suppressing the SOC strength. This is evident from the spin-dependent TA signals in CsSnBr<sub>3</sub> nanocrystals, which can last more than 30 ps[58].

## 6.3. Experiment design

### 6.3.1. System design

Despite the relatively short spin lifetime in perovskite NPLs, they present a promising opportunity for detecting spin-polarized charges using CPL. Additionally, chirality can be introduced to these perovskite NPLs through a phenomenon known as "chirality transfer" or "chiral imprinting." As a result, they are highly promising candidates for developing a system to test the CISS effect. In this section, we will explore the concept of chirality transfer and propose a system design based on chiral perovskite NPLs for testing the CISS effect. Furthermore, we will address the potential challenges that may arise during the implementation of this proposal.

#### Chirality transfer

Chirality transfer refers to the process of transferring the optical activity from a chiral species to an initially achiral species, resulting in chiroptical properties in the latter. In 2007, Molone *et al* reported the first work on chirality transfer from chiral surface ligands (D-/L- penicillamine) to CdS QDs[59], leading to strong circular dichroism in semiconductor nanoparticles. Since then, considerable efforts have been made to further explore and understand chiral semiconductor nanoparticles[60–62].

Recently, the growing interest in metal halide perovskite has fueled numerous chiroptical studies on chiral perovskite nanoparticles, with a number of reports emerging since 2017[63–70]. Typically, the chiral perovskite nanoparticles can be prepared by direct synthesis with chiral ligands[64–68] or by post-synthetic ligand exchange with chiral molecules[63, 66]. Furthermore, they have demonstrated remarkable chiroptical properties, such as strong circular dichroism in atomically thin chiral lead bromide NPLs[68] and high circularly polarized luminescence in chiral FAPbBr<sub>3</sub> nanocrystals[66].

Although our understanding of the origin of chirality transfer is still in its nascent stage, considerable progress has been made in exploring several

determining parameters and studying the underlying mechanisms. In the context of chiral semiconductor nanoparticles, their chiroptical properties can be influenced by various factors, including the size, shape, composition and surface ligands[62, 71]. For instance, it has been reported that the optical activity increases dramatically with the shape change from spherical QDs to 1D nanorods and then to 2D NPLs[61, 72]. Regarding the origin of chirality transfer, two mechanisms have been proposed to rationalize the ligand-induced chirality in perovskite nanoparticles. One is the surface-lattice distortion of inorganic nanoparticles introduced by the chiral ligands[64, 70], and the other one is the electrostatic perturbation of the surface ligands to the wavefunction of the perovskite nanoparticles[65, 67]. Accordingly, it should be possible to systematically tune the chirality of the perovskite nanoparticles, for instance by varying the surface-to-volume ratio and the density of the chiral ligands.

#### Perovskite nanoplatelets + chiral functional chromophores

Given the exciting possibility to detect spin polarization optically and to introduce chirality in perovskite NPLs, they can be further used for studying the CISS effect. Specifically, we can study the photoinduced charge transfer in a chiral D(B)A system and determine whether initially unpolarized charges become spin-polarized depending on the chirality of the system. Inspired by the hybrid system in Chapter 5, we propose a chiral DA system where chiral PDI molecules are attached to the surface of 2D perovskite NPLs (Figure 6.7).

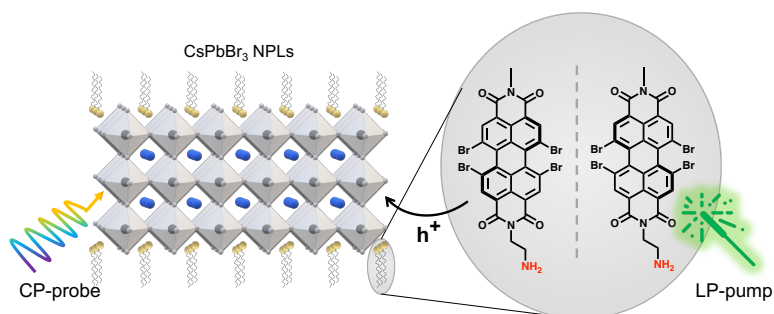


**Figure 6.7.** Proposed chiral hybrid system for testing the CISS effect. The chirality of the PDI molecules arises from its twisted perylene core due to tetrahalogen substituents in the bay area. LP-pump: linearly polarized pump; CP-probe: circularly polarized probe.

The entire hybrid system is anticipated to be chiral due to chirality transfer from chiral PDI molecules to the perovskite NPLs. Upon selectively exciting the PDI molecules, we can study the photoinduced charge transfer from the HOMO of the acceptor molecules to the VB of the NPLs can be monitored by the formation of NPLs bleach in the TA spectra. When the PDI molecules are excited with linearly polarized light, the initial excited state generated by photoexcitation will not be spin-polarized. If the chirality of the system induces selectivity of different spin

states, the transferred charges will become spin-polarized. Furthermore, considering the efficient angular momentum transfer between the electron spin and circularly polarized photons in the perovskite NPLs, spin-polarized charges in NPLs should be detectable in the TA spectra with a circularly polarized probe (Section 6.2.4).

This approach is promising to provide valuable insight into the CISS effect for four reasons. Firstly, by using CPL to measure the spin polarization of charges transferred through a chiral system, it can directly verify the existence of the CISS effect in a microscopic system without the need for metal substances or magnetic fields. Secondly, this approach circumvents the short spin lifetime in perovskite NPLs while capitalizing on their capability for detecting spin polarization using CPL. Thirdly, utilizing chirality transfer offers a favorable strategy to extend the chirality from chiral molecules to perovskite NPLs, enabling further modulation of the degree of chirality within the system. Finally, this platform allows facile tunability of molecular parameters intimately associated with the CISS effect, such as SOC. By substituting the composition in either perovskite NPLs or chiral PDI molecules, the SOC strength in this hybrid system can be systematically varied.

Alternatively, it is equally interesting to study the photoinduced charge transfer by selectively exciting the NPLs with CPL. In this way, the efficient optical spin injection will initiate a spin-dependent charge transfer. A correlation between the charge transfer rate and handedness of the incident light may be observed, analogous to the work of Bloom *et al*[33].

### Potential challenges

The first big challenge is to acquire the chiral PDI molecules. In principle, this can be accomplished by synthesizing racemic mixtures of the target molecule and subsequently separating the enantiomers. The latter is typically achieved using chiral chromatography, where enantiomers interact differently with the chiral stationary phase and are subsequently separated as they pass through the column. Unfortunately, predicting the chiral interaction that plays a crucial role in the separation of enantiomers is challenging. To alleviate this problem, the current molecular design has already taken into account some factors that can potentially hamper this chiral interaction. For instance, a methyl group is designed at the imide position instead of a typically used diisopropylphenyl group, as the latter may be too bulky to enable effective interaction between the chiral column and the twisted perylene core.

However, obtaining the chiral PDI molecules may still prove to be a difficult task for several reasons. Firstly, the problem may arise from the ethylamine group that is necessary as an anchoring group. When the column interaction with the amine group is stronger than that with the chiral perylene core, the enantiomers separation may not work. Secondly, the incorporation of the amine group and the methyl group at the imide positions could considerably reduce the solubility of the molecules. As a result, the chiral chromatography may have to be run at a very low concentration, making the process too time-consuming to

be experimentally practical.

To tackle the potential problems of the enantiomers separation with the chiral chromatography, an alternative approach is to directly synthesize the amine-terminated chiral acceptors from chiral precursors, similar to the synthesis of the DBA molecule shown in Figure D.1. Importantly, this chiral precursor should have a high racemic barrier to retain its chirality throughout the synthesis process. Accordingly, 2,2'-difunctionalized-1,1'-binaphthalene and 1,14-difunctionalized [5]helicenes [73] are examples of promising candidates (Figure 6.8).

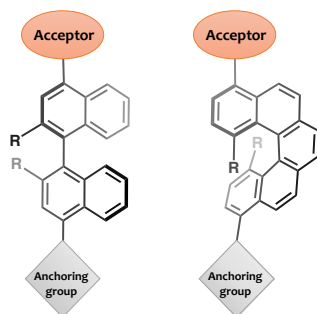


**Figure 6.8.** Schematic illustrations of proposed chiral bridge-acceptor molecules based on 2,2'-difunctionalized-1,1'-binaphthalene and 1,14-difunctionalized [5]helicenes.

Once the chiral acceptors are obtained, the next potential challenge is to detect any changes in the spin polarization. Although the spin polarization can relax rapidly in perovskite NPLs, its detection should still be feasible given the high temporal resolution offered by the TA measurement. Moreover, comparing the difference in the spectral shape should be more definitive than comparing the difference in kinetics. For instance, an asymmetric response as low as 5% in CsPbBr<sub>3</sub> NPLs is clearly noticeable in the TA spectra (Figure D.9). In the case of a negative result, meaning no detectable spin polarization in the perovskite NPLs, it implies spin selectivity is too low to be measurable at room temperature. This indicates the CISS effect of this chiral system is too minute to be captured in the absence of the metal-molecule interface and/or an external magnetic field. To bolster the validity of this hypothesis, conducting complementary measurements on the same molecular system would provide valuable support. For example, widely used magnetic conductive atomic force microscopy measurements on the same chiral molecules/NPLs to study the CISS effect. Details will be discussed in the following section.

### 6.3.2. Proposed measurements

#### Circular dichroism

Circular dichroism (CD) spectroscopy is an essential technique to quantify the chirality of a system. A CD spectrum measures the absorption difference between left and right CPL, which is an intrinsic absorption property of any optically active (chiral) molecules. Accordingly, the CD spectrum provides direct information on whether a system is chiral and the strength of its chirality. For example, it has been used to demonstrate the strong chiroptical properties of 1-monolayer chiral perovskite NPLs[68]. As displayed in Figure 6.9, the strong CD peak close to the absorption peak of the NPLs is direct evidence of the chirality transfer from the chiral ligands to the previously achiral NPLs.

Therefore, we can use CD measurements to characterize the optical strength of the synthesized chiral molecules and investigate the chirality transfer to the perovskite NPLs. For example, to study how the chirality of the system can be tuned by varying the density of the chiral molecules on the NPLs surface and how it will be influenced by the properties of the NPLs themselves. By quantifying the chiroptical properties with CD spectra, we may then correlate the strength of the chirality with the degree of spin polarization determined from the TA spectra. Furthermore, it is crucial to measure the CD spectra of the systems both before and after the TA measurements to ensure the preservation of chirality throughout the spin-dependent experiments.

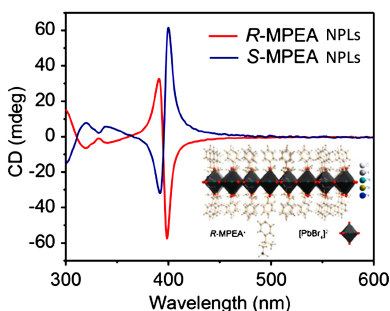


**Figure 6.9.** CD spectra of chiral perovskite nanoplatelets capped with R- or S- $\beta$ -methylphenethylamine (R-/S-MPEA) ligands. Adapted from ref [68].

#### Magnetic-conductive atomic force microscopy

A highly debatable and yet widely used technique to demonstrate the CISS effect is magnetic conductive atomic force microscopy (mc-AFM)[9, 10, 12, 21, 22, 74, 75]. During these experiments, the current-voltage (I-V) curves of a layer of chiral assemblies can be measured with different spin-polarized electrons. Subsequently, the CISS effect is demonstrated by the difference in the current response of a chiral system upon the reversal of spin orientation. Typically, the degree of spin polarization ( $P_{\text{spin}}$ ) in current is characterized by

$$P_{\text{spin}} = \frac{I_{\text{up}} - I_{\text{down}}}{I_{\text{up}} + I_{\text{down}}} \times 100\% \quad (6.1)$$

Subsequently, the CISS effect can be demonstrated by the spin-dependent conduction that significantly depends on the chirality of the system.

In general, the spin-dependent current can be generated with an external magnetic field in two ways. One is to pre-magnetize the conducting tip with preferred spin orientation[21, 75, 76], and the other one is to inject spin-polarized electrons using a ferromagnetic substrate underneath the sample[9, 10, 22]. The first one is also known as magnetic conductive-probe atomic force microscopy (mCP-AFM). Recently, Kim *et al* demonstrated a room-temperature spin-LED based on the CISS effect of a 2D chiral perovskite layer[76]. In this work, their mCP-AFM measurements on the stack of a part of a spin-LED device show the degree of polarized spin current is as large as +81% and -80% for the (R-MBA)<sub>2</sub>PbI<sub>4</sub> and (S-MBA)<sub>2</sub>PbI<sub>4</sub> active layer, respectively (Figure 6.10). The mCP-AFM technique has also been applied to monolayers of chiral molecules, such as chiral helicenes, showing similar spin filtering effect[12]. Note that with mCP-AFM measurements, the I-V curves are typically obtained by averaging a large number of curves measured at different spots on each sample. During the measurement, there is no control over the magnetization of the tip, which may decrease over time. This potentially limits the reproducibility of the results due to data selection and possible sample variations.

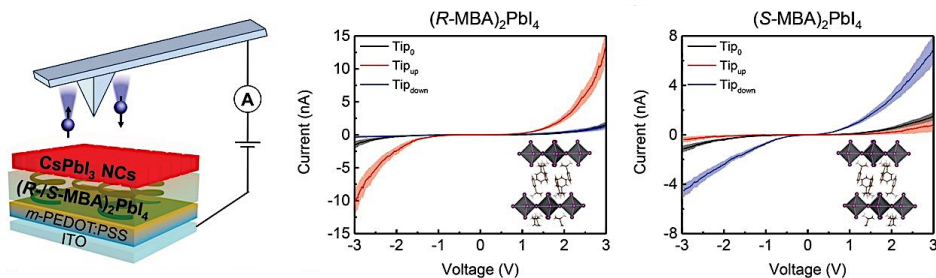


**Figure 6.10.** Schematic illustration of mCP-AFM measurements and spin-dependant current–voltage curves. Adapted from ref [76].

The second method, injecting spin from a ferromagnetic substrate, has also been widely used to measure the spin-dependent conduction of chiral samples. For instance, Naaman and co-workers have demonstrated 85-90% spin polarization at room temperature in helical supramolecular nanofibers using mc-AFM measurements with a ferromagnetic substrate[9]. In this work, the supramolecular nanofibers were dropcasted on a gold-coated nickel surface (Au/Ni), where Ni is magnetized with its magnetization perpendicular to the surface (Figure 6.11). Later, they used the same mc-AFM setup to show the CISS



effect can also manifest itself in helical supramolecular polymers solely assembled from achiral monomers[10]. In comparison with mCP-AFM, this approach should enable in situ switching of the magnetization orientation, allowing spin-dependent measurement at the same spot. In addition, the strength of the magnetization during the measurement should be controllable with an external circuit.

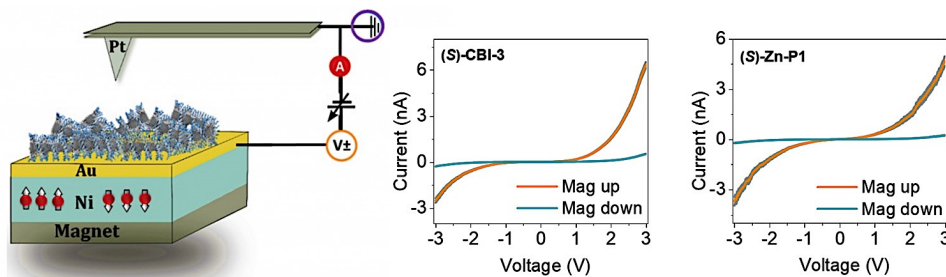


**Figure 6.11.** Schematic illustration of magnetic conductive atomic force microscopy (mc-AFM) measurements using a ferromagnetic substrate and spin-dependant current-voltage curves. Adapted from ref [9].

6

To obtain additional insights into spin-dependent charge transport in our proposed system, mc-AFM measurement can be performed on a monolayer of the proposed chiral molecules. If the same chiral molecules are found to show spin selectivity with spin-dependent conduction measurement, the negative results of TA measurements will indicate the importance of magnetic field and/or electrodes for observing the CISS effect. Therefore, this widely used and easily accessible technique is promising to provide complementary information to the TA measurement on the same chiral molecules and/or the chiral hybrid system.

#### Extend the capabilities of circularly polarized transient absorption

Currently, we have adapted the conventional TA setup to effectively generate CPL using broadband circular polarizers. However, the wavelength range of these thin film polarizers is restricted to 400–700 nm due to the limitations of the surface coating. Consequently, the range of samples that can be probed is limited to those exhibiting TA features within this wavelength range.

To further extend the wavelength range of the circularly polarized probe pulse, we can use a super-achromatic quarter-wave plate that provides nearly constant retardation across a broad range of wavelengths, such as 325–1100 nm. Nevertheless, these super-achromatic wave plates tend to be costly, with prices typically amounting to thousands of euros per unit. An alternative approach is to directly generate a circularly polarized white-light continuum. Specifically, a quarter-wave plate for 1030 nm can be used to convert the linearly polarized fundamental line to be circularly polarized. This circularly polarized 1030 nm light can subsequently be focused into the translating crystal to generate the

white-light continuum. The resulting white-light continuum should have the same polarization state as the seed beam[77]. In several papers, this method has been used to generate broadband circularly polarized probe beam[76, 78].

### 6.4. Conclusions

In this chapter, we have explored the possibility to generate and detect spin polarization optically with the aim to probe CISS in an electrodeless way. Specifically, we have investigated optical spin injection using circularly polarized TA in three different systems: covalent DBA molecule with a chiral bridge, a thin film of metal halide perovskite and colloidal perovskite nanoplatelets. In spite of the organic molecule, both bulk and nanoscale perovskites enable optical spin injection and detection with CPL.

To further probe the CISS effect, we have proposed a system based on the hybrid assemblies of perovskite NPLs and chiral electron acceptors. This chiral system is designed to enable optically detecting spin polarization of transferred charges that were initially unpolarized. The same system can be used to study the spin-dependent charge transfer by optically generating a spin-polarized excited state. If the change in the spin polarization is shown to be chirality dependent, this will be direct proof of CISS in the absence of metal or ferromagnetic materials and provide valuable insight into the origin of CISS. To further explore the relation between CISS and molecular parameters, such as optical rotation and SOC, we can systematically modulate the properties of the hybrid system. For instance, varying the chirality of the hybrid system by tuning the chirality transfer from the chiral molecules to the perovskite NPLs and varying the strength of SOC by tuning the composition in the perovskite nanostructures.

Considering that scientific research is never smooth sailing, we further discuss the possible challenges in implementing the proposal, such as the potential difficulties of obtaining functional chiral molecules and detecting measurable spin polarization. Alternative approaches and additional measurements were proposed to mitigate these potential challenges and rationalize the research findings, respectively. Hopefully, the designed experiment will provide a valuable piece to the puzzle of understanding the CISS effect.



## References

1. Naaman, R. & Waldeck, D. H. Chiral-induced spin selectivity effect. *The journal of physical chemistry letters* **3**, 2178–2187 (2012).
2. Evers, F., Aharony, A., Bar-Gill, N., Entin-Wohlman, O., Hedegård, P., Hod, O., Jelinek, P., Kamieniarz, G., Lemeshko, M., Michaeli, K., et al. Theory of chirality induced spin selectivity: Progress and challenges. *Advanced Materials* **34**, 2106629 (2022).
3. Naaman, R., Paltiel, Y. & Waldeck, D. H. Chiral molecules and the electron spin. *Nature Reviews Chemistry* **3**, 250–260 (2019).
4. Aiello, C. D., Abendroth, J. M., Abbas, M., Afanasev, A., Agarwal, S., Banerjee, A. S., Beratan, D. N., Belling, J. N., Berche, B., Botana, A., et al. A Chirality-Based Quantum Leap. *ACS nano* **16**, 4989–5035 (2022).
5. Göhler, B., Hamelbeck, V., Markus, T., Kettner, M., Hanne, G., Vager, Z., Naaman, R. & Zacharias, H. Spin selectivity in electron transmission through self-assembled monolayers of double-stranded DNA. *Science* **331**, 894–897 (2011).
6. Xie, Z., Markus, T. Z., Cohen, S. R., Vager, Z., Gutierrez, R. & Naaman, R. Spin specific electron conduction through DNA oligomers. *Nano letters* **11**, 4652–4655 (2011).
7. Abendroth, J. M., Nakatsuka, N., Ye, M., Kim, D., Fullerton, E. E., Andrews, A. M. & Weiss, P. S. Analyzing spin selectivity in DNA-mediated charge transfer via fluorescence microscopy. *ACS nano* **11**, 7516–7526 (2017).
8. Zwang, T. J., Hurlimann, S., Hill, M. G. & Barton, J. K. Helix-dependent spin filtering through the DNA duplex. *Journal of the American Chemical Society* **138**, 15551–15554 (2016).
9. Kulkarni, C., Mondal, A. K., Das, T. K., Grinbom, G., Tassinari, F., Mabesoone, M. F., Meijer, E. & Naaman, R. Highly efficient and tunable filtering of Electrons' spin by supramolecular chirality of nanofiber-based materials. *Advanced Materials* **32**, 1904965 (2020).
10. Mondal, A. K., Preuss, M. D., Ślęczkowski, M. L., Das, T. K., Vantomme, G., Meijer, E. & Naaman, R. Spin filtering in supramolecular polymers assembled from achiral monomers mediated by chiral solvents. *Journal of the American Chemical Society* **143**, 7189–7195 (2021).
11. Kettner, M., Maslyuk, V. V., Nürenberg, D., Seibel, J., Gutierrez, R., Cuniberti, G., Ernst, K.-H. & Zacharias, H. Chirality-dependent electron spin filtering by molecular monolayers of helicenes. *The journal of physical chemistry letters* **9**, 2025–2030 (2018).
12. Kiran, V., Mathew, S. P., Cohen, S. R., Hernández Delgado, I., Lacour, J. & Naaman, R. Helicenes—A new class of organic spin filter. *Advanced Materials* **28**, 1957–1962 (2016).

13. Yang, C., Li, Y., Zhou, S., Guo, Y., Jia, C., Liu, Z., Houk, K. N., Dubi, Y. & Guo, X. Real-time monitoring of reaction stereochemistry through single-molecule observations of chirality-induced spin selectivity. *Nature Chemistry*, 1–8 (2023).
14. Naaman, R. & Waldeck, D. H. Spintronics and chirality: Spin selectivity in electron transport through chiral molecules. *Annual review of physical chemistry* **66**, 263–281 (2015).
15. Yang, S.-H., Naaman, R., Paltiel, Y. & Parkin, S. S. Chiral spintronics. *Nature Reviews Physics* **3**, 328–343 (2021).
16. Shang, Z., Liu, T., Yang, Q., Cui, S., Xu, K., Zhang, Y., Deng, J., Zhai, T. & Wang, X. Chiral-Molecule-Based Spintronic Devices. *Small* **18**, 2203015 (2022).
17. Banerjee-Ghosh, K., Ben Dor, O., Tassinari, F., Capua, E., Yochelis, S., Capua, A., Yang, S.-H., Parkin, S. S., Sarkar, S., Kronik, L., et al. Separation of enantiomers by their enantiospecific interaction with achiral magnetic substrates. *Science* **360**, 1331–1334 (2018).
18. Naaman, R., Paltiel, Y. & Waldeck, D. H. Chiral induced spin selectivity and its implications for biological functions. *Annual review of biophysics* **51**, 99–114 (2022).
19. Michaeli, K., Kantor-Uriel, N., Naaman, R. & Waldeck, D. H. The electron's spin and molecular chirality—how are they related and how do they affect life processes? *Chemical Society Reviews* **45**, 6478–6487 (2016).
20. Niño, M. Á., Kowalik, I. A., Luque, F. J., Arvanitis, D., Miranda, R. & de Miguel, J. J. Enantiospecific spin polarization of electrons photoemitted through layers of homochiral organic molecules. *Advanced Materials* **26**, 7474–7479 (2014).
21. Mishra, S., Mondal, A. K., Smolinsky, E. Z., Naaman, R., Maeda, K., Nishimura, T., Taniguchi, T., Yoshida, T., Takayama, K. & Yashima, E. Spin filtering along chiral polymers. *Angewandte Chemie International Edition* **59**, 14671–14676 (2020).
22. Mondal, A. K., Brown, N., Mishra, S., Makam, P., Wing, D., Gilead, S., Wiesenfeld, Y., Leitus, G., Shimon, L. J., Carmieli, R., et al. Long-range spin-selective transport in chiral metal–organic crystals with temperature-activated magnetization. *ACS nano* **14**, 16624–16633 (2020).
23. Ravi, S., Sowmiya, P. & Karthikeyan, A. *Magnetoresistance and spin-filtering efficiency of DNA-sandwiched ferromagnetic nanostructures in Spin* **3** (2013), 1350003.
24. Ben Dor, O., Morali, N., Yochelis, S., Baczewski, L. T. & Paltiel, Y. Local light-induced magnetization using nanodots and chiral molecules. *Nano letters* **14**, 6042–6049 (2014).
25. Mishra, D., Markus, T. Z., Naaman, R., Kettner, M., Göhler, B., Zacharias, H., Friedman, N., Sheves, M. & Fontanesi, C. Spin-dependent electron transmission through bacteriorhodopsin embedded in purple membrane. *Proceedings of the National Academy of Sciences* **110**, 14872–14876 (2013).
26. Mondal, P. C., Fontanesi, C., Waldeck, D. H. & Naaman, R. Spin-dependent transport through chiral molecules studied by spin-dependent electrochemistry. *Accounts of chemical research* **49**, 2560–2568 (2016).

27. Dianat, A., Gutierrez, R., Alpern, H., Mujica, V., Ziv, A., Yochelis, S., Millo, O., Paltiel, Y. & Cuniberti, G. Role of exchange interactions in the magnetic response and intermolecular recognition of chiral molecules. *Nano Letters* **20**, 7077–7086 (2020).
28. Ziv, A., Saha, A., Alpern, H., Sukenik, N., Baczewski, L. T., Yochelis, S., Rechtes, M. & Paltiel, Y. AFM-Based Spin-Exchange Microscopy Using Chiral Molecules. *Advanced Materials* **31**, 1904206 (2019).
29. Alwan, S. & Dubi, Y. Spinterface origin for the chirality-induced spin-selectivity effect. *Journal of the American Chemical Society* **143**, 14235–14241 (2021).
30. Yang, X., van der Wal, C. H. & van Wees, B. J. Detecting chirality in two-terminal electronic nanodevices. *Nano letters* **20**, 6148–6154 (2020).
31. Yang, X. & van Wees, B. J. Linear-response magnetoresistance effects in chiral systems. *Physical Review B* **104**, 155420 (2021).
32. Huisman, K. H. & Thijssen, J. M. CISS Effect: A Magnetoresistance Through Inelastic Scattering. *The Journal of Physical Chemistry C* **125**, 23364–23369 (2021).
33. Bloom, B. P., Graff, B. M., Ghosh, S., Beratan, D. N. & Waldeck, D. H. Chirality control of electron transfer in quantum dot assemblies. *Journal of the American Chemical Society* **139**, 9038–9043 (2017).
34. Guo, L., Qin, Y., Gu, X., Zhu, X., Zhou, Q. & Sun, X. Spin transport in organic molecules. *Frontiers in Chemistry* **7**, 428 (2019).
35. Privitera, A., Righetto, M., Cacialli, F. & Riede, M. K. Perspectives of Organic and Perovskite-Based Spintronics. *Advanced Optical Materials* **9**, 2100215 (2021).
36. Tanaka, K., Takahashi, T., Ban, T., Kondo, T., Uchida, K. & Miura, N. Comparative study on the excitons in lead-halide-based perovskite-type crystals CH<sub>3</sub>NH<sub>3</sub>PbBr<sub>3</sub> CH<sub>3</sub>NH<sub>3</sub>PbI<sub>3</sub>. *Solid state communications* **127**, 619–623 (2003).
37. Even, J., Pedesseau, L. & Katan, C. Analysis of multivalley and multibandgap absorption and enhancement of free carriers related to exciton screening in hybrid perovskites. *The Journal of Physical Chemistry C* **118**, 11566–11572 (2014).
38. Zhao, J., Caselli, V. M., Bus, M., Boshuizen, B. & Savenije, T. J. How Deep Hole Traps Affect the Charge Dynamics and Collection in Bare and Bilayers of Methylammonium Lead Bromide. *ACS applied materials & interfaces* **13**, 16309–16316 (2021).
39. Stamplecoskie, K. G., Manser, J. S. & Kamat, P. V. Dual nature of the excited state in organic–inorganic lead halide perovskites. *Energy & Environmental Science* **8**, 208–215 (2015).
40. Anand, B., Sampat, S., Danilov, E. O., Peng, W., Rupich, S. M., Chabal, Y. J., Gartstein, Y. N. & Malko, A. V. Broadband transient absorption study of photoexcitations in lead halide perovskites: Towards a multiband picture. *Physical Review B* **93**, 161205 (2016).
41. Price, M. B., Butkus, J., Jellicoe, T. C., Sadhanala, A., Briane, A., Halpert, J. E., Broch, K., Hodgkiss, J. M., Friend, R. H. & Deschler, F. Hot-carrier cooling and photoinduced refractive index changes in organic–inorganic lead halide perovskites. *Nature communications* **6**, 8420 (2015).
42. Pasanen, H. P., Vivo, P., Canil, L., Abate, A. & Tkachenko, N. Refractive index change dominates the transient absorption response of metal halide perovskite thin films in the near infrared. *Physical Chemistry Chemical Physics* **21**, 14663–14670 (2019).

43. Liu, J., Leng, J., Wang, S., Zhang, J. & Jin, S. *Artifacts in transient absorption measurements of perovskite films induced by transient reflection from morphological microstructures* 2019.
44. Ashoka, A., Tamming, R. R., Girija, A. V., Bretscher, H., Verma, S. D., Yang, S.-D., Lu, C.-H., Hodgkiss, J. M., Ritchie, D., Chen, C., et al. Extracting quantitative dielectric properties from pump-probe spectroscopy. *Nature Communications* **13**, 1437 (2022).
45. Zhao, W., Su, R., Huang, Y., Wu, J., Fong, C. F., Feng, J. & Xiong, Q. Transient circular dichroism and exciton spin dynamics in all-inorganic halide perovskites. *Nature Communications* **11**, 5665 (2020).
46. Giovanni, D., Chong, W. K., Liu, Y. Y. F., Dewi, H. A., Yin, T., Lekina, Y., Shen, Z. X., Mathews, N., Gan, C. K. & Sum, T. C. Coherent spin and quasiparticle dynamics in solution-processed layered 2d lead halide perovskites. *Advanced Science* **5**, 1800664 (2018).
47. Bourelle, S. A., Shivanna, R., Camargo, F. V., Ghosh, S., Gillett, A. J., Senanayak, S. P., Feldmann, S., Eyre, L., Ashoka, A., van de Goor, T. W., et al. How exciton interactions control spin-depolarization in layered hybrid perovskites. *Nano Letters* **20**, 5678–5685 (2020).
48. Chen, X., Lu, H., Yang, Y. & Beard, M. C. Excitonic effects in methylammonium lead halide perovskites. *The journal of physical chemistry letters* **9**, 2595–2603 (2018).
49. Zhou, M., Sarmiento, J. S., Fei, C., Zhang, X. & Wang, H. Effect of composition on the spin relaxation of lead halide perovskites. *The journal of physical chemistry letters* **11**, 1502–1507 (2020).
50. Žutić, I., Fabian, J. & Sarma, S. D. Spintronics: Fundamentals and applications. *Reviews of modern physics* **76**, 323 (2004).
51. Chen, Y., Liu, Z., Li, J., Cheng, X., Ma, J., Wang, H. & Li, D. Robust interlayer coupling in two-dimensional perovskite/monolayer transition metal dichalcogenide heterostructures. *ACS nano* **14**, 10258–10264 (2020).
52. Wang, Q., Zhu, H., Chen, W., Hao, J., Wang, Z., Tang, J., Yang, Y., Sun, X. W., Wu, D. & Wang, K. Strong circularly polarized luminescence from quantum dots/2D chiral perovskites composites. *Nano Research*, 1–7 (2023).
53. Rossi, D., Wang, H., Dong, Y., Qiao, T., Qian, X. & Son, D. H. Light-induced activation of forbidden exciton transition in strongly confined perovskite quantum dots. *ACS nano* **12**, 12436–12443 (2018).
54. Villamil Franco, C., Trippé-Allard, G., Mahler, B., Cornaggia, C., Lauret, J.-S., Gustavsson, T. & Cassette, E. Exciton Cooling in 2D Perovskite Nanoplatelets: Rationalized Carrier-Induced Stark and Phonon Bottleneck Effects. *The Journal of Physical Chemistry Letters* **13**, 393–399 (2022).
55. Li, Y., Luo, X., Liu, Y., Lu, X. & Wu, K. Size- and composition-dependent exciton spin relaxation in lead halide perovskite quantum dots. *ACS Energy Letters* **5**, 1701–1708 (2020).
56. Huxter, V. M., Kovalevskij, V. & Scholes, G. D. Dynamics within the exciton fine structure of colloidal CdSe quantum dots. *The Journal of Physical Chemistry B* **109**, 20060–20063 (2005).

57. Rodina, A. & Efros, A. L. Magnetic properties of nonmagnetic nanostructures: dangling bond magnetic polaron in CdSe nanocrystals. *Nano Letters* **15**, 4214–4222 (2015).
58. Liang, W., Li, Y., Xiang, D., Han, Y., Jiang, Q., Zhang, W. & Wu, K. Efficient optical orientation and slow spin relaxation in lead-free CsSnBr<sub>3</sub> perovskite nanocrystals. *ACS Energy Letters* **6**, 1670–1676 (2021).
59. Moloney, M. P., Gun'ko, Y. K. & Kelly, J. M. Chiral highly luminescent CdS quantum dots. *Chemical Communications*, 3900–3902 (2007).
60. Tohgha, U., Deol, K. K., Porter, A. G., Bartko, S. G., Choi, J. K., Leonard, B. M., Varga, K., Kubelka, J., Muller, G. & Balaz, M. Ligand induced circular dichroism and circularly polarized luminescence in CdSe quantum dots. *ACS nano* **7**, 11094–11102 (2013).
61. Gao, X., Zhang, X., Deng, K., Han, B., Zhao, L., Wu, M., Shi, L., Lv, J. & Tang, Z. Excitonic circular dichroism of chiral quantum rods. *Journal of the American Chemical Society* **139**, 8734–8739 (2017).
62. Kuznetsova, V., Gromova, Y., Martinez-Carmona, M., Purcell-Milton, F., Ushakova, E., Cherevko, S., Maslov, V. & Gun'ko, Y. K. Ligand-induced chirality and optical activity in semiconductor nanocrystals: theory and applications. *Nanophotonics* **10**, 797–824 (2020).
63. He, T., Li, J., Li, X., Ren, C., Luo, Y., Zhao, F., Chen, R., Lin, X. & Zhang, J. Spectroscopic studies of chiral perovskite nanocrystals. *Applied Physics Letters* **111**, 151102 (2017).
64. Chen, W., Zhang, S., Zhou, M., Zhao, T., Qin, X., Liu, X., Liu, M. & Duan, P. Two-photon absorption-based upconverted circularly polarized luminescence generated in chiral perovskite nanocrystals. *The Journal of Physical Chemistry Letters* **10**, 3290–3295 (2019).
65. Georgieva, Z. N., Bloom, B. P., Ghosh, S. & Waldeck, D. H. Imprinting chirality onto the electronic states of colloidal perovskite nanoplatelets. *Advanced Materials* **30**, 1800097 (2018).
66. Kim, Y.-H., Zhai, Y., Gaubling, E. A., Habisreutinger, S. N., Moot, T., Rosales, B. A., Lu, H., Hazarika, A., Brunecky, R., Wheeler, L. M., et al. Strategies to achieve high circularly polarized luminescence from colloidal organic–inorganic hybrid perovskite nanocrystals. *ACS nano* **14**, 8816–8825 (2020).
67. Georgieva, Z. N., Zhang, Z., Zhang, P., Bloom, B. P., Beratan, D. N. & Waldeck, D. H. Ligand Coverage and Exciton Delocalization Control Chiral Imprinting in Perovskite Nanoplatelets. *The Journal of Physical Chemistry C* **126**, 15986–15995 (2022).
68. Ren, H., Wu, Y., Wang, C. & Yan, Y. 2D perovskite nanosheets with intrinsic chirality. *The Journal of Physical Chemistry Letters* **12**, 2676–2681 (2021).
69. Hubley, A., Bensalah-Ledoux, A., Baguenard, B., Guy, S., Abécassis, B. & Mahler, B. Chiral perovskite nanoplatelets exhibiting circularly polarized luminescence through ligand optimization. *Advanced Optical Materials* **10**, 2200394 (2022).
70. Kim, Y.-H., Song, R., Hao, J., Zhai, Y., Yan, L., Moot, T., Palmstrom, A. F., Brunecky, R., You, W., Berry, J. J., et al. The Structural Origin of Chiroptical Properties in Perovskite Nanocrystals with Chiral Organic Ligands. *Advanced Functional Materials* **32**, 2200454 (2022).



71. Gao, X., Han, B., Yang, X. & Tang, Z. Perspective of chiral colloidal semiconductor nanocrystals: opportunity and challenge. *Journal of the American Chemical Society* **141**, 13700–13707 (2019).
72. Gao, X., Zhang, X., Zhao, L., Huang, P., Han, B., Lv, J., Qiu, X., Wei, S.-H. & Tang, Z. Distinct excitonic circular dichroism between wurtzite and zincblende CdSe nanoplatelets. *Nano Letters* **18**, 6665–6671 (2018).
73. Ravat, P., Hinkelmann, R., Steinebrunner, D., Prescimone, A., Bodoky, I. & Juriček, M. Configurational stability of [5] helicenes. *Organic letters* **19**, 3707–3710 (2017).
74. Bian, Z., Kato, K., Ogoshi, T., Cui, Z., Sa, B., Tsutsui, Y., Seki, S. & Suda, M. Hybrid Chiral MoS<sub>2</sub> Layers for Spin-Polarized Charge Transport and Spin-Dependent Electrocatalytic Applications. *Advanced Science* **9**, 2201063 (2022).
75. Lu, H., Wang, J., Xiao, C., Pan, X., Chen, X., Brunecky, R., Berry, J. J., Zhu, K., Beard, M. C. & Vardeny, Z. V. Spin-dependent charge transport through 2D chiral hybrid lead-iodide perovskites. *Science advances* **5**, eaay0571 (2019).
76. Kim, Y.-H., Zhai, Y., Lu, H., Pan, X., Xiao, C., Gauling, E. A., Harvey, S. P., Berry, J. J., Vardeny, Z. V., Luther, J. M., et al. Chiral-induced spin selectivity enables a room-temperature spin light-emitting diode. *Science* **371**, 1129–1133 (2021).
77. Trifonov, A., Buchvarov, I., Lohr, A., Würthner, F. & Fiebig, T. Broadband femtosecond circular dichroism spectrometer with white-light polarization control. *Review of Scientific Instruments* **81**, 043104 (2010).
78. Scholz, M., Morgenroth, M., Cho, M. J., Choi, D. H., Oum, K. & Lenzer, T. Ultrafast broadband transient absorption and circular dichroism reveal relaxation of a chiral copolymer. *The Journal of Physical Chemistry Letters* **10**, 5160–5166 (2019).

# D

## Appendix to Chapter 6

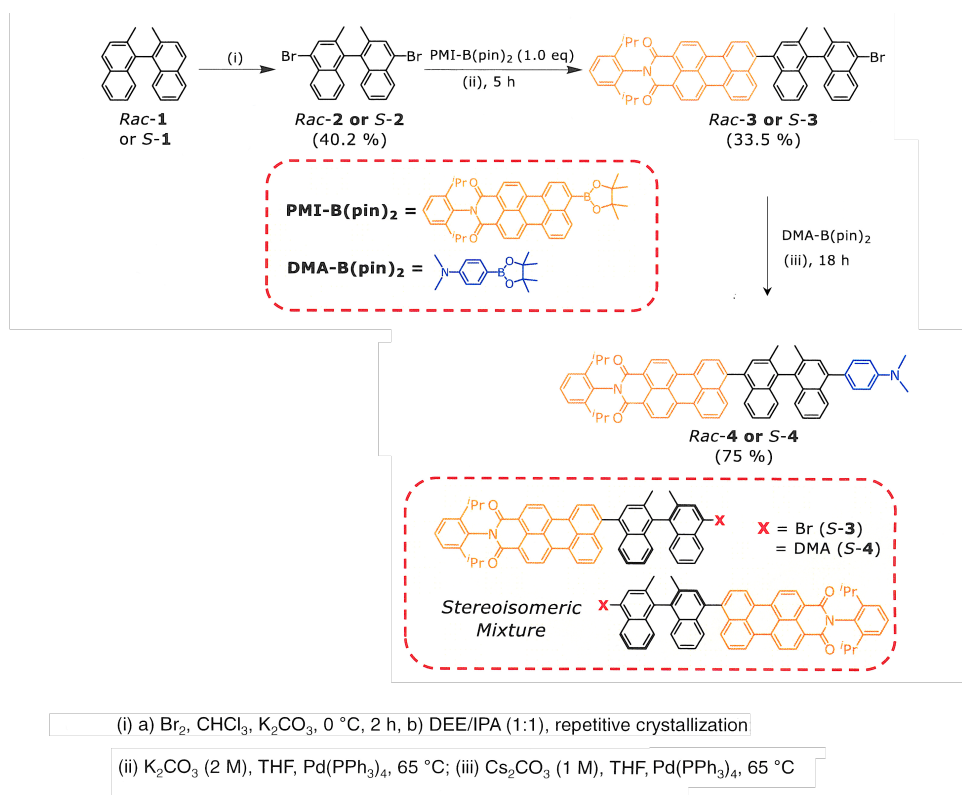


**Figure D.1.** Syntheses of binaphthyl based donor—bridge—acceptor molecules.

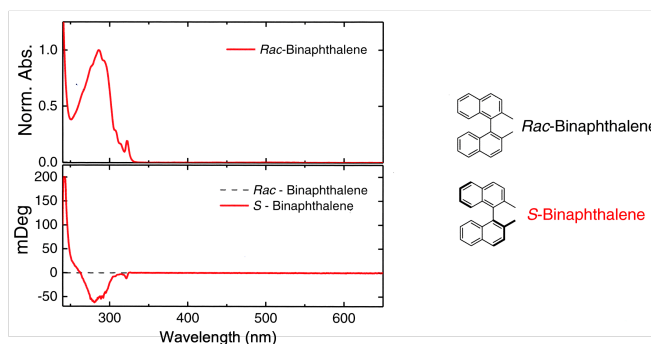


**Figure D.2.** Absorption spectrum and circular dichroism spectra of (S)-2,2'-dimethyl-1,1'-binaphthalene and racemic 2,2'-dimethyl-1,1'-binaphthalene measured in dichloromethane.

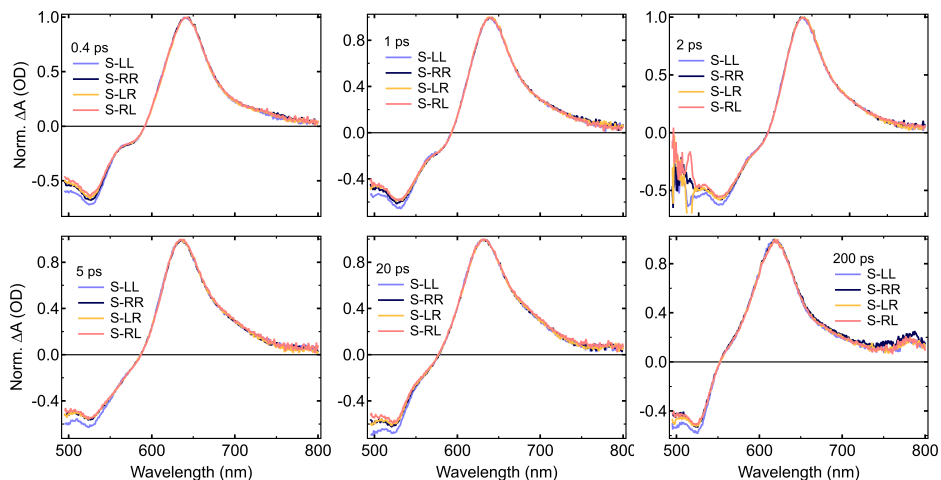


**Figure D.3.** Normalized TA spectra of S-DBA molecule with different pump and probe configurations at time delays of 0.4 ps, 1 ps, 2 ps, 5 ps, 20 ps, and 200 ps.

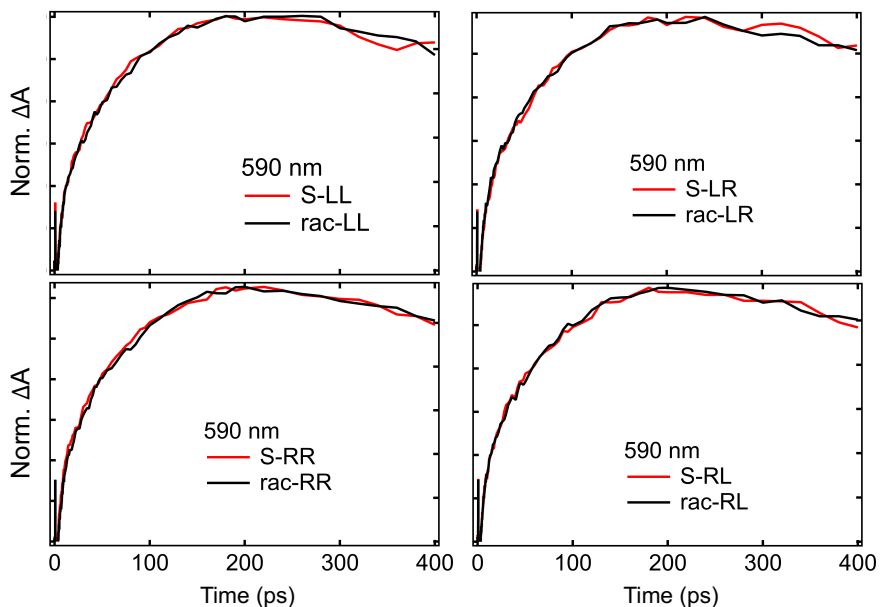


**Figure D.4.** Normalized TA traces at 590 nm of rac-DAB and S-DBA molecules with different pump and probe configurations. Note that the kinetics at 590 nm characterizes the charge transfer rate.

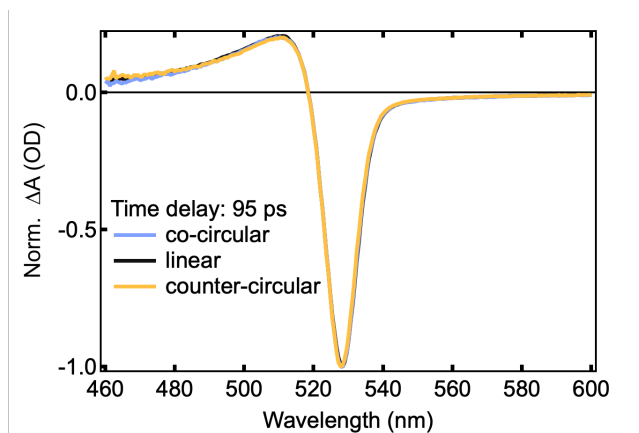


**Figure D.5.** Normalized TA spectra at 95 ps for the  $\text{CH}_3\text{NH}_3\text{PbBr}_3$  film excited at 525 nm with linear, co-circular, and counter-circular pump and probe configurations.

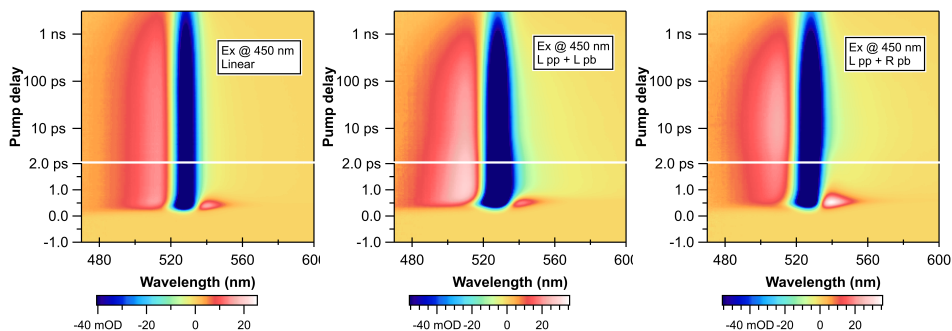


**Figure D.6.** 2D contour plot of TA spectra for the  $\text{CH}_3\text{NH}_3\text{PbBr}_3$  thin film excited 450 nm with linear, co-circular, and counter-circular pump and probe configurations.

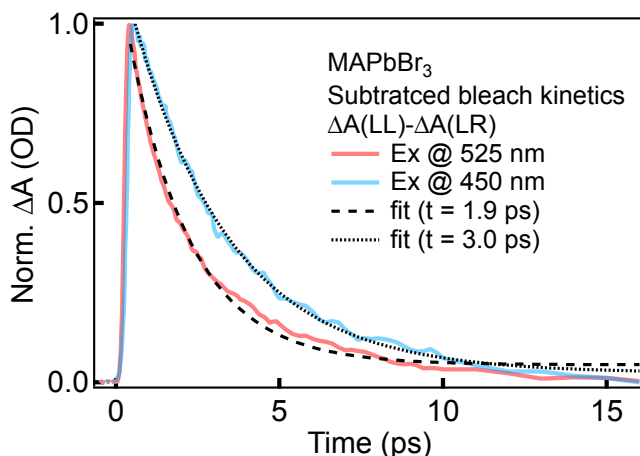
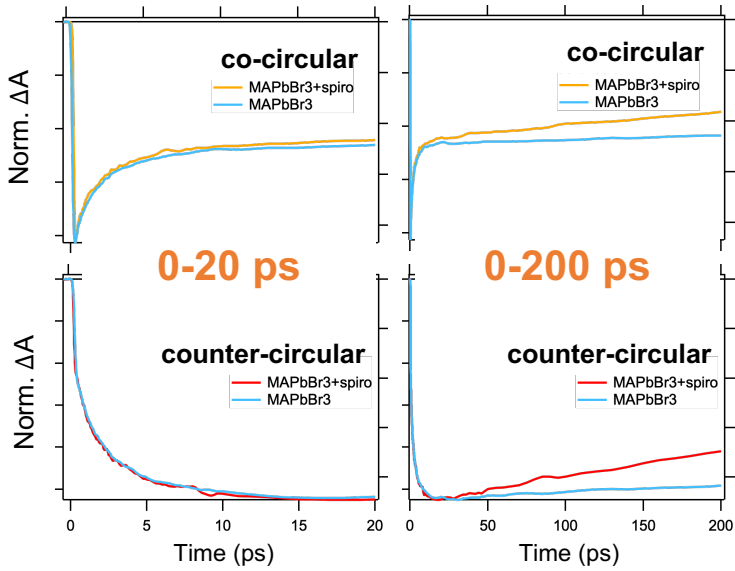


**Figure D.7.** Spin-dependent dynamics and fitted spin lifetimes in  $\text{CH}_3\text{NH}_3\text{PbBr}_3$  thin film upon excitation at 525 nm and 450 nm. Note that the plotted traces were obtained by subtracting the bleach kinetics by counter-circular polarization from that by co-circular polarization. And the fitted spin lifetimes were obtained by an exponential fit.



D

**Figure D.8.** Normalized TA traces at 528 nm of  $\text{CH}_3\text{NH}_3\text{PbBr}_3$  thin film and of  $\text{CH}_3\text{NH}_3\text{PbBr}_3$  thin film spin-coated with spiro transport layer. The faster decay with spiro indicates the charge extraction process.

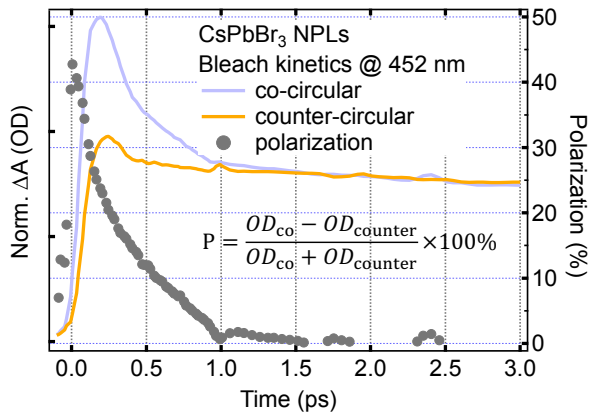


**Figure D.9.** Spin-dependent dynamics and corresponding spin polarization in  $\text{CsPbBr}_3$  nanoplatelets upon excitation at 452 nm.

**Table D.1.** Full spin lifetime in colloidal perovskite nanostructures

Composition	Dimension	Full spin lifetime	Ref
CsPbI <sub>3</sub>	4.2 nm	5±0.5 ps	[20]
	5.0 nm	5±0.5 ps	
	5.5 nm	5±0.5 ps	
	6.3 nm	6±0.5 ps	
	7.3 nm	9±0.5 ps	
	8.3 nm	9±1.0 ps	
	8 nm	7±0.5 ps	[21]
CsPbBr <sub>3</sub>	3.5 nm	3±0.5 ps	[20]
	4.1 nm	4±0.5 ps	
	4.6 nm	4±0.5 ps	
	5.6 nm	4.5±0.5 ps	
	7.5 nm	4.5±0.5 ps	
CsSnBr <sub>3</sub>	8.4 nm	35±5 ps	[21]

Note that the listed spin lifetimes refer to the point where the differences in spin-dependent signals diminish in the raw TA data.

## References to Appendices

1. Kowski, A. On the estimation of excited-state dipole moments from solvatochromic shifts of absorption and fluorescence spectra. *Zeitschrift für Naturforschung A* **57**, 255–262 (2002).
2. Lippert, E. v. Spektroskopische Bestimmung des Dipolmomentes aromatischer Verbindungen im ersten angeregten Singulettzustand. *Zeitschrift für Elektrochemie, Berichte der Bunsengesellschaft für physikalische Chemie* **61**, 962–975 (1957).
3. Sucre-Rosales, E., Fernandez-Teran, R., Urdaneta, N., Hernandez, F. E. & Echevarria, L. Solvatochromism and intramolecular charge transfer in dialkylamino-substituted halogenated thienyl chalcone analogues. *Chemical Physics* **537**, 110854 (2020).
4. Weller, A. Photoinduced electron transfer in solution: exciplex and radical ion pair formation free enthalpies and their solvent dependence. *Zeitschrift für Physikalische Chemie* **133**, 93–98 (1982).
5. Liu, Y., Zhao, J., Iagatti, A., Bussotti, L., Foggi, P., Castellucci, E., Di Donato, M. & Han, K.-L. A revisit to the orthogonal bodipy dimers: experimental evidence for the symmetry breaking charge transfer-induced intersystem crossing. *The Journal of Physical Chemistry C* **122**, 2502–2511 (2018).
6. Guo, Y., Ma, Z., Niu, X., Zhang, W., Tao, M., Guo, Q., Wang, Z. & Xia, A. Bridge-mediated charge separation in isomeric N-annulated perylene diimide dimers. *Journal of the American Chemical Society* **141**, 12789–12796 (2019).
7. Marcus, R. A. & Sutin, N. Electron transfers in chemistry and biology. *Biochimica et Biophysica Acta (BBA)-Reviews on Bioenergetics* **811**, 265–322 (1985).
8. Klamt, A. & Schüürmann, G. COSMO: a new approach to dielectric screening in solvents with explicit expressions for the screening energy and its gradient. *Journal of the Chemical Society, Perkin Transactions 2*, 799–805 (1993).
9. Dubey, R. K., Westerveld, N., Sudhölter, E. J., Grozema, F. C. & Jager, W. F. Novel derivatives of 1, 6, 7, 12-tetrachloroperylene-3, 4, 9, 10-tetracarboxylic acid: synthesis, electrochemical and optical properties. *Organic Chemistry Frontiers* **3**, 1481–1492 (2016).
10. Grim, J. Q., Christodoulou, S., Di Stasio, F., Krahne, R., Cingolani, R., Manna, L. & Moreels, I. Continuous-wave biexciton lasing at room temperature using solution-processed quantum wells. *Nature nanotechnology* **9**, 891–895 (2014).
11. Naeem, A., Masia, F., Christodoulou, S., Moreels, I., Borri, P. & Langbein, W. Giant exciton oscillator strength and radiatively limited dephasing in two-dimensional platelets. *Physical Review B* **91**, 121302 (2015).
12. Peng, S., Wei, Q., Wang, B., Zhang, Z., Yang, H., Pang, G., Wang, K., Xing, G., Sun, X. W. & Tang, Z. Suppressing Strong Exciton–Phonon Coupling in Blue Perovskite Nanoplatelet Solids by Binary Systems. *Angewandte Chemie International Edition* **59**, 22156–22162 (2020).



13. Vale, B. R., Socie, E., Burgos-Caminal, A., Bettini, J., Schiavon, M. A. & Moser, J.-E. Exciton, biexciton, and hot exciton dynamics in CsPbBr<sub>3</sub> colloidal nanoplatelets. *The Journal of Physical Chemistry Letters* **11**, 387–394 (2019).
14. Li, Q. & Lian, T. Ultrafast charge separation in two-dimensional CsPbBr<sub>3</sub> perovskite nanoplatelets. *The Journal of Physical Chemistry Letters* **10**, 566–573 (2019).
15. Wang, J., Ding, T., Gao, K., Wang, L., Zhou, P. & Wu, K. Marcus inverted region of charge transfer from low-dimensional semiconductor materials. *Nature Communications* **12**, 6333 (2021).
16. Akkerman, Q. A., Motti, S. G., Srimath Kandada, A. R., Mosconi, E., D’Innocenzo, V., Bertoni, G., Marras, S., Kamino, B. A., Miranda, L., De Angelis, F., et al. Solution synthesis approach to colloidal cesium lead halide perovskite nanoplatelets with monolayer-level thickness control. *Journal of the American Chemical Society* **138**, 1010–1016 (2016).
17. Maes, J., Balcaen, L., Drijvers, E., Zhao, Q., De Roo, J., Vantomme, A., Vanhaecke, F., Geiregat, P. & Hens, Z. Light absorption coefficient of CsPbBr<sub>3</sub> perovskite nanocrystals. *The journal of physical chemistry letters* **9**, 3093–3097 (2018).
18. Grimaldi, G., Geuchies, J. J., Van Der Stam, W., Du Fossé, I., Brynjarsson, B., Kirkwood, N., Kinge, S., Siebbeles, L. D. & Houtepen, A. J. Spectroscopic evidence for the contribution of holes to the bleach of Cd-chalcogenide quantum dots. *Nano Letters* **19**, 3002–3010 (2019).
19. Snellenburg, J. J., Laptенок, S., Seger, R., Mullen, K. M. & van Stokkum, I. H. Glotaran: A Java-based graphical user interface for the R package TIMP. *Journal of Statistical Software* **49**, 1–22 (2012).
20. Li, Y., Luo, X., Liu, Y., Lu, X. & Wu, K. Size- and composition-dependent exciton spin relaxation in lead halide perovskite quantum dots. *ACS Energy Letters* **5**, 1701–1708 (2020).
21. Liang, W., Li, Y., Xiang, D., Han, Y., Jiang, Q., Zhang, W. & Wu, K. Efficient optical orientation and slow spin relaxation in lead-free CsSnBr<sub>3</sub> perovskite nanocrystals. *ACS Energy Letters* **6**, 1670–1676 (2021).

*Although the Universe is under no obligation to make sense,  
students in pursuit of the Ph.D. are.*

Robert Kirshner



## Summary

Photoinduced charge transfer (CT) is a fundamental photophysical process that prevails in nature but also plays a pivotal role in various technological fields. Naturally, seeking to understand this process has been a long-standing scientific endeavour. To achieve such understanding, model systems such as "donor-bridge-acceptor" (DBA) systems have been extensively explored to shed light on the mechanisms and dynamics of CT. In these systems, photoinduced CT typically takes place on an ultrafast timescale, ranging from a few nanoseconds ( $10^{-9}$  s) up to hundreds of femtoseconds ( $10^{-15}$  s). Therefore, ultrafast spectroscopy techniques, such as femtosecond transient absorption (TA), are essential approaches to study photoinduced CT in DBA systems.

This thesis describes spectroscopic studies on photoinduced CT in DBA systems and their derivatives. The main focus is on understanding the interplay between the molecular structure and the resulting CT behavior, paving the way for tailoring and optimizing these systems for specific applications. Throughout this work, we employ femtosecond TA spectroscopy to capture the excited state dynamics in ensembles of isolated molecular systems in solution. In [Chapter 6](#), we use an adapted version of the TA experiment to study spin-dependent dynamics using circularly polarized light. In [Chapters 3 to 5](#), we use global and target analysis as implemented in the open software Glotaran as an analytical tool to extract rate constants of photoinduced processes from the TA spectra. In [Chapters 3 and 4](#), (time-dependent) density functional theory (DFT) is employed to interpret the experimental observations. Together, these experimental, analytical and theoretical tools provide a comprehensive perspective for understanding photophysics in DBA systems.

In [Chapter 1](#), we provide a brief introduction to the concept of photoinduced CT, its relevance, and the two types of model systems used in this thesis to study the CT process. The purpose is to offer a conceptual description of photoinduced CT, particularly in DBA systems. Finally, we outline the structure of this thesis to assist readers in navigating between the chapters.

In [Chapter 2](#), we introduce the theoretical background and the main technique used in this work. We begin with the well-known Marcus-Hush theory and its three key parameters: the reorganization energy, the driving force, and the electronic coupling. Additionally, we discuss the main assumptions and limitations of this theory when studying the CT process in DBA systems. In [Chapters 3 to 5](#), we demonstrate how subtle variations in these three parameters can result in significant changes in CT properties, and how complex excited state dynamics can challenge some of the assumptions and lead to anomalous CT trends. In the second half of this chapter, we introduce the basic

working principles of femtosecond TA spectroscopy, which is used extensively throughout this thesis. In this section, we cover the generation of pump and probe pulses, the interpretation of spectra, and the generation and verification of circularly polarized light.

We begin our research on photoinduced CT with a series of interesting acceptor–donor–acceptor (ADA) molecules in [Chapter 3](#). These triads consist of one benzodithiophene donor and two boron dipyrromethene (BODIPY) acceptors. Exploring the excited state dynamics of these triads provides insight into the relationship between their molecular structures and their photophysical behaviors in different environments. Regardless of the solvent polarity, photoexcitation yields a delocalized vertical excited state through conformational relaxation. In toluene, a non-polar solvent, this excited state further undergoes structural relaxation, leading to a partial CT character. In THF, a more polar solvent, this excited state is followed by a fast CT process. Increasing the distance between the donor and acceptors reduces the degree of delocalization in the excited state and slows down the CT process. Additionally, this study highlights the role of steric hindrance in impeding the CT process by restricting conformational relaxation and disrupting the electronic coupling between the donor and acceptor.

In [Chapter 4](#), we look deeper into how the DA distance dictates the photophysics of three molecular dyads with a varying number of phenyl bridges ( $n = 0, 1, 2$ ). The electron donor and acceptor in these DBA derivatives are dimethylaniline and perylenemonoimide, respectively. At the shortest distance, strong DA interaction leads to a hot excited state with significant CT character upon excitation, resulting in charge separation (CS) within a picosecond. The incorporation of a p-oligophenylene bridge effectively decouples the donor and acceptor, thereby reducing CT polarization in the hot excited state. Theoretically, this would lead to slower CS at longer distances, but TA results show that CS remains fast even at longer distances. Further target analysis and DFT calculations reveal that the hot excited state undergoes ultrafast geometry relaxation, forming a relaxed excited state with enhanced charge delocalization and CT character. This enhanced excited state delocalization contributes to the observed fast CS at the longest distance. These findings underscore the importance of considering factors like hot excited state relaxation and concomitantly enhanced charge delocalization in understanding CS trends.

[Chapter 5](#) is devoted to exploring the effect of tuning the driving force on the CT properties in a series of hybrid DA systems. Specifically, this study focuses on the mechanism of interfacial CT between colloidal CsPbBr<sub>3</sub> nanoplatelets (NPLs) and surface-anchored perylene derivatives. We systematically change the CT driving force through the use of acceptors with different electron affinities and by varying the bandgap of NPLs via thickness-controlled quantum confinement. We begin by demonstrating the formation of a CS state by selectively exciting either the electron donors or acceptors within the same system. Subsequently, we delve into the interplay between kinetics and energetics and its implications on the CT mechanism. TA results on the same

---

NPLs with different acceptors show that excitation of the electron acceptor triggers hole transfer on a picosecond timescale, exhibiting an energetic behavior consistent with the Marcus-normal regime. Interestingly, an opposite energetic behavior is observed when exciting the electron donor, suggesting that the dominant CT mechanism is ultrafast energy transfer followed by hole transfer in the opposite direction. This chapter provides valuable insights into the photophysics of perovskite–molecule systems, offering guidance for the future customization of these hybrid systems for specific applications.

In [Chapter 6](#), we turn to an intriguing phenomenon, known as the "chirality-induced spin selectivity" (CISS), where it is assumed that chiral molecules can have spin-filtering properties. Our goal is to probe the CISS effect in an electrodeless way. In particular, we explore the possibility to study spin-dependent CT in a chiral DA system using circularly polarized TA spectroscopy. In this chapter, we first discuss the generation and detection of spin-polarized excited states in three systems: a chiral DBA molecule, a  $\text{CH}_3\text{NH}_3\text{PbBr}_3$  thin film, and  $\text{CsPbBr}_3$  NPLs. Building upon these findings, we propose a system design for testing the CISS effect based on the hybrid DA systems investigated in [Chapter 5](#). Finally, we address the potential challenges associated with realizing the proposed system and interpreting the results, and suggest additional measurements to overcome these challenges.

Overall, this thesis provides systematic studies on the ultrafast photophysics of various DBA systems, with a focus on the mechanism and dynamics of photoinduced CT in these systems. In addition to the foundational TA spectroscopy, global and target analysis play a crucial role in elucidating the photophysical processes and extracting the CT rate constants. In [Chapters 3](#) and [4](#), we showcase the usefulness of excited state geometry optimizations in understanding the experimental findings that are otherwise difficult to grasp based solely on the ground state DFT/TDDFT calculations. Furthermore, the investigations on DBA molecules in [Chapter 4](#) and hybrid DA systems in [Chapter 5](#) set the stage for insightful discussions in [Chapter 6](#). Obviously, the next logical step is to continue the research presented in [Chapter 6](#). It should be noted that the proposed system design is just one of many potential candidates that may be suitable for such studies. More importantly, the circularly polarized TA data and the literature discussion deepen our understanding of spin-dependent dynamics in various systems. These valuable insights guide the future design of candidate systems that may eventually lead to a better understanding of the CISS effect.



# Samenvatting

Foto-geïnduceerde ladingsoverdracht (LO) is een fundamenteel proces dat op veel plaatsen in de natuur een cruciale rol speelt. Hiernaast is het belangrijk in verschillende technologische toepassingen. Het begrijpen van dit proces is al lange tijd een wetenschappelijk streven. Om inzicht te krijgen in de mechanismen en dynamica van ladingsoverdracht zijn synthetische modelsystemen zoals "donor-brug-acceptor"(DBA) van groot belang. In deze systemen vindt foto-geïnduceerde ladingsoverdracht doorgaans plaats op een ultrasnelle tijdschaal, variërend van enkele nanoseconden ( $10^{-9}$  s) tot honderden femtoseconden ( $10^{-15}$  s). Daarom zijn ultrasnelle spectroscopische technieken, zoals femtoseconde transient absorptie (TA) spectroscopie, essentieel om de processen in real-time te kunnen bestuderen.

In dit proefschrift worden zulke ultrasnelle spectroscopische technieken gebruikt om inzicht te krijgen foto-geïnduceerde ladingsoverdracht (LO) in DBA-systemen en hun derivaten. De nadruk ligt op het begrijpen van de wisselwerking tussen de moleculaire structuur en het resulterende LO-gedrag, wat de weg vrijmaakt voor het aanpassen en optimaliseren van deze systemen voor specifieke toepassingen. In dit werk wordt gebruik gemaakt van femtoseconde-transient absorptiespectroscopie (TA) om de dynamica van de aangeslagen toestand te bestuderen in ensembles van geïsoleerde moleculen in oplossing. Naast de standaard TA techniek wordt in [Chapter 6](#) een aangepaste versie van TA opstelling gebruikt om spin-afhankelijke dynamica te bestuderen met behulp van circulair gepolariseerd licht. Voor het analyseren van de data afkomstig uit TA metingen wordt in [Chapters 3 to 5](#) gebruik gemaakt van 'global- en target analysis' methoden, zoals geïmplementeerd in de open-source software Glotaran. In [Chapters 3 and 4](#) wordt (tijdafhankelijke) dichtheidsfunctionaaltheorie (DFT) toegepast om de experimentele waarnemingen te interpreteren. Samen bieden deze experimentele, analytische en theoretische technieken een alomvattend framework voor het begrijpen van de fotofysica in DBA systemen.

In [Chapter 1](#) geven we een beknopte introductie van het concept van foto-geïnduceerde ladingsoverdracht (LO), de relevantie ervan en de twee typen modelsystemen die in dit proefschrift worden gebruikt om het LO proces te bestuderen. Het doel is om een conceptuele beschrijving te bieden van foto-geïnduceerde LO, met name in DBA systemen. Tot slot schetsen we de structuur van dit proefschrift om lezers te helpen bij het navigeren tussen de hoofdstukken.

In [Chapter 2](#) introduceren we de theoretische achtergrond en de belangrijkste techniek die in dit werk wordt gebruikt. We beginnen met de bekende



Marcus-Hush-theorie en de drie belangrijkste parameters in deze theorie: de reorganisatie energie, drijvende kracht van ladingsoverdracht en de elektronische koppeling. Hiernaast bespreken we de belangrijkste aannames en beperkingen van deze theorie bij het bestuderen van het LO proces in DBA systemen. In [Chapters 3 to 5](#) laten we zien hoe subtiele variaties in deze drie parameters kunnen leiden tot significante veranderingen in LO-eigenschappen en hoe de complexe dynamica van aangeslagen toestanden sommige aannames kan uitdagen en leiden tot anomalieën in de trends in LO. In de tweede helft van dit hoofdstuk introduceren we de basisprincipes van femtoseconde TA spectroscopie, een techniek die uitgebreid wordt gebruikt in dit proefschrift. In deze sectie behandelen we de generatie van ‘pump’- en ‘probe-’ pulsen, de interpretatie van spectra, en de generatie en verificatie van circulair gepolariseerd licht.

We beginnen ons onderzoek naar foto-geïnduceerde ladingsoverdracht met een reeks acceptor-donor-acceptor (ADA) moleculen in [Chapter 3](#). Deze triaden bestaan uit één benzodithiofeen donor-groep en twee boor-dipyrrromethene (BODIPY) acceptoren. Het onderzoeken van de aangeslagentoestandsdynamica van deze triaden geeft inzicht in de relatie tussen hun moleculaire structuren en hun fotofysisch gedrag in verschillende omgevingen. Ongeacht de polariteit van het oplosmiddel resulteert foto-excitatie in een gedelokaliseerde verticale aangeslagen toestand door relaxatie van de moleculaire conformatie. In toluen, een niet-polair oplosmiddel, ondergaat deze aangeslagen toestand een verdere structurele relaxatie, waarbij een toestand met gedeeltelijk LO-karakter wordt gevormd. In THF, een meer polair oplosmiddel, wordt deze initiële relaxatie gevolgd door een snelle vorming van een volledig ladingsgescheiden toestand. Het vergroten van de afstand tussen de donor en acceptor vermindert de mate van delokalisatie in de aangeslagen toestand en vertraagt het LO proces. Deze studie benadrukt de rol van sterische hindering bij het belemmeren van het LO proces door beperking van conformationele relaxatie en verstoring van de elektronische koppeling tussen de donor en de acceptoren.

In [Chapter 4](#) gaan we dieper in op hoe verschillende DA afstanden de fotofysica bepalen van drie moleculaire ‘dyads’ met een variërend aantal fenyl groepen tussen de donor en acceptor ( $n = 0, 1, 2$ ). De elektron-donor en -acceptor in deze DBA-moleculen zijn dimethylaniline en perylenemonoïmide, respectievelijk. Bij de kortste afstand leidt sterke interactie tussen donor en acceptor tot een aangeslagen toestand met aanzienlijk LO-karakter bij excitatie, wat resulteert in ladings scheiding binnen een picoseconde. De introductie van een p-oligofenyleenbrug ontkoppelt de donor en acceptor, waardoor de LO-polarisatie in de initiële aangeslagen toestand wordt verminderd. Theoretisch zou dit leiden tot een langzamere ladings scheiding bij langere afstanden, maar TA-resultaten tonen aan dat ladings scheiding zelfs bij langere afstanden opmerkelijk snel blijft. ‘Target analysis’ en DFT-berekeningen onthullen dat de initiële aangeslagen toestand een ultrasnelle geometrische relaxatie ondergaat, waarbij een gerelaxeerde toestand wordt gevormd met een grotere ladingdelokalisatie en LO-karakter. Deze groetere mate van

---

delokalisatie in de aangeslagen toestand draagt bij aan de waargenomen snelle ladingsscheiding bij de langste afstand. Deze bevindingen benadrukken het belang van subtiele factoren zoals relaxatie van de hete aangeslagen toestand en gelijktijdig verbeterde ladingdelokalisatie bij het begrijpen van trends in de snelheid van ladingsscheiding.

**Chapter 5** is gewijd aan het onderzoeken van het effect van het variëren van de drijvende kracht van LO op de LO-eigenschappen in een reeks hybride DA systemen. Specifiek richt deze studie zich op het mechanisme van LO op het interface tussen colloïdale CsPbBr<sub>3</sub> 'nanoplatelets' (NPLs) en peryleén-moleculen die gekoppeld zijn aan het oppervlak. De drijvende kracht voor LO wordt systematisch gevarieerd door het gebruik van acceptoren met verschillende elektronenaffiniteiten en het variëren van de band gap van NPLs door hun dikte te variëren. We tonen eerst de vorming van een ladingsgescheiden toestand aan door selectief de elektron-donor of -acceptor binnen hetzelfde molecuul te exciteren. Vervolgens duiken we in de wisselwerking tussen kinetiek van het proces en energieën van de verschillende toestanden, en de implicaties hiervan op het LO mechanisme. TA resultaten op dezelfde NPLs met verschillende acceptoren laten zien dat excitatie van de elektron-acceptor leidt tot overdracht van 'gaten' op een picoseconde tijdschaal, waarbij een energetisch gedrag wordt vertoond dat consistent is met het 'Marcus-normal' regime. Interessant genoeg wordt een tegenovergesteld energetisch gedrag waargenomen bij het excitatie van de elektron-donoren, wat suggereert dat het dominante LO mechanisme bestaat uit twee stappen: ultrasnelle energieoverdracht gevolgd door overdracht van een 'gat' in tegenovergestelde richting. Dit hoofdstuk biedt nieuwe inzichten in de fotofysica van perovskiet-molecuulsystemen en geeft richting aan toekomstige modificaties van deze hybride systemen voor specifieke toepassingen.

In **Chapter 6** richten we ons op een intrigerend fenomeen dat bekend staat als "chirality-induced spinselectivity"(CISS), waarin wordt verondersteld dat een chiraal molecuul spin-filterende eigenschappen heeft. Ons doel is om het CISS effect te onderzoeken op een elektrodeloze manier. In het bijzonder onderzoeken we de mogelijkheid om spin-afhankelijke LO te bestuderen in een chiraal DA systeem met behulp van circulair gepolariseerde TA spectroscopie. In dit hoofdstuk bespreken we eerst de generatie en detectie van spin-gepolariseerde aangeslagen toestanden in drie systemen: een chiraal DBA molecuul, een dunne film van CH<sub>3</sub>NH<sub>3</sub>PbBr<sub>3</sub> en CsPbBr<sub>3</sub> nanoplaatjes. Voortbouwend op deze bevindingen stellen we een experiment voor om het CISS effect te testen op basis van de hybride DA systemen die onderzocht zijn in **Chapter 5**. Ten slotte behandelen we de mogelijke uitdagingen die gepaard gaan met het realiseren van het voorgestelde systeem en het interpreteren van de resultaten, en suggereren we aanvullende metingen om deze complicaties te omzeilen.

In het algemeen beschrijft dit proefschrift systematische studies naar de ultrasnelle fotofysica van verschillende DBA systemen, met een focus op het mechanisme en de dynamica van foto-geïnduceerde LO in deze systemen.

Naast de fundamentele TA spectroscopie spelen ‘target en global analysis’ een cruciale rol bij het ophelderen van de fotofysische processen en het extraheren van de LO-snelheidsconstanten. In [Chapters 3 and 4](#) tonen we het nut aan van geoptimaliseerde geometrieën van aangeslagen toestanden bij het begrijpen van de experimentele bevindingen die op basis van alleen grondtoestands DFT/TDDFT berekeningen niet te verklaren zijn. Verder leggen experimenten aan de DBA moleculen in [Chapter 4](#) en hybride DA systemen in [Chapter 5](#) de basis voor inzichtelijke discussies in [Chapter 6](#). Het is vanzelfsprekend dat de volgende logische stap is om het onderzoek dat wordt gepresenteerd in [Chapter 6](#) voort te zetten. Het moet worden opgemerkt dat het voorgestelde systeemontwerp slechts een van de vele potentiële kandidaten is die geschikt kunnen zijn voor dergelijke studies. Belangrijker nog is dat de circulair gepolariseerde TA gegevens en de beschrijving van de relevante literatuurons begrip verdiepen van spin-afhankelijke dynamica in verschillende systemen. Deze waardevolle inzichten geven richting aan het toekomstige experimenten die uiteindelijk kunnen leiden tot een beter begrip van het CISS effect.

# Acknowledgments

Only when I was writing this thesis did I realize that the acknowledgments are actually optional, as I had never come across a thesis that left this part out. After seriously considering the environmental benefits of saving a few pages, I decided not to disappoint certain readers. After all, the acknowledgments and propositions are admittedly my favorite parts of any PhD thesis. More importantly, there are a number of people I do wish to thank.

**Ferdinand**, you may not remember hosting a group of students in your office and introducing them to the OM group's research in August 2016. That encounter marked our first meet and you became the first PI I ever knew at TU Delft. Who could have possibly predicted that three years later, that quiet student who sat in the back would be working in your group as a PhD student? Now, with another four years having passed, my decision to work with you remains devoid of regret. The liberating autonomy you offered bolstered my research independence, and yet your guidance and encouragement were unwavering along the way. Many wonderful memories from this journey are, unsurprisingly, not directly related to science, and some possibly involve a few lobster rolls. Many of these good memories would not have been possible without you and your support, so I would like to thank you for that.

**Herre**, even though we did not meet as frequently as we initially proposed in the PhD agreement, somehow, during each meeting, you always provided advice that I found invaluable. **Tom**, you were the first guide on my academic journey. I consider myself a lucky student, who showed up at the right time for the right project. The email I sent to you, asking for a Master's project, started my wonderful journey in the OM group. Since then, you have always supported me in the exact way I needed, whether through constructive feedback and ideas for my project or assistance in my other career endeavors. **Arjan**, I thoroughly enjoyed all the group meetings you hosted, including the occasional long yet interesting discussions. While having scientific discussions with you sometimes requires a good level of serotonin (to calm my heart rate), your incisive remarks never fail to stimulate my critical thinking. **Laurens**, I would like to thank you for the friendly small talks we have shared during lunch and in the coffee corners.

There is one magician in the group, without whom any spectroscopy work would not have been done as smoothly as it was. **Jos**, I would like to thank you for your tremendous help since my time as a Master's student. I cannot emphasize enough how much I have learned from you about the inner workings of the TRMC, TA, and streak camera labs. I honestly wish I had learned more, so it would have spared me from those recent dreadful moments during the alignment process involving an SHG box.

After all these years in the OM group, I am both grateful and astounded by the multitude of incredible colleagues who have graced my journey. Some taught me a lot in the lab, some directly contributed to my thesis, and some have been instrumental in fostering a vibrant working environment. I would like to begin by thanking those who played various roles in enhancing my PhD journey in the pre-pandemic time. **Jaco** and **Magnus**, thank both of you for training me to use the TA setup. **Solrun** and **Maryam**, I enjoyed sharing many pleasant dinners with both of you and hearing many captivating stories during these gatherings.

Even when the pandemic hit, my incredible colleagues and collaborators managed to produce hard work under restricted conditions. So, **Abbey**, I want to extend my heartfelt thanks to you for your beautiful molecules. Without them, Chapter 4 would not exist. **Maria**, it was a strange time doing experiments together when we had to wear masks and keep our distance. But it was fun exploring spin dynamics in these 2D chiral perovskites together.

Finally, Covid restrictions were lifted and I was able to get to know more about my colleagues' interesting souls. **Bahiya**, thank you for taking care of the lab. Without your dedicated care, it would be far less orderly. **Deepika**, if we had got to know each other earlier, we would have had a lot more fun. I deeply enjoyed exchanging cultural insights with you, our jokes over lunch, and laughing together during comedy shows. And I'm honored for your trust in me photographing your PhD defense. **Indy**, for the record, your acknowledgment was the most epic one I have ever read, just like your blooming muscari and hyacinths. **Jasmeen**, we have agreed on many fundamental things, from strawberries to the coolest office (D1.120) in the building. These core values we share make me believe you are the perfect representative for the OM group in the ChemE PhD council. And I'm glad you agreed with me on this, too. **Jence**, I really appreciated the energy and unique personality you brought to the group. Each time I ran into you in the corridor, I felt a small boost of energy from your engagement. Also, thank you for rescuing me in the TEM lab for countless times and for teaching me how to make these nerve-racking nanoplatelets. **Lara**, it was great sharing an office with you and enjoying our lunch and beer times together. **Maarten**, you are the nicest Maarten I have ever met (not only because I only met one). We shared the same level of enthusiasm for food, especially free food. Although we couldn't agree on the coconut and sandwich, it was a lot of fun looking for the invisible edible gold during the gala dinner. Also, thank you for increasing my Dutch vocabulary by one very important word. **Michael**, you were an exceptional colleague, always with insightful advice and witty jokes. And you organized so many fun activities; among them, the beer tasting was definitely the highlight. It was reassuring to discover that you are not a master of everything, as your chopstick skills are about as sharp as my Dutch. **Reinder**, it was a pleasure to have you as our office visitor from time to time. I enjoyed our chats and liked your science communication story about having a hole in the solar cell. **Reinout**, my quiet colleague, who occasionally surprises us with remarkable comments, thank you for all the favors in the lab. **Valentina**, there is no better way to start a day than by receiving your emails

---

about an incoming Tiramisu. The recipe you shared with me is possibly the most important takeaway message from my PhD. **Yan**, your immense passion for science is just like the craziness of your adventurous life stories. It was a pleasure to discuss with you about Marcus theory and charge transfer in QD-molecule complexes.

Of course, I did not forget about my dear compatriots. **Jiashang**, how come you are always so kind? I cannot remember how many times you have helped me in one way or another without any hesitations over the past 4 years. And thank you once more for being my paronymph. **Jin**, sometimes you understand me better than I do myself. Your prompt suggestion of a dinner at Lychee after my paper rejection was one such example. The Sunday we spent, from a BBQ under the scorching sun until the hotpot under the silvered moon, was one of the best days I can remember. **Hua**, you joined the group during the final months of my PhD, but as they say, better late than never. I'm so glad that you lit up that faint little red dot in the glove box, and as always, the light is light.

And to my fellow master student, **Clementine**, your enthusiasm and independence made me believe I couldn't have asked for a better student to work with. I'm very proud and delighted for you to achieve a 9 for your thesis, and I'm excited to see the bright future that lies ahead for you.

Fortunately, I also had a life during my PhD, during which I shared some memorable times with my dear friends. **Yuting**, our camaraderie began when we were desk mates in high school. I'm extremely grateful that our life paths crossed again in the Netherlands during our Master's times. All these brutally honest conversations, embracing the most vulnerability, make you feel more like a family to me than a friend. **Qianli**, we soon became friends since we were both newcomers to the Netherlands. Over these years, we have spent so much good time together, from exploring food in Den Haag and Rotterdam to traveling in Nice and Venice. I'm delighted that you can be my paronymph. **Lili**, my worthy badminton opponent and my dear meal pal (fàn dā zi), thank you for nudging me to be more sporty, although it does not always work. I wish **Nobel** and **Marie** all the best as they are the first cats I have ever petted. I look forward to meeting you and **Yunlong** in the UK.

I have been truly fortunate to have my family standing by my side throughout these years. My deepest thanks go to my parents and in-laws for their unwavering, unconditional support. Words alone cannot express the depth of my gratitude. As for my partner, **Zhijin**, my greatest achievement during my undergraduate years was finding you. I'm glad you didn't score one grade higher on the university entry exam; otherwise, we wouldn't have known each other. You have been an important part of my life since we were barely adults. I am very grateful that both of us have grown together not apart, and the version of myself when I'm with you is still my favorite.

*Zimu Wei*  
*October 2023*



## Curriculum Vitae



Zimu Wei was born in Ma'anshan, China on 23 October 1995. In 2013, she moved 985 km away from home, to a coastal city in northeastern China to study Chemical Engineering at the Dalian University of Technology. In 2016, she was awarded a scholarship for a 6-month undergraduate exchange program at the Delft University of Technology. After receiving her Bachelor's degree in 2017, she returned to TU Delft for her MSc in Chemical Engineering. In 2019, she obtained her Master's degree (*cum laude*) with a thesis entitled "Two-Photon

Absorption and Sub-Bandgap Linear Absorption in Hybrid Lead Halide Perovskite" under the supervision of Dr. Tom Savenije.

The same year, she continued her academic journey in Delft by joining the group of Prof. Ferdinand Grozema for her PhD. Her research focused on using transient absorption spectroscopy to understand charge transfer in organic donor-acceptor molecules and perovskite-based hybrid assemblies. From 2021 to 2023, she was a member of the PhD Council for the Department of Chemical Engineering, where she promoted communications within the department regarding PhD-related issues, such as PhD trajectory. In addition, she assisted in several bachelor courses and supervised three bachelor's students and one master's student.

Since September 2023, she has joined the group of Prof. Sam Stranks as a postdoc at the University of Cambridge, where she works on time-resolved microscopy and spectroscopy of emerging materials, such as metal halide perovskites.





# List of Publications

## This thesis was based on the following publications:

- Zimu Wei, Jence T. Mulder, Rajeev K. Dubey, Wiel H. Evers, Wolter F. Jager, Arjan J. Houtepen, Ferdinand C. Grozema, *Tuning the Driving Force for Charge Transfer in Perovskite–Chromophore Systems*, The Journal of Physical Chemistry C, 2023, 127 (31), 15406–15415.
- Zimu Wei<sup>#</sup>, Abbey M. Philip<sup>#</sup>, Wolter F. Jager, Ferdinand C. Grozema, *Fast Charge Separation in Distant Donor–Acceptor Dyads Driven by Relaxation of a Hot Excited State*, The Journal of Physical Chemistry C, 2022, 126 (45), 19250–19261. <sup>#</sup>Authors contributed equally.
- Zimu Wei, Sushil Sharma, Abbey M. Philip, Sanchita Sengupta, Ferdinand C. Grozema, *Excited state dynamics of BODIPY-based acceptor–donor–acceptor systems: A combined experimental and computational study*, Physical Chemistry Chemical Physics, 2021, 23 (14), 8900–8907.

## Other publications:

- Valentina M. Caselli, Zimu Wei, Marnix M. Ackermans, Eline M. Hutter, Bruno Ehrler, Tom J. Savenije, *Charge carrier dynamics upon sub-bandgap excitation in methylammonium lead iodide thin films: Effects of Urbach tail, deep defects, and two-photon absorption*, ACS Energy Letters, 2020, 5 (12), 3821–3827.
- Abbey M. Philip, Chao Chun Hsu, Zimu Wei, Magnus B. Fridriksson, Ferdinand C. Grozema, Wolter F. Jager, *Directing charge transfer in perylene based light-harvesting antenna molecules*, The Journal of Chemical Physics, 2020, 153 (14), 144302.
- Sushil Sharma, Zimu Wei, Ferdinand C. Grozema, Sanchita Sengupta, *Structure–Property relationships in multi-stimuli responsive BODIPY-biphenyl-benzodithiophene TICT rigidochromic rotors exhibiting (pseudo-) Stokes shifts up to 221 nm*, Physical Chemistry Chemical Physics, 2020, 22 (44), 25514–25521.
- Zimu Wei, Dengyang Guo, Jos Thieme, Claudine Katan, Valentina M. Caselli, Jacky Even, Tom J. Savenije, *The importance of relativistic effects on two-photon absorption spectra in metal halide perovskites*, Nature communications, 2019, 10 (1), 5342.
- Yao Kang, Wen Sun, Jiangli Fan, Zimu Wei, Suzhen Wang, Mingle Li, Zhen Zhang, Yahui Xie, Jianjun Du, Xiaojun Peng, *Ratiometric real-time monitoring of hydroxyapatite–doxorubicin nanotheranostic agents for on-demand tumor targeted chemotherapy*, Materials Chemistry Frontiers, 2018, 2 (10), 1791–1798.



# List of Presentations

**The work in this thesis was presented at the following conferences:**

## *Poster*

- Sep 2021 - CPR Horizons Conference: Photonics in Chemical Physics (online)
- Jan 2022 - NWO Physics (online)
- Jul 2022 - 6th HRSMC Summer School on Photochemistry (Noordwijk, The Netherlands)
- Jul 2023 - Gordon Research Seminar: Photochemistry (Lewiston, ME, USA)
- Aug 2023 - Gordon Research Conference: Photochemistry (Lewiston, ME, USA)

## *Oral*

- Oct 2020 - 5th International Conference on Bioinspired and Biobased Chemistry & Materials (online).
- Mar 2021 - KNCV - Computational and Theoretical Chemistry Symposium (online).
- Dec 2021 - NWO CHAINS (online)
- Jul 2022 - 28th IUPAC Symposium on Photochemistry (Amsterdam, The Netherlands)
- Sep 2022 - NWO CHAINS (Veldhoven, The Netherlands)
- Apr 2023 - NWO Physics (Veldhoven, The Netherlands)
- Jul 2023 - Gordon Research Seminar: Photochemistry (Lewiston, ME, USA)
- Aug 2023 - IUPAC|CHAINS 2023 (The Hague, The Netherlands)